UNIVERSIDADE ESTADUAL DE CAMPINAS
FACULDADE DE ENGENHARIA ELÉTRICA E DE COMPUTAÇÃO

UNIVERSITY OF CAMPINAS
SCHOOL OF ELECTRICAL AND COMPUTER ENGINEERING

VRIJE UNIVERSITEIT BRUSSEL
APPLIED SCIENCES AND ENGINEERING

UNIVERSIDADE LIVRE DE BRUXELAS
CIÊNCIAS APLICADAS E ENGENHARIA

SALOMÃO MORAES DA SILVA JUNIOR

MICROFABRICATION PROCESS OF PASSIVE AND ACTIVE MICROFLUIDIC DEVICES

PROCESSO DE MICROFABRICAÇÃO DE DISPOSITIVOS MICROFLUÍDICOS PASSIVOS E ATIVOS

CAMPINAS
2019

SALOMÃO MORAES DA SILVA JUNIOR

MICROFABRICATION PROCESS OF PASSIVE AND ACTIVE MICROFLUIDIC DEVICES

PROCESSO DE MICROFABRICAÇÃO DE DISPOSITIVOS MICROFLUÍDICOS PASSIVOS E ATIVOS

Thesis presented to the School of Electrical and Computer Engineering of the University of Campinas in partial fulfillment of the requirements for the degree of Doctor in Electrical Engineering, in the area of Electronics, Microelectronics and Optoelectronics. The Thesis was produced under Cotutela Agreement signed between Unicamp and Vrije Universiteit Brussel.

Tese de Doutorado apresentada ao Programa de Pós-Graduação em Engenharia Elétrica da Faculdade de Engenharia Elétrica e de Computação da Universidade Estadual de Campinas para obtenção do título de Doutor em Engenharia Elétrica, na área de Eletrônica, Microeletrônica e Optoeletrônica. A Tese foi produzida no âmbito de Acordo de Cotutela firmado entre a Unicamp e a Vrije Universiteit Brussel.

Supervisor: Prof. Dr. Jacobus Willibrordus Swart
Co-supervisor: Prof. Dr. Stanislav Moshkalev
Co-supervisor: Prof. Dr. Johan Stiens

THIS CORRESPONDS TO THE FINAL VERSION OF THE THESIS DEFENDED BY PHD STUDENT SALOMÃO MORAES DA SILVA JUNIOR AND SUPERVISED BY PROF. DR. JACOBUS WILLIBRORDUS SWART, PROF. DR. STANISLAV MOSHKALEV AND PROF. DR. JOHAN STIENS.

ESTE EXEMPLAR CORRESPONDENTE À VERSÃO FINAL DA TESE DEFENDIDA PELO ESTUDANTE DE DOUTORADO SALOMÃO MORAES DA SILVA JUNIOR E SUPERVISIONADA PELO PROF. DR. JACOBUS WILLIBRORDUS SWART, PROF. DR. STANISLAV MOSHKALEV E PROF. DR. JOHAN STIENS.

CAMPINAS
2019

Ficha catalográfica
Universidade Estadual de Campinas
Biblioteca da Área de Engenharia e Arquitetura
Rose Meire da Silva - CRB 8/5974

Si38m

Silva Junior, Salomão Moraes da, 1986-
Microfabrication process of passive and active microfluidic devices / Salomão Moraes da Silva Junior. – Campinas, SP : [s.n.], 2019.

Orientadores: Jacobus Willibrordus Swart e Johan Stiens.
Coorientador: Stanislav Moshkalev.
Tese (doutorado) – Universidade Estadual de Campinas, Faculdade de Engenharia Elétrica e de Computação.
Em cotutela com: Vrije Universiteit Brussel.

1. Microfabricação. 2. Microfluídica. 3. Dispositivos microfluídicos. 4. Silício - Corrosão. 5. Microsensores. 6. Fluxo laminar. I. Swart, Jacobus Willibrordus, 1950-. II. Stiens, Johan. III. Moshkalev, Stanislav. IV. Universidade Estadual de Campinas. Faculdade de Engenharia Elétrica e de Computação. VI. Título.

Informações para Biblioteca Digital

Título em outro idioma: Processo de microfabricação de dispositivos microfluídicos passivos e ativos
Palavras-chave em inglês:
Microfabrication
Microfluidics
Microfluidic devices
Silicon - Etching
Microsensors
Laminar flow
Área de concentração: Eletrônica, Microeletrônica e Optoeletrônica
Titulação: Doutor em Engenharia Elétrica
Banca examinadora:
Jacobus Willibrordus Swart [Orientador]
Leandro Tiago Manera
José Alexandre Diniz
Ricardo Cotrin Teixeira
Antônio Carlos Seabra
Johan Stiens
Wim De Malsche
Rik Pintelon
Chiara Galletti
Data de defesa: 17-04-2019
Programa de Pós-Graduação: Engenharia Elétrica

Identificação e informações acadêmicas do(a) aluno(a)
- ORCID do autor: 0000-0003-0793-7464
- Currículo Lattes do autor: http://lattes.cnpq.br/5316005083146655

COMISSÃO JULGADORA – TESE DE DOUTORADO
JUDGMENT COMMITTEE - DOCTORAL THESIS

Candidato - PhD candidate: Salomão Moraes da Silva Junior **RA:**142353
Data da Defesa - Public defense date: 17/04/2019

Data da deliberação VUB - Deliberation date VUB: 21/06/2019

Título da Tese: “PROCESSO DE MICROFABRICAÇÃO DE DISPOSITIVOS MICROFLUÍDICOS PASSIVOS E ATIVOS”

Thesis title: “MICROFABRICATION PROCESS OF PASSIVE AND ACTIVE MICROFLUIDIC DEVICES”

JUDGMENT COMMITTEE UNICAMP - COMISSÃO JULGADORA UNICAMP

Prof. Dr. Jacobus Willibrordus Swart (chairman /presidente, FEEC/UNICAMP)
Prof. Dr. Leandro Tiago Manera (FEEC/UNICAMP)
Prof. Dr. José Alexandre Diniz (FEEC/UNICAMP)
Dr. Ricardo Cotrin Teixeira (CTI)
Prof. Dr. Antônio Carlos Seabra (EP/USP)
Prof. Dr. Johan Stiens (ETRO/VUB)
Prof. Dr. Wim De Malsche (VUB)
Prof. Dr. Rik Pintelon (VUB)
Prof. Dr. Chiara Galletti (University of Pisa)

JUDGMENT COMMITTEE VUB - COMISSÃO JULGADORA VUB

Prof. Dr. Johan Stiens (ETRO/VUB)
Prof. Dr. Wim De Malsche (chairman / presidente, VUB)
Prof. Dr. Rik Pintelon (vice-chairman / vice-presidente, VUB)
Prof. Dr. Chiara Galletti (University of Pisa)
Prof. Dr. Stanislav Moshkalev (CCS/UNICAMP)
Prof. Dr. Jacobus Willibrordus Swart (FEEC/UNICAMP)
Prof. Dr. Leandro Tiago Manera (FEEC/UNICAMP)
Prof. Dr. José Alexandre Diniz (FEEC/UNICAMP)
Dr. Ricardo Cotrin Teixeira (CTI)
Prof. Dr. Antônio Carlos Seabra (EP/USP)

The defense minutes, with the respective signatures of the members of the Judging Commission, they are located in the students' academic life process.

A ata de defesa, com as respectivas assinaturas dos membros da Comissão Julgadora, encontra-se no processo de vida acadêmica do aluno.

DEDICATION

I dedicate this work to God and the Lord Jesus Christ, the gift of life, and the wonderful plan of salvation. I dedicate to my entire family, especially my mother who is a reference in my life, she always encouraged me to follow the academic life since my childhood until today, taught me the values about life and people, taught me to never give up and mainly to work hard to realize my dreams. I dedicate to my love, to my wife. I dedicate this to all who supported and helped during the whole process.

ACKNOWLEDGMENTS

In this section I would like to make public all my thanks to the people who contributed directly or indirectly to the development of this doctoral thesis. Citing names is a very delicate process, but necessary. If perhaps, I end up forgetting the name of someone, I'm sorry, because my memory always fails.

- ✓ Thanks God first because the Lord has so far helped me, I thank God that I have never lacked faith, health and motivation to continue. I thank my family, my brothers and friends in Manaus city.
- ✓ I want to make public my thanks to my companion, my partner, my love, my friend and wife, Patricia Salviani Moraes, for the kindness, companionship, support, help and understanding. I love you.
- ✓ Thanks to my advisor, Prof. Dr. Jacobus Willibrordus Swart for the opportunity, the trust deposited, for the freedom and autonomy that allowed me to develop this academic work.
- ✓ Thanks to my Russian co-advisor, Prof. Dr. Stanislav Moshkalev for the discussions and directions developed throughout this work, for attention, confidence, patience and all support. Thank you for the partnership and contribution in the formation of my profile as a researcher and academic life.
- ✓ Thanks to my Belgian co-supervisor, Prof. Dr. Johan Stiens, for the opportunity of a sandwich doctorate in the city of Brussels in Belgium for 10 months, thank you for the partnership, discussions and guidelines developed throughout this work, for the attention, confidence, patience and all support. Thank you for the partnership that eventually evolved into a double degree. Thank you for contributing to the formation of my researcher profile and academic life, for sure this experience was a watershed in my trajectory.
- ✓ Thanks to Prof. Dr. Leandro Tiago Manera for the fellowship, for the advice and teachings throughout the master's and doctorate, and for contributing in a significant way in my academic formation with many precious advices. Thanks to Prof. Dr. José Alexandre Diniz, Prof. Dr. Fabiano Fruett, for the tips and punctual contributions in this work, for the conversations, directions and for having

contributed significantly in my academic formation, thank Prof. Dr. Ioshiaki Doi for the talks and tips for the development of this work.

- ✓ Thanks to Prof. Dr. Gustavo Fraidenraich and Prof. Dr. Orio Lacerda, for the companionship for the partnership, for the friendship, for the precise counsels and enriching conversations, thank you!
- ✓ Thank you for joining us with graduate colleagues and staff who develop or develop their work at CCS / Unicamp.
- ✓ I would especially like to thank my friends Prof. Dr. Luiz Gustavo Turatti and Marco Aurélio Keiler for the pleasant conversations, lunches, companionship, advice, help and support, contributions and corrections made for this work.
- ✓ I thank my colleague and master Mario Eduardo who helped me a lot with advice, tips and archival models for the sandwich doctorate in Belgium.
- ✓ Thanks to all technical and administrative staff of the CCS, thank you all without exception. I thank the entire IFGW / Lamult team, especially the lab technician Eduardo for his attention and concern in teaching to handle the equipment and evaluation of the measures.
- ✓ I thank the CTI team, especially Dr. Ricardo Cotrin, Cristina Adamo and Alexander Flacker. Dr. Ricardo Cotrin who has helped me a lot during my PhD journey.
- ✓ Thanks to Prof. Dr. Alberto Fracassi and Dosil for support with fluorescence measurements.
- ✓ Thank you to all LNLS / LMF technical staff, especially to Mr. Angelo Luiz Gobbi, who allowed me to access the facilities of this renowned research laboratory. I especially thank Maria Helena de Oliveira Piazzeta for all the affection, attention, advice, teachings and intelligent solutions for my propositions, thank you for the patience, companionship, trust, dedication and objectivity without which I would not be able to leverage my learning in the area of Microfluidics and in carrying out this research work, with the important contribution of this special person, thank you Maria Helena! Thank you to technician Rui for the help in using the profilometer and the entire LMF family, thank you very much!

✓ I thank all my friends and wanderers I met at Unicamp in Campinas. The class of the house for the always pleasant meetings, philosophical talks, laughter, companionship, friendship and for all help and encouragement.

✓ I thank all my friends and companions of the IBBG, and especially the friends who were at my wedding ceremony, in particular I thank Pastor Laurencie, friend and companion, Pastor Mateus and Pastor Clademilson.

✓ In this last part, I thank in particular the friends and professors of the State University of Amazonas - UEA, in particular I thank Prof. Roberto Higino Pereira da Silva, who motivated me to become a graduate student and helped me very importantly in my transition from Manaus to Campinas, helped me significantly in my training. I thank the teachers Jozias Parente, André Printes, Cleto Leal, Júlio Feitosa and Charles Melo for the conversations, tips, advice, confidence, and encouragement to get involved in postgraduate studies. Thank you to the teachers: Victor Valenzuela, Claudionor, Júlio Tóta, Maria Betania, Maria das Graças, Laurimar, Raimundo Cláudio, José Costa, Almir Kimura and all EST / UEA professors who contributed in some way to my training. Thanks to all the researchers and friends of the Nucleus of Embedded Systems - NSE / UEA, especially Luis, Guido, Josi, Nilson, Leonardo Ramos and all friends of the NSE without exception, I especially thank Patricia for answered my request and sent my documents for postgraduate enrollment.

✓ I thank the financial support of the Foundation for Research Support of Amazonas - FAPEAM, with a PhD grant from the "RH-Doutorado" – "Fluxo contínuo", nº 001/2014.

✓ I thank everyone who has contributed in some way to my life, cheering, supporting, helping, sharing this achievement with all of you!

“Only discovers the great talent, giving them an opportunity.”

(Unknown author)

ABSTRACT

The miniaturization process allows reactions of liquid mixtures and faster analyzes, in smaller volumes, with portable and more reliable devices. The main challenges are in the manufacturing with high precision and integration of microchannels with sensors. We have developed complete protocols for obtaining microchannels with integrated actuators and sensors, involving conventional microfabrication and characterization techniques compatible with clean room facilities. Resulting in devices fabricated in silicon, glass and polydimethylsiloxane (PDMS), with microchannels widths between 100 and 458 µm, depth between 20 and 64 µm. We present new methodologies for Lab-On-a-Chip (LOC) applications: 1) System with microchannels integrated to a capacitive sensor. 2) Active mixer with electromagnetic actuators in microchannels. 3) Passive mixer with coupled terahertz sensor for control of concentration of ethanol on demand. We present the complete microfluidic system for the micro droplets generation of water/oil and micro capacitive sensor, for detection and control of volume and droplet velocity up to 1mm in length. We present an active mixer, with integrated PDMS membrane with electromagnetic actuators, establishing the correlation between the liquid mixture improvement and the oscillation frequency. We present sub-THz sensor coupled to microfluidic platform with non-invasive, contactless and label-free measurements for determination of ethanol concentration and control on demand. We demonstrated on-line sensing, operating at 60 GHz, with a dynamic range of 2.79 dB, ethanol concentration control with a variation of 0.32% (v / v) and passive micro-mixer with curved channels operating in laminar flow with number of Reynolds <16.26 and Peclet> 25700. In addition, we present a preliminary study with simulation of finite element method (FEM) in comparison with theoretical models. We presented the fluid characterization regime and application of microfluidic devices.

Keywords: Microfabrication, Microfluidic, Microfluidic devices, Silicon - etching, Microsensors, Laminar flow.

RESUMO

O processo de miniaturização permite reações de misturas líquidas e análises mais rápidas, em volumes menores, com dispositivos portáteis e mais confiáveis. Os principais desafios estão na fabricação com alta precisão e integração de microcanais com sensores. Nós desenvolvemos protocolos completos de obtenção de microcanais com atuadores e sensores integrados, envolvendo técnicas convencionais de microfabricação e caracterização compatíveis com instalações em sala limpa. Resultando em dispositivos fabricados em silício, vidro e polidimetilsiloxano (PDMS), com microcanais com largura entre 100 e 458 µm, profundidade entre 20 e 64 µm. Apresentamos novas metodologias para aplicações em Lab-On-a-Chip (LOC): 1) Sistema com microcanais integrados a um sensor capacitivo. 2) Misturador ativo com atuadores eletromagnéticos em microcanais. 3) Misturador passivo com sensor terahertz acoplado, para controle de concentração de etanol sob demanda. Apresentamos o sistema microfluídico completo de geração de micro gotas de água/óleo e micros sensor capacitivo para detecção e controle de volume e velocidade de gotas de até 1mm de comprimento. Apresentamos misturador ativo, com membrana de PDMS integrada com atuadores eletromagnéticos, estabelecendo a correlação entre a melhoria de mistura líquida e a frequência de oscilação. Apresentamos sensor sub-THz acoplado a plataforma microfluídica com medições não invasivas, sem contato e livre de rótulos para a determinação da concentração de etanol e controle sob demanda. Demonstramos sensoriamento on-line operando a 60 GHz, com faixa dinâmica de 2,79 dB, controle da concentração de etanol com variação de 0,32% (v / v) e micro misturador passivo com canais curvos operando em fluxo laminar, com número de Reynolds <16.26 e Peclet >25700. Em adição, apresentamos um estudo preliminar com simulação de método de elementos finitos (MEF) em comparação com modelos teóricos. Apresentamos a caracterização de fluidos e a aplicação de dispositivos microfluídicos.

Palavras-chave: Microfabricação, Microfluídica, Dispositivos microfluídicos, Corrosão - silício, Microsensores, Fluxo laminar.

LIST OF FIGURES

Figure 2.1 – Microfluidic devices market in $B (Adapted from DÉVELOPPMENT YOLE, 2015). 29

Figure 2.2 – Illustration of the first microsystem for gas chromatography made on silicon substrate at Stanford University in the late 1970s (Adapted from TERRY, 1979). 30

Figure 2.3 – General microfluidic system (BSOUL, 2016)............................... 31

Figure 2.4 – Flow regimes. (a) Laminar flow regime with Reynold number < 2000; (b) Transitional flow regime with 2000< Reynold number < 4000; (b) Turbulent flow with Reynolds number > 4000. Adapted from Omega Engineering Ltd. 36

Figure 2.5 – The thermal movement of molecules and diffusion. (a) and (b) Molecules of two species with distinct concentrations and concentration graph; (c) Increased molecular agitation increases diffusion between species; (d) Gradient of concentration in modification, from an area of higher concentration to a lower concentration; (e) Thermal and kinetic equilibrium of species molecules; (f) Concentration gradient at equilibrium, totally different from the initial condition. Adapted from (CUSSLER, 1997). 37

Figure 2.6 –Sodium chloride diffusion in water. Adapted from (www.quora.com). 39

Figure 2.7 – Microfabrication cycle. Adapted from (BESSELER, 2008).......... 40

Figure 2.8 – Microfabrication processes of the MOS transistor. (I) Substrate selection; (II) Thin film deposition; (III) and (IV) lithographic processes; (V) Thin film etching; (VI) Photoresist removal; (VII) and (VIII) Stages of ion implantation; (IX) Oxidation of the silicon wafer; (X) Etching after lithography; (XI) Growth of the gate oxide; (XII) Deposition of aluminum; (XIII) Etching of aluminum (Adapted from TURATTI, 2003; SWART 2008).. 41

Figure 2.9 – Channels microfabrication process in glass substrates. (I) Substrate coated with Cr layer and photoresist AZ-1500; (II) Positioning of the mask and exposure to UV radiation; (III) Photoresist development; (IV) Thin film etching; (V) Glass etching

with HF-NH4F; (VI) Obtaining the microchannel with semicircular profile; (VII) Glass-glass thermal sealing. Adapted from (COLTRO, 2008). 43

Figure 2.10 – Wet etching silicon with isotropic and anisotropic channel profiles. Adapted from (SEIDEL, 1990). 44

Figure 2.11 – (a) Cavities used to make membranes; (b) Microchannels used for microfluidic devices. Adapted from (CYRO, 2004). 47

Figure 2.12 - Chemical structure contained in SU-8 formulations. Eight reactive epoxy groups allow a high degree of polymerization. Adapted from (CAMPO and GREINER, 2007). 48

Figure 2.13 - Thickness of the layer of different photoresist of the SU-8 2000 group as a function of the speed of rotation of the deposition (Microchem SU-8 datasheet). 49

Figure 2.14 – Chemical structure of PDMS. Adapted from (KUNCOVA-KALLIO et al., 2006). 49

Figure 2.15 – Schematic of the soft lithography technique, molding / demolding of elastomers. Adapted from (CUTKOSKY, 2008). 51

Figure 2.16 – Molding / demolding with PDMS. (a) SU-8 template; (b) PDMS deposited on the SU-8 template; (c) Conformation of the PDMS on the curing mold; (d) Manual extraction of the cured PDMS; (e) Plasma treatment for surface activation; (e) Microchannel sealing; (f) removing the cover layer. Adapted from (SCHIANTI, 2008). 52

Figure 2.17 – Anodic bonding between glass and silicon substrates. Adapted from (GREENWOOD, 1988). 53

Figure 2.18 – Anodic bonding between glass-glass, glass-silicon and silicon-silicon substrates. (a), (b), (c) and (f) with self-aligned microchannel on top and bottom. (d) and (e) with microchannel in the bottom substrate. Adapted from (GAD-EL-HAK, 2006; GREENWOOD, 1988). 54

Figure 2.19 – (a) Substrate with polymer SU-8 with the photo chromed microchannels; (b) Substrates with intermediate layer with SU-8 for sealing; (c) Substrates with intermediate layer SU-8 and PMMA. Adapted from (SCHIANTI, 2008). 55

Figure 2.20 – Mechanism of direct bonding reaction. (a) surface activation reaction; (b) formation of the Si-O-Si bond (JIA et al., 2004). 58

Figure 2.21 – Subareas in the field of microfluidics. (Adapted from YANG et al., 2018). 58

Figure 2.22 - Representation of a microsystem made of polyester-toner containing integrated electrodes and channels. Points 1, 2, 3 and 4 indicate reservoirs for sample, buffer, sample discard and buffer discard, respectively. The points *i* and *ii* indicate the electrodes for cell excitation and recording of the resulting signal, respectively. (Adapted from COLTRO, 2008). 59

Figure 2.23 – Photographs of (a) microparticles migrating through the multi-orifice microchannel with at Re_c channel, Re_c ~ 63, and snapshots in a sudden expansion of the channel showing different scales of vortex flows; (b) Vortices generated with Re_c = 16; (c) Migration vortices of the particles generated with Re_c = 47; (d) Vortices generated with Re_c = 78; (e) Vortices generated with Re_c = 109 (PARK et al., 2009). . 60

Figure 2.24 – DMF device used for multiplexed cell-based assays. a) Top-view schematic of full device bearing six assay zones. b) Top- and side-view schematics of one assay zone. (BOGOJEVIC et al., 2012). 61

Figure 2.25 – The integration of synthetic biology and optofluidics. Synthetic biological systems of different length scales, ranging from single molecule, to single cell, and cellular population have been engineered for both biotechnology and therapeutic applications. (Adapted from CHENG et al., 2012). 62

Figure 3.1 – General overview of microfluidic designs. 63

Figure 3.2 - Mask of microfluidic devices. (a) Serpentine and Spiral; (b) Triangular structure and Y; (c) Cross and H; (d) Trident structure and Y with two outlets, based on passive devices applied to liquid mixers. 64

Figure 3.3 - Illustration of the fabrication processes of microfluidic devices in silicon. 67

Figure 3.4 – Block diagram of the fabrication processes of microfluidic devices in silicon. 68

Figure 3.5 – Silicon [100] etching rate in KOH, taking into account temperature and concentration of etching solution. Etching rate in function of the concentration and temperature. (Adapted from CYRO, 2004; PAL, 2017). 70

Figure 3.6 – Etching rate in silicon dioxide. Etching rate taking into account concentration. and temperature. (Adapted from CYRO, 2004). 71

Figure 3.7 – On the left is the system for silicon etching, on the right is the wafer holder with the silicon in the etching process... 72

Figure 3.8 – Profilometer measurements, depth and roughness. In the top part, microchannel depth and width. In the bottom part, roughness measurements made in the bottom part of the microchannel.. 74

Figure 3.9 – SEM and AFM Micrographs. (a) Microchannel top view. (b) Profile roughness at the bottom of the microchannel. Micrograph in perspective with roughness measurement of the microchannel. Micrograph and roughness graph, silicon characterization. (c) Micrograph of the roughness in an area of 5 x 5 μm2. (d) Microchannel roughness plot. (e) Angle formation of 54.14º between the planes (100) and (111). 75

Figure 3.10 – Measurement of microchannels with more precision with 3D profilometer Dektak 150, technique of styles contact. 77

Figure 3.11 – Microchannel micrograph and convex edge etching................... 78

Figure 3.12 – Stages of microfabrication in glass: (I) Photoresist deposition on clean substrate; (II) Photogravure; (III) Disclosure and Heat Treatment; (IV) Etching in HF; (V) Photoresist Removal and Cleaning; (VI) Surface activation; (VII) Sealing..... 80

Figure 3.13 – PVC and teflon supports used in glass etching processes for different substrate sizes; (a) For glass substrates 10”and adjustable, (b) 3” and (c) 5”. 82

Figure 3.14 – Etching steps in glass after lithography process, starting from hard-baking: step III thermal treatment, step IV - support placement and etching in buffer and HF 20%.. 82

Figure 3.15 – Depth obtained from microchannels, achieved with 5 minutes etching time. Microchannel depth measured with profilometer.................................... 86

Figure 3.16 – Design with etched cross curves and zoom in section of the microchannels intersections.. 87

Figure 3.17 – Device fabricated with glass etching technique. Design 'H' shaped curve and zoom in the microchannels cross section. 87

Figure 3.18 – Glass microchannel 3D profile obtained by contact stylus profilometry technique (a) Measurement scheme with diamond tip of 12.5 µm. (b) 3D channel profile acquired. 88

Figure 3.19 – Microfabrication stages for PDMS mold: (I) Cleaning the silicon substrate; (II) Photoresist deposition; (III) Photolithography; (IV) Developing; (V) PDMS deposition on the curing template; (VI) Demolding of the PDMS................................ 90

Figure 3.20 – SU-8 microfabrication molds in PDMS: (a) Circular metallic mold, containing at its base a quartz slide with SU-8 photographed; (b) Magnification of the SU-8 mold with microchannel shaped design. 91

Figure 3.21 – Flat molds: (a) and (b) square metallic molds, each containing a glass slide with printed design on paper and placed in the bottom part of the mold...... 92

Figure 3.22 – Tubes alignment system: (a) Silicone tubes with nails at the ends to avoid obstruction for PDMS; (b) Metallic mold containing the SU-8 design; (c) Acrylic fixed on the mold, containing holes aligned to design reservoir. 92

Figure 3.23 – Preparation of PDMS for sealing: (a) Removal of PDMS nails and silicone tubes; (b) Removal of excess PDMS for sealing. 93

Figure 3.24 – Profile of a Microcanal mold in SU-8 for molding in PDMS. 94

Figure 4.1 – Profiles of microchannels obtained by profilometer measurements. (a) Trapezoidal profile obtained in silicon by etching with KOH; (b) Circular segment profile obtained in glass by etching with HF; (c) SU-8 (soft lithography) quasi-rectangular mold profile. 97

Figure 4.2 –3D profile of measured PDMS microchannel, using Dektak 3D profilometer. 98

Figure 4.3 – (a) Profiles of glass microchannels obtained with etching techniques with HF. (b) Profile of PDMS microchannels, depths of 20 µm. 99

Figure 4.4 – Simulation tree in COMSOL 4.3a. 105

Figure 4.5 – (a) Behavior of fluid velocity along the microchannel (50 µm). (b) Pressure behavior of the fluid along the microchannel. (c) Behavior of the concentration gradient along the “H” channel. 107

Figure 4.6 – Curve in H with two liquids without mixture. (a) Model simulated in Comsol; (b) Result obtained in laboratory. 108

Figure 4.7 – (a) H curve in Comsol, modulating the width of the liquids as a function of the flow, the inflow of the inlet 1 greater than the inlet 2. (b) H- shaped curve with laboratory test. 108

Figure 4.8 – H-curve with two liquids without mixing, with the addition of an edge contour marker. 109

Figure 4.9 – H-shaped curve with two liquids without mixing: (I), (II), (III) and (IV) Modulation of the green liquid with a slightly larger flow rate than the red liquid; (V) equalized flow rates for liquids; (VI), (VII) and (VIII) Modulation of the green liquid slightly lower than that of the red liquid; (IX) Region chosen for image enlargement and evaluation of modulation. 110

Figure 4.10 – (a) Fluid velocity along the microchannel in Y-Curve. (b) Pressure along the microchannel at the Y-Curve. (c) Surface diffusion coefficient. 111

Figure 4.11 – Y-curve with two liquids without mixing: (a) Model simulated in Comsol; (b) Result obtained in laboratory. 112

Figure 4.12 – Y- shaped curve with two unmixed liquids: (a) Equal volumetric flow rates for blue and red liquids; (b), (c), (d), (e), (f), (g) and (h) Modulation of the red liquid with a slightly larger volumetric flow rate than that of the blue liquid; (i), (j), (k) and (l) Modulation of the liquid in red slightly smaller than that of the blue liquid. ... 112

Figure 4.13 – (a) Velocity along the microchannel in the Cross Curve. (b) Pressure along the microchannel in the Cross Curve. (c) Focused flow and graph of concentration, simulation in the Comsol in the Cross Curve. 113

Figure 4.14 – (a), (b), (c) and (d) Modulation of the blue liquid with a slightly larger volumetric flow rate than the liquid in red; (e), (f), (g) and (h) Modulation of the blue liquid with flow approximately equal to that of the liquids in red; (i), (j) and (k) Modulation of the blue liquid with a slightly lower volumetric flow rate than the liquid in red (l) Same flow for the blue liquids and the two liquids in red. 114

Figure 4.15 – (a) and (b) Modulation of the blue liquid with a slightly larger volumetric flow rate than the liquid ones in red; (c) Modulation of the blue liquid with

flow approximately equal to the liquid in red; (d), (e) and (f) Modulation of the blue liquid with a slightly lower volumetric flow rate than the red liquids. 114

Figure 4.16 – (a)Velocity behavior along the microchannel in T-Curve. (b) Pressure behavior along the T-curve microchannel. (c) T-curve diffusivity of liquids 115

Figure 4.17 – T-curve shaped design, diffusion coefficient not increased along the channel path, with volumetric flow ratio Q_{blue}/Q_{red} (1:1). 116

Figure 4.18 – Laboratory setup for performing microfluidics experiments. 117

Figure 4.19 – Spiral concentric diffusivity scale along the microchannel 117

Figure 4.20 – Curve H laboratory test, red liquid capillary effect: (I) Strangulation of the green liquid with the decrease of the flow in relation to the red liquid; (II), (III) and (IV) Deformation between the liquids generated by the shear point. 118

Figure 4.21 – Curve H, laboratory test diffusivity control from the flow: (I) Dirt particle generating instability at the liquid-liquid interface; (II), (III), (IV), (V) and (VI). Controlling the diffusivity with the increase of the flow applied in the system........... 119

Figure 4.22 – Dirt particle and region at the liquid-liquid interface before and after instability, Qred = Qgreen = 100 µl/min. 120

Figure 4.23 – Measurement of the diffusivity region Qred and Qgreen = 50 ul/min. (a) Line of diffusivity without mixing enhancement element (b) Line of diffusivity with mixing enhancement element. 120

Figure 4.24 – Multilayer structure schematic of the mixer design and fabrication process step by step. (a)Active micromixer formation by three layers, from bottom to top, glass, membrane and structural PDMS. (b) Microfabrication step by step of micromixer. 122

Figure 4.25 – Experimental setup with microfluidic plattform actuation. 124

Figure 4.26 – Active micro mixer. (a) Device on top of electromagnet. (b) Chamber side view and actuation. (c) Chamber top view with liquid stream lines. 124

Figure 4.27 – Effect of frequency sweep on the inter diffusivity of liquids in the actuation chamber. 125

Figure 4.29 - Spontaneus droplet generation in a Ψ-Shaped microchannel and RSE sketch. 127

Figure 4.30 - Experimental setup used to acquire the capacitive and resistive response. 128

Figure 4.31 - Capacitance oscillation due to droplet water/oil passage during 60 seconds. 129

Figure 4.32 - Synchronized pictures of droplets over RSE sensor. 130

Figure 4.33 - THz sensing scheme. (a) Capillary tube inserted into wave path in ZY plane. (b) Electromagnetic field along the wave-guide in the XY plane. (c) Waveguide to be attached to the MVNA. 132

Figure 4.34 - Microchannel and micromixer. (a) 3D image of microchannel profile measured by profilometer. (b) Microfluidic device fabricated in a glass microscope slide and sealed by PDMS. 133

Figure 4.35 – Dean vortices effect and generation of secondary flow. (SUDARSAN et al., 2006). 135

Figure 4.36 - Two configurations of the microfluidic chemical sensing platform: (a) Validation with standard samples solutions of alcohol. (b) Microfluidic configuration: passive micromixer characterization and flow control by syringes pumps. 136

Figure 4.37 - Experimental setup. (a) Capillary tube integrated into a wave-guide. (b) Syringe pumps and mass flow rate controlling. (c) Micromixer with blue dye color (ethanol), red dye color (water) and purple as real liquid mixture along the microchannel. 137

Figure 4.38 - Sub-THz sensor response versus ethanol concentration for known ethanol concentration freshly pre-prepared. 138

Figure 4.39 - Fitted curve of raw data, THz sensor response for known ethanol concentration. 139

Figure 4.40 - Experimental correlation between ethanol mass flow rate in ethanol concentration. 140

Figure 4.41 - Experimental calibration of linear control, in micromixer device ethanol concentration, with five required concentration points on demand, for each selected concentration point there is a specific experimental mass flow rate, in this particular, to reach desired concentration. 142

Figure 4.42 - Comparison between points of required ethanol concentration on demand versus real concentration measured. 144
Figure A.1 – Cell Reynolds number plot with channel width of 100 μm and depth of 33 μm. 162
Figure A.2 – Plot of error and iteration number to converge solution. 164
Figure A.3 – Plot of free tetrahedral mesh with a COMSOL Multiphysics ® predetermined element size of "extra fine" was utilized. 165
Figure A.4 – Parameters of fluid discretization P1+P1 utilized in COMSOL. 166

LIST OF TABLES

Table 3.1 – Parameters of oxidation furnace, at the temperature of 1000ºC. (Process adapted from (SWART, 2008)... 66

Table 3.2 – It shows the conditions and results for samples from 1 to 6, containing etching parameters, such as temperature and time correlated with depth, etching time, etching rate and roughness. 73

Table 3.4 – Etching rate evaluation for Perfecta microscope glass slides.......... 84

Table 3.5 – Microfluidic channels achieved with glass etching technique, after 5 minutes. 86

Table 4.1 - Dimensions of some designs obtained during the Microfabrication process. 96

Table 4.2 – Volumetric flow rate sweeping, aiming for leakage tests and Reynolds number evaluation, microchannel fluid time and velocity in silicon channels. 101

Table 4.3 – Volumetric flow rate sweeping, aiming for leakage tests and Reynolds number evaluation, microchannel fluid time and velocity in PDMS channels. 101

Table 4.4 – Dimensions, cross section, velocity and diameter for the calculation of the Reynolds number.. 102

Table 4.5 – Comparison between the results obtained in the experiments and simulation at Comsol.. 106

TABLE 4.6. Typical liquid properties at room temperature (20ºC) (ZAKURENOV et al., 1975; STREET et al., 1996). 136

TABLE 4.7 The Characterization of water-alcohol mixtures into a microfluidic device and joint section, based on mass flow rate sweeping. Expected alcohol concentration versus real concentration measured, the alcohol absorption measured was translated in sample concentration. 141

TABLE 4.8. Calculated flow rate for required concentration on demand. Comparison between ethanol concentrations controlled on demand and measured. ... 144

Table A.1 – Results obtained in the experiments and simulation at Comsol. .. 163

LIST OF ACRONYMS AND ABBREVIATIONS

AFM - Atomic Force Microscopy

BOE - Buffered Oxide Etchant

CCSNano - Center Semiconductors Components and Nanotechnologies

CFD - Computational Fluid Dynamics

C^4D – Capacitively-Coupled Contactless Conductivity Detection

CMOS - Complementary Metal Oxide Semiconductor

CVD - Chemical Vapor Deposition

DMF – Digital Microfluidic

DI – Deionized

DRIE – Deep Reactive Ion Etching

EDS - Energy Dispersive X-Ray Spectrometry

EOF – Electroosmotic Flow

ETRO –Department of Electronics and Informatics at VUB

FIB - Focused Ion Beam

IC – Integrated Circuit

ICP – Inductively Coupled Plasma

IDE – Interdigitated Electrode

LMF – Microfabrication Laboratory

LNLS - Synchrotron Light National Laboratory

LOC - Lab On a Chip

MEMS - Micro Electrical Mechanical Systems

MIF – Metal Ion Free

MOS – Metal Oxide Semiconductor

mm-wave – Millimeter wave

MSE - Electrophoretic microsystems

PDMS - Polydimethylsiloxane

PECVD - Plasma Enhanced CVD

RCA - Radio Corporation of America

RF – Radio frequency

RIE – Reactive Ion Etching

RSE – Ring shaped electrode

SEM - Scanning Electron Microscopy

SIP – System In a Package

SOI – Silicon On Insulator

μTas – Total Analyses micro systems

UV – Ultraviolet

VPE - Vapor-Phase Epitaxy

XPS - X-ray photoelectron spectroscopy

SUMMARY

1 INTRODUCTION 26
2 MICROFLUIDIC AND MICROFABRICATION TECHNIQUES 29
2.1. Miniaturization 30
2.2. Microfluidics and Fluids Mechanics 32
2.3. Diffusivity in liquids 37
2.4. Microfabrication Techniques and Processes 39
2.4.1. Microfabrication Stages 40
2.4.2. Chemical Etching Processes 44
2.4.3. Polymer Microfabrication Techniques and Processes - SU8 and PDMS 47
2.5. Microchannel sealing 53
2.5.1. Anodic bonding technique 53
2.5.2. Polymer bonding technique 55
2.5.3. Adhesive bonding technique 56
2.5.4. Direct bonding technique 57
2.6. MICROFLUIDIC AREAS 58
3 MICROFLUIDIC DEVICES FABRICATION 62
3.1. Hard Mask set design 62
3.2. Microfabrication process 64
3.2.1. Microfabrication process on silicon 65
3.2.1.1. Process stages 67
3.2.1.2. Microchannels and Silicon etching 70
3.2.2. Microfabrication process in glass 78
3.2.2.1. Microfabrication steps in glass 79
3.2.2.2. Etching of glass slides 81
3.2.3. Microfabrication process with PDMS 89
3.2.3.1. Microchannel fabrication in PDMS 89
3.2.3.2. Microchannels sealing and External interconnection 91
3.2.3.3. Profile of Microchannels in PDMS with SU-8 94
3.2.3.4. Fabrication of ring shaped electrodes (RSE) 95
4 RESULTS AND DISCUSSION 96
4.1. Characterization of microchannels 96
4.2. Reynolds number calculations 100
4.3. Devices Modelling 103
4.3.1. Simulation Tool 103
4.4. Input window for the simulation parameter and simulation results using Comsol software 105
4.4.1. Comparison between Simulations and Experiments; 107
4.4.2. Microfluidic device application with performed experiments 116
4.5. Active microfluidic device applied to enhancement of liquid mixtures 121

122

4.6. Microfluidic droplet generation with detection system based on embedded ring shaped electrodes 126
4.6.1. Measurement procedure 128
4.6.2. Fabrication and droplet detection experimental setup 129
4.7. Sub terahertz sensor in microfluidic devices for determination and control of ethanol concentration on demand 131
4.7.1. On-line sub-terahertz liquid sensor and experimental setup 132
4.7.2. Sub-terahertz sensor response, calibration and controlling of ethanol concentration 138
5 CONCLUSIONS AND FUTURE WORK 145
5.1. Conclusions 145
5.2. Final considerations and Future works 149
6 LIST OF PUBLICATIONS 151
6.1. Peer-reviewed journal 151
6.2. Peer-reviewed conferences 151
6.3. Conferences 152
7 REFERENCES 154
8 APPENDIX 162

1 INTRODUCTION

Microfluidics appeared in the late 1970s, with the manufacture of devices using Microelectronic processes to make microchannels on silicon substrates (LEE, 1969). In recent years, Microfluidics has attracted great interest of the academic community, technological, economic and the industrial sector, due to possibility to manipulate small amounts of fluids in emerging applications. There is a growing concern with reducing costs of raw materials in industrialized processes. Microfluidic devices microfabrication processes have enabled advances in the manufacture of complex analysis of microsystems distributed, in low cost substrates with microchannels of a few micromeres and total area around a few square centimeters (WHITESIDES, 2006). We developed a low cost fabrication protocol for microfluidic applications. Devices were made in glass slides for microscopy, each one having unit cost of USD 0.26 dollars (€$ 0.22 euros). There are several advantages in the use of devices with micrometric channels, which include: ease of operation and manipulation of these systems, as they are mostly portable and depending on the application are disposable, there is a considerable reduction in the use of sample, solvents and chemical reactants, because they operate with volumes in the order of micro to picoliters. With such a small sample volume, it is possible to optimize reactions in continuous flow. In-flow chemistry enables a more effective control of the reactions, analyzes with shorter times, reduction of residence time, reduction in waste disposal and dead volume, which is a very important factor in the contribution of pollution reduction to the environment (JANASEK et al., 2006). In addition to the advantages mentioned above, Microfluidics also offers a new field of studies. Fluids in the microscale exhibit different behavior from those found in macro systems, but there is still a possibility to be better studied and create reliable models, due to the scaling of systems similar to the downsizing phenomena that have happened in Microelectronics (ATENCIA et al., 2004).

Microfluidic systems are formed by channels molded or etched on substrates, encapsulated and placed with liquid inlet and outlet reservoirs (WHITESIDES, 2006; MADOU, 2011). In a more complete system, they are integrated into work microchannel with control and / or detection electrodes, with valves, pumps and sensors, the latter three with the possibility of external insertion or to be embedded in the same substrate. These devices perform parallel processes of several functions on the same substrate, such as: detection, separation, filtration, controlled mixtures and particle focusing, widely used in cell counting (ZHU, 2012). With these characteristics, the microfluidic systems are known in the literature as Total Analysis Microsystems (μTAS) or Lab-on-a-Chip (LOC), which means laboratory in a chip, literally,

since several analyzes are performed in a single microsystem, in the same way that it is processed in large laboratories (DITTRICH, 2006; KHALID, 2017). The possibilities of applications of these devices are quite interesting, and may play an important role in the production of clinical and toxicological analyzes from small blood samples (COLTRO, 2008), following the steps of commercial meters of glycemic index, using metal electrodes for conductivity detection. In the study of cellular migration using microchannels with multi-orifice, it was possible to allow modification of the migration by varying Reynolds number in the hydrodynamic interaction of the system (PARK et al., 2009). Bogojevic applied the manipulation of volumes on the order of microliters in a hydrophobic substrate, for the discovery of new drugs for cancer treatment using Digital Microfluidics (BOGOJEVIC et al., 2012). Cheng and his research group applied the Optofluidic in the synthetic biology area, for photo detection of biological processes in microchannels (CHENG et al., 2012; TAN et al., 2012).

It is important to note that silicon has been gradually replaced by alternative materials, such as glass and polymers, mainly because they offer good optical transmission, and the glasses still offer high chemical and thermal resistance, making them ideal for many applications in chemical processes (DUFFY et al., 1998). However, the non-use of silicon in the manufacture of microfluidic devices, still is under discussion because much of the detection systems such as microelectronic silicon-based sensors as bolometers, pressure sensors, accelerometers, ion-sensitive sensor, temperature among others, can be easily added to microchannel systems.

The main goal of this work is to study and use different microfabrication techniques, applied to microfluidic devices on silicon, glass and polydimethylsiloxane (PDMS). Aiming mainly at hydrodynamic applications as a proof of concept, in micro reactors applied to liquid mixtures, this investigation was focused on the effects of parameters like channel curvature and format of two parallel flows most commonly used in the literature, where we applied some design modifications and added an electrode and THz sensor to performing experiments and simulation models. The microfabrication processes of the systems were carried out using the combination of the techniques used in cleanroom facilities, such as, cleaning, lithography, wet etching by hydrofluoric acid and potassium hydroxide, sealing with PDMS and interconnection with silicone tubes.

This thesis is organized and divided into the following chapters: Chapter 1 - Introduction; Chapter 2 - Literature Review: Microfluidics Theory and Microfabrication Processes, procedures and experimental methods used in the manufacture of microfluidic devices; Chapter 3 - Experimental procedures of the microfabrication stages of Microfluidic Devices; Chapter 4 - Discussion of Results and Chapter 5 - Conclusions and Future Work.

2 MICROFLUIDIC AND MICROFABRICATION TECHNIQUES

There is a great interest of the scientific community in the development of systems focused on lower energy consumption, faster processing speed and faster response, applications with the miniaturization of systems in different areas, which is becoming increasingly important (WHITESIDES, 2006; MADOU 2012). This section addresses to the recent contributions in miniaturization systems, compatible with fluidic applications and microfabrication techniques linked to Microfluidics and its market projection. The Microfluidics include studies over flows that are mono or multiphase circulating in artificial microsystems, simple or complex systems that are made using microfabrication technologies that involve various techniques, including photolithography, etching, deposition, sealing and others which allow the manufacture of miniaturized systems (TABELING, 2014). WHITESIDES (2006) states that microfluidic systems generally use fluid volumes in the range of 10^{-9} (nanoliters) to 10^{-18} (attoliters).

Microfluidics is considered a multidisciplinary science because it involves areas such as Physics, Chemistry, Micro technology and Biotechnology (ATENCIA et al., 2004). Strong indications that Microfluidics is becoming increasingly important for Chemical and Biological Analysis, as Microelectronics has been for Engineering and especially for Computing, are given by the Royal Chemistry Society – RSC, who points out the growth in the number of published articles in this area, from 200 in 1998 to 1600 in 2010 (MARK et al., 2010) and that Microfluidics roadmap from 2013 up to 2020 shows that microfluidic devices market is rapidly growing, as shown in Fig. 2.1., with projection of market ~ 6B$ in 2020.

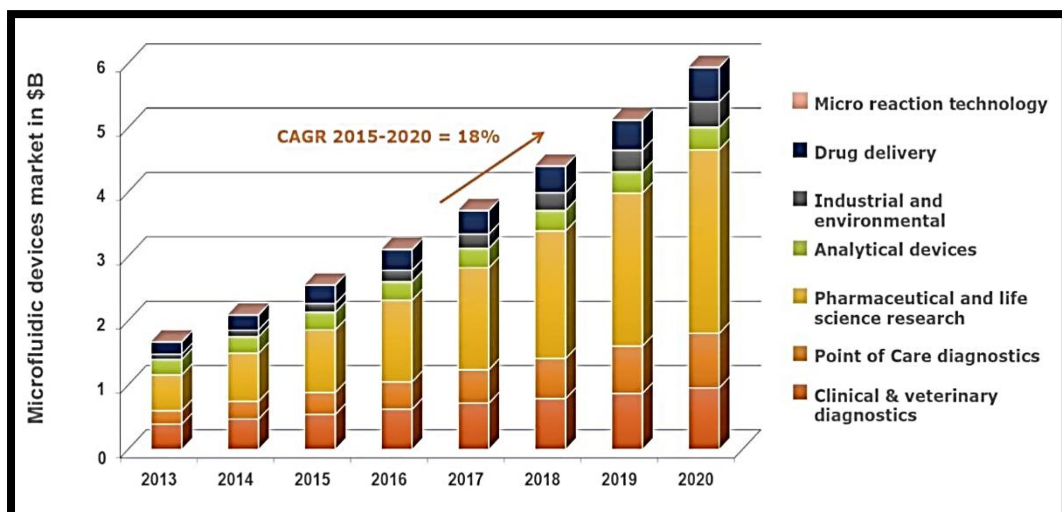

Figure 2.1 – Microfluidic devices market in $B (Adapted from DÉVELOPPMENT YOLE, 2015).

2.1. Miniaturization

The quest to miniaturize systems began in the late 1970s, and microfluidics began to emerge in conjunction with microelectromechanical systems (MEMS) technology. The first device considered microfluidic was produced in the late 1970s and was published by a group of researchers at Stanford University, and its working principle was based on the analysis of gases by chromatography, as shown in Fig. 2.2.

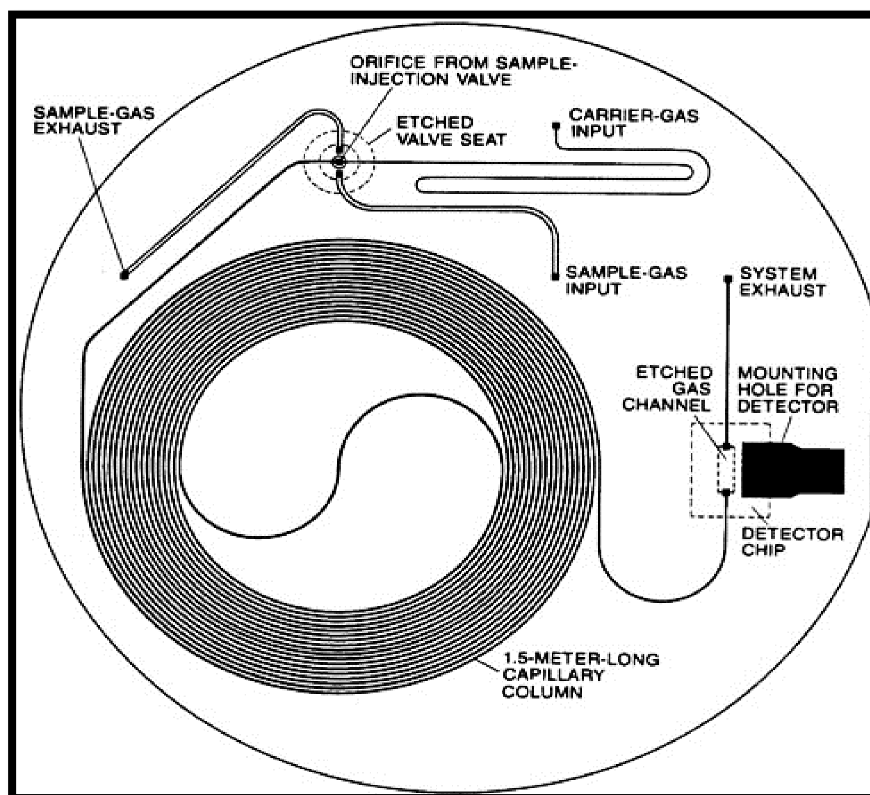

Figure 2.2 – Illustration of the first microsystem for gas chromatography made on silicon substrate at Stanford University in the late 1970s (Adapted from TERRY, 1979).

Silicon was the substrate most used in the manufacture of microfluidic devices, however, silicon has been replaced by other ceramic, glassy and polymeric materials. Microfluidic systems consist of microchannels, micro reservoirs, microvalves and micropumps and when grouped can be used as: mixers, separators of substances in the microscale, among other diverse applications. Microanalysis systems that perform reaction processing, and in some cases in the same device can be used for quantification of the reaction. New terms and nomenclatures have emerged to describe this phenomenon of fluid miniaturization, such as: Lab-on-a-Chip (LOC), which literally means laboratory on a Chip, μTAS (total analysis

microsystems), and sometimes named System-in-a-Package (SIP), Lab-on-a-Printer and System-in-a-Chip (SIC) (LO 2017; KHALID, 2017).

According to Fig. 2.3, the input interface of the chip is made through fluidic connections with the sample at the entrance to the system, usually using plastic, metal or needle tubes. The part of the actuators is responsible for controlling the movement of fluids considering the liquid samples, reagents and tailings, along the microchannels that connect the process steps, including sample preparation and analysis. At the beginning, the sample goes through the preparation stage that consists of microfluidic components such as filters, reaction chambers, concentrator and separator. Then, it goes through the analysis stage, that is associated to the detectors that can be chemical, thermal or optical transduction detectors. The reagents can be used both in the preparation of the samples and in the analysis, for example when it is desired to label an analyte with fluorescent molecules for further detection. An electronic platform controls the actuator system and detectors and collects the data (ABGRALL, 2007; BSOUL, 2016).

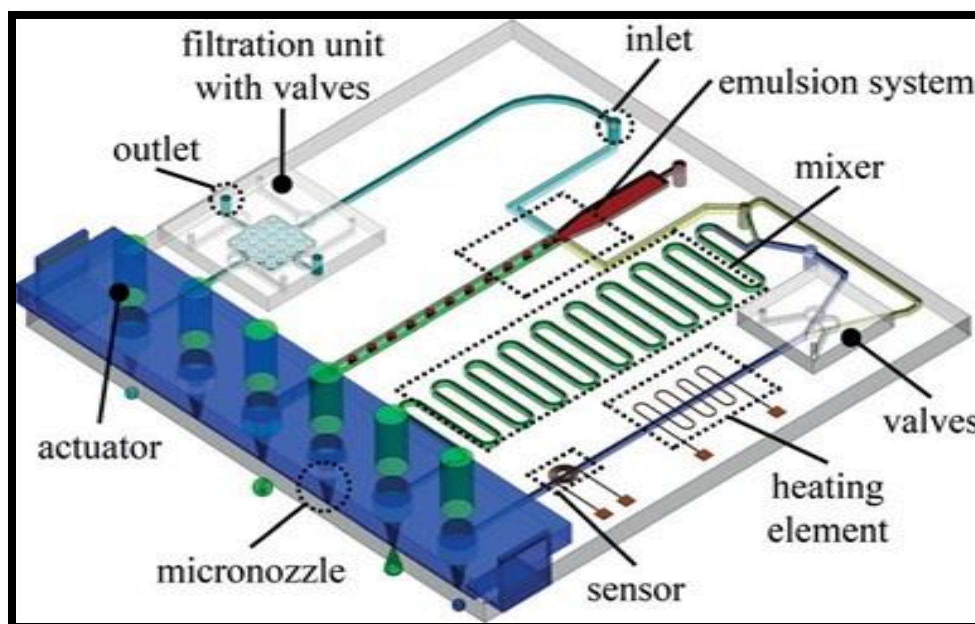

Figure 2.3 – General microfluidic system (BSOUL, 2016).

According to YAGER (2006), WHITESIDES (2006) and TABELING (2014), LOC systems present some advantages: small system area dimensions, typically between several mm^2 or cm^2; the dimensions from tens to hundreds of microns of the channels, thus generating a low fluid consumption (reagents, samples, low waste production), generally in the order of pico to milliliters. Further, as there are rapid transfers of mass and heat, it is possible to perform

time resolved analysis. The control process is simplified due to the acceleration of the system response and the low energy consumption. According to WHITESIDES (2006) and YAGER (2006), there are physical effects such as capillarity and surface tension, among others that dominate effects at the microscale and can make processes more complex than in a traditional equipment, because they require a more complex form of system modeling. Just to mention some other important issues, not all devices have the same ease of miniaturization, microfabrication techniques still require cost reductions, there is a need to develop new materials to supply wide range of applications in a variety of areas.

By convention, some characteristic dimensions are associated to microfluidics such as: small fluid volumes (pL to mL), small dimensions of the structures (µm to mm), dimensional scale where not all effects between the macro and the micro transition are not well defined and investigated and must be considered, forces such as capillarity, surface tension, free energy, contact angle among others, leading to another model of analysis of these systems, which interact with the fluidic behavior in microscale (YAGER, 2006).

2.2. Microfluidics and Fluids Mechanics

In Fluid Mechanics, fluids in general can be modeled as a molecular flow or continuous flow, and the fluids in the microscale exhibit behavior different from the macro scale. For the case of molecular flow (ZHU, 2012; WANG, 2018), the fluid is modeled as a set of particles and the physics that describes this type of model can be deterministic or probabilistic, where the Molecular Dynamics and Monte Carlo methods are used for this study. The fluid can also be modeled as in the case of the Continuous Hypothesis, characterized by the Navier-Stokes and Bernoulli equations, thus ignoring the molecular nature of the fluids, these being described in terms of spatial and temporal variations of density, viscosity, shear force, speed, pressure and temperature. The liquids, placed in microchannels can still be treated by the continuous hypothesis model, and the gases under the same conditions must be treated by the molecular model. In addition to the differential equations, some dimensionless numbers are used to characterize fluid behavior at the microscale (SQUIRES and QUAKE, 2005; LEE, 2011).

A fluid can be defined as a material that continuously deforms under the action of a shear stress. The fluids can be generally classified according to the shear stress applied and the rate of deformation. Also, in this relation, the definition of fluid viscosity is applied to fluids in general, whose behavior is independent of time (FOX et al., 2010). Newtonian fluids are those that follow a linear relationship between the shear stress and the shear strain or velocity

gradient, being directly proportional to the coefficient of absolute viscosity μ, according to the equation proposed by Newton, also known as Newton's Law of Viscosity, as shown in Eq. 2.1.

$$\tau_{xy} = \mu \frac{du}{dy} \qquad \text{Equation (2.1)}$$

The proportionality constant μ is called absolute or dynamic viscosity, τ_{xy} is the shear stress, being $\frac{du}{dy}$ the rate of shear deformation, it is the derivative of the velocity component that is parallel to the direction of shear. Fluids where this ratio is obeyed linearly are called Newtonian fluids. In the case of shear stresses and shear forces are considered to be nonlinear, and the fluids do not obey Eq. 2.1, so they are called non-Newtonian fluids (FOX et al., 2010).

Viscous and non-viscous fluids: The main subdivision is indicated between viscous and non-viscous flows. The flows where the viscosity is considered are regarded as viscous and in the case where the viscosity effects are neglected are termed non-viscous. For the non-viscous flows, the viscosity of the fluid μ is assumed to be nil or negligible.

Laminar and Turbulent Flow: Viscous flow regimes are classified as laminar or turbulent, based on their structure. In the laminar regime, the flow structure is characterized by smooth movement in smooth layers or substrates. The structure in the turbulent regime is characterized by the random motion of fluidic particles due to random fluctuations in the three-dimensional field of velocities. In a one-dimensional laminar flow, the shear stress is related to the velocity gradient, by Newton's law of viscosity, according to Eq. 2.1. In the turbulent flow this simple equation is not valid. For turbulent flows, there are no universal relations between the tensile field and the mean velocity field, so semi-empirical theories and experimental data are used (FOX et al., 2010).

Compressible and Incompressible Flows: The flow is said incompressible when the variations in the specific mass are negligible, otherwise it is compressible. The gases are considered to be fluids with compressible flow, whereas the liquids, in general, have incompressible flow. Some factors make the specific mass increase or decrease. The main factors are temperature and pressure. For liquids, the temperature has little influence on the

specific mass and under moderate pressures the liquids can be considered incompressible (FOX et al., 2010).

Navier-Stokes Equations: The equations governing hydrodynamics can be derived from fundamental equations of non-relativistic mechanics, which describe mass conservation, momentum, and energy (GAD-EL-HAK, 1999; YANG 2013; MADOU, 2011), taking into account the hypotheses and concepts presented previously. The equation that describes the movement of fluids is obtained by combining the differential equations of conservation of mass and momentum. Considering a compressible fluid, isotropic and disregarding the action of field forces, the equation describing the motion for Euler velocity field is called the Navier-Stokes equation, which in a vector form is presented as:

$$\rho\left(\frac{\partial v}{\partial t} + v \cdot \nabla v\right) = -\nabla\bar{p} + \mu\nabla^2 + \frac{1}{3}\mu\nabla(\nabla \cdot v) + \rho g \qquad \text{Equation (2.2)}$$

where:

$\boldsymbol{\rho}$: is the specific mass, $(v \cdot \nabla v)$ is the convective term that can be neglected in incompressible fluids (BATCHELOR, 2002);

$\boldsymbol{v}$: is the velocity vector of the fluid;

p: is pressure;

g: is gravity;

$\boldsymbol{\mu}$: is the absolute viscosity of the fluid.

The left side of Eq. 2.2 is related to momentum and inertial forces and the right side to pressure and viscosity force. This equation, in its complete form, has no analytical solution, but there are some boundary conditions that make analytic solutions possible only for some specific cases. According to Bruus (2008), one of these analytical solutions of the Navier-Stokes equation results in a so-called Poiseuille-Hagen flow, which considers: a fully developed laminar flow of an incompressible Newtonian fluid in a straight channel, triggered by a pressure difference between the two ends of the same (BRUUS, 2008). This solution was chosen to

describe the fluid flow in the system analyzed in this work, mainly in the computational simulation.

Reynolds number: The Reynolds number is a dimensionless quantity, important in the mechanics of the fluids, obtained through the Navier-Stokes equation. For a Newtonian, incompressible fluid with uniform density, the Reynolds number is given by, as shown in Eq. 2.3:

$$R_e = \frac{\rho v D_h}{\mu} \qquad \text{Equation (2.3)}$$

where:

$\boldsymbol{\rho}$ = specific mass of the fluid (absolute density);

$\boldsymbol{\mu}$ = absolute viscosity of the fluid (dynamic viscosity);

$\boldsymbol{v}$ = fluid velocity;

$\mathbf{D_h}$ = hydraulic diameter.

The calculation of the hydraulic diameter follows Eq. 2.4:

$$D_h = \frac{4A}{P} \qquad \text{Equation (2.4)}$$

Where:

$\boldsymbol{D_h}$ is the hydraulic diameter, in µm;

A is the cross-sectional area of the microchannel, in μm^2;

P is the perimeter of the microchannel, µm.

The magnitude of the Reynolds number, R_e, can provide an estimate of the relative importance of viscous and non-viscous forces acting on a fluid element (BATCHELOR, 2002; NGUYEN, 2016). In practice it is common to use the Reynolds number to determine whether a flow is laminar or turbulent. But for this it is necessary to define a transition Reynolds number R_{et}. Thus, if $R_e < R_{et}$, the flow is said to be laminar, otherwise $R_e > R_{et}$, the regime is said to be turbulent. The transition Reynolds number depends directly on the characteristics of the system to be analyzed. Among these characteristics are the assumed conditions for the flow and geometric aspects of the system (BATCHELOR, 2002). In order to determine if a flow is laminar or turbulent, it is common to evaluate the Reynolds number and compare it with the transition number of 2000. However, in general, the Reynolds number of transition for microfluidic systems are smaller than 2000, being able to assume values down to 15 (GRAVESEN, 1993).

Even with low value of transitional Reynolds numbers, microfluidic systems still tend to have laminar flow, due to the low velocities involved and small dimensions, as a result generating low Reynolds numbers, generally smaller than 100 (WHITESIDES, 2004). One of the practical implications of Reynolds number is the influence on fluid mixing ability. While in the turbulent regime, the fluids readily mix, in the laminar regime this mixing occurs much less effectively and usually due to particle diffusion alone. Thus, since microfluidics involve low Reynolds numbers, the ability to mix fluids becomes a challenge in this area. Fig. 2.4 shows two systems, one under laminar flow regime, i.e., Reynolds number below the transition Reynolds number, and another with a completely turbulent flow regime.

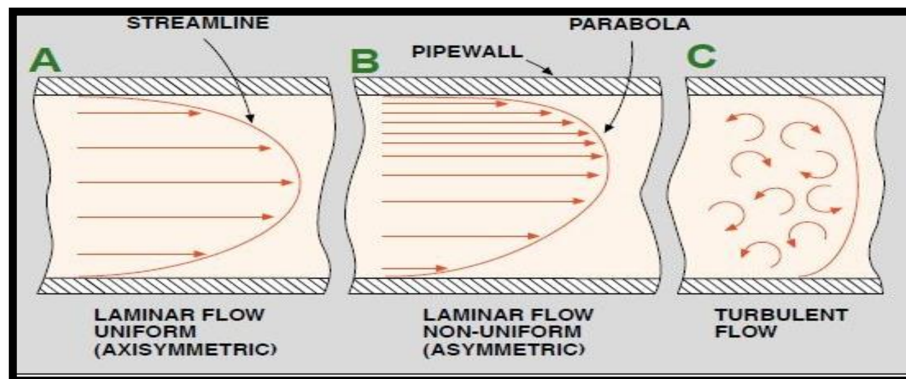

Figure 2.4 – Flow regimes. (a) Laminar flow regime with Reynold number < 2000; (b) Transitional flow regime with 2000< Reynold number < 4000; (b) Turbulent flow with Reynolds number > 4000. Adapted from Omega Engineering Ltd.

2.3. Diffusivity in liquids

According to Cussler (1997), the definition of diffusion coefficient or mass diffusivity is a value that represents the ease with which each determined solute moves in a specific solvent, being a constant proportionality between the molar flow caused by the molecular diffusion, free movement of the particles in a solution, and the gradient in concentration.

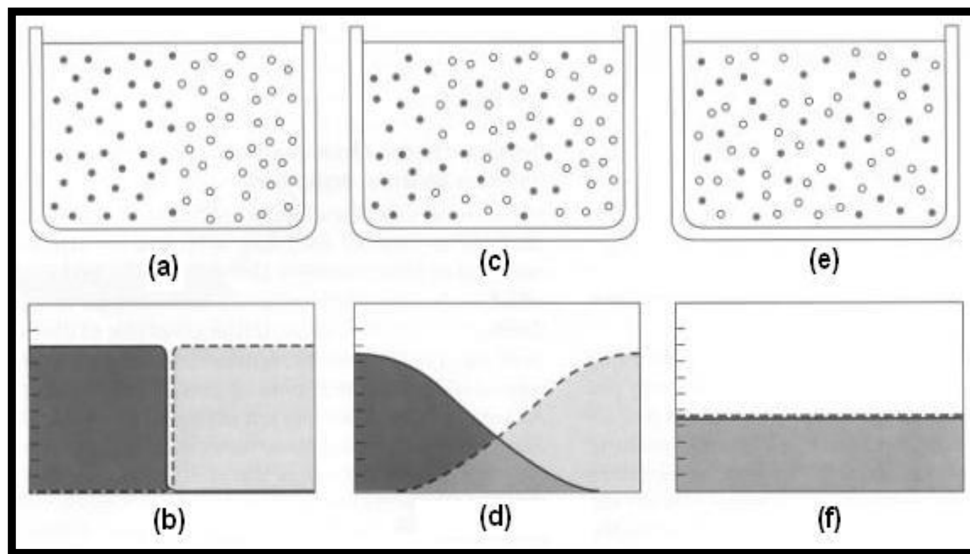

Figure 2.5 – The thermal movement of molecules and diffusion. (a) and (b) Molecules of two species with distinct concentrations and concentration graph; (c) Increased molecular agitation increases diffusion between species; (d) Gradient of concentration in modification, from an area of higher concentration to a lower concentration; (e) Thermal and kinetic equilibrium of species molecules; (f) Concentration gradient at equilibrium, totally different from the initial condition. Adapted from (CUSSLER, 1997).

Diffusion is the process by which the molecules of different substances are mixed due to their agitation. In the specific case of water, the molecules of water in a solution are not completely static but in permanent movement, colliding with each other and exchanging kinetic energy (CUSSLER, 1997; GAIDUK, 2017). This kinetic energy is converted into thermal energy through the intermolecular collisions inside the liquid. This molecular agitation, analogous to the Brownian motion, generates movements in substances of places where they exist with greater free energy to the places of lower free energy, trying to organize the molecules in a condition of stability and of less possible energy, according to Fig. 2.5.

The movement of the molecules due to the increase of temperature leads to a greater intermolecular displacement, so the diffusion increases, the molecular agitation causes gradual mixing of the molecules that produces a decrease in the difference of concentrations over time. So, the mixing between the liquids happens because of the molecular movement, and this movement is diminishing as the concentrations are equalized, arriving at a stable condition of minimum possible free energy. As long as there are no other forces to act on liquid molecules, such as magnetic, electric, pressure, diffusion causes molecules to move from high concentration zones to low concentration zones, thus creating a decreasing gradient concentrations (CUSSLER, 1998; GAIDUK, 2017). This phenomenon was examined quantitatively by A. Fick who in 1855 formulated the mathematical relation of this process, which was called by Fick Law of diffusion, according to Eq. 2.5:

$$J = -D\frac{d\varphi}{dx} \qquad \text{Equation (2.5)}$$

where:

J is the diffusion flux; i.e. it is the amount of the substance that traverses the unit area per unit time (mol m^{-2} s^{-1});

D is the diffusion coefficient or diffusivity. Its dimension is area per unit time, so typical units for expressing it would be (m^2/s);

φ is the concentration, of which the dimension is the amount of substance per unit volume. It might be expressed in units of (mol/m^3);

x is position, the dimension of which is length. It might thus be expressed in the unit (m).

The difference of concentrations between two points where the diffusion occurs, that is, the concentration gradient is the driving force for simple diffusion (HOPKINS, 1995; GAIDUK, 2017). Diffusivity is found in Fick's law and physical-chemical equations related to the diffusion of matter or energy. Being generally suitable for a given pair of known chemical species, for a multicomponent system the recommendation to separate for each pair of species of the system is shown in Fig. 2.6.

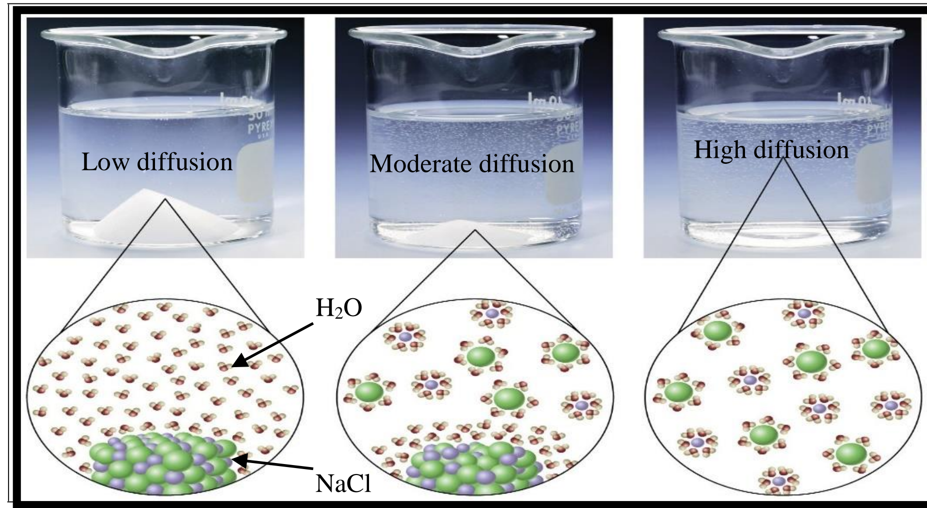

Figure 2.6 –Sodium chloride diffusion in water. Adapted from (www.quora.com).

Normally the diffusion coefficient depends strongly on these four factors: size and shape of the solute, solvent viscosity and temperature. Certain molecules diffuse as particles, while others, designated as electrolytic ions, diffuse as ions in solution. Although each ion has a mobility difference, the electrical neutrality of the solution indicates that the ions must diffuse at the same rate, for example the diffusivity of sodium chloride in the water. The greater the diffusivity between two substances, the greater the mixing ratio between them, that is, they diffuse further into each other (GAIDUK, 2017).

2.4. Microfabrication Techniques and Processes

In this section, we will present microfabrication techniques and processes associated to the manufacture of microfluidic devices, reporting microfabrication techniques related or correlated with materials used in this thesis for the manufacture of devices such as silicon, glass and polymers.

2.4.1. Microfabrication Stages

The majority of microfabrication processes in microelectronics occurs in a given repetitive cycle, as shown in Fig. 2.7, involving the following steps:

- Deposition of thin films;
- Lithography for transferring patterns;
- Etching (etching) for removal of material not protected by the mask;
- Photoresist removal.

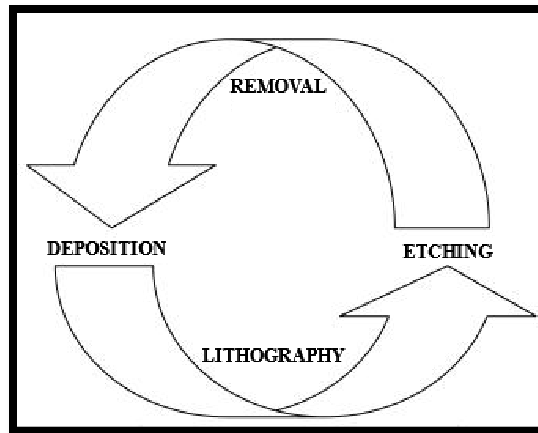

Figure 2.7 – Microfabrication cycle. Adapted from (BESSELER, 2008).

These steps are repeated according to a flow, as in the example, shown in Fig. 2.8. However, the cleaning and characterization stages of the processes could be included.

Microchips or micro devices can be fabricated using conventional or alternative microfabrication technologies using different substrates. In technologies involving conventional microfabrication processes, for example, to transfer the pattern of the mask to the substrate, a process known as lithography is very common. This pattern transfer process is initially done on the surface of a polymer sensitive to the radiation used, light radiation or electron beam. (UTKE and MOSHKALEV et al., 2012).

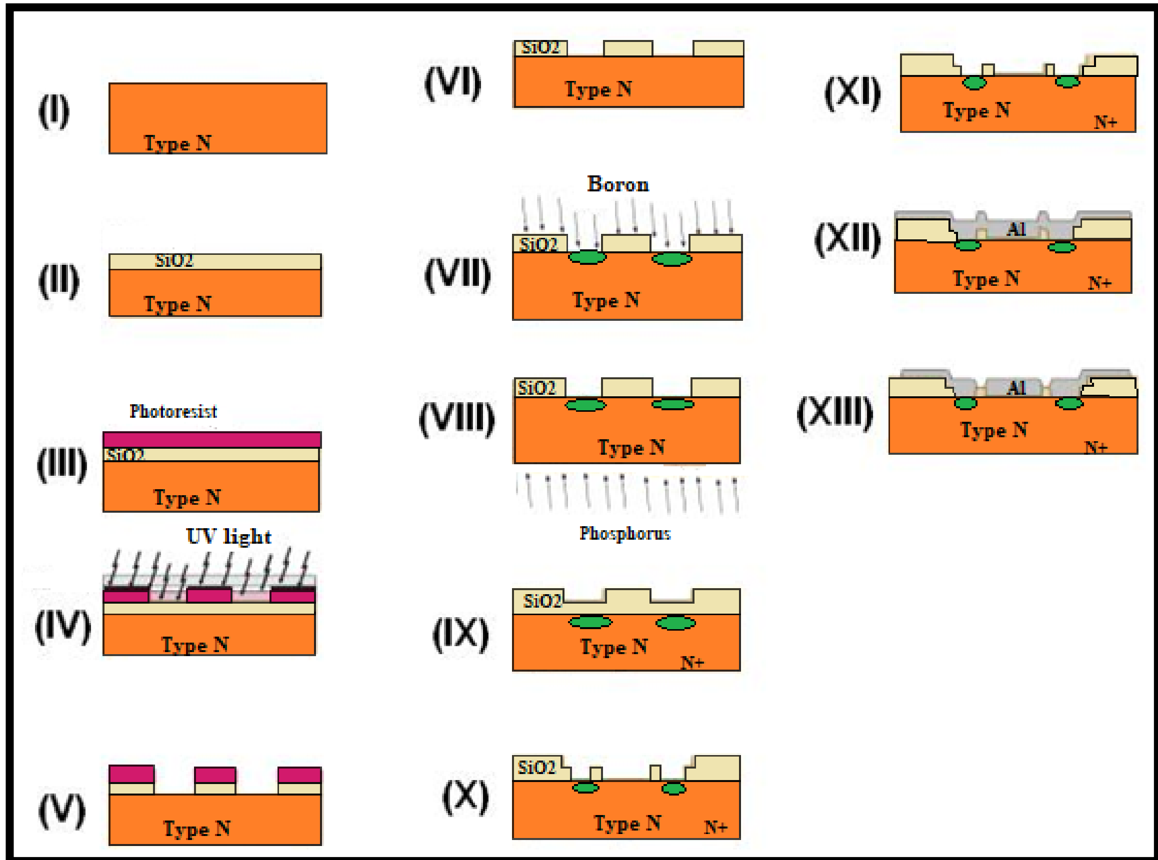

Figure 2.8 – Microfabrication processes of the MOS transistor. (I) Substrate selection; (II) Thin film deposition; (III) and (IV) lithographic processes; (V) Thin film etching; (VI) Photoresist removal; (VII) and (VIII) Stages of ion implantation; (IX) Oxidation of the silicon wafer; (X) Etching after lithography; (XI) Growth of the gate oxide; (XII) Deposition of aluminum; (XIII) Etching of aluminum (Adapted from TURATTI, 2003; SWART 2008).

This exposure of the resist to radiation promotes an interaction and causes the absorption of this light that can affect the chemical structure of the photoresist altering its solubility, allowing the development of the photographed image. Lithographic processes, such as soft lithography, electron beam lithography or ultraviolet (UV) lithography, are the most commonly used (CHEN and PÉPIN, 2002). Following are the microfabrication steps similar to those used in the microfabrication process of the MOS - Metal Oxide Semiconductor transistor, as follows in Fig. 2.8.

The typical microfabrication process of the MOS transistor, as shown in Fig. 2.8, starts with the choice of the silicon substrate, including the orientation, type, size and resistivity of the wafer. After the wafer has been defined, the RCA cleaning is done, followed by oxide growth by the thermal oxidation process, then the transfer of mask patterns to the substrate in the lithographic process, later the photoresist developing and etching of oxide, implantation of dopants in the source and drain regions (MESSAOUD et al., 1970). This whole cycle is repeated several times until the conclusion of the device, with the deposition of the interconnection lines of aluminum and definition by lithography.

For the manufacture of microchannels in silicon it is not necessary to use all the steps as described above, in particular ion implantation is not required. This methodology was developed to make the microfluidic devices in silicon of this work, as described in chapter 3.

The microfabrication processes of microchannels using glass as a substrate follow similar procedures of the processes of obtaining microchannels in silicon. These steps are shown in Fig. 2.9 that can also be used for the fabrication of microstructures in other types of substrates. Generally, the microfabrication process is initiated with substrate cleaning, thin film deposition as a protective mask, microchannel lithography, thin film etching, photoresist removal, substrate etching and microchannel sealing.

The steps of cleaning the glass slides, normally glass cleaners such as alkali, borosilicate or silica, with a thickness of less than 10 mm, are done with deionized (DI) water, detergents (extran, nonionic detergent), organic solvents (isopropanol and acetone) and highly oxidizing solutions, as for example H_2SO_4 / H_2O_2 (piranha solution), commonly used to remove organic residue from the substrate. A thin film, such as a thin metal layer (20-100 nm) may be deposited on the substrate after cleaning and drying of the glass substrate (I). Deposition of the film can be done by sputtering or thermal evaporation, to act as a mask in the stage of etching of the substrate. This metallic layer, in many cases generally consists of a chromium and gold alloy (Cr / Au), considering that the Cr layer is deposited to increase the adhesion of the Au layer to the surface of the substrate. The lithographic process was initially done with a layer of photoresist deposited on the metallic film, by the process of spin coating (I). Ultraviolet (UV) radiation selectively reaches the surface of the photoresist after passing through a mask containing the desired pattern to be transferred to the substrate, positioned between the light source and the glass substrate (II).

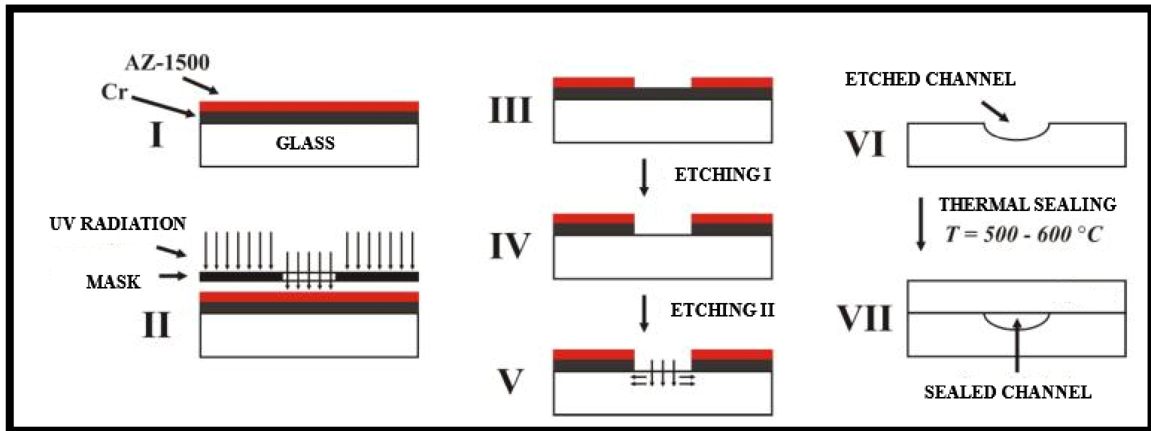

Figure 2.9 – Channels microfabrication process in glass substrates. (I) Substrate coated with Cr layer and photoresist AZ-1500; (II) Positioning of the mask and exposure to UV radiation; (III) Photoresist development; (IV) Thin film etching; (V) Glass etching with HF-NH4F; (VI) Obtaining the microchannel with semicircular profile; (VII) Glass-glass thermal sealing. Adapted from (COLTRO, 2008).

Conventional masks used in microfabrication processes have typical minimum resolution of the order of 1 µm, and are manufactured in a high resolution glass plate covered with Cr film by lithographic process. The mask contains the geometric pattern to be transferred to the substrate. Masks with a resolution of up to 30 µm can be made from alternative materials such as photolith, whose microfabrication technology is faster and becomes economically more feasible for some applications. Depending on the characteristics of the photoresist, there is a need for heat treatment steps before and after development in order to eliminate any presence of solvent and reduce the intrinsic stress of the material. The photographed image is revealed (III) with adequate organic solvents for each type of photoresist.

After transfer of the geometric patterns of the microchannels to the photoresist and thermal treatment for solvent removal, the metallic layer that has been exposed after the development of the photoresist (IV) is done. In order to etch the metal film, the etching of Au is started, and solutions containing KI / I_2 or HCl / HNO_3 (Aqua Regia) are used. For etching of the second thin film layer, Cr, K_3Fe solution $(CN)_6$ or Ce $(NH_4)2$ $(NO_3)_6$ is used. The mask pattern was transferred to the substrate via contact lithography step, and it allows to etch substrate in a desirable area, using wet etching process (using HF / NH_4F or HF / HNO_3

solutions) or dry etching (by low density plasma in a reactive ion etching - RIE, or by high density inductively coupled plasma – ICP, in a ICP-RIE process), thus transferring the geometric patterns of the microchannels to the substrate itself (V). The depth of the microchannels, and width in some cases, can be controlled by the etching time, as long as the etching rate is known in the process. Etching rate depends on the substrate material, the chemical composition of the solution, the analytical concentration and the temperature and agitation. Normally, channels with depths of a few tens of micrometers and widths of tens to hundreds of micrometers are used (COLTRO, 2008; SCHIANTI, 2008, 2017).

2.4.2. Chemical Etching Processes

Wet etching processes are generally more selective and faster than dry etching processes. There are types of etching occurring in isotropic and anisotropic forms. Isotropy and anisotropy is nothing more than the ratio of the lateral etching rate to the vertical etching rate, as shown in Fig. 2.10. Anisotropic etching is more common for microfabrication processes.

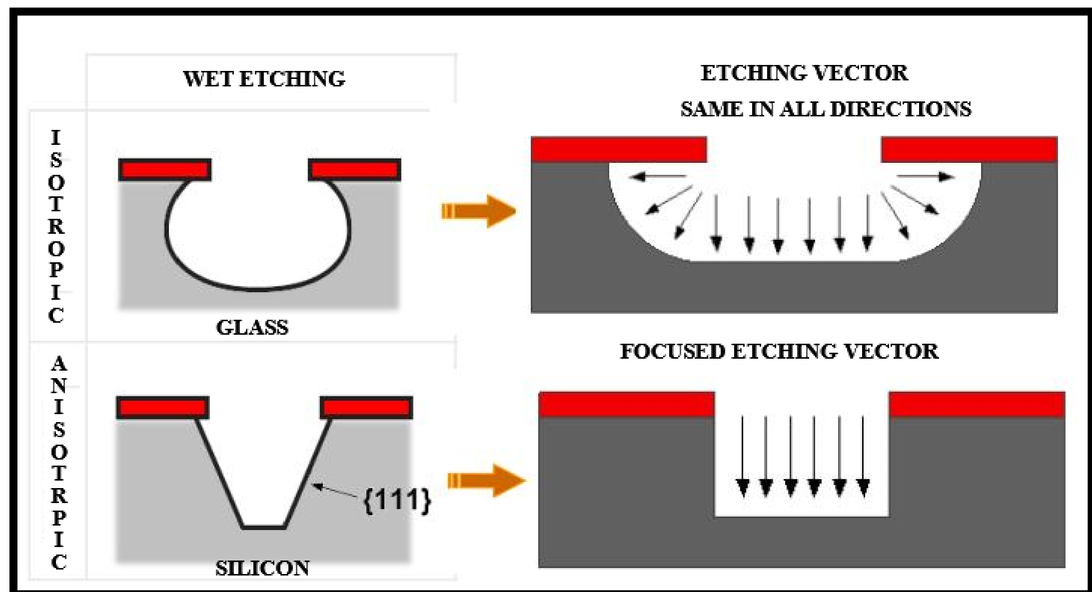

Figure 2.10 – Wet etching silicon with isotropic and anisotropic channel profiles. Adapted from (SEIDEL, 1990).

As can be observed in isotropic etching, the etching rate is the same in all directions, while in anisotropic etching the etching rate is not the same in all directions. The first works considering the effects of the anisotropy in the process of silicon etching were done in the late sixties, associated to the development of the microelectronics industry, being the main

advantage of the anisotropic process its reproducibility and control. In his paper, Lee (1969) showed some structures obtained during the process of etching of silicon in a hydrazine-based solution using aluminum masks. Later in the 70's, Bassous (1978) studied the etching process in the manufacture of channels and holes in silicon substrates.

Etching processes can be performed with various solutions, which have certain specific advantages and disadvantages. Among the best known are solutions based on Ethylene Diamine (EDP), Tetra-Methyl Ammonium Hydroxide (TMAH), based on alkali metals, particularly on Potassium Hydroxide (KOH). The following will address each of the processes with their basic characteristics, advantages and disadvantages.

✓ **Hydrazine:** Hydrazine solutions are rarely used because of the care needed in handling this type of compound. Hydrazine is a powerful oxidant commonly employed as a rocket liquid fuel and therefore flammable and dangerous. When reacting with oxygen in the air, it forms nitrogen and water. In addition to handling and its explosive characteristics, this compound also presents a high degree of toxicity. A great advantage in the use of hydrazine in microfabrication process, is that there is no reaction with aluminum. It allows to be used in post-processing of devices with aluminum contacts (GAJDA et al., 1994).

✓ **EDP:** Ethylene diamine-pyrocatechol are alternative solutions employed in the process of silicon etching. Initial work on this solution was made by Reisman et. al. (1979), and subsequently by H. Seidel et. al. (1999). EDP solutions are generally employed at elevated temperatures near their boiling point. The presence of oxygen in the solution is responsible for the increased etching rates. The EDP reaction can be evidenced by the color change of the solution from amber to dark red (REISMAN et al., 1979). According to Seidel et. al. the etching ratio is 10 times for the silicon in relation to its oxide. This confirms a reasonable selectivity and an excellent efficiency of this type of silicon etching. The main disadvantages of using this solution are the high degree of toxicity (ELWENSPOEK and JANSEN, 1998) because it is a carcinogenic and highly corrosive product for non-noble metals.

✓ **TMAH:** The solution of Tetra Methyl Ammonium Hydroxide is the only one that has full compatibility with the MOS and CMOS processes, as it does not contain alkali metals and does not etch aluminum in a significant way (ELWENSPOEK and JANSEN, 1998). Usually TMAH is one of the compounds present in the photoresist developing solutions employed in the lithography process. According to Elwenspoek and Jansen, TMAH solutions do not exhibit the toxicity of EDP and flammability of hydrazine, but in the case of a strong base some precautions need to be taken. And, according to the work of Tabata et. al. (1992),

for TMAH with concentration of 20% at 60ºC, etching rate in SiO_2 surface is approximately 12 nanometers per minute, which is much lower than that of the EDP solution.

✓ **Alkaline Hydroxide Solutions**: In principle all alkaline hydroxides can be used in the process of anisotropic silicon etching, among them the most used are NaOH and KOH due to their production facility, low cost and low toxicity. The only disadvantage of the use of NaOH is related to the high mobility of sodium ions within the silicon oxide, much larger than that of potassium, because NaOH has molecules smaller than KOH (TABATA et al., 1992). The work of Zubel et. al. (1998) presents comparisons between the etching processes using NaOH and KOH concludes that due to the small disadvantage of sodium hydroxide in relation to potassium hydroxide is due to the ionic mobility.

✓ **Potassium hydroxide - KOH:** Alkaline solutions based on KOH are certainly the most used in application to define three-dimensional structures in silicon. One of the earliest studies mentioning the use of KOH-based solutions was published in the 1970s by K.E. Bean (1978). Later in the 90's the work of Seidel et. al. (1990) developed one of the most complete studies on anisotropy and etching rates as a function of concentration and temperature of the solution. The results obtained are cited worldwide making the work of H. Seidel one of the main references when it comes to anisotropic silicon etching. The reaction of silicon in alkaline solutions is a reason for much discussion and, so far, is not perfectly understood. Several authors have studied the reaction and there are different proposals, according to H. Seidel, who proposed an equation for the three-step reaction consisting of:

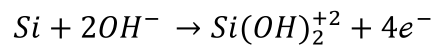

$$Si + 2OH^- \rightarrow Si(OH)_2^{+2} + 4e^-$$

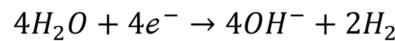

$$4H_2O + 4e^- \rightarrow 4OH^- + 2H_2$$

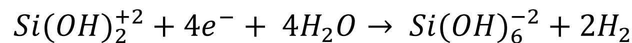

$$Si(OH)_2^{+2} + 4e^- + 4H_2O \rightarrow Si(OH)_6^{-2} + 2H_2$$

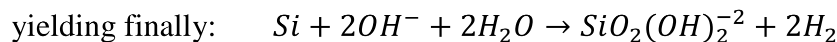

yielding finally: $$Si + 2OH^- + 2H_2O \rightarrow SiO_2(OH)_2^{-2} + 2H_2$$

Equation. 2.6 – Etching reaction in silicon. (SEIDEL et. al., 1990)

The overall gross reaction is summarized by the following Eq. 2.6 last line. In this model, the etching rate is limited by the reaction (redox) of the water molecules that are adsorbed to the silicon surface and by the formation of the double charge layer at the Si-solution interface.

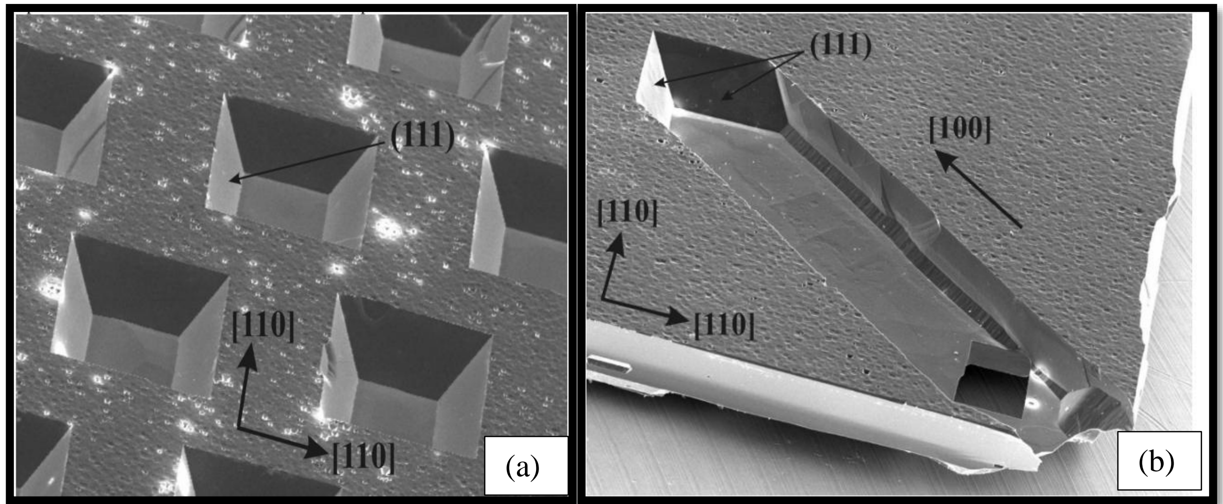

Figure 2.11 – (a) Cavities used to make membranes; (b) Microchannels used for microfluidic devices. Adapted from (CYRO, 2004).

The required electrons for the reaction are produced by the reaction of the hydroxyl ions with the silicon and are injected into the conducting band of the semiconductor. These results indicate the electrochemical nature of the silicon reaction in alkaline solution, and this is effectively employed to control the membrane thickness and silicon channel depth during the etching process, as shown in Fig. 2.11 (COLLINS, 1997). The orientation of etched silicon plane is changed by selectivity caused by different etching rates for each crystallographic plan in silicon wafer (CYRO, 2004; SEIDEL, 1990; PAL, 2017).

2.4.3. Polymer Microfabrication Techniques and Processes - SU8 and PDMS

The use of silicon wafers to fabricate microchannels has some limitations, due to its high cost. It also has limited physical, chemical and electrical properties for some applications, such as wet etching technique applied for microchannels (CYRO, 2004; PAL, 2017). Other materials have been used, as alternative solution to replace silicon in microfluidic fabrication, such as polymers, for rapid prototyping and greater chemical and bio-compatibility in various applications.

Photoresist SU-8: SU-8 is a negative photoresist, based on an epoxy compound (HAMMACHER et al., 2008). The chemical structure of SU-8 is represented in Fig. 2.12.

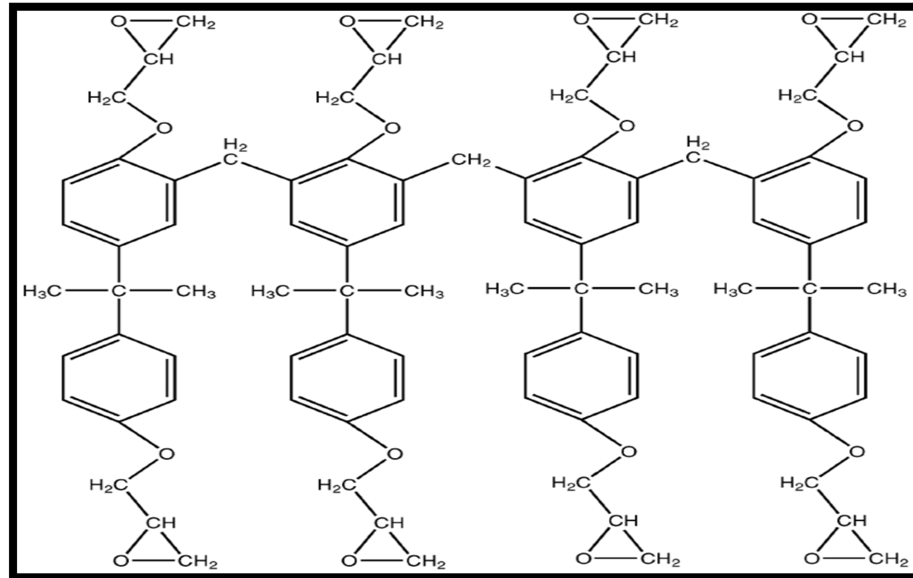

Figure 2.12 - Chemical structure contained in SU-8 formulations. Eight reactive epoxy groups allow a high degree of polymerization. Adapted from (CAMPO and GREINER, 2007).

The SU-8 photoresist exhibits high polymerization efficiency shortly after exposure to an irradiated UV light source, thereby having a suitable response to achieve high contrast, high resolution and sensitivity. In the post-processing of this resin an increasing change occurs in the modulus of elasticity (Young's Modulus) which represents in practical terms a high mechanical and thermal stability. For this reason, SU-8 is a very suitable material for the microfabrication of microstructures with high aspect ratio (HAR), as reported in the literature (CAMPO and GREINER, 2007). Because it is a high viscosity polymer, there is the possibility of deposition on silicon or glass substrates with thick and stable layers (from 2 μm to a few millimeters), which makes it suitable for microfluidic channels (SUN and KWOK, 2006). To determine the SU-8 thickness, it is necessary to consult the manufacturer´s datasheets. It provides us with SU-8 specification of thickness versus rotation of spin coating. There are different SU-8 families, with different degrees of viscosity. They relate to the rotational speeds, to forming different layer thicknesses, as shown in Fig. 2.13, for SU-8 2000 families (Microchem, USA).

As can be observed in Fig. 2.13, there is a dependence of the thickness of the photoresist with the speed of rotation, being that for the same speed, different thicknesses can be obtained

in the same family of the SU-8 2000. In the lithography step, the reticulation is initiated due to the presence of the eight epoxy groups per monomer, which are very reactive to UV light. This fact makes the chemical, mechanical and thermal properties of SU-8 very good, making it compatible with several applications (CAMPO and GREINER, 2007).

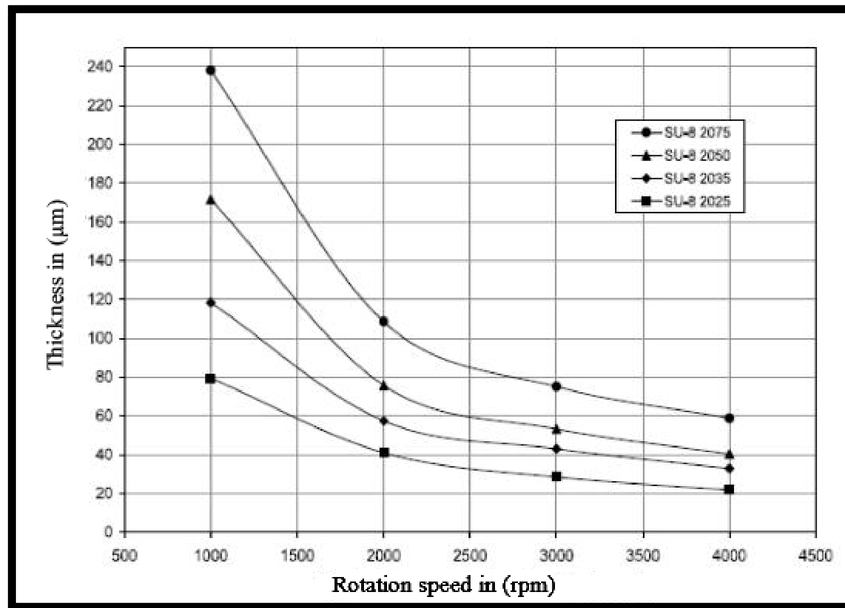

Figure 2.13 - Thickness of the layer of different photoresist of the SU-8 2000 group as a function of the speed of rotation of the deposition (Microchem SU-8 datasheet).

PDMS: Polydimethylsiloxane (PDMS) is an elastomer which is part of the siloxanes µ group. In the structure, an inorganic siloxane group and two methyl groups are present (KUNCOVA-KALLIO et al., 2006). Each monomer in the polymer chain is represented by [-Si $(CH_3)_2$ - O], as shown in Fig. 2.14.

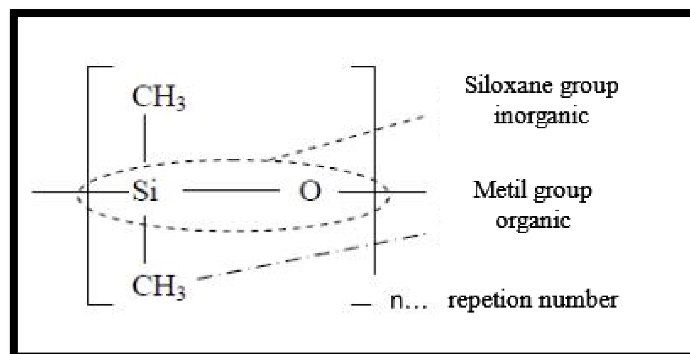

Figure 2.14 – Chemical structure of PDMS. Adapted from (KUNCOVA-KALLIO et al., 2006).

The PDMS is an excellent material for the manufacture of microchannel systems, because with its use, it is possible to reproduce structures on the scale of the micrometer with great precision through the molding / demolding process from one mold, creating replicas (replica molding). PDMS is usually commercialized in a liquid form, containing the polymer and the secant material (polymerization agent), which is converted to the solid state after cross-linking of its monomeric chains (XIA and WHITESIDES, 1998). One of the advantages of the PDMS is its optical property, being optically transparent, and responding to the wavelength range down to 280 nm, and can be applied in several detection schemes involving absorbance and fluorescence, its polymerization happens at low temperatures and can be reversibly deformed after being processed and cured. This feature also allows reversibly sealing with the PDMS itself or with other compatible materials, which in the case, have silicon bonds. Its adhesion with other surfaces occurs by simple contact between them, thus forming Van der Walls bonds. It also allows irreversible adhesion, soon after the surface exposure to an oxygen plasma, which eventually forms covalent bonds between the surfaces involved. In addition, it is a non-toxic, flexible and inert material (McDONALD et al., 2000; KUNCOVA-KALLIO et al., 2006).

Some disadvantages of PDMS arise from having a low surface tension, as this reduces the action of capillarity for aqueous solutions. It is noteworthy that, by treatment of plasma applied to its surface, the PDMS can become hydrophilic for some time, then returning to its initial hydrophobic condition. Another disadvantage is that it does not exhibit much resistance to solvents. Due to its very large Young's modulus, and absorption of some molecules it may be a limiting factor for some applications, such as: valve membranes, lenses and optical inspection windows, and liquid inlet and outlet ports (KUNCOVA-KALLIO, et al., 2006), thus becoming not compatible with many applications, such as involving hard solvents for causing PDMS polymerization (COLTRO, 2008)

Soft lithography with SU-8 and PDMS: Soft lithography is a non-photolithographic process based on rapid prototyping and replica molding of polymers, especially elastomers, through a master replication template. It is possible to manufacture the mold by several techniques of microfabrication, considering among them photolithography, which transfers the pattern drawn in a mask, previously defined and drawn in a CAD tool. Once the mask pattern

has been transferred to the mold, which can be done with the SU-8 photoresist with desired thickness, which defines channels height. This mold is covered with a prepolymer, which contours the template structure, and generates a negative replica of the template after polymerization (SUN and KWOK, 2006; McDONALD et al., 2000). The steps of a smooth lithographic process are illustrated, as shown in Fig. 2.15.

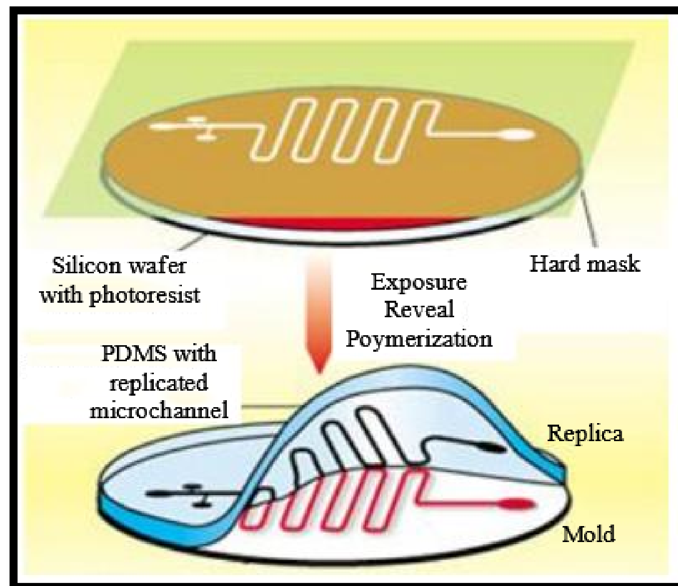

Figure 2.15 – Schematic of the soft lithography technique, molding / demolding of elastomers. Adapted from (CUTKOSKY, 2008).

For the application of the soft lithography technique, the most used materials are the elastomers, in particular the PDMS, due to the ease of extraction of the rigid molds, with a good coverage of surfaces, even if they are not flat, being able to replicate with extreme resolution all the structures of the mold (XIA and WHITESIDES, 1998). As it is a rapid prototyping, and with flexible procedures, this microfabrication technique is the most used for microfluidic systems, as shown in Fig. 2.16.

For the irreversible sealing of the microchannels with PDMS, it is necessary to treat the surfaces by oxygen plasma., The treatment of surfaces with plasma involves very complex mechanisms associated with the type of plasma, the material to be treated, the atmosphere and the conditions of treatment. The plasma treatment changes only the top surface layer and not the entire volume of material. In the treatment of polymeric substrates containing microstructures, the generation of plasma is done in a cold environment in order to prevent the

deformation of the polymers by thermal stress (WU et al., 2002; TANG and WHITESIDES, 2010). The treatment of the substrates by plasma with oxygen atmosphere, aims to activate the surface layer of the PDMS and the substrate, in the case of the glass, for the formation of strong Si-O-Si bonds between the two surfaces, ensuring the perfect and irreversible sealing of the channels.

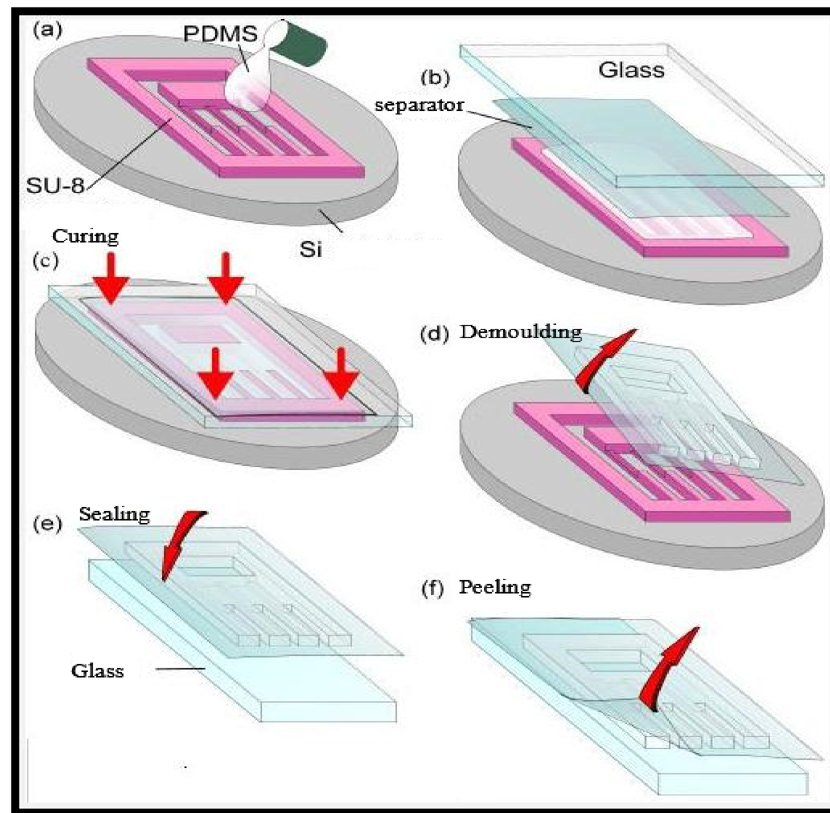

Figure 2.16 – Molding / demolding with PDMS. (a) SU-8 template; (b) PDMS deposited on the SU-8 template; (c) Conformation of the PDMS on the curing mold; (d) Manual extraction of the cured PDMS; (e) Plasma treatment for surface activation; (e) Microchannel sealing; (f) removing the cover layer. Adapted from (SCHIANTI, 2008).

Rapid prototyping of devices by conventional microfabrication processes, especially focused in microfluidic devices, can be done at a fairly low cost by using photolithography machines and resins used in the printing industry, lines up to 10 µm in width can be obtained in combination with a collimator (MADOU, 2011). The connection of the microfluidic channels to the external medium is done through tubes of either metal or polymer. However, to add this connection, it is necessary to attach these tubes with well-alignment to the upper part of the channel inlet (reservoir). The adhesion between substrates and connection points of inlet and outlet, with the external medium, can be made with adhesives, for example, epoxy. In a metal-

glass connection, adhesion of the silicone tube can be made directly to PDMS, using the PDMS irreversible sealing approach (TANG and WHITESIDES, 2010).

2.5. Microchannel sealing

The packaging processes of microfluidic devices involve techniques different from those used in the packaging of integrated circuits. In the packaging of microfluidic devices there is sealing of substrates to cover the microchannels of the device, and this cover contains the means of connection with the outside, where the fluid inlet and outlet of the device are fixed.

2.5.1. Anodic bonding technique

Anodic bonding is well-known technique for soldering glass and silicon substrates, and other possible combinations such as: glass-silicon, glass-glass and silicon-silicon, the latter being used also with Silicon On Isolator - SOI technique. The weld occurs at temperatures in the order of 400°C, it involves bias application in the order of magnitude of tens kV, requiring a high voltage source with good insulation (GAD-EL-HAK, 2006).

Fig. 2.17 shows the process of anodic bonding and the migration of charges between the silicon and glass substrates.

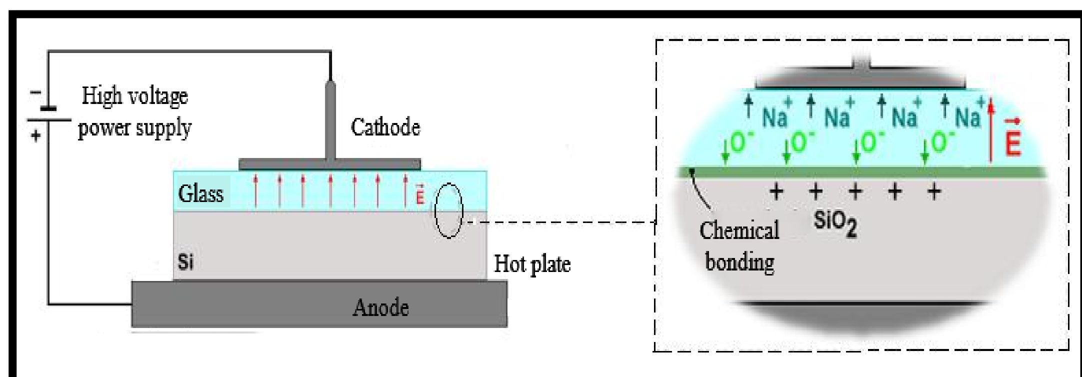

Figure 2.17 – Anodic bonding between glass and silicon substrates. Adapted from (GREENWOOD, 1988).

Bonding depends critically on the presence of sodium ions (Na^+) in the glass, which must migrate away from the glass / silicon interface when a bias is applied. This releases negative oxygen ions (O^-) that migrate to the surface of the silicon (Si), where they induce an equivalent positive charge.

The electrostatic attraction generated between the loads keeps the glass and the silicon connected, and this, promotes the chemical reactions at the interface silicon oxide formation (SiO_2) that complete the process of bonding between the two substrates. Note that the silicon must be positively polarized related to the glass and that the weld is complete when the external current falls to zero, i.e. when all moving charges (Na^+) have reached the cathode. There is a need to apply high temperatures, around 400 ^oC, to increase the mobility of Na^+ and O^- ions inside the glass. Since the high content of Na^+ ions, the glasses must have a coefficient of thermal expansion close to that of the silicon, so that they avoid breakages during the cooling process, which can cause mechanical stress on the substrate due to abrupt temperature changes from 400°C to room temperature. In order to weld glass with glass it is necessary to deposit an intermediate film, and one commonly used is hydrogenated amorphous silicon (a-Si: H) deposited by PECVD. Fig. 2.18 shows examples of bonding between substrates. (GAD-EL-HAK, 2006; GREENWOOD, 1988).

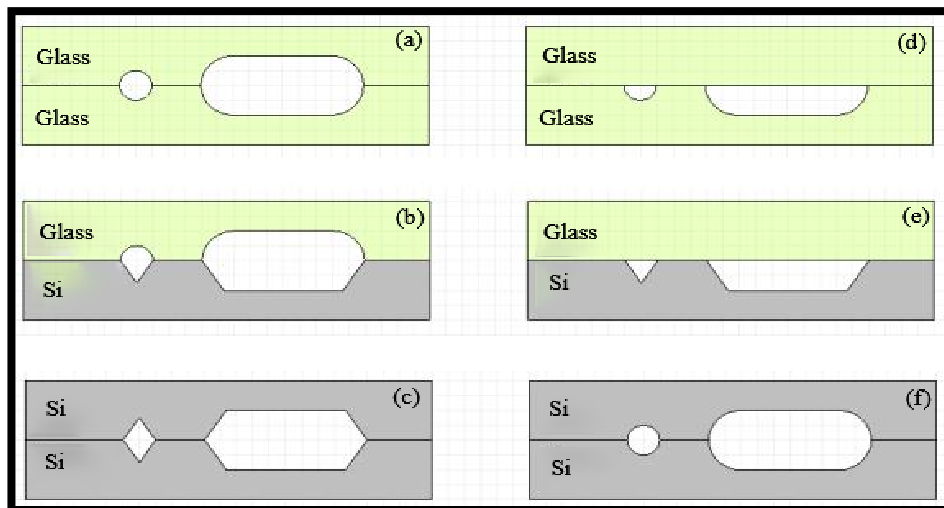

Figure 2.18 – Anodic bonding between glass-glass, glass-silicon and silicon-silicon substrates. (a), (b), (c) and (f) with self-aligned microchannel on top and bottom. (d) and (e) with microchannel in the bottom substrate. Adapted from (GAD-EL-HAK, 2006; GREENWOOD, 1988).

2.5.2. Polymer bonding technique

There are several techniques of sealing with polymers. We used the technique that combines temperature and pressure, also called the thermo-compression, in which the procedure consists in supplying thermal energy to the system, with the increase of temperature of the assembly till the glass transition of the polymer occurs, and then a certain pressure value is applied (BILENBERG et al., 2004; ILIESCU et al., 2006). In this way the solder is then determined by a melting process, due to the increase in temperature and pressure application. This technique has great versatility and is able to use several polymers. However, it has the disadvantage of not offering good uniformity in the sealing, thus generating a less hermetic result when compared to other techniques. In the literature, there are some examples of thermo-compression sealing with polymers, as shown in Fig. 2.19.

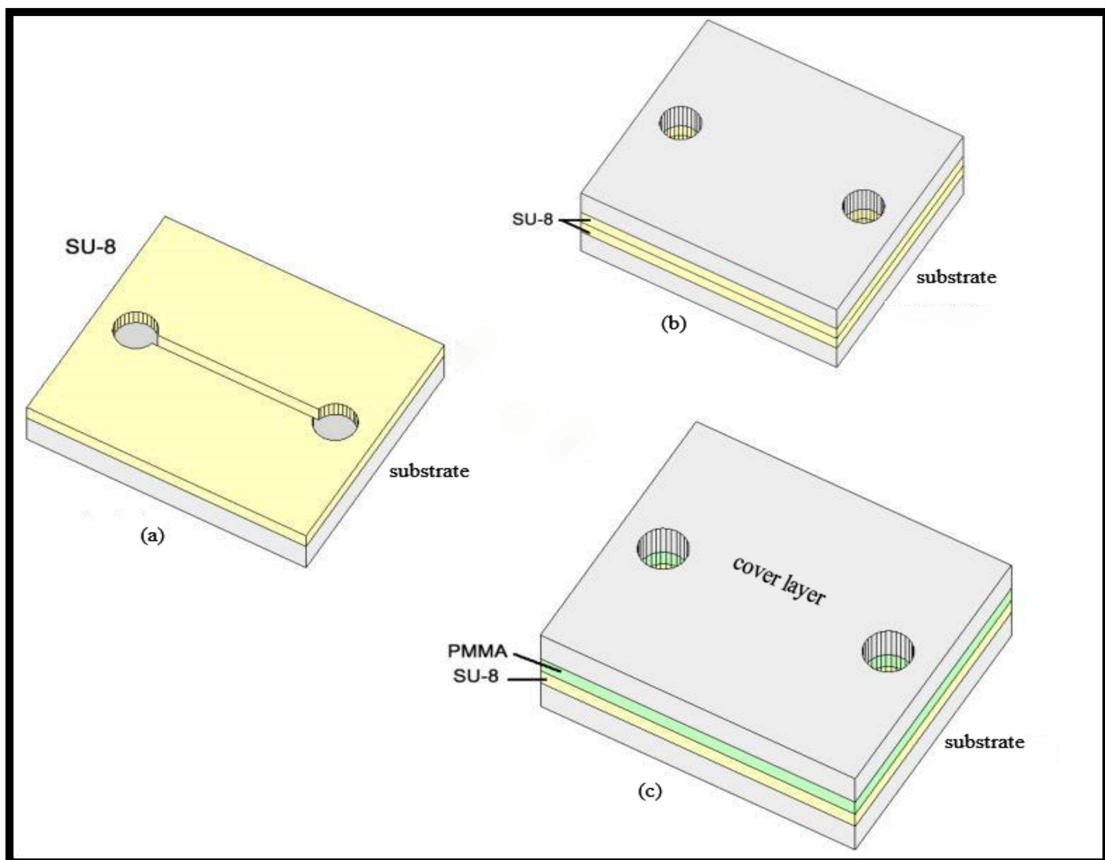

Figure 2.19 – (a) Substrate with polymer SU-8 with the photo chromed microchannels; (b) Substrates with intermediate layer with SU-8 for sealing; (c) Substrates with intermediate layer SU-8 and PMMA. Adapted from (SCHIANTI, 2008).

Bilenberg (2004) applied this technique with two polymers using them as an intermediate layer for bonding between the substrates. SU-8 was deposited on the substrate, photographed with the microchannel pattern, developed but the polymer not removed, as commonly done in the photo-lithography step. In this case SU-8 was used in the two intermediate layers for the sealing. Another possible variation of this technique is to merge polymers as intermediate layer, as shown in Fig. 2.19c.

The substrate containing the structures is pressed against another substrate. Usually the glass substrate is used, containing a layer of the polymeric film. To process the sealing with SU-8, the temperature used for the thermocompression process is 90°C and the pressure is 20.6 MPa, while for the PMMA, the temperature has reached 200°C and the pressure is 16 MPa. These temperatures correspond to values very close to those of the glassy temperature of each of the polymers used. However, this is a technique of sealing that is extremely dependent on the temperature and the applied pressure, and it is necessary to apply a uniform force on the surfaces for better bonding (BILENBERG et al., 2004). Another polymer widely used for sealing microfluidic devices is PDMS. Since PDMS is a polymer with low surface energy, it is possible to activate the surfaces using oxygen plasmas and to weld surfaces even at room temperature. This topic will be better detailed in the methodology section of this work.

2.5.3. Adhesive bonding technique

The technique of bonding with ultraviolet light sensitive polymer is used for the packaging of microchannels with the use of epoxy resins curable to UV light. Pan (2006) developed the use of UV curing adhesive for the bonding of micro structures made from glass slides (PAN et al., 2006). The glass slides were cleaned, then the epoxy resin deposited on one of the substrates, and the substrates were placed in contact. The glasses were pressed for a few seconds and then exposed to UV radiation for a few minutes. The advantage of this process is that this bonding is considered reversible, since it is possible to separate the two substrates with the application of temperatures around 100 ° C.

The process can be defined as low cost and fast, when compared to other bonding processes, still considering that there is a disadvantage in this technique as sometimes the channels can be obstructed, thus requiring a rework to clear the channels with acetone. Another limiting factor of this technique is low resistance of the resin to chemicals, being superior to a

few polymers, but very limited when compared to other processes such as direct bonding that does not make use of an intermediate adhesion layer.

2.5.4. Direct bonding technique

The direct bonding technique is applied using both high temperatures and low temperatures. Direct sealing at high temperatures is usually used to obtain Silicon On Insulator (SOI) slides by sealing two silicon substrate with oxide. Direct low temperature bonding can be applied by activating the surface of glasses. The activation of the surface can be through long cleanings in acid media or by plasmas. The bonding applied with acid activation has a great advantage in relation to the bonding obtained by dry activation. Considering the cost of acquiring and operating the reactors, according to Gabriel (2006) this turns almost impractical to allow large scale use of plasma bonding (GABRIEL et al., 2006). The direct bonding by means of acids has a simpler operational form and also of low cost, when compared with the activation by plasma, and results can be obtained equivalent to the other techniques of bonding (SCHIANTI, 2008).

More closely the sequence for obtaining direct soldering in acidic media is described by Jia (2004) which consists initially of cleaning the glass slides to remove particulates. Thereafter, the substrates are dried with nitrogen and hot plate, submerged in sulfuric acid (H_2SO_4) for a period ranging from 8 to 12 hours (JIA et al., 2004). After the time elapses, the substrates are rinsed in tap water for five minutes, and another five minutes in deionized water (DI). Still under DI water flow, the substrates are aligned and then placed to dry at room temperature under pressure, ranging from hundreds of kPa to 1 MPa.

During the period in which the glasses remain in contact with the sulfuric acid, a process of activation of the surface of the glasses takes place. In this process the Si-ONa bonds are transformed into Si-OH. When the substrates are brought into contact with each other, the Si-OH group of one slide gradually reacts with the same group of the other substrate, resulting in Si-O- Si and H_2O, as is the case in bonding at high temperatures. This mechanism is reproduced in Fig. 2.11 and also shown in Fig. 2.20.

The surface activation happens in a break of Si-ONa bonding, the chemical reactions of dehydration and condensation of Si-OH bonds, thus forming Si-O-Si (GABRIEL et al., 2006; JIA et al., 2004; SCHIANTI, 2008).

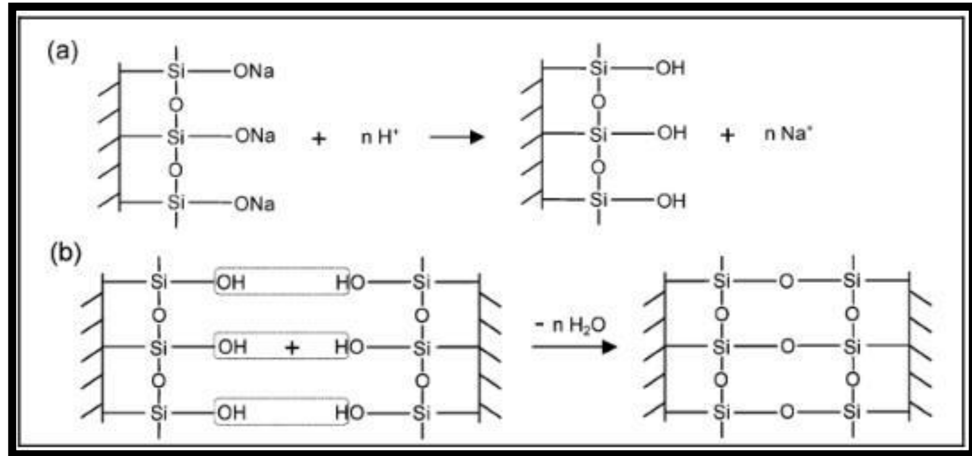

Figure 2.20 – Mechanism of direct bonding reaction. (a) surface activation reaction; (b) formation of the Si-O-Si bond (JIA et al., 2004).

2.6. MICROFLUIDIC AREAS

In this section we present some microfluidic application sub-areas involving several techniques of microfabrication. All collected from the literature review (YANG et al., 2018), some highlighted sub-areas of Microfluidics are shown in Fig. 2.21. This work is inserted in the Microfluidic sub-area named hydrodynamic.

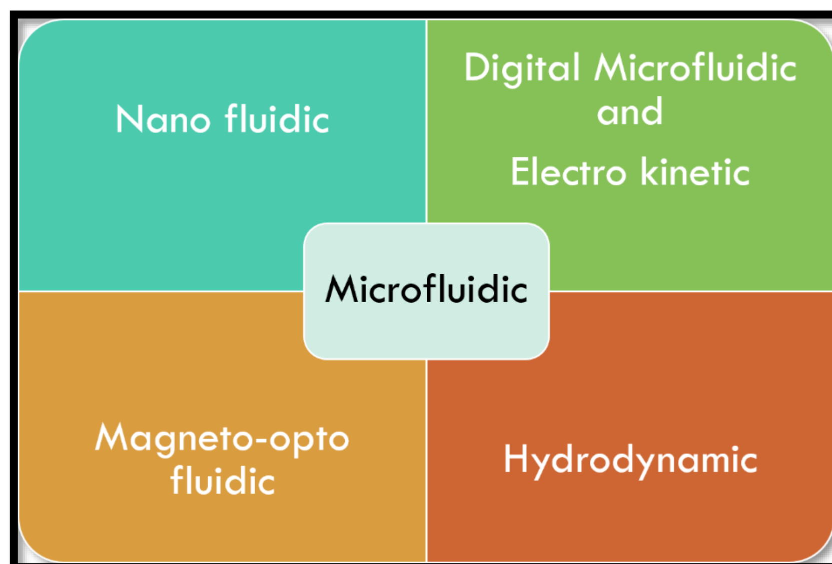

Figure 2.21 – Subareas in the field of microfluidics. (Adapted from YANG et al., 2018).

In the domain of Optofluidics, combination of geometry and the optical part are usually used for quantization and analysis of systems. In the electro-kinetic sub-area there are works related to the application of electric fields, to cause changes in fluids, these systems are also known as electroosmotic flows. This area is widely applied in separation microsystems, usually combined with systems of capacitive and optical measurements. In Digital Microfluidic (DMF) there is no need for micro-pumps and micro-valves. DMF is widely applied in chemical analysis systems, with control of micro volumes of liquids along a hydrophobic substrate. DMF is a fluid manipulation technique in which fluid picoliters, micrometric droplets, are manipulated electrostatically in a series of electrodes. It has recently become popular for applications in chemistry and biology. Hydrodynamics is an area that uses fluid mechanics and its interactions. It is worth emphasizing that, increasingly, it is inserted in the proposal of new theoretical models.

Electroosmotic Flow: Coltro (2008) developed his research project focused on the construction of an oscillometric multi-detector, using the technique of electrophoretic microsystems (MSE) with the insertion of contactless capacitance-coupled conductometric detection (C_4D), aimed at detection of diseases such as: Chagas' disease, Leishmaniasis, and for the monitoring of uric acid and glucose levels in patients. Fig. 2.22 shows the proposed system scheme involving MSE with integrated electrodes for C_4D. According to Coltro, the electrical contact of the planar electrodes was obtained with the aid of a conductive glue and epoxy resin (Araldite) (COLTRO, 2008).

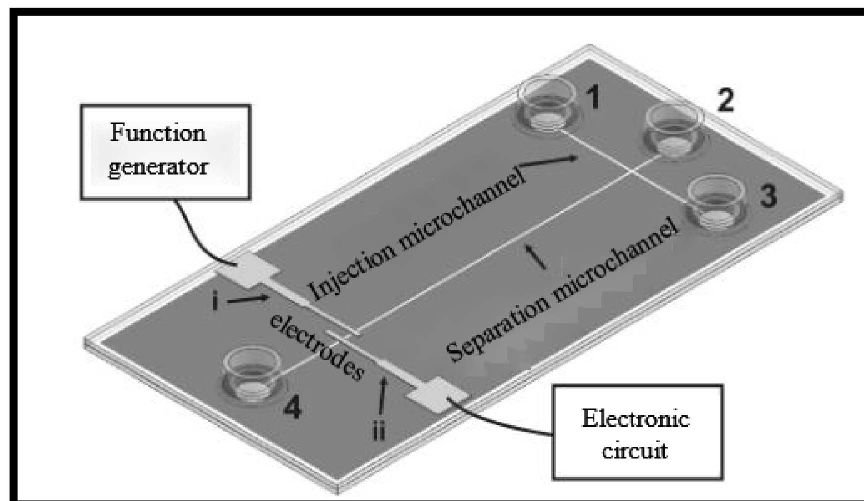

Figure 2.22 - Representation of a microsystem made of polyester-toner containing integrated electrodes and channels. Points 1, 2, 3 and 4 indicate reservoirs for sample, buffer, sample discard and buffer

discard, respectively. The points *i* and *ii* indicate the electrodes for cell excitation and recording of the resulting signal, respectively. (Adapted from COLTRO, 2008).

Hydrodynamic Flow: Park (2009) and his team developed a work within the hydrodynamic subarea, with study of the microparticles alignment in microchannels. According to PARK, the principle of applied technique was based on the combination of inertial support forces and secondary turbulent flows generated in a microchannel with topographically standardized geometry. The particle focusing mechanism is based on the forces of hydrodynamic inertia exerted on the particles migrating along a non-circular microchannel, that is, analogous to the tightening effect of the tubular wall, which induces the movement of the particles away from the walls, as can be seen in Fig. 2.23.

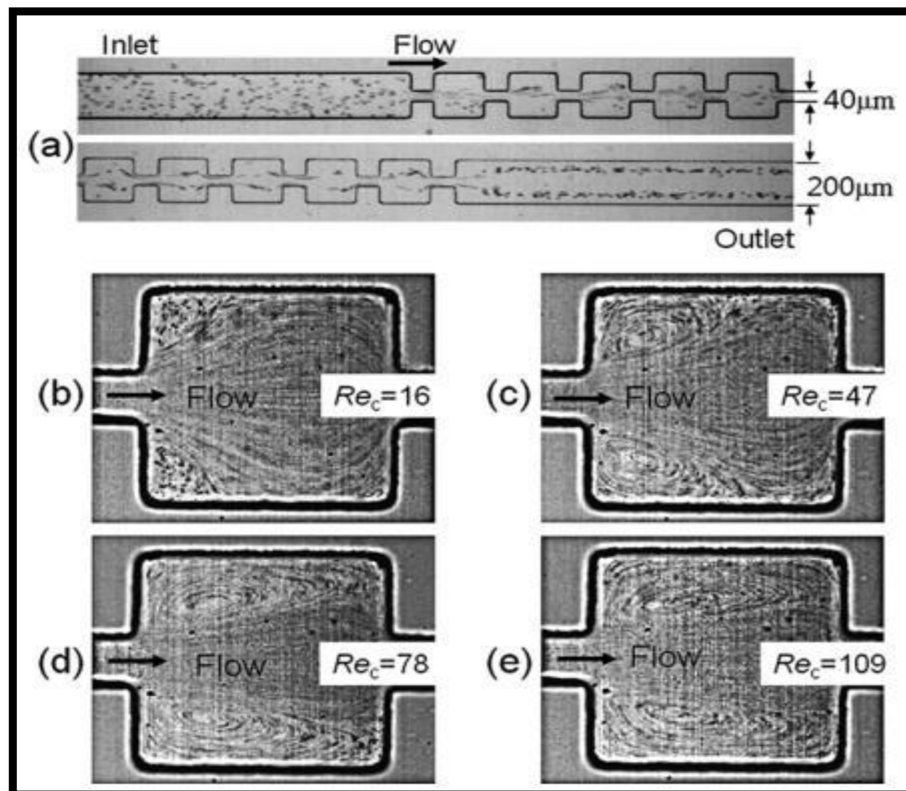

Figure 2.23 – Photographs of (a) microparticles migrating through the multi-orifice microchannel with at Re_c channel, Re_c ~ 63, and snapshots in a sudden expansion of the channel showing different scales of vortex flows; (b) Vortices generated with Re_c = 16; (c) Migration vortices of the particles generated with Re_c = 47; (d) Vortices generated with Re_c = 78; (e) Vortices generated with Re_c = 109 (PARK et al., 2009).

With the application of the standardized topology of multiple microchannel holes, there is a distribution of ordered particles and concentrating in central or lateral regions according to the Reynolds number, which in turn is controlled by the system inlet pressure. It can be observed

in Fig. 2.23 that the larger the Reynolds number, the larger the migration of the particles through the process of vortex generation along the holes in the microchannel (PARK, 2009).

Digital Microfluidic – DMF: Bogojevic (2012) and his research group have developed DMF devices that have some advantages because they are reconfigurable, have no moving parts, and show compatibility with the conventional high-throughput selection infrastructure, such as plate readers multiple wells.

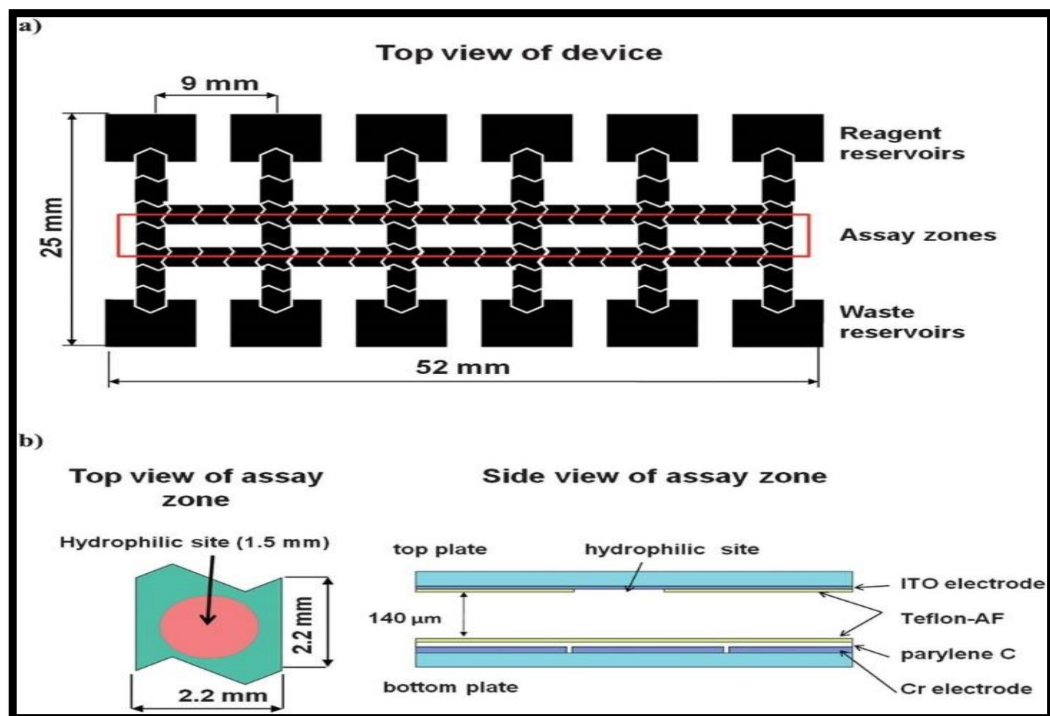

Figure 2.24 – DMF device used for multiplexed cell-based assays. a) Top-view schematic of full device bearing six assay zones. b) Top- and side-view schematics of one assay zone. (BOGOJEVIC et al., 2012).

For these and other reasons, digital microfluidics was presented as a potentially useful new tool for multiplexed tracking applications. In the application of cell-based assays in parallel, developed a fluorogenic apoptosis assay for caspase activity. Fig. 2.24 illustrates the proposed system for this study (BOGOJEVIC, 2012).

Optofluidic: The development of technology based on optofluidics has ushered in a new era of functionalities for Lab-On-a-Chip (LOC), including the miniaturization of biomedical devices, increased sensitivity for molecular detection and multiplexing of optical measurements. Despite having great potential, optofluidic devices have only begun to be

exploited in many biotech applications. Cheng (2012) and his group highlight the potential of integrating fluidic opto-devices with synthetic biological systems, which is a field focused on the creation of novel cellular systems engineering gene networks and synthetic proteins.

According to Cheng, synthetic light-sensitive biological systems would be relevant for integration with optofluidic devices for optofluidics applications in synthetic biology. The integration of optofluidics and synthetic biology would have a broad impact on point-of-care diagnostics and biotechnology. This system of optofluidics applied to synthetic biology is shown in Fig. 2.25.

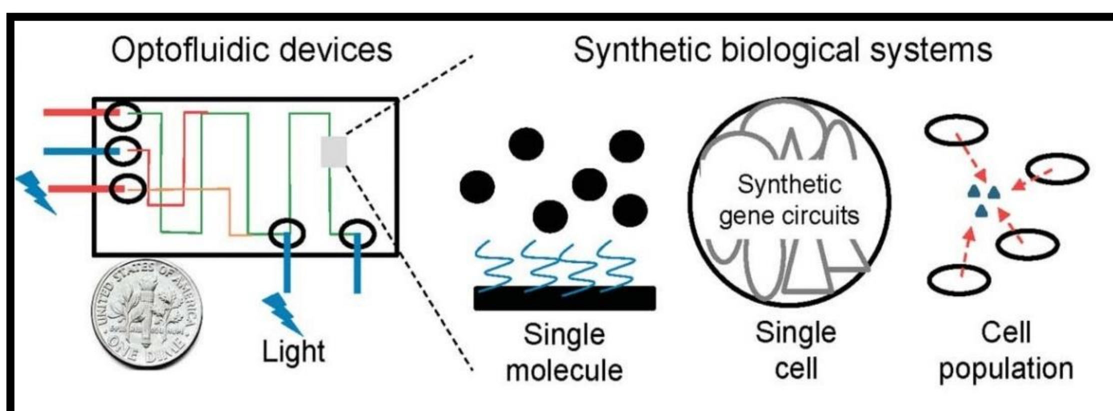

Figure 2.25 – The integration of synthetic biology and optofluidics. Synthetic biological systems of different length scales, ranging from single molecule, to single cell, and cellular population have been engineered for both biotechnology and therapeutic applications. (Adapted from CHENG et al., 2012).

3 MICROFLUIDIC DEVICES FABRICATION

In this chapter, we describe a computational tool for mask set, selected fabrication materials, microfabrication process, device characterization, experimental procedures and preliminary study of device modeling. All related steps are intended to describe the methodological steps used in the manufacture of microfluidic devices.

3.1. Hard Mask set design

After the preliminary simulations and definition of some geometries of the devices, the design of the masks was made, using CAD software, AutoCAD® 2007 (Auto Desk, Inc.). Taking into account the initial requirements of micro-channel widths, it was decided to use as hard mask, the photolith film printed with the photo plotter machine of the company DGM-Design with resolution of 8000 DPI, with reliable smallest printable trace of 25.4 μm (1 milli-inch).

The task was to create the masks in micro-microfabrication processes cheaper, faster and by meeting the minimum resolution specifications required for this project, with smallest feature of 50 μm. Given the diversity of techniques involved in the processes it was necessary to use negative and positive photolithographic masks, due to the use of different applied materials and techniques. The mask sets of micro fluidic devices applied in this work, were defined based in most common and classical passive microfluidic devices, for mixing, filtering and droplet generation (SCHIANTI, 2008; LEE, 2011; MADOU, 2011; TABELING, 2014), as shown in Fig. 3.1.

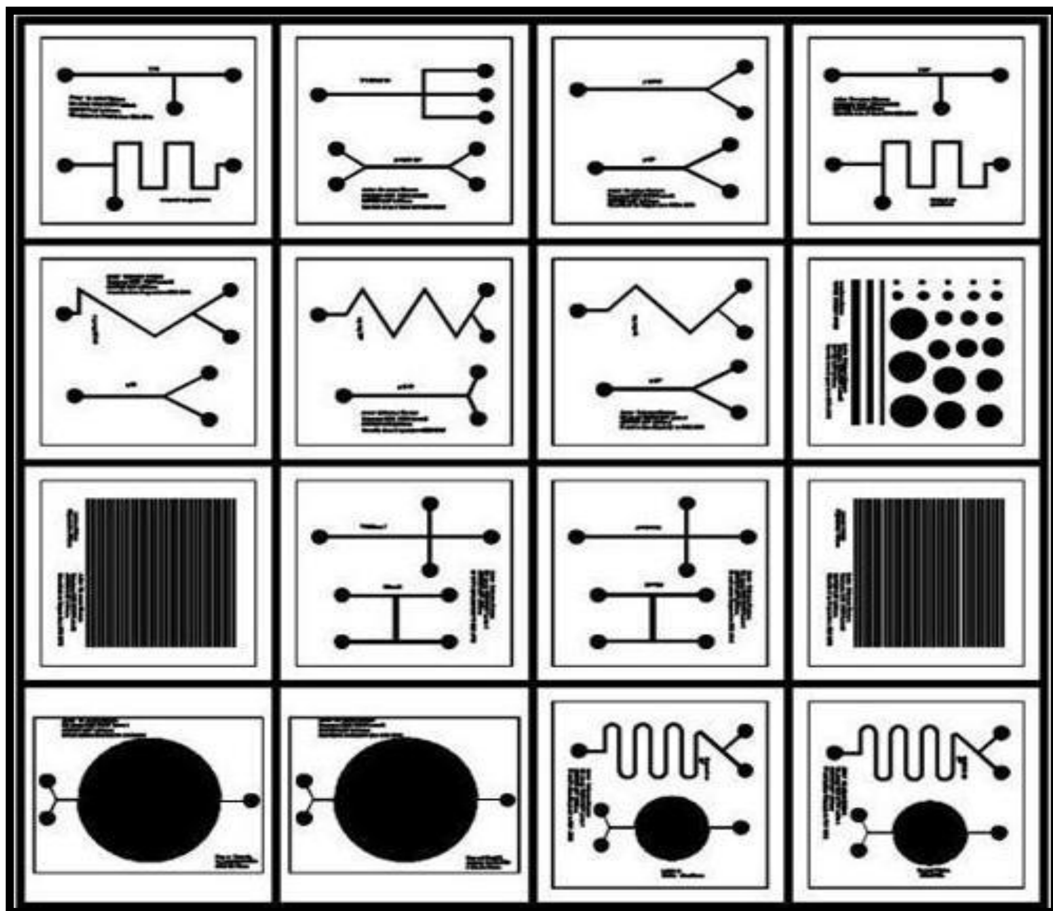

Figure 3.1 – General overview of microfluidic designs.

Hard masks are presented, as shown in Fig. 3.2. Some of them were already well applied and consolidated, as observed in some studies during the literature review (LEE, 2011; MADOU, 2011; TABELING, 2014), such as the Y curve used for micro mixtures, the H curve used in particle separation and electroosmotic flows. Some variations of these geometries were proposed with different input angles of the originals. We started approaching ways to optimize liquid mixtures inside these microchannels, we fabricated some shape curved devices with long channels such as "serpentine", "concentric spiral", 12.5m and 25m long, as shown in Fig. 3.2.

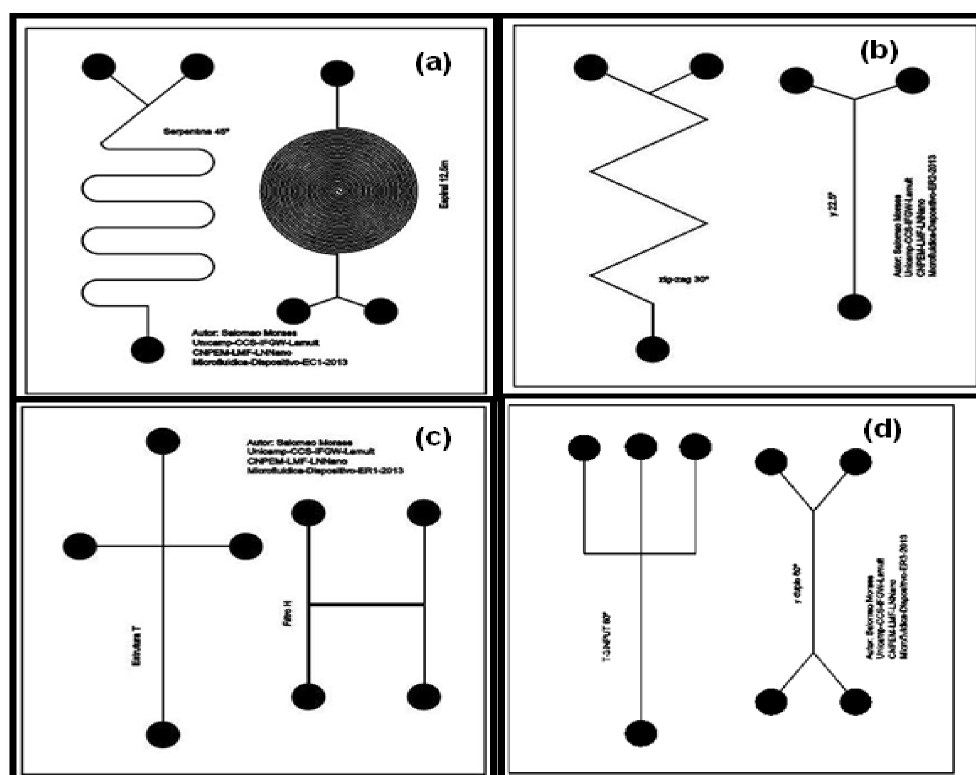

Figure 3.2 - Mask of microfluidic devices. (a) Serpentine and Spiral; (b) Triangular structure and Y; (c) Cross and H; (d) Trident structure and Y with two outlets, based on passive devices applied to liquid mixers.

3.2. Microfabrication process

In this section, the fabrication and characterization procedures of the microfluidic devices are described, in three different substrates: silicon, glass and PDMS.

3.2.1. Microfabrication process on silicon

We achieved micro channels in silicon wafers size of 2” and 3”, N type (phosphorous dopant material), crystallographic orientation <100>, total thickness 380 μm and sheet resistivity of 1 to 10 ohm.cm. Silicon was chosen as material with a view to the possibility of future integration with Microelectronics, with insertion of pressure sensors, chemical sensors like Ion Sensitive FET (ISFET), resistors for temperature control, optical coupling with waveguides and other integration possibilities. In addition, to enable the use of microfabrication techniques, which are already widely known and consolidated. Another advantage is that the sacrificial material is silicon dioxide (SiO_2), which is easily grown over silicon by the oxidation process (chemical inert), as well as the surface compatibility for thin film deposition, silicon thermal stability and the ability to withstand high temperatures. In the silicon etching process, we tested and investigated a process optimization to achieve well-controlled and reproducible channel depth, taking into account three main parameters: silicon wafer orientation, temperature and etchant solution concentration. We used solutions with basic pH, based on potassium hydroxide (KOH 42%, General Chemical), as a control parameter to change in temperatures at three points: KOH at 70º C, 80ºC and 90ºC. This methodology was used to survey the etching rate and roughness of the microchannels. Channel roughness is a key parameter that affects low Reynolds number in a fully developed fluid flows, steady state, increases the drop pressure and friction factor in microchannels (SABRY 2000; BAHRAMI 2007). The chemical solution, Buffered Oxide Etchant (BOE), consists of HF + NH_4F (1:6). The KOH solution used at higher temperatures is more aggressive, increasing the etching rate, and thus the roughness (CYRO, 2004).

For the transfer of the mask design to the substrate, we used the technique of contact lithography. Before opening the etching window on the SiO_2, we protected the remainder of the photographed area with the positive photoresist AZ-1518 deposited by *spin coating* technique. For the improvement of adhesion of photoresist on the SiO_2 surface we used the adhesion promoter hexamethyldisilazane (HMDS), with deposition time of 30 seconds and rotation at 6000 rpm. To produce films with 1.45 μm thickness, the SiO_2 was obtained via wet oxidation process. The silicon wafers oxidation protocol used the following parameters, as shown in Table 3.1:

Table 3.1 – Parameters of oxidation furnace, at the temperature of 1000ºC. (Process adapted from (SWART, 2008).

Environment	**Time (minute)**
N_2	10
O_2	10
$O_2 + H_2O$	480
N_2	10
N_2	> 3

The wet oxidation steps according to the parameters are for (SWART, 2008):

- ✓ N2 environment with time 10 minutes: For thermal stabilization, avoiding thermal stress on the wafers;
- ✓ O_2 environment with time of 10 minutes: It serves to create a thin layer of silicon oxide;
- ✓ O_2 + H_2O environment with time of 480 minutes (8 hours): Silicon oxide growth process, at an average growth rate of 38.9 Angstrom/minute, that is not a linear process, with a water volumetric flow rate of approximately 63 drops/minute;
- ✓ N_2 environment with time of 10 minutes;
- ✓ N_2 environment with time>3 minutes: Finalization of the densification and gradual cooling of the wafers avoiding thermal stress during removal of the furnace.

3.2.1.1. Process stages

The fabrication processes on silicon involve the sequences of steps illustrated in Fig. 3.3:

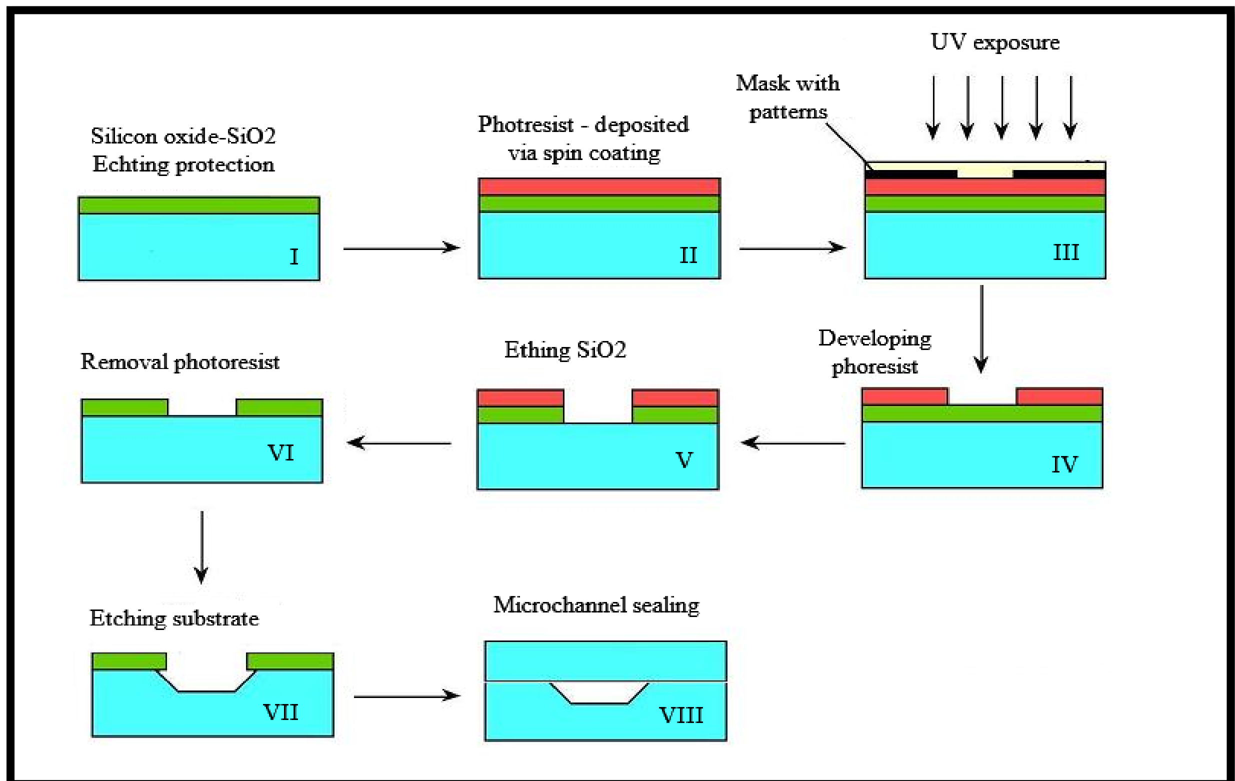

Figure 3.3 - Illustration of the fabrication processes of microfluidic devices in silicon.

The fabrication procedure of microfluidic devices in silicon follows the block diagram containing the simplified sequence of these processes. Fig. 3.4 shows main steps on the silicon wet etching process, the anisotropic etching process was adopted with basic solutions based on potassium, with constant concentration and sweeping temperature solution.

Below are some descriptions of processes in the block diagram, steps made based on (SWART, 2008):

- ✓ **Material:** Silicon with specifications mentioned in section 3.2.1.
- ✓ **Cleaning:** The RCA cleaning of the substrates is done to avoid accumulation of impurities at the interface between Si and SiO_2 that will be formed. Following the solutions used in cleaning RCA complete items **c)** and **d)**:

a) **H_2SO_4/H_2O_2** (4:1) at 80ºC for 10 minutes ("piranha solution"), this solution is useful for removing residual organic;

b) **HF/H_2O** at room temperature for 10 seconds, this step removes native oxide from the silicon surface;

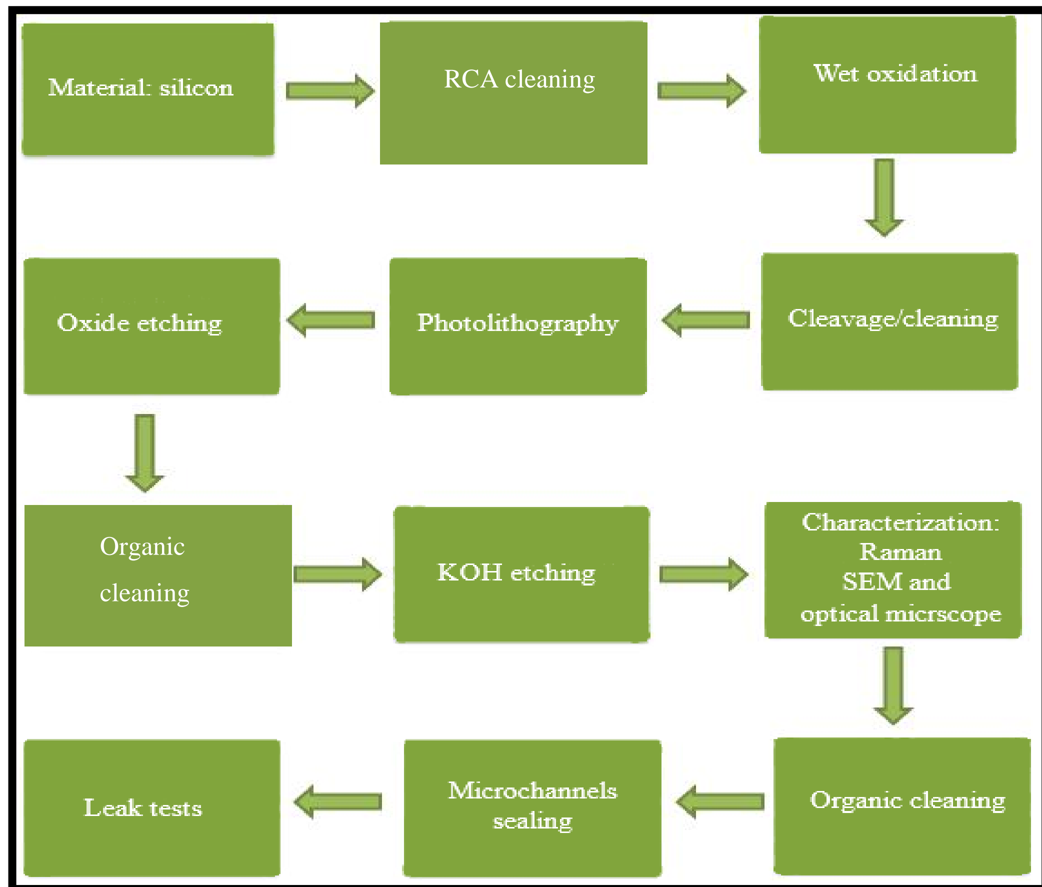

Figure 3.4 – Block diagram of the fabrication processes of microfluidic devices in silicon.

c) **$NH_4OH/H_2O_2/H_2O$** (1:1:5) at 80ºC for 10 minutes, removal of metal ions Cu^{2+}, Na^{+} and K^{+};

d) **$HCl/H_2O_2/H_2O$** (1:1:5) at 80ºC for 10 minutes, removal of metal ions as Mg^{2+}, Fe^{2+}, Fe^{3+}, Cu^{1+} and Ca^{2+} make removal of organic material.

✓ **Wet oxidation, Cleavage/Cleaning:** we used the wet oxidation protocol mentioned in section 3.2.1. After oxidation the substrates were cleaved in smaller sizes. Then we made an organic cleaning to prevent microparticles generated in the cleavage from sticking together in the microchannels.

- **Photolithography and oxide etching:** photoresist deposition, AZ-1518 cited in section 3.2.1. Conventional photolithography which is used to transfer the patterns from the mask to the photoresist. A simple process the photoresist is used as a masking material for SiO_2, with photoresist development desired regions in the silicon wafer are exposed. The wafers are placed on the hot plate to remove moisture, at a temperature of 90ºC for 5 minutes. The photoresist deposition and soft-bake in 90ºC for 1 minute, flood exposure time of 17 seconds with power of $9mW/cm^2$, development with Metal Ion Free (MIF - AZ 400K) developer 1:4 for approximately 1 minute, the hard-bake temperature of 120ºC for 30 minutes. After of the photoresist densification step, the SiO_2 etching is made with HF buffer at room temperature to complete removal of exposed SiO_2, always making the observation on optical microscope, this step took 13 minutes.
- **Organic cleaning and Si etching:** After of the SiO_2 etching, organic cleaning is done, immersion in boiling acetone for 10 minutes, boiling isopropanol for 10 minutes, DI water 18 Mohm.cm at room temperature and thorough rising. The etching process is done with KOH diluted in water, with a KOH concentration of 42%, with solution temperatures in the range of 70ºC to 90ºC, solution agitation with magnetic stirring. A description of the full procedure is presented in section 3.2.1.2.
- **Characterization/Organic Cleaning:** In order to characterize the etching in the silicon substrate, measurements of roughness were made by atomic force microscope (AFM). We measured width and height of the channels, also using optical microscopy and scanning electron microscope (SEM), shown in section 3.2.1.2.
- **Microchannel sealing and leak tests:** The microchannel sealing was made with PDMS irreversible activation technique, already with silicone tubes on the reservoirs. The test setup is described in the Results chapter.

3.2.1.2. Microchannels and Silicon etching

The wet etching process by means of KOH of the Microchannels in silicon have been optimized by selecting the right combination of the following parameters: concentration, temperature and agitation. According to Cyro (2004), the etching rate depends directly on the concentration and temperature, both in the silicon and silicon dioxide etching behavior, which can be observed in Fig. 3.5.

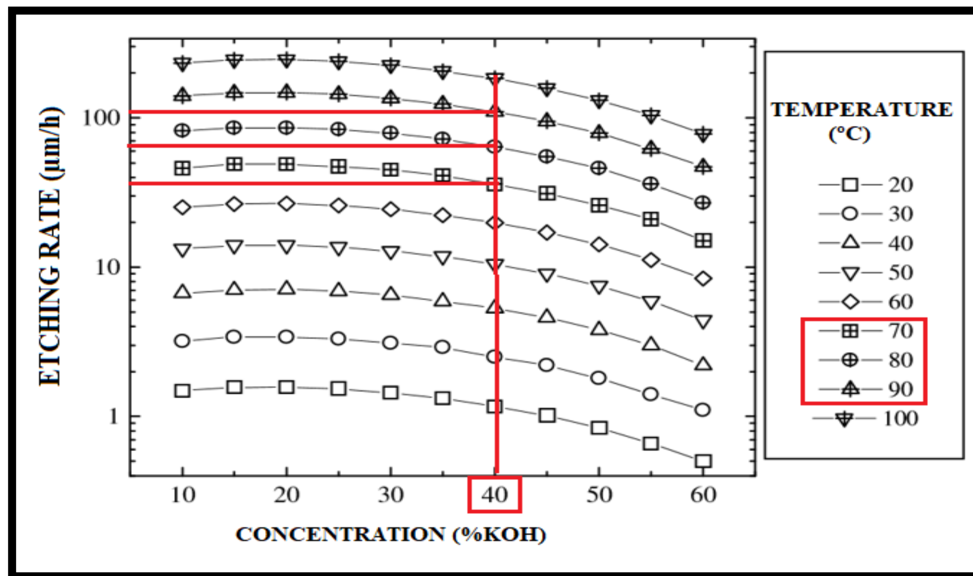

Figure 3.5 – Silicon [100] etching rate in KOH, taking into account temperature and concentration of etching solution. Etching rate in function of the concentration and temperature. (Adapted from CYRO, 2004; PAL, 2017).

We used an etching protocol with well know pattern structures, namely parallel lines spaced by 50µm and width of 50 µm. The achieved etching rate was calculated, taking into account, time and measured channel aspect ratio, which is width x depth ratio. Based on these experiments, we achieved an optimum etching process with channels with low roughness and high depth.

The key parameters, to achieve high reproducibility and reliable etching, are based on solution agitation speed, concentration and temperature. Taking as starting point, we fixed the parameters agitation and concentration, stirring was set up to 700 rpm, starting with increments of 100 from 0 rpm up to 700 rpm. During this set up, we did visual inspection for control micro vortices generation in the KOH solution and air bubbles formation around the silicon wafer.

We developed our etching process based on the region highlighted in the graph, as shown in Fig. 3.5, the concentration of KOH chosen was 42%. After fixing the agitation speed and concentration, we focused on the region of interest of Fig. 3.5, marked with red dots and lines, taking into account the commitment to obtain the highest etching rate with the lowest roughness, for spending less time during the etching process, and avoiding increase of the channel roughness, than can increase the drop pressure in the channel (SABRY, 2000; BAHRAMI, 2009). Always observing the selectivity with the oxide and the desired aspect ratio, without forming the "V grooves" being in this process of wet and anisotropic etching, as the morphology of the silicon privileges certain crystallographic planes.

The masking material also undergoes etching when submitted to the KOH solution, but its rate is much lower than that of silicon. Fig. 3.6 shows the etching rate of silicon oxide (SEIDEL, 1990; CYRO 2004; PAL, 20017). The lines and dots actually highlight the working region, previously defined for silicon. With the defined operating range, it is possible to have an estimate of the selectivity, etching rate and estimated time for certain etch depths, which served as a reference for the processes performed in the laboratory.

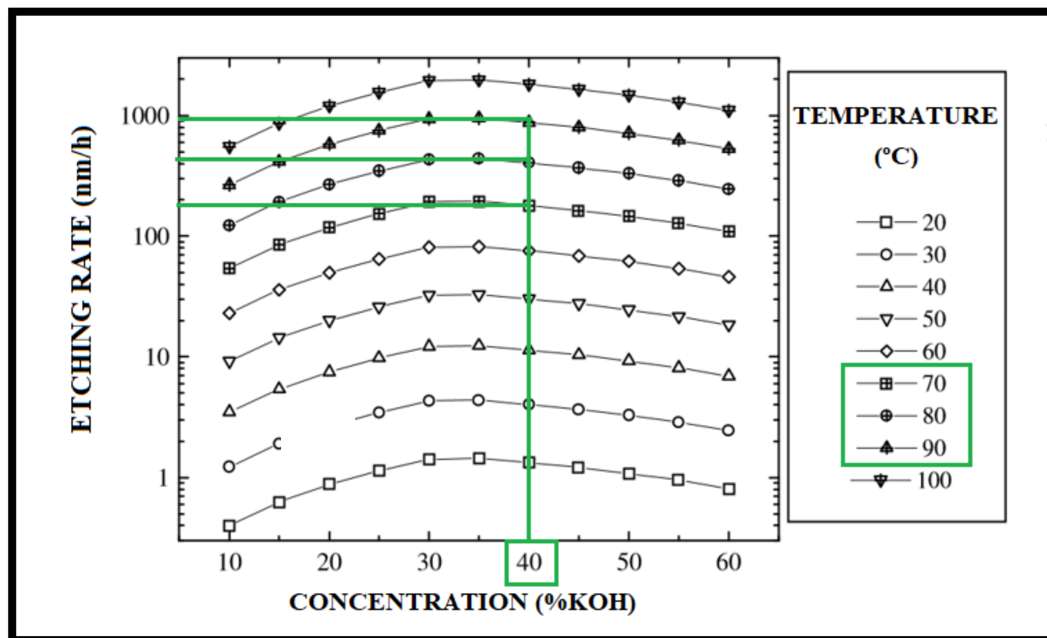

Figure 3.6 – Etching rate in silicon dioxide. Etching rate taking into account concentration. and temperature. (Adapted from CYRO, 2004).

In the silicon etching the etch rate is estimated between 40 and 100 μm/h, that is, between 0.67 and 1.67 μm/min., while the etch rate of SiO_2 under the same conditions is between 200 and 1700 nm / h, that is, between 3.33 and 28.33 nm/min. Therefore, the etching

selectivity between Si and SiO_2 under these conditions is between 59 and 201, thus, the maximum real etching time is up to 40 minutes for a SiO_2 film mask, with a thickness of 1.15 μm to avoid SiO_2 be completely etched away.

Fig. 3.7 shows the setup used in the experimental procedure for etching of silicon. In that, the control of temperature and part of the agitation are made by a hot plate, in the upper part was placed a thermometer to make indication of temperature of the solution, in the upper part also is the agitation system with wafers support up to 3", that hold wafer in vertical position, which is attached to a secondary rotational control speed.

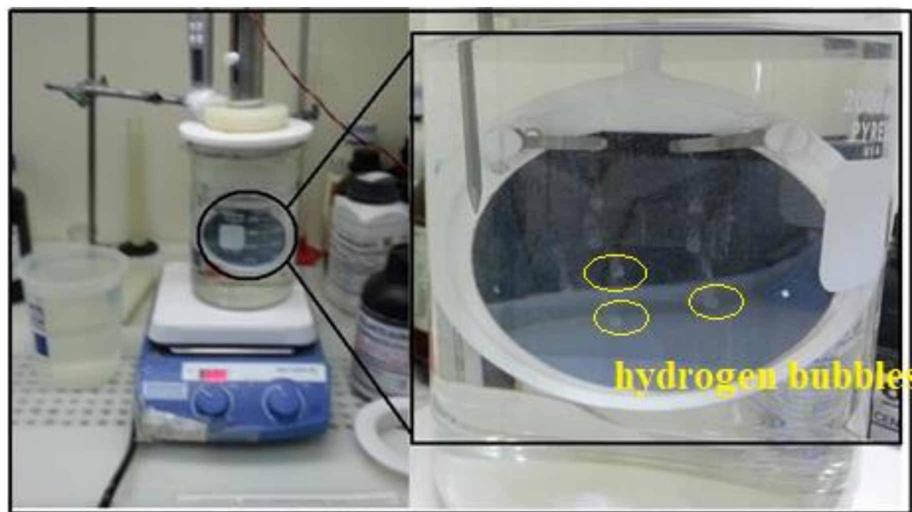

Figure 3.7 – On the left is the system for silicon etching, on the right is the wafer holder with the silicon in the etching process.

The etching processes took place in three stages divided into tests of 6 samples.: sample 1, sample 2, sample 3, sample 4, sample 5 and sample 6. The 3" silicon wafer was cleaved into 6 parts, and the procedure was chosen to vary the temperature from lowest to highest, 70°C to 90°C, with etching tests at 70°C, 80°C and 90°C, being a ± 2°C variation in each temperature point, reducing the etching time in 5 minutes for each step, starting with 20 minutes. Etchings of each sample were made separately one by one. With setup of fixed temperature at 70ºC samples 1 and 2 were etched, with the time of 20 minutes for each. The temperature of the solution was then increased in 10°C, it was stabilized at 80°C, etching samples 2 and 3 were etched separately, and each of them etched approximately 15 minutes. With the addition of 10ºC at the temperature of KOH solution and new stabilization for 90ºC, samples 5 and 6 were etched with the time of 10 minutes, for each one separately. After the etching process,

measurements were made in the profilometer to obtain etching rate, and taking into account depth and roughness, as shown in Table 3.2.

Table 3.2 – It shows the conditions and results for samples from 1 to 6, containing etching parameters, such as temperature and time correlated with depth, etching time, etching rate and roughness.

Sample number	Temperature (ºC)	Etching time (min.)	Depth (μm)	Etching rate (μm/min)	Average roughness (nm)
1	70	20	12,50	0,63	9
2	70	20	12,80	0,64	13
3	80	15	16,80	1,12	16
4	80	15	15,70	1,05	20
5	90	10	18,80	1,88	22
6	90	10	18,70	1,87	25

All measurements were made to verify the channel profile, and we measured the roughness at the bottom part of the channels, as shown in Fig. 3.8. We achieved reproducible etching process with etching rate of 1μm/minute, with roughness smaller than 25 nm. Shortly after the etching step, the characterization of the channels was done using profilometer (Dektak®150, Veeco Instruments Inc., USA), to obtain the cross-sectional profile, width, depth and average roughness. Also for roughness we used *Atomic Force Microscopy* (AFM) with equipment *Raman Spectroscopy AFM System – Model NTEGRA Spectra*. Thus helps us to calculate the etching rates, all of them based on real channels measurements. The micrographs presented in this section and sections 3.2.2 and 3.2.3 were obtained using optical microscopy with *Olympus optical microscope*, *BH2* model and *Carl Zeiss*, *Citoval* model, scanning electron microscopy technique – SEM (Microscope PHENOM).

Sabry (2000) reported the roughness effect on fluid flow and heat transfer in microchannels. He formulated a hypothesis taking into account average roughness measured from microchannels and its effect on the drop pressure, friction factor and Reynolds number variation. Prentner (2010) presented the roughness effect on blood plasma with increase of blood flow and drop pressure, in microchannels with aspect ratio of 50:1, height of 50 μm and roughness of 1.8 μm. Taking into account this roughness effect inside microchannels, we created a characterization protocol measuring the dimensions of microchannel: width, height and roughness, as shown in Fig. 3.8, to be able to present which regime flow with fully developed and steady state occurs more often in our microfluidic devices. We pumped DI water 18 mohm.cm with well-known volumetric flow rates via syringe pump injection

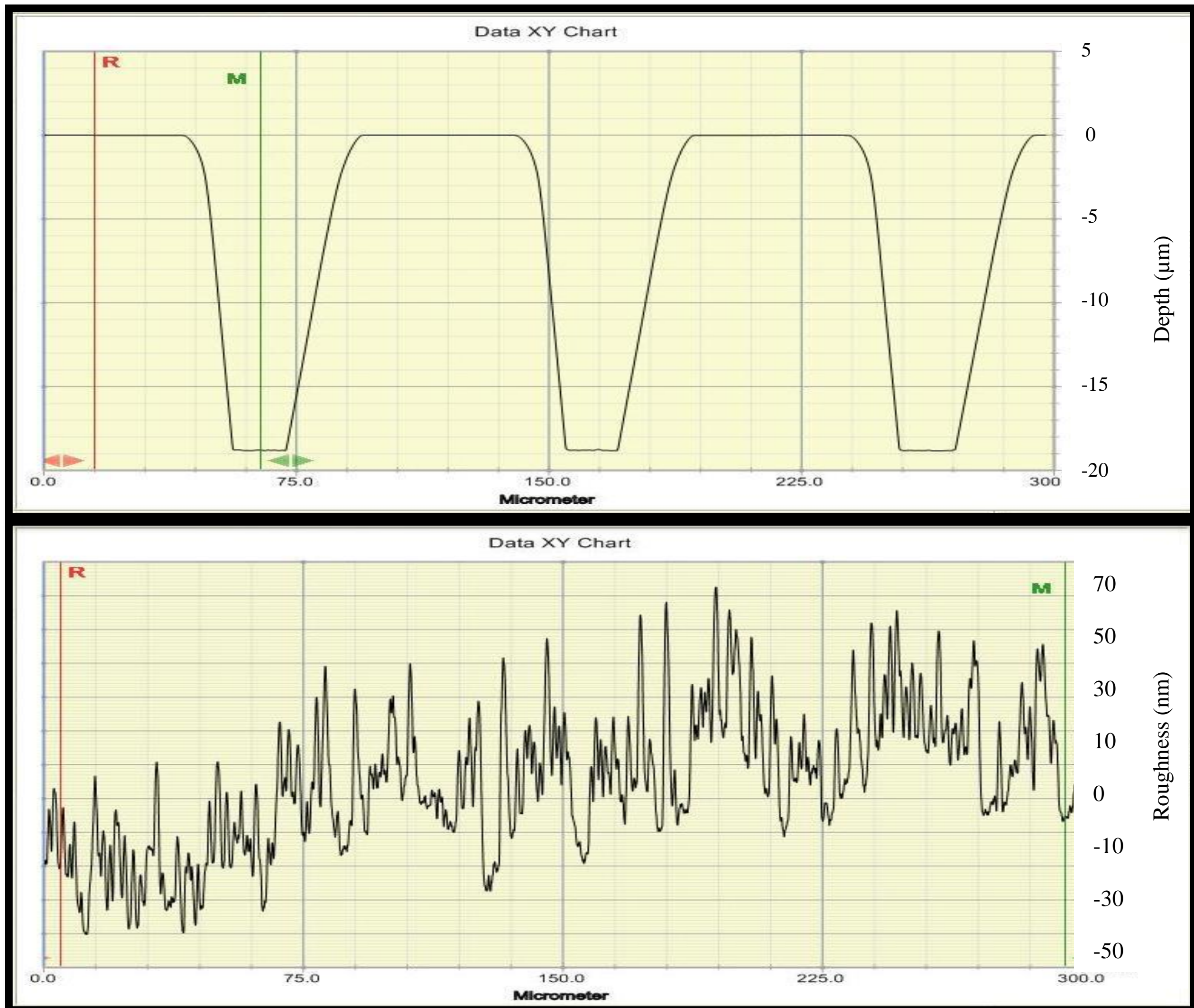

Figure 3.8 – Profilometer measurements, depth and roughness. In the top part, microchannel depth and width. In the bottom part, roughness measurements made in the bottom part of the microchannel.

It can be observed in Table 3.2 that the roughness obtained in this etching process is less than 25 nanometers, being more than a thousand times lower than the target depth of the channels, this shows that it would be possible to choose any temperature between 70°C, 80°C and 90°C. By simple and direct relation, we can obtain the desired depth of the channels based on the etching time, for example, if we choose the temperature of 80°C and we want the depth of 40 micrometers, the etching time will be of 40 minutes. Another observation that can be made is the rate of variation of the maximum roughness between samples around 34%, and the overall average roughness of 17 nanometers, it is also observed that the higher the temperature the higher the etching rate, with the etching rate varying from 70°C to 90°C, ranging from 0.63 µm/min to approximately 1.87 µm/min, so the etching rate increased in three times. As a

complement to the measurements of profilometer, some micrographs were taken with a scanning electron microscope to obtain the microchannel profile and Raman-AFM measurement to obtain roughness, according to Fig. 3.9, respectively.

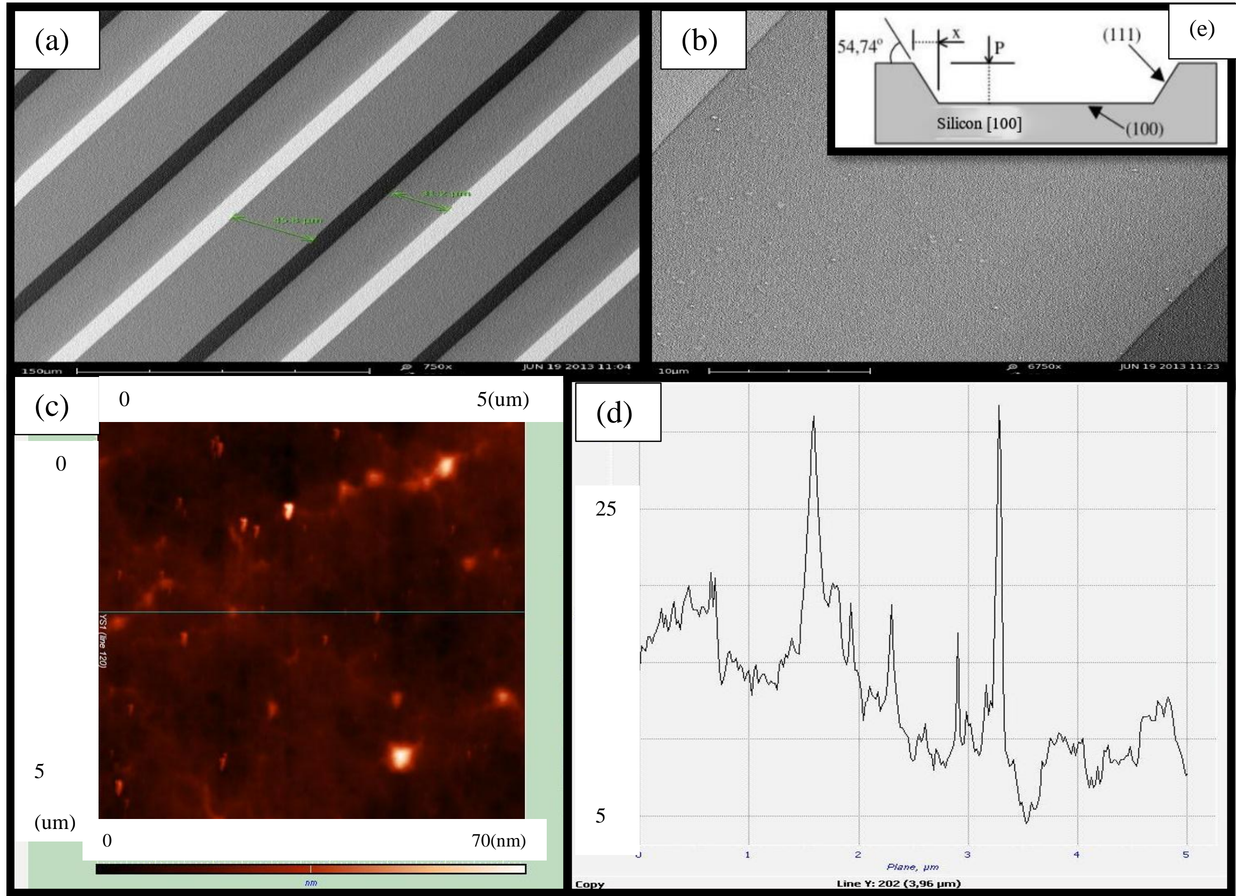

Figure 3.9 – SEM and AFM Micrographs. (a) Microchannel top view. (b) Profile roughness at the bottom of the microchannel. Micrograph in perspective with roughness measurement of the microchannel. Micrograph and roughness graph, silicon characterization. (c) Micrograph of the roughness in an area of 5 x 5 µm2. (d) Microchannel roughness plot. (e) Angle formation of 54.14° between the planes (100) and (111).

Channel roughness measurements were performed using AFM to compare the roughness measurements obtained with the profilometer. We obtained a mean roughness of 40 nm, according to the AFM measurement, as shown in Fig. 3.8 and Fig. 3.9, where the roughness was measured in an area of 5 x 5 μm^2 and next to the graph with the cross-section of the roughness of this measured area, respectively. Based on the results obtained, the process was adjusted to the temperature of 80 ° C, and based on the measurements in Table 3.2, we used the fixed and constant etching rate around 1 µm/min., This value was defined for a better control of the depth and less time of etching and roughness. Based on the etching time, the silicon

favors certain crystallographic planes, with the substrate used in the etching having orientation (100), there is a formation of an angle of 54.74º with the plane that forms the walls of the channel (111) as can be seen in Fig.3.9, thus forming the trapezoidal channel profile. In order to determine the depth, we used Eq. (3.1), with the purpose of simplifying the control of etching depth via etching time, the etching rate being well known in the process, and a simple equation for depth control was defined as below:

$$P = \alpha t \qquad \text{Equation (3.1)}$$

where: ***P***: is the depth in (µm);

α: is the etching rate in (µm/minute);

t: is the etching time in (minutes).

An important observation to be made when defining this methodology is that in order to determine the depth it is indispensable that the etching process be kept stable and with the same depth reproducibility, taking into account that microchannel depth is defined by time, e.g. 30 µm in depth we spend 30 minutes in etching time, considering 1µm/minute of etching rate

Keeping the KOH solution at the same concentration and with very small temperature variation (less than 3°C) and with stirring of the constant solution, it is possible to keep the etching rate always the same and constant. So, the parameters involved in the process of obtaining the microchannels have been defined and characterized. Based on theoretical and simulation models, we defined our microchannel depth, as 30 µm, with lines width of 100 µm. For the manufacture of the devices, the time of 30 minutes was used to guarantee a depth of approximately 30 µm. As a reference point for a fast measurement a micrometer was used in the reservoirs with a diameter of 3 mm, at the entrance and exit of the microchannels, which are the points of communication with external medium, according to Fig. 3.10.

For detailed analysis, we decided to complement the information by measuring the profile of the microchannels with 3D profilometer (Dektak®150, Veeco Instruments Inc., USA), and generated the 3D profile of the microchannels, according to Fig. 3.10, in order to

investigate the accuracy and reproducibility of the microchannel acquisition processes. All 3D measurements were done at LNLS lab.

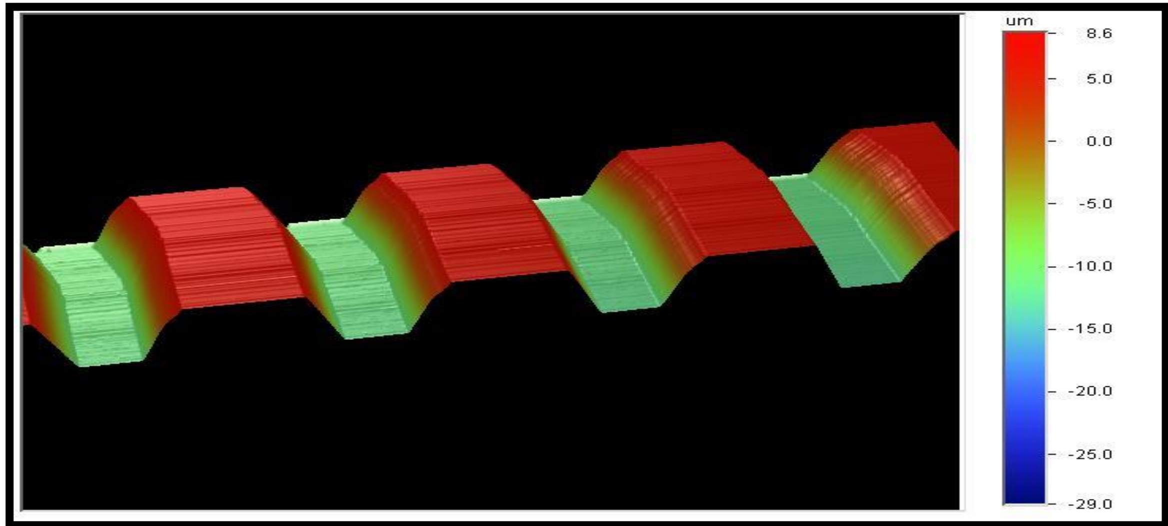

Figure 3.10 – Measurement of microchannels with more precision with 3D profilometer Dektak 150, technique of styles contact.

We acquired data about channel dimensions, some considerations have to be taken regarding the process of obtaining microchannels in silicon from the wet etching in KOH, according to (BARBAROTO, 2002; PAL, 2017), due to the anisotropic etching mechanism of silicon (100), in which there is a big difference in etch rates for certain crystallographic planes. In case of etching of convex corners, this affects directly in the geometry of the devices, as the corners are the points of intersections between planes. As the consequence, the anisotropic etching in regions of corners resulting in distortion of the initial geometry and the desired dimensions, thus making it necessary to use additional techniques to correct this problem. The most usual is the technique of compensation of convex corners, as can be observed in the micrographs obtained by optical microscope of Fig. 3.11 (BARBAROTO, 2002; PAL, 2017).

The etching of convex corners, according to both Barbaroto (2002) and Pal (2017), it is necessary to make masks based on calculations of the formed polygons and the measurement of their angles, a commonly used compensation structure, which are added to the corners of the geometries. We would like to emphasize, that convex corner compensation study, has not been covered in this work, we just used these results as guide to avoid making more complex structures in silicon wafer with etching based on KOH solution.

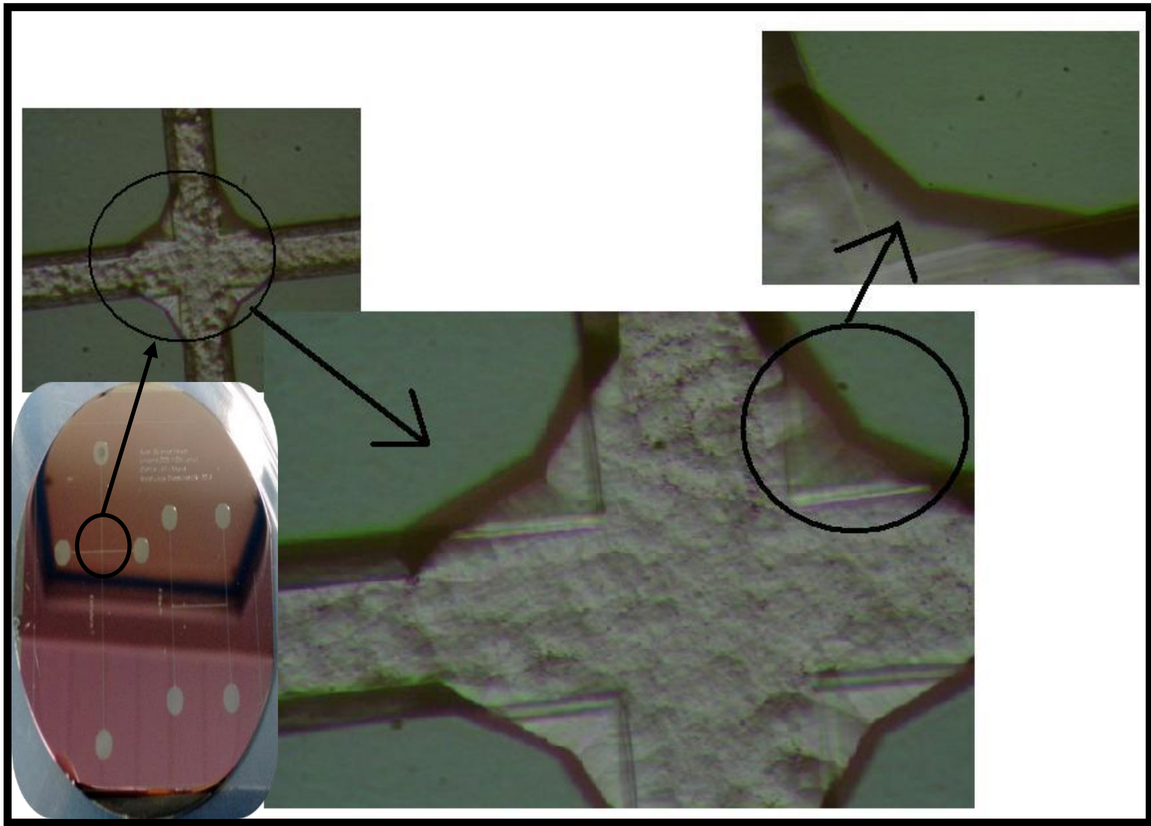

Figure 3.11 – Microchannel micrograph and convex edge etching.

3.2.2. Microfabrication process in glass

For the fabrication of the microfluidic devices in glass, we used the microscopy glass slides from Perfecta®, code 201, slides in plain and non-stoned form (dimensions: 25.4 cm x 76.2 cm x 1.0 to 1.2 mm, Perfecta, Brazil). There are many advantages of using glass as a substrate in the fabrication of microfluidic devices, which include: good thermal stability, chemical inertness and optical transparency (SCHIANTI, 2008). In addition, microfabrication processes are well known and consolidated, this directly influences the reproducibility, another advantage is the surface compatibility for deposition of thin films, great for insertion of interdigitated electrodes, for applications with capacitive measurements or impedance. Microscopy slides were chosen with the main objective of reducing the device microfabrication costs and time, with faster prototyping, making them cheaper when compared to silicon processes. However, because the substrates are low cost and normally used for microscopy, the glass composition information is not specified by the manufacturer, so it is necessary to add a measuring step to identify the doping materials in the glass to perform the characterization.

For the etching processes in glass, acid solutions based on hydrofluoric acid (HF), concentration of 40% were used from General Chemical, being diluted in water in the proportion: HF + H2O (1:1); with the use of hydrochloric acid (HCl) 38%, General Chemical according to works made by Coltro (2008) and Shianti (2008). HCl is used for removal of residual glass microparticles generated in the microchannels during the glass etching process. The etching solution based in HF is very aggressive, we used HF + NH_4F (1:6), its requiring the use of hard material to mask the wafer. For the use of ammonium fluoride NH_4F (40%), it is recommended to make a pre-etching, being used in the form of BOE-Buffered Oxide Etchant solution (SCHIANTI, 2008). Considering that for the etching experiments, solutions of HF diluted in deionized water of 18 Mohm.cm were used, thus diluting the concentration of the solutions and rendering them less aggressive to the glass. The photoresist AZ-4620 (Clariant Corporation, USA) deposited by the spin coating process was used in order to achieve better uniformity, which are normally required as masking materials of the substrate in the etching processes. The depositions of the hexamethyldisilazane adhesion promoter (HMDS) and of the AZ-4620 photoresist were defined with a time of 30 seconds and with a rotation of 3000 rpm, obtaining films with a thickness of approximately 7 μm, according to the manufacturer's datasheet. However, we chose to use control substrates to make comparative measurements with the profilometer, to verify the quality, uniformity and reliability of our process.

The glass microchannels sealing was done with PDMS with irreversible activation by oxygen plasma (O_2). In this sealing process, both the top and bottom substrates are exposed to the O_2 plasma simultaneously, the channels were irreversible sealed, as Coltro and Schianti (2008) described this irreversible sealing process. The insertion of inlet/outlet ports were done with silicone tubes (Perfimed, nº140), sealed directly to PDMS cover. Tubes with internal and external diameter dimensions of 1.0 mm (ID) x 2.2 mm (OD), were previously aligned and sealed directly in the curing of the PDMS. For the alignment system, acrylic plates (2.0 x 15.0 x 0.5 cm) were used with holes made in the positions of the inlet and outlet reservoirs.

3.2.2.1. Microfabrication steps in glass

The microfabrication steps of microfluidic glass devices, in a short form, begin with steps of wet etching to obtain microchannels, as mentioned in section 3.2.2, then the microchannels are sealed with PDMS. Fig. 3.12 shows the detailed process flow:

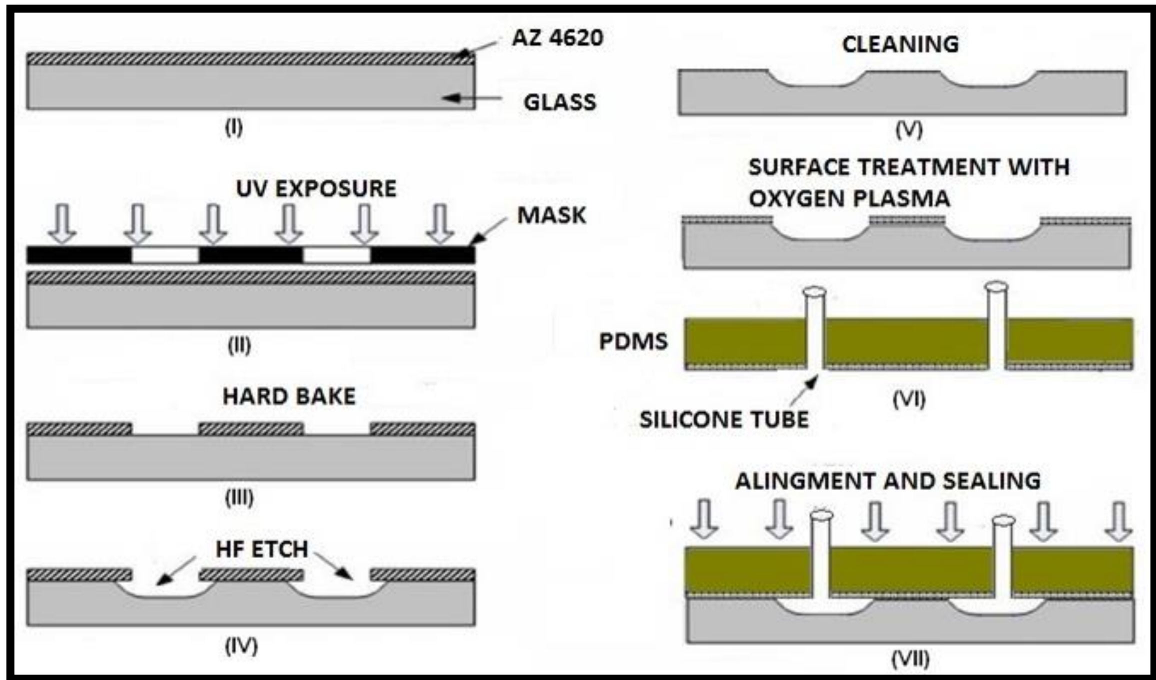

Figure 3.12 – Stages of microfabrication in glass: (I) Photoresist deposition on clean substrate; (II) Photogravure; (III) Disclosure and Heat Treatment; (IV) Etching in HF; (V) Photoresist Removal and Cleaning; (VI) Surface activation; (VII) Sealing.

(I) Cleaning the glass substrate and depositing the masking material: The glass slides need to be thoroughly cleaned at the outset and throughout the entire process, the cleaning of the glass slides is done to remove glass microparticles, organic materials and contaminants. The cleaning is done initially with rinse in deionized water, then with immersion of the wafers in nonionic detergent (Extran) for 10 minutes. Preferably the glass slides are spaced apart from one another and are then dipped into the ultrasonic bath (THORTON®, 25kHz, 160w) for 5 minutes. And finally the substrates are cleaned manually with soft sponge, and then they are washed and rinsed with deionized water 18 Mohm.cm, then all the substrates are dried with nitrogen jet and placed on the hot plate at 90°C for a period of 20 minutes, to remove moisture. The photoresist AZ-4620 is then deposited, applied at 3000 rpm for 30 seconds to achieve 7μm thickness, then applied by adjusting the temperature to 95°C for a time of 10 minutes.

(II) and (III) Photolithography, Development and Thermal Treatment (hard-baking): Conventional contact photolithography is used to transfer mask patterns to the substrate. Thus, the direct transfer of standards for etching was adopted, and the photoresist AZ-4620 itself was used as a masking material for glass etching. After deposition of the photoresist, exposure to ultraviolet light was performed using the MJB3 photomask aligner (Karl Zuss), with energy of 10mJ / cm^2, with exposure time of 70 seconds, then using the

developer K400 in a ratio of 1:3 with DI water. With the development stage completed, the substrate was placed for heat treatment, aiming to reduce the amount of solvent in the photoresist AZ-4620. Placing the substrate on the hot plate with a temperature ramp of 60°C to 150°C, with increments of 10°C and intervals of 2 minutes from 60°C, to avoid cracking of the photoresist film, remaining then for 30 minutes at 150°C.

(IV) and (V) Etching in HF and Photoresist Removal and Cleaning: Shortly after the heat treatment and cooling of the glass substrate, the etching in HF is done using Teflon beakers, at room temperature and with magnetic stirring. To obtain the etching rates and maximum durability time of the film without degradation, some etching tests were done on control substrates. The following solutions were used in the sequential steps: HF + H_2O (1:1) and HCl (without dilution in water), with varying etching time reaching a depth in the range of 30 μm to 50 μm, with time intervals of 1 to 8 minutes in HF. With the etching step completed, after observation of non-obstruction of the microchannels and absence of glass microparticles, another cleaning is applied to the substrates, firstly the organic cleaning to remove the photoresist, then the cleaning and drying steps mentioned in step I) and when necessary the cleaning with piranha solution (H_2SO_4: H_2O_2, 7:3) is applied for 30 minutes. And in a solution composed of H_2O, H_2O_2 and isopropanol alcohol, electronic grade of purity, heated in a 'water bath' for 15 minutes. Observations of the profiles, uniformity of the structures, depth and roughness measurements were made with profilometer and optical microscope.

(VI) and (VII) Activation of Surfaces and Sealing: After a further step of drying the glass slide with microchannels, in parallel the cover substrate was prepared with PDMS and the silicone tubes. The top and bottom substrates are sealed together, being the substrate of the top made of PDMS and the bottom of the glass slide with the microchannels. The sealing technique chosen is the irreversible activation of the PDMS where both substrates are submitted to an oxygen plasma, O_2 at 70 sccm, chamber pressure 70 mTor, power 100w and time of 10 seconds. Since, the sealing is done at room temperature and with pressure application, manually handled on both substrates already aligned on a flat surface.

3.2.2.2. Etching of glass slides

During the post-baking process, the photoresist AZ-4620 solvent release occurs. And greater durability is obtained for the photoresist used as a mask when exposed during the etching stages. Fig. 3.14 shows the steps of etching in the laboratory, from the heat treatment, placement of the substrates in the supports and etching. For the etching processes of the glass

slides, in addition a preparation of some PVC and Teflon supports was required. Fig. 3.13 shows the supports developed for the etching processes.

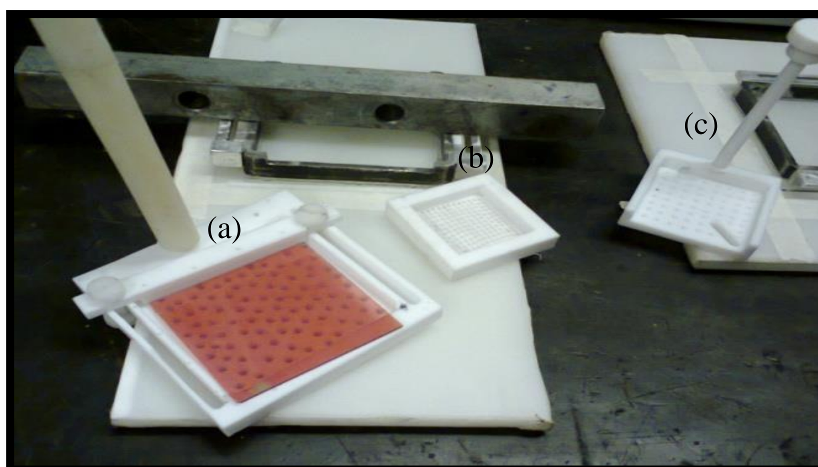

Figure 3.13 – PVC and teflon supports used in glass etching processes for different substrate sizes; (a) For glass substrates 10”and adjustable, (b) 3” and (c) 5”.

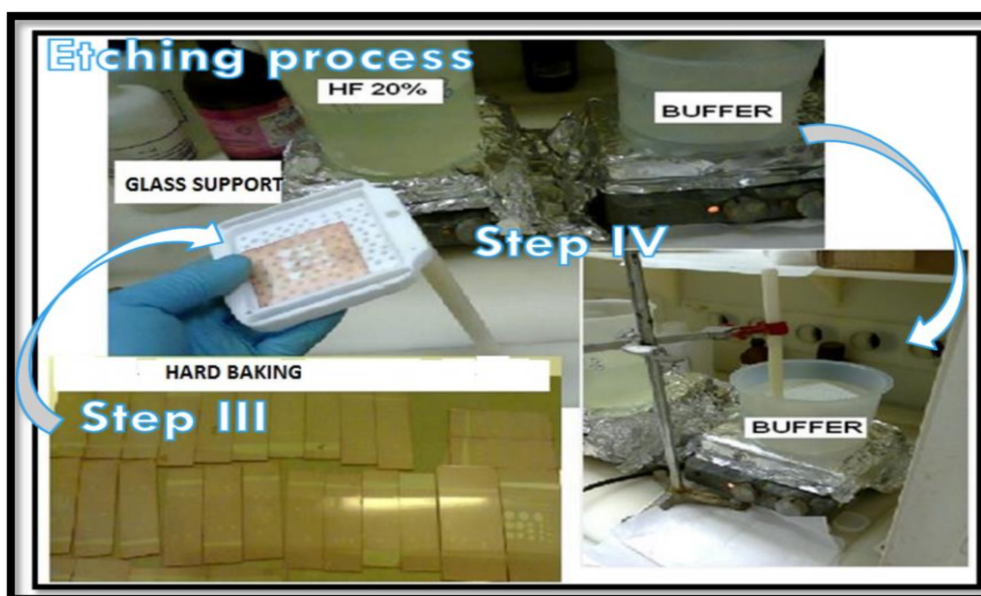

Figure 3.14 – Etching steps in glass after lithography process, starting from hard-baking: step III thermal treatment, step IV - support placement and etching in buffer and HF 20%.

We decided to do a more detailed analysis on the glass slides before beginning the etching steps, as we failed to obtain the detailed composition of the glass from the local supplier.

Hence, we made EDS measurements on Perfecta glass. We proceed with EDS measurements in the absence of datasheet information from the manufacturer, with quantitative values of its glass composition.

We made a comparison with the reference table of approximate percentage composition of some glasses, these indicators show that our glass microscope slides are more close to soda lime glass composition, according to our EDS measurements crossed with the manual supplied by the manufacturer (Corning Glass®) containing the approximate composition of the glasses per code, such as glass code 0080, as shown in Table 3.3.

Table 3.3 – Approximate composition of Corning glasses. (Adapted from Corning glass website*.)

Corning glass	Type	Composition (%)								
		SiO_2	BaO_3	B_2O_3	AlO_3	Na_2O	K_2O	ZnO	FeO_3	**Other**
7740	Borosilicate	80.9	-	12.7	2.3	4	0.04	-	0.03	-
7059	Barium Borosilicate	49	25	15	10	-	-	-	-	1
0211	Zinc borosilicate	65	-	9	2	7	7	7	-	3
0080	Soda lime	73	-	-	1	17	-	-	-	9

*The author adapted table 3.3 from several datasheet collections from Corning glass. Available in https://www.corning.com/worldwide/en.html

Additional information for code 0080 of the table, which has as percentage composition 9% of other elements, which would probably be distributed between: 4% MgO (magnesium oxide) and 5% CaO, then this information indicates that the glasses chosen for the process are similar to the soda lime type. This fact that could be verified with greater precision of the percentage composition with X-ray photoelectron spectroscopy (XPS). The type of percent composition of the glass directly influences the rate of etching and the formation of microparticles that could obstruct the microchannels or generate a high roughness in the microchannels. Usually the following glass type (7740, 7059, 0211) are used for the production of microfluidic systems. However, many disadvantages appear, among them is their cost: the

net unit price of the glass slides is about 6 time more expensive than microscope slides (USD $ 1.75 versus 0.28). The purpose of this research was to make the results more accessible and useful to be reproduced by other research groups, aiming to reduce costs and mainly not be dependent on a single supplier. We developed a full microfluidic fabrication process using low cost substrates, such as, soda lime glass with reliability, reproducibility in well-controlled etching process, and achieving low roughness.

The etching solution used based on HF + H_2O (1:5), modified and adapted previous works from Schianti (2008) and Coltro (2008). Prior to the etching step, roughness measurements were made on the surface of the substrates to measure the etching quality with the aim of minimizing roughness within the microchannels at the end of the etching, an initial average roughness of 7 nm was measured. For the etching processes, the pre-etching method with Buffer HF was adopted for 5 minutes, followed by etching in HF with 5 minutes, without cleaning wafer with DI water between previous steps. To define the etching time, we first raised the etching rate by etching 4 substrates at each equivalent etching time of: 1; 1.5; 2; 3 and 5 minutes, and we calculated the average of the depths measured as shown in table 3.4. After immersion in HF, we rinsed the substrates in DI water before finally cleaning in HCl. Then, we inserted the etched substrates in an ultrasonic bath with 38% HCl for a time of 10 minutes, right after this stage optical microscope inspection of the microchannels and evaluation of total removal of micro particles are done, following with measurements in the profilometer for depth, etching rate and roughness.

Table 3.4 – Etching rate evaluation for Perfecta microscope glass slides.

Etching time (min.)	**Depth in (μm)**	**Etching rate (μm/min)**
1,0	19	19
1,5	24	16
2,0	29	15
3,0	35	12
5,0	50	10
6,0	55	9

Table 3.4 shows the depths reached for each etching time in HF. It can be observed that the etching rate is not constant during this etching process, achieving the same non-linear etching behavior as reported by Schianti (2008) and Coltro (2008). However, using well-known parameters, such as the times evaluated in the Table 3.4, solution concentration and temperature, type of glass, it is possible to have a good reproducibility of the etching process, having depth and roughness of the microchannels. The time chosen to fabricated the microchannels was between 4 to 6 minutes at room temperature. Some tests were performed on the durability of the masking material were made, in this case the photoresist AZ-4620, which began to suffer degradation visually after 8 minutes and in some cases without damage up to a maximum of 10 minutes in exposure to the etching solution. According to the known variables of this process, temperature, glass type, solution concentration and temperature, desired depth and smaller roughness possible, to maintain in laminar flow in our systems. Hence, the relative channel roughness (channel roughness/channel depth scale) was found to be less than 1.5%, smaller than the 3% presented by Akbari et al. (2009) and 3.6% presented by Prentner et al. (2010). However, very few works were done aiming at understanding the effect of surface roughness on momentum and heat transfer (MALA et al., 1999; QU et al., 2000). They investigated flow in trapezoidal silicon microchannels, and a significant difference between the experimental data and the theoretical predictions was found. Experimental results indicated that the pressure gradient and flow friction in microchannel are higher than those given by conventional laminar flow theory (AKBARI et al., 2009). The measured higher pressure gradient and flow friction was attributed to the surface roughness of microchannels (MALA 1999, QU et al. 2000). Thus, the effect of roughness on the pressure drop of the fully developed flow cannot be neglected. Our results were more promising and less sensitive to roughness effect with low Reynolds number, based on very small ratio roughness/depth criteria. The ratio of the height of surface roughness to the height of the channel ranges from 0.5% to 3%, presented by (KULKARNI, 2004). Therefore, the surface roughness higher than 3% may have a profound effect on the velocity field and the flow friction in microchannels (KULKARNI, 2004). From known etching times, 5 minutes, it was possible to obtain depths around 50 µm of the microchannels in the microfluidic devices, an expected result in the depth of the microchannels, as shown in Fig. 3.15 and Table 3.5. Measurements were made with the profilometer, that is a surface contact measurement technique where a very low force stylus is dragged across a surface. The display range of the data is in (µm) with a maximum vertical resolution of ~ 0.1 nm, with Standard stylus radius is 12.5 µm.

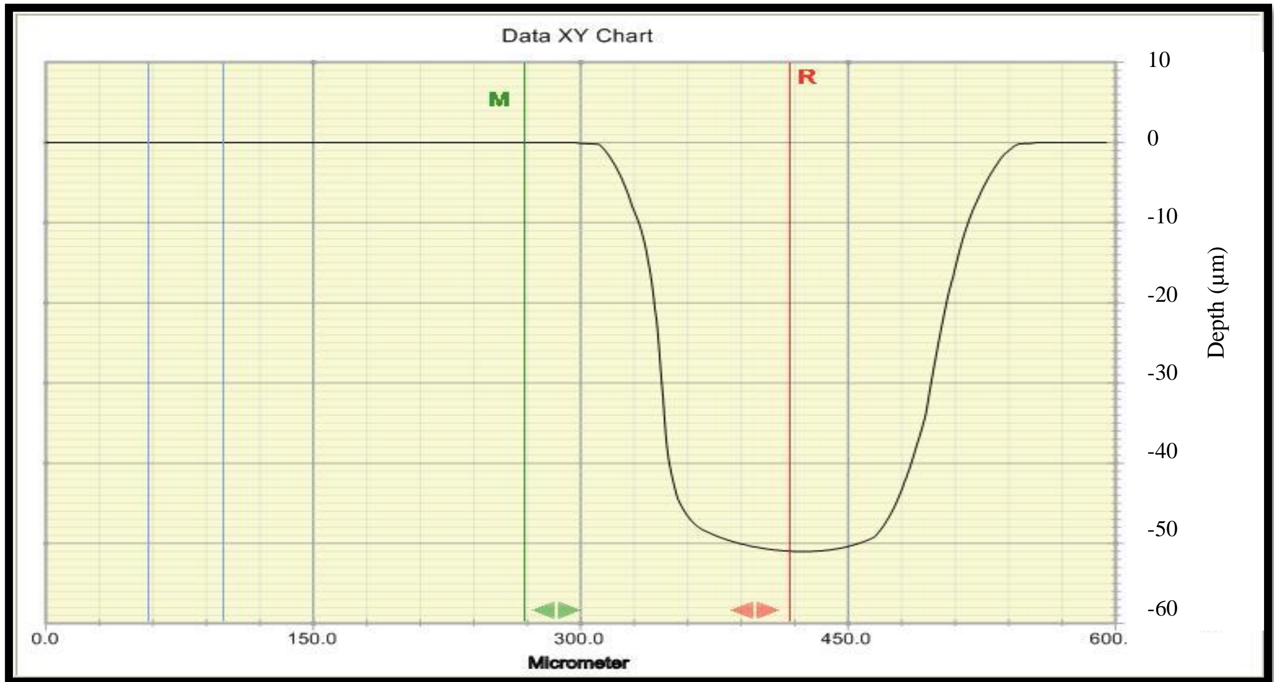

Figure 3.15 – Depth obtained from microchannels, achieved with 5 minutes etching time. Microchannel depth measured with profilometer.

Table 3.5 shows the measures of width, depth and roughness of some devices made of glass. It can be observed that the width ranged from 366 to 458 μm, the depth of the microchannels varied from 43 to 64 μm and the roughness from 132 to 471 nm. Micrographs of the microchannels were also made with the aid of the optical microscope, as shown in Fig. 3.16 and 3.17.

Table 3.5 – Microfluidic channels achieved with glass etching technique, after 5 minutes.

Time in (minutes)	Width in (μm)	Depth in (μm)	Average roughness in (nm)
4	366	43	132
5	407	57	223
6	458	64	471

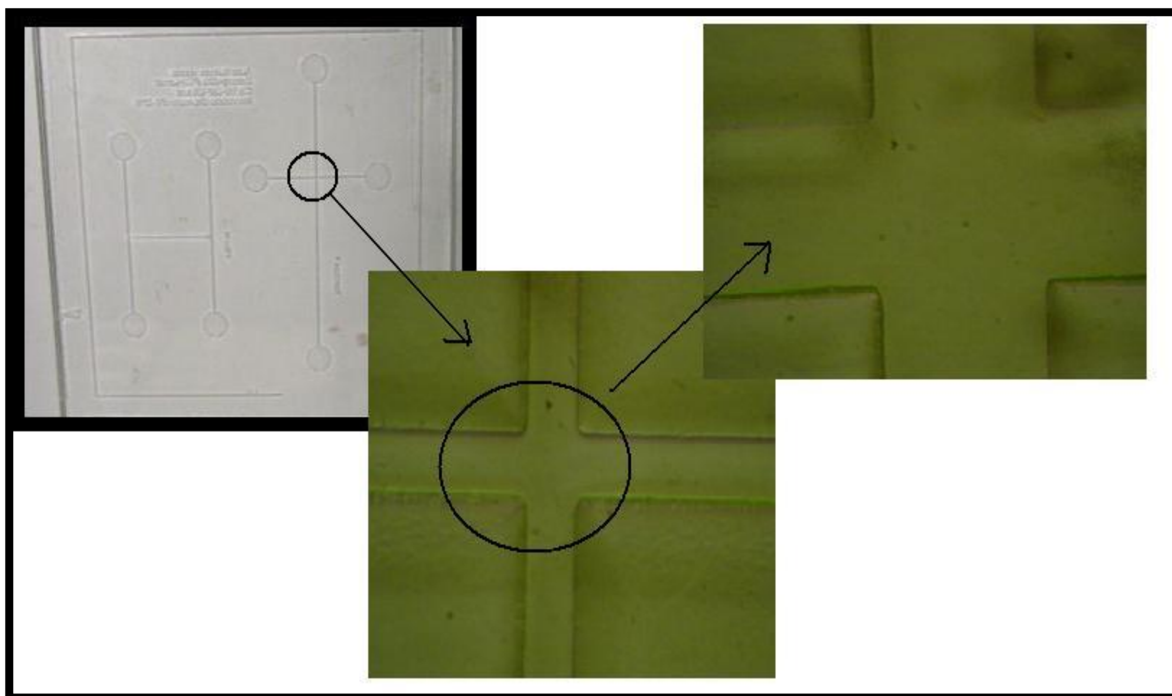

Figure 3.16 – Design with etched cross curves and zoom in section of the microchannels intersections.

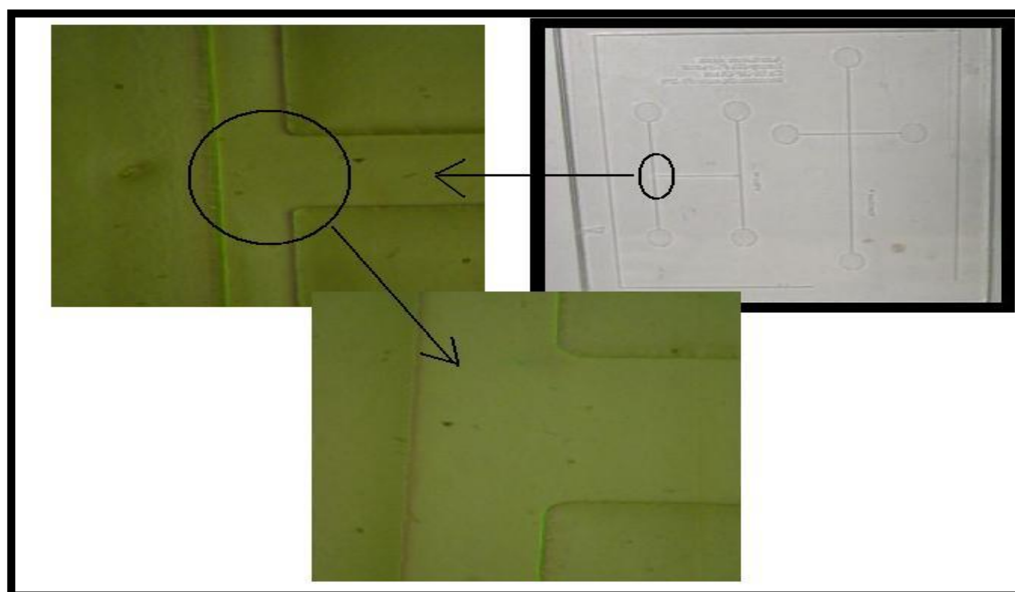

Figure 3.17 – Device fabricated with glass etching technique. Design 'H' shaped curve and zoom in the microchannels cross section.

We have presented the possibility of fabricating microfluidic devices on glass, reducing regular steps done with metal film deposition, as a protective mask for glass etching (COLTRO,

2008; SCHIANTI, 2008, 2017). These metal thin film deposition, are usually more expensive, for example in the case of use of masking material the gold-chromium, its deposition and etching of the gold-chromium film (COLTRO, 2008; SCHIANTI, 2008, 2017).

To make the measurements of the surface profile, the system uses the technique of contact stylus profilometry. This method is based on measuring of the mechanical movement of a cantilever as it shifts across the wafer. A diamond needle connected to a tip with radius of ~12.5 μm serves as the electromagnetic pickup. The cantilever force is adjustable from 1 to 15mg, with optional sensor is possible from 0.3 mg to 15 mg, and vertical magnifications of a few thousand up to a million times are possible. The channel depth is directly read out as the depth of the resulting step-contour trace. There are some adjustable reading parameters, such as, leveling and measurement functions are computer-controlled. The vertical cantilever movement is converted to digital signal, and the data processed to magnify areas of interest and yield best profile fits.

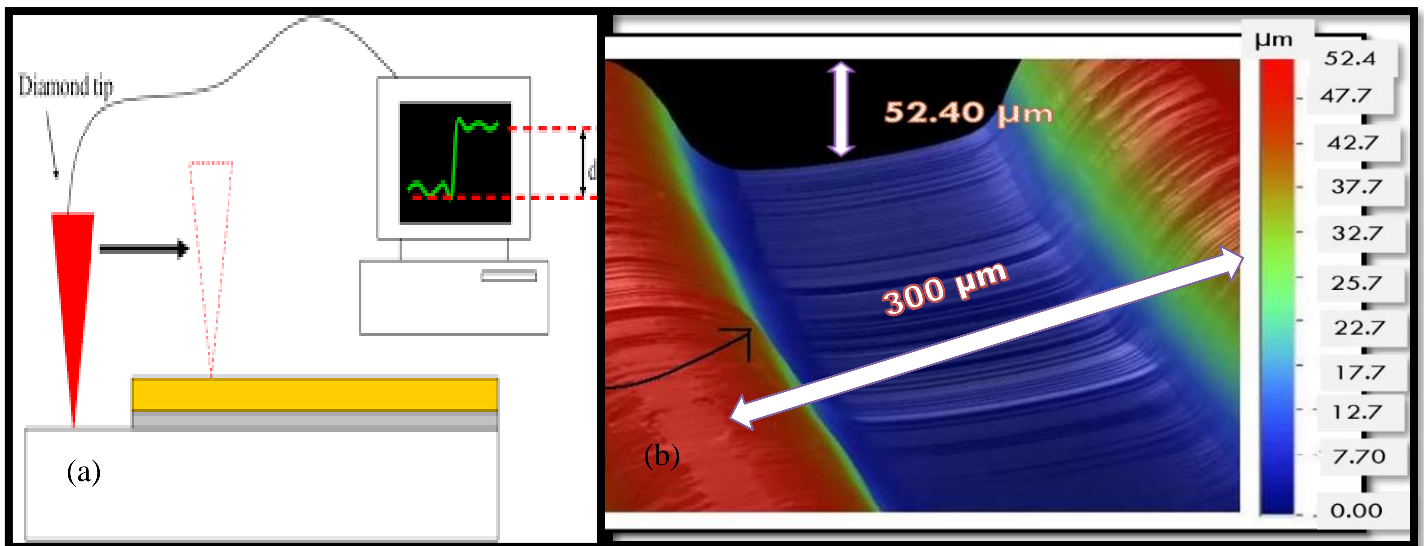

Figure 3.18 – Glass microchannel 3D profile obtained by contact stylus profilometry technique (a) Measurement scheme with diamond tip of 12.5 μm. (b) 3D channel profile acquired.

Subsequent to the etching process, observations and micrographs were made using an optical microscope, as shown in Figs. 3.16 and 3.17, we achieved microchannel with great reliability and fidelity, just using AZ4620 masking substrate surface. The channel was made in a well-controlled fabrication protocol developed by the author using cleanroom facilities. As a complement to the measurements, 3D measurements of the profile of microchannels obtained

on glass slides were performed, as can be seen in Fig. 3.18. We can have observed, channels are without microparticles, reliable low roughness and height, obtained in an accurate and reproducible process.

3.2.3. Microfabrication process with PDMS

To obtain microchannels in microfluidic devices, specific polymeric materials, PDMS and SU-8 were used as an alternative. Since microchannels in polymeric materials can be fabricated using conventional or alternative processes such as: soft lithography, laser ablation, multilayer lithography, hot stamping and direct printing, some of these micro-fabrication techniques were cited and detailed in Chapter 2. It is worth mentioning that, among the polymers used as materials for the microfabrication of microchannels, PDMS is the most used in microfluidic applications, due to relative simplicity in prototyping of devices, and the low cost of the elastomer used in the process.

The PDMS has interesting properties for microfluidic applications, being a material with good optical transparency, mechanical flexibility and can be easily used in molds, such as SU-8 mold, for soft lithography technique. The PDMS can be a flexible and soft material, this is another versatility that can be explored in the manufacture of devices, and can also be used in the construction of Quake valves (UNGER and QUAKE et. al. 2000), actuators and micro pumps. Another advantage of PDMS is its practicality in the use of microchannel sealing in different types of substrates such as: silicon, glass and PDMS itself. Another advantage to be observed of the PDMS is the direct adhesion in the curing process with silicone tubes. These tubes are used as means of interconnecting with the external environment, at the inputs and outputs of the devices connecting the reservoirs of the devices to the external environment.

There are also some disadvantages in the use of PDMS, among them is their hydrophobic property which may lead to the adsorption of analyte and some monomers of the unpolymerized PDMS in the walls of the microchannel (COLTRO, 2008). This means that the PDMS has a lower efficiency when applied in the analytical separation, comparing with microsystems in glass. Another disadvantage is the limitation in application of temperature and the difficulty in the integration of electrodes, being limited up to a maximum of 90ºC, one more disadvantage is the use of solvents that can cause the degradation of the PDMS and modification of the microchannel.

3.2.3.1. Microchannel fabrication in PDMS

The initial step of microchannels fabrication in PDMS, it uses the soft lithography technique (molding/demolding), using a mold commonly defined with photoresist SU-8 deposited on silicon substrate or quartz. Shown in Fig. 3.19 is a sequential procedure of a microfluidic fabrication protocol in PDMS developed in this work.

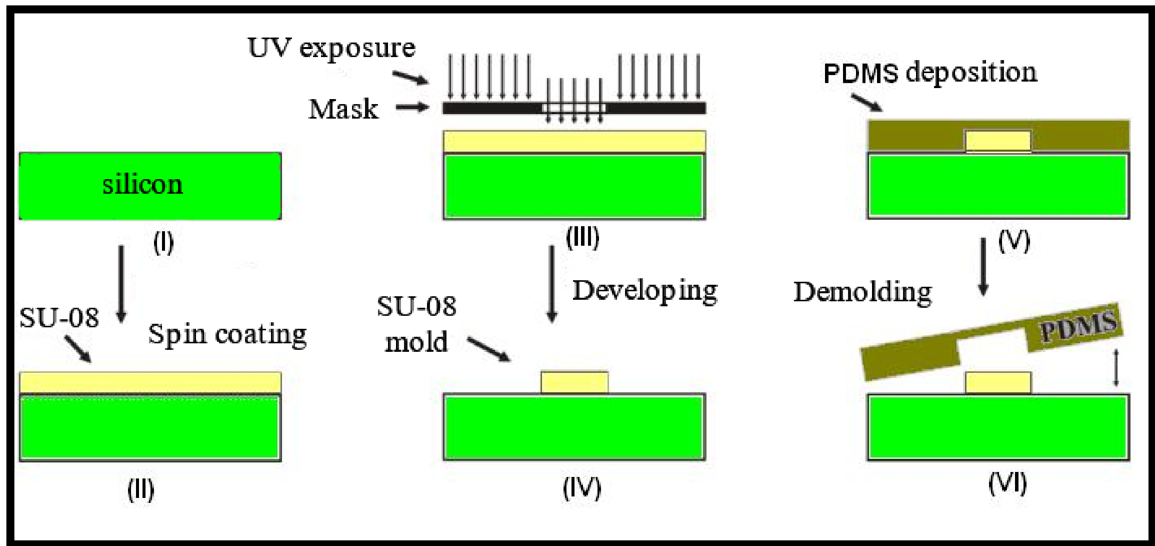

Figure 3.19 – Microfabrication stages for PDMS mold: (I) Cleaning the silicon substrate; (II) Photoresist deposition; (III) Photolithography; (IV) Developing; (V) PDMS deposition on the curing template; (VI) Demolding of the PDMS.

(I) and (II) Cleaning the Silicon Substrate and Deposition of the Photoresist SU-8: The initial step is to clean the silicon wafer; this was the same as done in section 3.2.1.1. The deposition of SU-8 was done by the spin-coating process using spinner speed of 2500 rpm for a time of 20 seconds, SU-8 was subjected to a temperature pretreatment of 95 ° C for the duration of 5 minutes to evaporate the excess solvent from this polymer.

(III) and (IV) Photolithography and Developing of SU-8 as a template: Subsequently, exposure to UV radiation occurred for 45 seconds, and after exposure, the substrate underwent another heat treatment step with a temperature of 95°C for a time of 5 minutes. The SU-8 region not exposed to UV light is removed with developer, thereby leaving a raised relief structure, serving as a template for replication of other structures.

(V) and (VI) Deposition of PDMS for curing and demolding: In the preparation of the PDMS, the silicon elastomer kit (SYLGARD^{TM} 184), base and the catalyst were used, where they were mixed in 10:1 ratio. After being mixed well, the material was placed in a vacuum

chamber for 40 minutes to remove air bubbles, and then deposited onto the SU-8 mold. The curing or polymerization process of the PDMS was obtained by leaving the substrate on a hot plate at a temperature of 90°C for 60 minutes, after which the hot plate was turned off for cooling the substrate. After cooling, the PDMS layer was demolded from the SU-8 mold, peeling of it carefully without damaging, mold/channel interface.

3.2.3.2. Microchannels sealing and External interconnection

In this section, the microchannel sealing steps are described. The PDMS was used in two situations: the first one containing the microchannels making use of the SU-8 template and the second one as a cover substrate without microchannels. We also made the microchannel sealing in PDMS on glass and silicon substrates.

After preparation of the PDMS using the 10:1 elastomer / secant ratio, with 17 grams of elastomer and 1.7 grams of secant, it is thoroughly mixed in a vessel until a homogeneous mixture is formed, then set aside for remove air bubbles in the vacuum chamber for 40 minutes. To obtain the side with the microchannels, we carefully pour the PDMS onto the mold containing the design in SU-8 for further demolding. And to obtain the substrate of PDMS without microchannel, we dump the PDMS on the base of glass or silicon with metallic mold around. The alignment points of the inlet and outlet tubes, shown in Fig. 3.20 and Fig. 3.21, in the SU-8 molds on the smooth quartz and glass slide, with the design printed on paper and placed on the bottom to assist the alignment of the Silicone tubes.

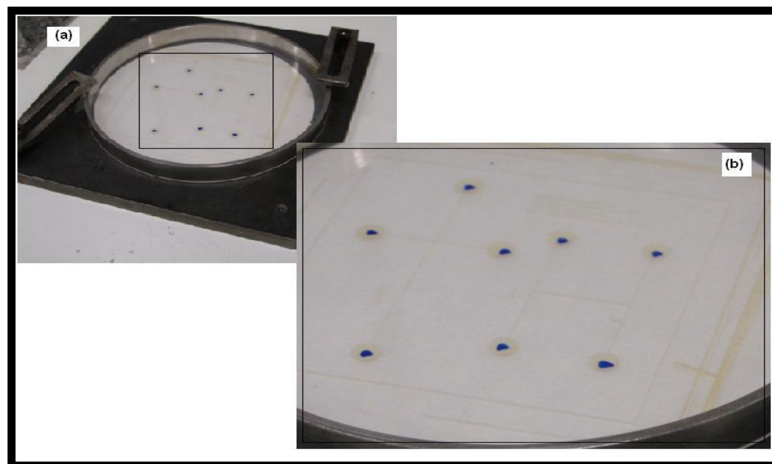

Figure 3.20 – SU-8 microfabrication molds in PDMS: (a) Circular metallic mold, containing at its base a quartz slide with SU-8 photographed; (b) Magnification of the SU-8 mold with microchannel shaped design.

After the PDMS is placed on the metal base, then it is moved on top of 5 mm thick glass. The curing process takes place on a hot plate at 90°C for 40 minutes. However, before deposition of the PDMS on the mold, it is necessary to prepare the tubes and the alignment system of the same.

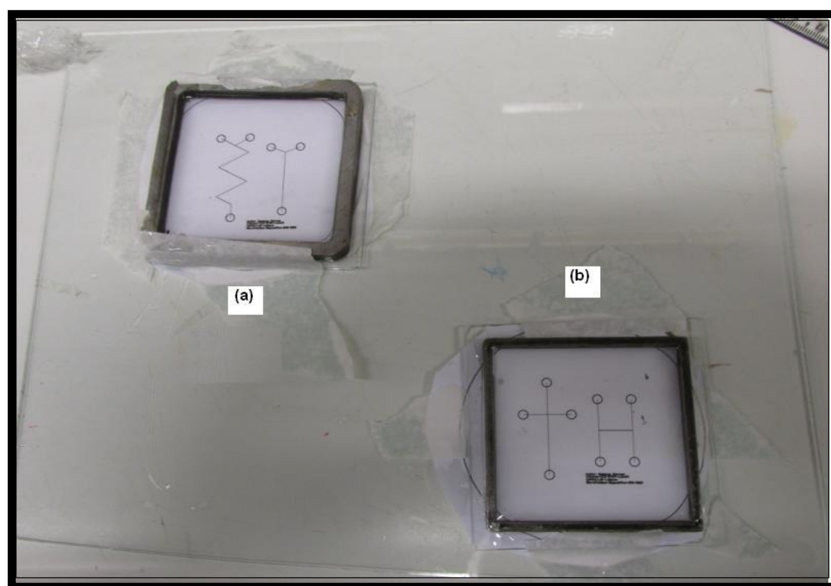

Figure 3.21 – Flat molds: (a) and (b) square metallic molds, each containing a glass slide with printed design on paper and placed in the bottom part of the mold.

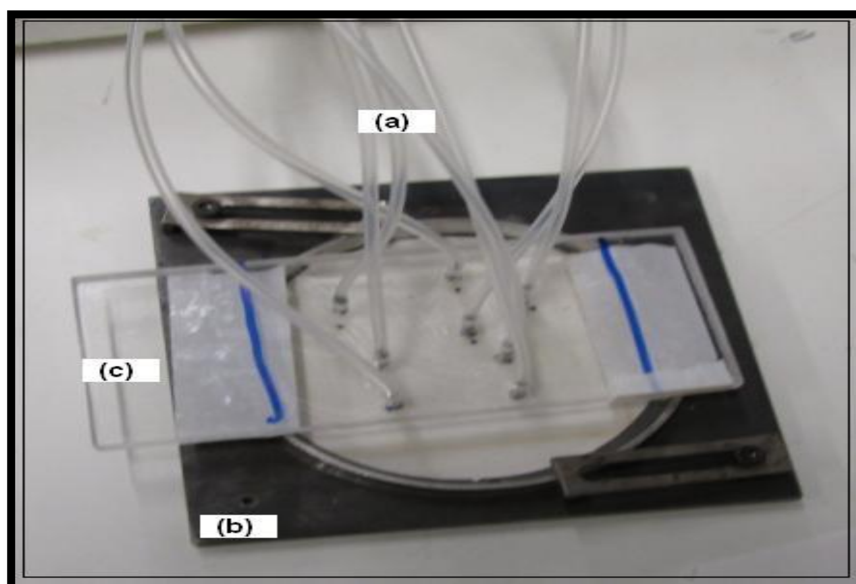

Figure 3.22 – Tubes alignment system: (a) Silicone tubes with nails at the ends to avoid obstruction for PDMS; (b) Metallic mold containing the SU-8 design; (c) Acrylic fixed on the mold, containing holes aligned to design reservoir.

In the preparation stage of the tubes, we first cut them in desirable sizes of 40 cm in length, taking into consideration the distance between the device, the injection system and the microscope. The tubes are cleaned first with detergent, then with non-ionic detergent and DI water, then placed on the isopropanol bath with magnetic stirring for 10 minutes, then the excess of isopropanol is removed from the tubes with nitrogen jet and set to dry on the hot plate protected with cloth clean room, at the temperature of 90ºC during 15 minutes.

In parallel we did the cleaning of metallic nails that serve as a barrier so that PDMS does not obstruct the tube and also is used as reference of alignment with the reservoir. The cleaning of the nails is done with cloth of nº1000, then the protocol of cleaning of the tubes with the nails is repeated. The assembly of the alignment system is done with the acrylic mold with holes aligned with double tape against the design reservoirs, the tubes and nails are aligned and fixed with the metal base, Fig. 3.22 shows the alignment protocol of the tubes.

After curing the PDMS and cooling the mold, it is removed from the mold, the nails are removed, the corners of the PDMS are cut and the excess is removed to leave the size necessary to cover the microchannels. The removal of the nails is done with tweezers. There is also the verification of possible obstructions in the tubes, inserting water and checking one by one. Fig. 3.23 shows the removal of nails from the tips of the silicone tubes and cutting of excess of PDMS, also checking if there is a good adhesion of the silicone tube to the substrate of PDMS.

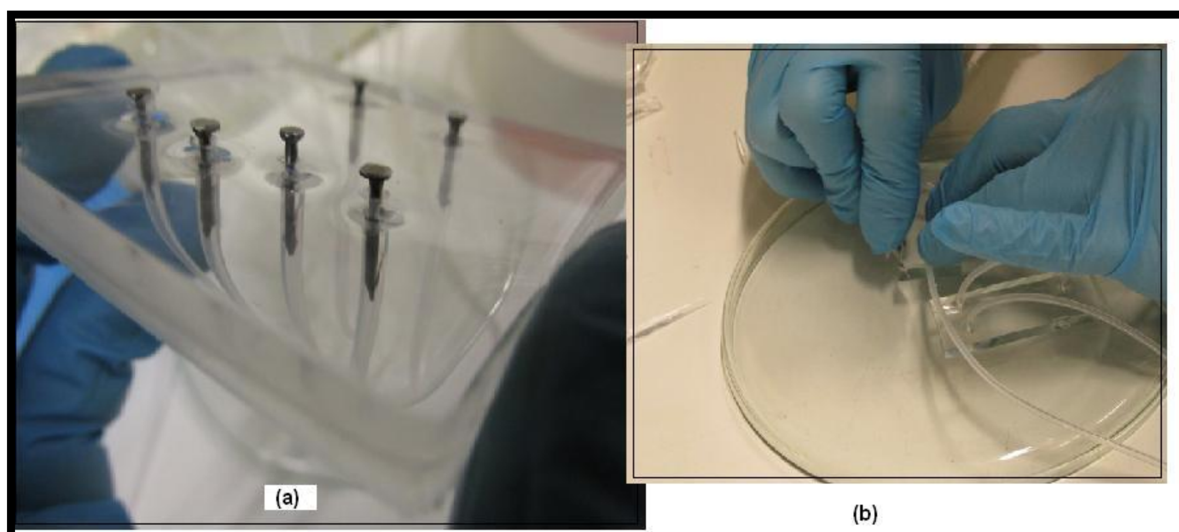

Figure 3.23 – Preparation of PDMS for sealing: (a) Removal of PDMS nails and silicone tubes; (b) Removal of excess PDMS for sealing.

Regarding the sealing steps, there are two possibilities of sealing with PDMS: reversible sealing and irreversible sealing. The reversible sealing is done at room temperature, and without further surface treatment steps, direct contact of the PDMS with the surface of the substrate is made. Thus, there is only the effect of van der Waals forces (MCDONALD; WHITESIDES, 2002), resulting in poor sealing. On the other hand, irreversible sealing is done with surface treatment by oxygen plasma, activating the surface of the substrate to be sealed (glass, silicon or PDMS) and PDMS. In this way we activate the covalent bonds between the polymer and the substrate (DUFFY at al., 1998), resulting in a stronger seal, resisting the working pressure of up to 6 atmospheres. The parameters used in the plasma activation recipe were: power of 100 watts, process pressure of 70 mTor, for a time of 10 seconds. After the surface activation, both surfaces are manually pressed together for 3 minutes, leading to the irreversible sealing of microfluidic devices.

3.2.3.3. Profile of Microchannels in PDMS with SU-8

The microchannels obtained in PDMS with SU-8 mold had a trapezoidal profile shape, having the following upper and lower width dimensions and depth, as shown in Fig. 3.24.

Figure 3.24 – Profile of a Microcanal mold in SU-8 for molding in PDMS.

In Fig. 3.24, the trapezoidal profile of the photo chromed microchannel in SU-8 can be observed, which was used in the molding / demolding process in PDMS. The dimensions are as follows: depth of 63.60 μm, width of the upper part L = 100 μm and width of the base F = 171.5 μm.

3.2.3.4. Fabrication of ring shaped electrodes (RSE)

The well-known Titanium-gold-titanium glass metallization scheme with conventional photolithographic patterning (RIBEIRO, et al., 2010) was used to form the electrodes. RSE electrode masks were designed using high-resolution direct writing photolithography with a laser beam (Model μPG101, Heidelberg Instruments). In the next step, a photoresist layer was deposited onto a square optical glass plate (60mm side Kodak 1A High Resolution Glass) and patterned by conventional ultraviolet light (UV) photolithographic method following the electrodes masks. The UV exposures were carried out in a MJB-3 UV300 contact mask aligner (Karl-Suss, Garching, Germany). Titanium-gold-titanium thin films, deposited with a Leybold Univex 300 e-beam evaporator (Cologne, Germany), were used as electrode materials. After thin-film depositions, by the lift-off technic, the devices were immersed in acetone to remove the photoresist layer and excess of metal, leaving the patterned electrodes on the glass surface. As a final step, a 5μm polydimethylsiloxane (PDMS) film was deposited by spinner to avoid the electrode to enter in direct contact with the fluid. Microchannel was fabricated using replication master mold of SU-8 photoresist over a silicon substrate, electrode design and measurements were described in section 4.6.

4 RESULTS AND DISCUSSION

In this chapter, the microfabrication processes results, device characterization (microchannel, liquid pressure and speed) including some preliminary theoretical modeling and applications are described.

4.1. Characterization of microchannels

This section deals with the characterization of microchannels fabricated in silicon, glass and PDMS. Using wet etching and soft lithography techniques, it was possible to obtain microchannels with different widths and depths for large variety of designs used in different applications. Table 4.1 shows some of the microchannels dimensions.

Table 4.1 - Dimensions of some designs obtained during the Microfabrication process.

Substrate (wafer)	**Design**	**Width (μm)**	**Depth (μm)**	**Length (mm)**
Glass	Long double spiral	252	42	25000
		283	41	25000
	Double spiral	111	20	12500
		129	24	12500
	Curved shaped ‘T’	458	64	30
	Trident	407	57	33
	Curved shaped lines	206	29	30
	Curved shaped serpentine	343	46	70
	Curved shaped Trident	366	29	35
Silicon	Miscellaneous design	109	33	27-35
PDMS	Miscellaneous design	100	63	27-35

We observed that the obtained microchannels’ profiles are directly related to the used microfabrication technique and material. The microchannels profile in glass are circular segments, which is due to the isotropic etching with HF, which etches the glass equally in all directions. The aspect ratio (which is the ratio between the width and depth of the microchannel) has been defined previously after measuring the HF etching rate in the glass microscope slides, where the widths of the microchannels are dependent on the etching time, that determines the microchannel depth.

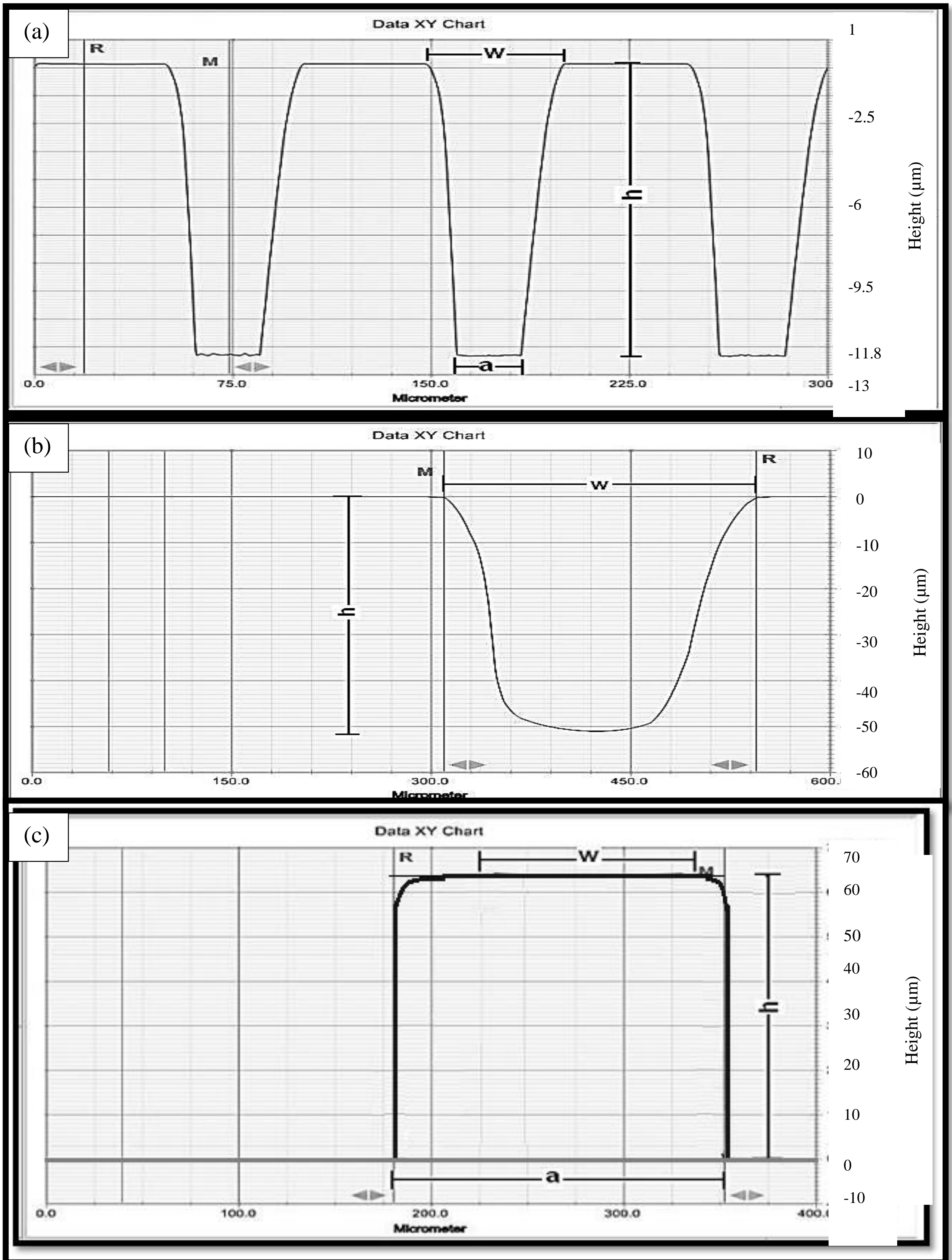

Figure 4.1 – Profiles of microchannels obtained by profilometer measurements. (a) Trapezoidal profile obtained in silicon by etching with KOH; (b) Circular segment profile obtained in glass by etching with HF; (c) SU-8 (soft lithography) quasi-rectangular mold profile.

The microchannels obtained in silicon in turn have their trapezoidal profiles, due to the anisotropic etching with KOH, as in the etching process of silicon there are different etching rates for certain directions of crystallographic orientations, where the walls of the microchannel form angles of inclination of 54,74° with the bottom part of the microchannel. The microchannels obtained in PDMS have an almost rectangular profile, as the process of soft lithography with SU-8 forming a rectangular shape due to channel aspect ratio. The profiles of the microchannels obtained in silicon, glass and PDMS are shown in Fig. 4.1, the dimensions of the microchannels were represented by: height = **h**, top width = **w** and bottom width or base = **a**, with measurements based on the profilometry.

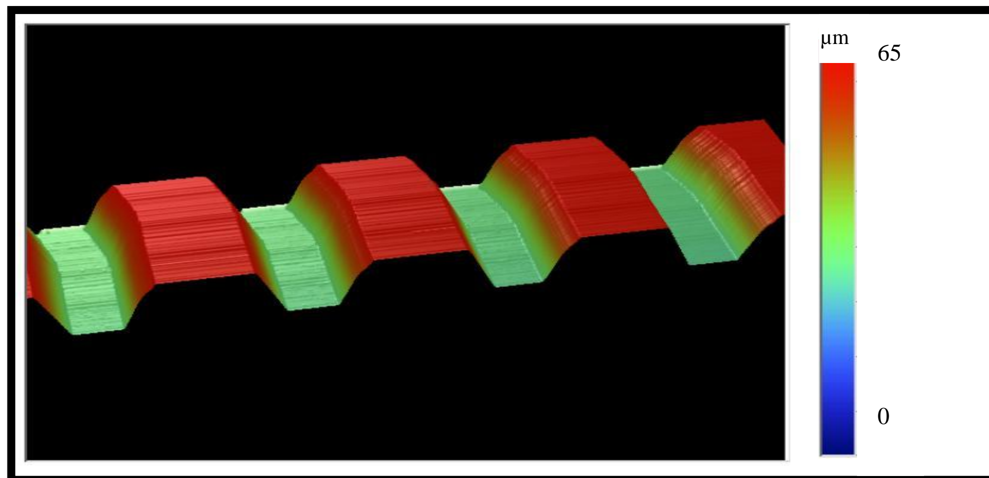

Figure 4.2 –3D profile of measured PDMS microchannel, using Dektak 3D profilometer.

Other measurements in 3D show the profiles of the microchannels along the microfluidic device. In Fig. 4.2 the microchannels profiles in silicon after wet etching techniques are shown. It followed by glass channel profile with a semi-circular shape, achieved with etching time of 5 minutes, as shown in Fig. 4.3 (a), and the PDMS channel profile after soft lithography, with SU-8 mold thickness of 20 µm, as shown in Fig. 4.3 (b).

We observed three types of microchannels profile obtained by different process fabrication. Note that even with the same process it was possible to obtain different profile shapes, for example in glass, with smaller etching times (< 2 minutes) it is possible to achieve nearly rectangular microchannel. In the case of PDMS, is possible to generate semicircular and trapezoidal profile, by using silicon as mold and etched glass by HF, instead of SU-8 molds.

This give us more possible combinations, that might be suitable to cover great variety of applications that might depend on the channel profile.

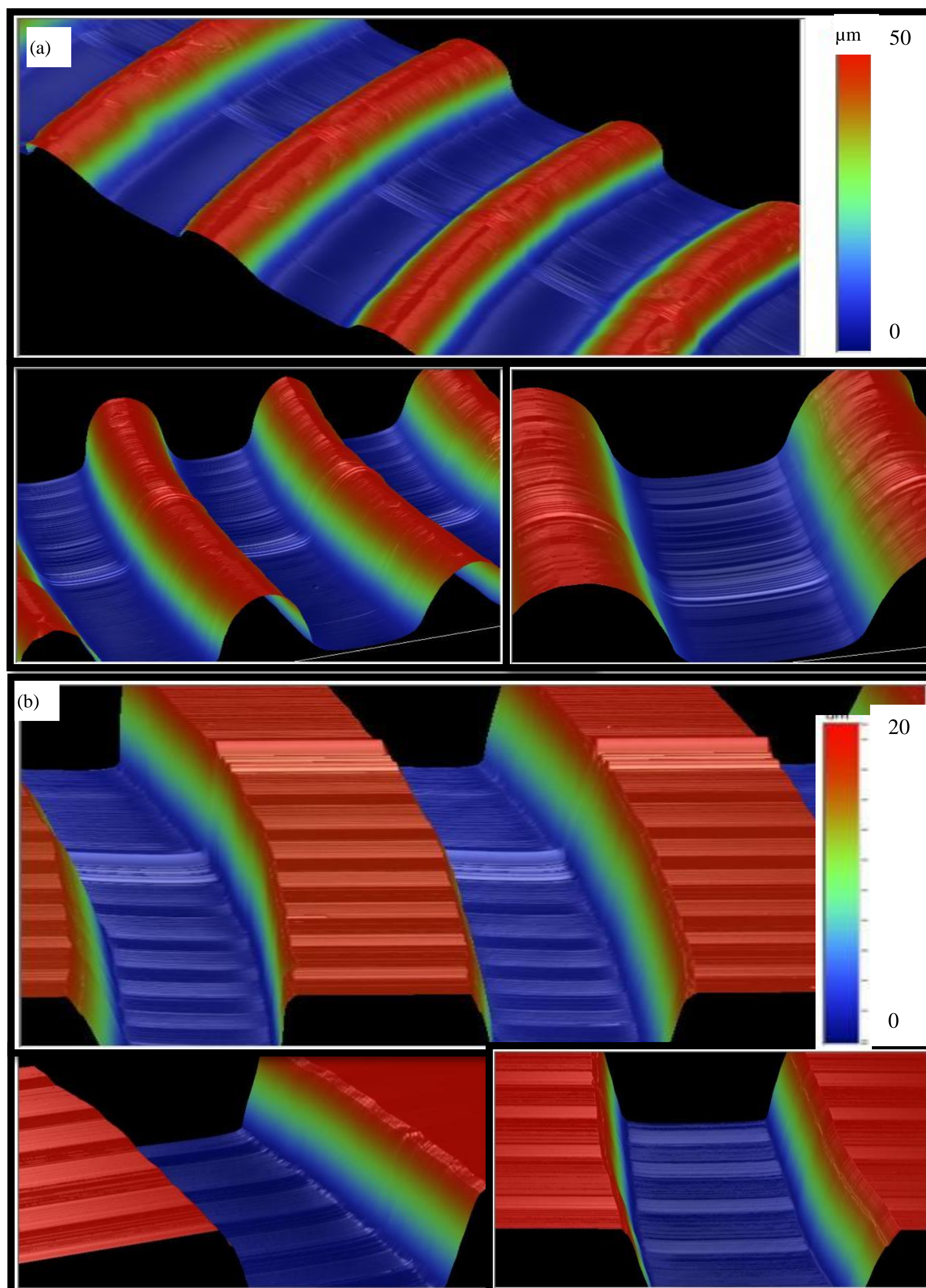

Figure 4.3 – (a) Profiles of glass microchannels obtained with etching techniques with HF. (b) Profile of PDMS microchannels, depths of 20 µm.

Etching processes in silicon and glass have some advantages and disadvantages in relation to soft lithography with SU-8.

The main advantages of using wet etching techniques are:

- ✓ Control over the microchannel depth by means of the etching time;
- ✓ Very small roughness;
- ✓ Reproducibility of processes;

The main disadvantages in relation to soft lithography are:

- ✓ Necessity of tests to estimate the etching rate;
- ✓ Substrate cleaning in post-etching;
- ✓ Hard-mask for protection;
- ✓ Longer process time;

4.2. Reynolds number calculations

The experimental part with the microfluidic devices was based on calculations making use of parameters such as: Reynolds number, velocity and pressure. By assuming that the viscosity of the fluids used in the experiments was very close to that of water, it was soon possible to approximate the modeling of fluid dynamics based on the kinematic viscosity of the water at room temperature.

Table 4.2 was generated based on calculations with a trapezoidal profile etched in silicon, and a circular segment obtained in glass. The experimental conditions were set as such that a laminar flow regime was secured in the microchannels. A flow value was adopted aiming at the smallest possible Reynolds number, but simultaneously keeping a reasonable injection time to obtain images inside the microchannels. The time of injection is the time necessary for the liquid samples to pass through the length of the microchannel, considering the range of device lengths of L = 27-35 mm.

Table 4.2, we show a flow test results with microchannels made of silicon. We aimed to observe the fluid velocity range, residence time and calculated Reynolds number for input flow rates parameters between 1 and 300 µl/minute, using Eq. 2.3. We performed calculations taking into account the actual measurements of the microchannels obtained with 3D

profilometer techniques. In this way, it was possible to find a direct relation between the applied flow rate and the type of working regime, respecting the maximum flow limit so that no leaks occur in the devices.

Table 4.2 – Volumetric flow rate sweeping, aiming for leakage tests and Reynolds number evaluation, microchannel fluid time and velocity in silicon channels.

Q=Volumetric flow rate (μl/min)	Microchannel dimensions (μm)	A=cross-sectional área (μm²)	v_c=Calculated speed (mm/s)	D_h=Hydraulic diameter (μm)	Reynolds Number (Re)	t= Average residence time (ms)
1	**w**=100; **h**=33;	2530	6,58	43,20	0,32	4700
10	**a**=53;	2530	65,80	43,20	3,20	470
50		2530	329,00	43,20	16,00	94
100	**w**=100; **h**=33;	2530	658,00	43,20	32,00	47
200	**a**=53;	2530	1316,00	43,20	64,00	23
300		2530	1974,00	43,20	96,00	15

Tables 4.2 and 4.3 present results for the same experiments performed on PDMS microchannels. Table 4.3 shows the dimensions of the microchannels. From the dimensions and the profile of the microchannel, the hydraulic diameter, cross-sectional area and perimeter of each microchannel have been numerically extracted.

Table 4.3 – Volumetric flow rate sweeping, aiming for leakage tests and Reynolds number evaluation, microchannel fluid time and velocity in PDMS channels.

Q=Volumetric flow rate (μl/min)	Microchannel dimensions (μm)	A=cross-sectional area (μm²)	v_c=Calculated speed (mm/s)	D_h=Hydraulic diameter (μm)	Reynolds Number (Re)	t=Average residence time (ms)
1	**w**=252;	7158	2,38	54,81	0,41	13000
10	**h**=42;	7158	23,80	54,81	4,10	1300
50		7158	119,00	54,81	20,50	260
100	**w**=252;	7158	238,00	54,81	41,00	130
200	**h**=42;	7158	476,00	54,81	82,00	65
300		7158	714,00	54,81	123,00	43

We have achieved similar parameters of flow regime, referred in others works (BSOUL, 2016; GOU, 2018), however, thus indicating the laminar flow regime and much less susceptible to the roughness effect, which causes increase of pressure, friction factor and Reynolds number, according to the channel height/roughness criteria presented by (SABRY, 2000; BAHRAMI, 2007).

In the tests with varying the volumetric flow rates, it was possible to control Reynolds number, by fixing the geometric and fluidic variables such as: channel length, cross-sectional area, hydraulic diameter and water viscosity. The kinematic viscosity of water obtained in the literature review is 0.9025 m^2/s, measured at the temperature of 20°C (KESTIN et. al., 1978). Based on Table 4.2, the volumetric flow rate was 10 µl/min and new theoretical tests were done with the other devices in silicon, PDMS and glass.

The hydraulic diameter is defined in Chapter 2, see Eq. (2.4). The volumetric flow rate, as defined by the experiment in Table 4.1, was 10µl/minute converted to velocity using the cross-sectional area of the microchannel v = Q / A, whereby the velocity is defined as the ratio of the flow over the area. It can be observed that by comparing the two methods the values are well close and the Reynolds number is less than 10, reinforcing that the laboratory tests were all in the laminar flow region, where the viscous forces become larger than the forces in the interior of liquids. Our parameters calculated from the regime flow, such as, velocity, pressure and Reynold number were smaller than presented by Liu et al. (2015), based on that, we have laminar flow in most of our performed experiments.

Table 4.4 – Dimensions, cross section, velocity and diameter for the calculation of the Reynolds number.

Substrate material	**Microchannel dimensions (μm)**	**A=Cross-sectional area (μm^2)**	**v_c=Calculated speed (mm/s)**	**D_h=Hydraulic diameter (μm)**	**Reynolds number (Re)**
Silicon	**w**=100; **h**=25; **a**=64,6;	2058	81	36,45	3,27
	w=200; **h**=25; **a**=164,7;	4558	37	42,81	1,73
	w=100; **h**=33; **a**=53,3;	2530	66	43,21	3,15
	w=200; **h**=33; **a**=153,3;	5830	29	53,71	1,70
PDMS	**w**=100,1; **h**=52; **a**=171,5;	8637	20	115,66	2,47
	w=100,1; **h**=63,6; **a**=171,5;	7062	24	102,53	2,68
Glass	**w**=252,20; **h**=41,72;	7159	23	54,81	1,41
	w=282,20; **h**=41,51;	7952	21	54,69	1,27
	w=458,50; **h**=64,30;	19944	8,4	84,80	0,79
	w=406,90; **h**=56,85;	15650	11	75,00	0,89
	w=201,30; **h**=47,67;	6666	25	61,80	1,71
	w=342,90; **h**=46,13;	10688	16	60,89	1,05
	w=366,60; **h**=43,08;	10638	16	57,00	0,99
	w=111,20; **h**=20,62;	1568	110	27,00	3,18
	w=129,10; **h**=23,96;	2115	78	31,36	2,74

The main goal of this part was to investigate the hydrodynamics in microchannels in a well-controlled experiment. The main issue concerns the applicability of the classical laws (drop pressure and laminar-turbulent transition) when the characteristic dimensions of the channel are of the order of several hundred to one hundred microns. The simulated microchannels used during the experiments were two-dimensional to avoid the influence of more complex geometrical configurations.

4.3. Devices Modelling

The modeling of the devices was divided in two steps: literature review on the geometries applied to passive micro mixers and observation of the equations that govern these systems, aiming at practical applications with applicable pressure values for real experiments, as a preliminary simulation study.

4.3.1. Simulation Tool

In this section a brief description was presented of the computational tool used in the devices modeling, the **Comsol Multiphysics version 4.3a** (formally named FEMLAB – *finite element analysis*). It is a *software* package of analyses based on finite elements method with multiple applications in Physics and Engineering, focused on coupled phenomena or multiphysics.

After the channels characterization with profilometry technique with measured micrometric precision, the geometries of the devices were inserted in the COMSOL software. The simulations were based on incompressible Newtonian fluids, and with the kinematic viscosity identical to that of water, at room temperature (20°C). The process control variables were defined: geometry format, micro-channel dimensions, aspect ratio (which is the ratio of microchannel width and depth), liquid viscosity, pressure and velocity. These variables were inserted in the simulator according to Fig. 4.4, that shows the main COMSOL window, more details of simulation, 2D models disadvantage, mesh criteria and discretization in appendix section.

In the theoretical model, pressure and/or flow calculations were performed, considering the optimum workflow for each geometry format to keep the system operating in the laminar flow. As starting point, we inserted an input parameter of volumetric flow rate of 10 μl/minute, obtained by Table 4.3, considering the size and shape of each device and fixing the fluids parameters, it can be obtained from the Reynolds number ratio. The reaction models can be

obtained from the diffusivity between the liquids and shaped design. Computational fluid dynamics simulations were carried out using Comsol Multiphysics 4.3a, which implements the finite element method. The simulations solve two main Equations 4.1 and 4.2 that describe the physics of mixing as follows:

- First, the Navier–Stokes and continuity equations to get the flow velocity field,

$$\rho(\vec{v}.\nabla)\vec{v} = -\nabla \mathrm{p} + \mu\nabla^2\vec{v}$$
$$\nabla.\vec{v} = 0$$
Equation (4.1)

where ρ is the density, $\vec{v}$ is the velocity vector, μ is the fluid viscosity, and p is the pressure, the Eq. 4.1 is reduced to $\nabla.\vec{v} = 0$, it represents the simplified notation of continuity equation of Navier-Stokes, for incompressible fluids. It means that the net rate for mass flow rate across any closed surface is zero.

- Second, the velocity field is then used in the convective mass-transport term of the convection-diffusion equation to determine the spatial fluid concentration under stationary condition,

$$\vec{v}.\nabla C = D\nabla^2 C \qquad \text{Equation (4.2)}$$

D denotes the diffusion coefficient and *C* represents the concentration.

The equations are solved for a steady-state, incompressible and laminar flow with the following boundary conditions: (1) a flat velocity profile was imposed normal to the inlet surface, (2) a no-slip condition at all the solid surfaces, (3) atmospheric pressure at the outlet, and (4) a normalized concentration 1 in one inlet, and concentration 0 in the other one, following the inlets path cross- section. For all simulations, water was used as working fluid with density of 998 kg m^{-3} and dynamic viscosity of 1.002 mPa s. The self-diffusion water coefficient was set to $2.4 \times 10^{-9} m^2 s^{-1}$ (HORN et al., 2004). First, a model of the micromixer was designed using commercial AutoCAD software. Then, the model is imported into Comsol for simulation. Extra Fine Meshing was used to simulate all these geometries, also based in (SAYAH, 2016).

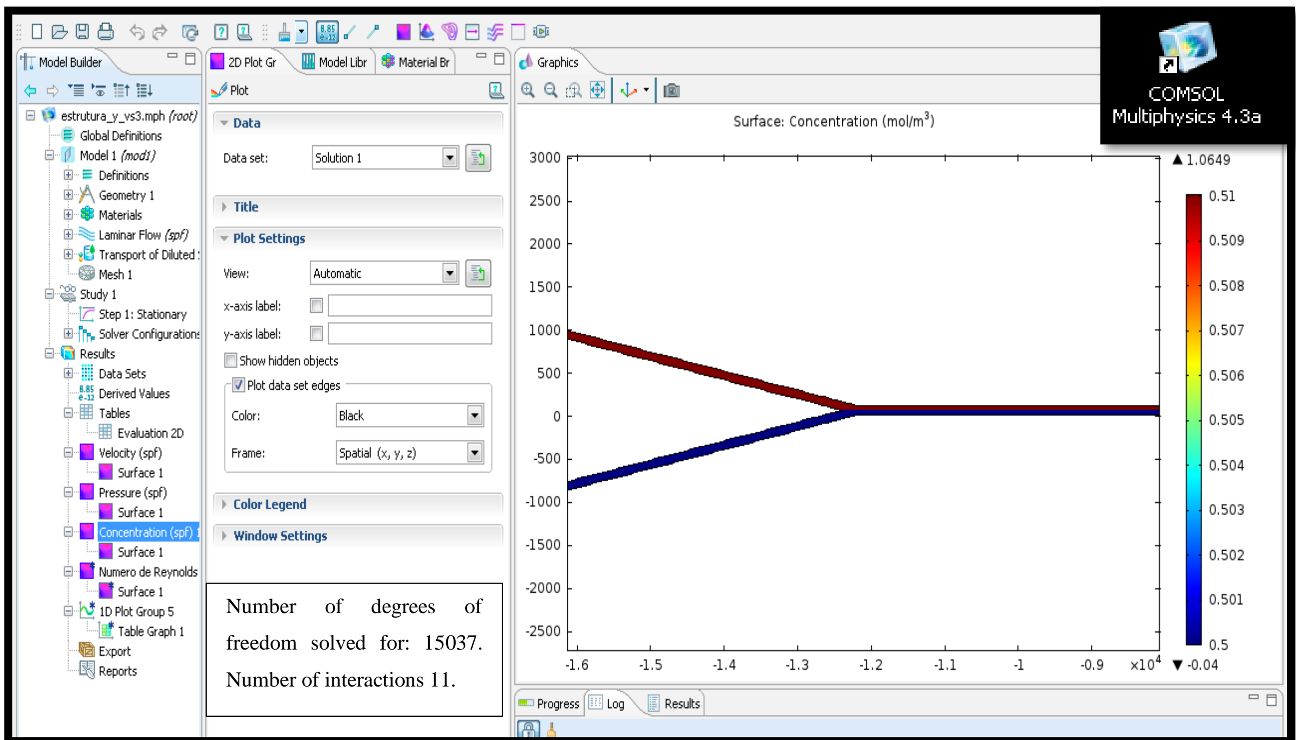

Figure 4.4 – Simulation tree in COMSOL 4.3a.

4.4. Input window for the simulation parameter and simulation results using Comsol software

The simulations are shown using the COMSOL® multiphysics computational tool, specifically the CFD-Computational Fluid Dynamics module, with the channel dimension parameters obtained from the characterization of the various fabricated microchannels. The methodology applied in the simulation was to insert the speed calculated from the flow used in the practical experiments and through models such as the Navier-Stokes equation and Reynolds number to obtain the velocity along the microchannel, pressure, Reynolds number and diffusivity.

The simulations were based on the experimental tests, with the velocity as input parameter, and as variables of velocity, pressure, Reynolds number and degree of diffusivity, with parameters of input, velocity and kinematic viscosity of the fluid. The graphs of the computational modeling are shown below, where the X and Y axes represent the microchannel dimensions in micrometers, and the sidebar represents the unit shown in the upper part, the simulations being based on the Navier-Stokes and Reynolds equations.

The velocity input variable was obtained from the relation of the flow with the cross-sectional area of the microchannel, and later inserted in the model. The velocity and pressure along the channel, concentration coefficient and Reynolds number along the channel were evaluated as output parameters, described in appendix section. The evaluation of the velocity, pressure, concentration and Reynolds number were based on the geometrical aspects of the microfluidic device, followed by performed experimental tests. According to Table 4.5, the calculations based on the microchannel dimensions and the laboratory tests were done, using the flow velocity used in the tests and the microchannel dimensions as input parameters in the simulation. In both cases, in the experimental test and in the simulated model, as shown in Fig. 4.5, the Reynolds number was below 4 and the flow regime is entirely in the laminar region. This facilitates the use of lower pressures in the laboratory tests, avoiding damage to the PDMS sealing of the channels. It is noteworthy that we observed some leaks only with volumetric flow rates higher than 400 µl/min, using three inlets with the same volumetric flow rate.

Table 4.5 – Comparison between the results obtained in the experiments and simulation at Comsol.

Substrate Material	**v_c=Calculated speed (mm/s)**	**v_s=Calculated speed in Comsol* (mm/s)**	**p_c=Calculated pressure (Pa)**	**p_s=Calculated pressure in Comsol* (Pa)**	**Calculated Reynolds number (Re)**
Silicon	81	70	795	900	3.27
	37	35	359	600	1.73
	66	60	646	800	3.15
	29	25	280	400	1.70
PDMS	20	20	189	250	2.47
	24	25	231	300	2.68
Glass	23	26	228	350	1.41
	21	20	205	350	1.27
	8,4	8	82	120	0.79
	11	12	104	150	0.89
	25	30	245	375	1.71
	16	15	153	250	1.05
	16	15	153	250	0.99
	110	12	1042	2000	3.18
	78	80	772	1200	2.74

*Approximation modelling the real device, all channels simulated were with rectangular channel and a fix height of 33 µm, fluid pumped in the inlets was water, floating parameters were channel width and length, without taking into account roughness and temperature, more details in appendix section.

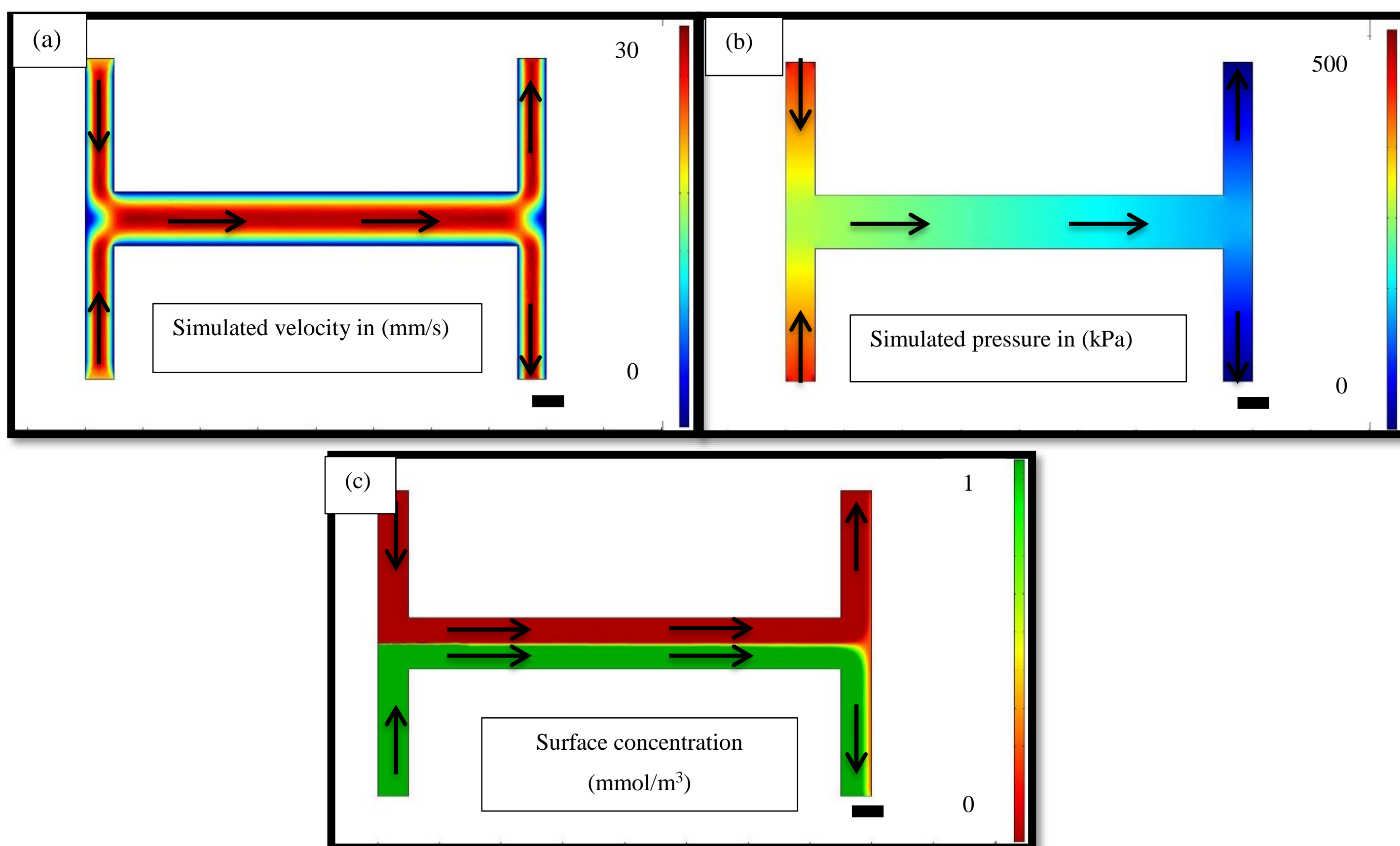

Figure 4.5 – (a) Behavior of fluid velocity along the microchannel (▬ 50 µm). (b) Pressure behavior of the fluid along the microchannel. (c) Behavior of the concentration gradient along the "H" channel.

We group together the output parameters achieved by simulation, for comparison with the experimental performed with syringe pumps and well-controlled parameters in the Microfluidic system, all simulations were based on glass material with height of 50 µm.

4.4.1. Comparison between Simulations and Experiments;

In this section we compare the simulated models in the COMSOL with the results of the laboratory tests with the microfluidic devices, emphasizing the edge contour of the two liquids along the microchannel, as shown in Fig. 4.6.

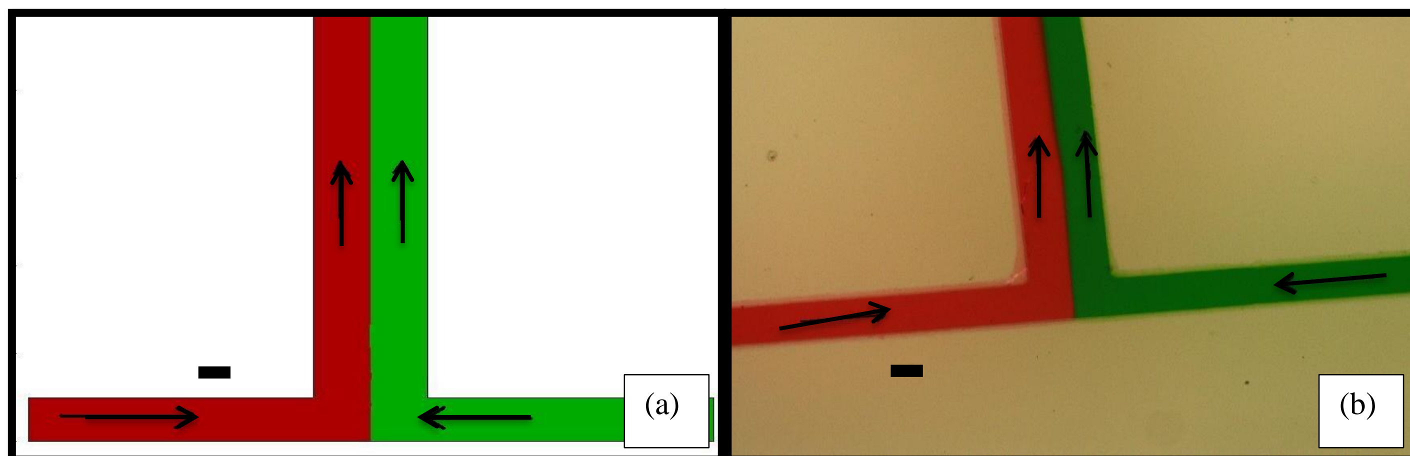

Figure 4.6 – Curve in H with two liquids without mixture (▬ 50 μm). (a) Model simulated in Comsol; (b) Result obtained in laboratory.

It can be observed that in Fig. 4.6, the red and green stream lines were modulated by each volumetric flow rate. The direction of injection is indicated by arrows, and it can be observed that there is no mixing between the two liquids that follow in parallel throughout microchannel, with the microfluidic device made of glass and PDMS. We have presented in Fig. 4.7 an unbalanced flow rate, where the green volumetric flow rate is bigger than the red one.

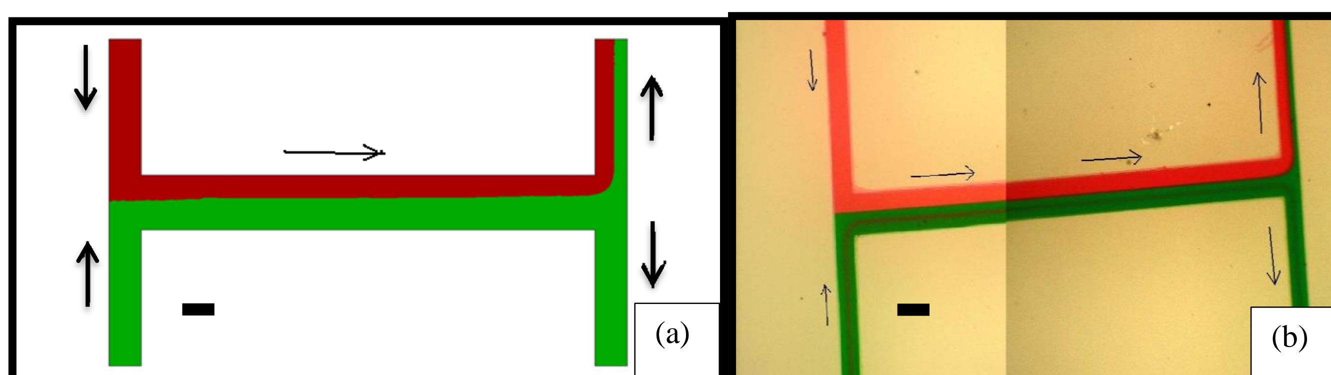

Figure 4.7 – (a) H curve in Comsol, modulating the width of the liquids as a function of the flow, the inflow of the inlet 1 greater than the inlet 2 (▬50μm). (b) H- shaped curve with laboratory test.

In the simulation of the microfluidic devices, the widths of each fluid was modulated according to the flow, based on volumetric flow rate parameters, and the coefficient of diffusivity between the liquids is very low without mixing, with the existence of a modulated stream line by flow rate. However, if the coefficient of diffusivity was lower, the degree of mixing could be controlled by the volumetric flow rate and the geometry of the microchannel used. The modulation of the fluid width in the laboratory was due to variation in the flow, however, in practice this is much more difficult to obtain the width adjustment with the flow, because the sensitivity of the system is very high.

The H-curve shown in Fig. 4.8 contains two unmixed liquids, one in red and one in green. In the green stream line another color, the brown, was added which functions as a marker to give the indication of the edge contour, or edge contour line. It is observed that the edge contour of the liquids in a 90° curve follows slightly different trajectories. It is worth mentioning that this principle could be used to separate substances in liquids, such as separation of blood platelets from the biological part of a blood sample, due to the fact that size of the particles could have different border contour paths.

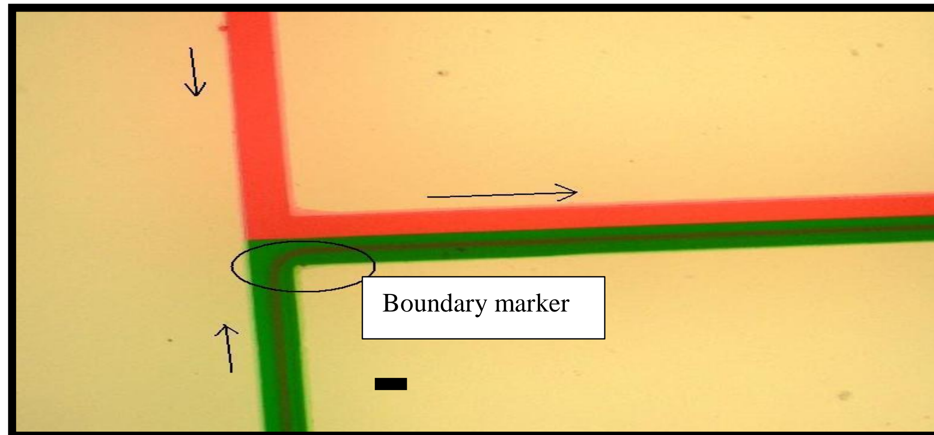

Figure 4.8 – H-curve with two liquids without mixing, with the addition of an edge contour marker (▬ 50 µm).

The following are examples of liquid width modulation from the flow control obtained in laboratory tests. Fig. 4.9 illustrates some forms of liquid width control in the edge contour region from the volumetric flow rate applied to each liquid. It can also be observed that in the liquid-liquid interface there is a brown line separating the two liquids, red and green. This region is the region of diffusivity. As in this case, no turbulence was introduced in this

experiment, i.e., the fluids are entirely in the region of laminarity, since the Reynolds number is less than 4.

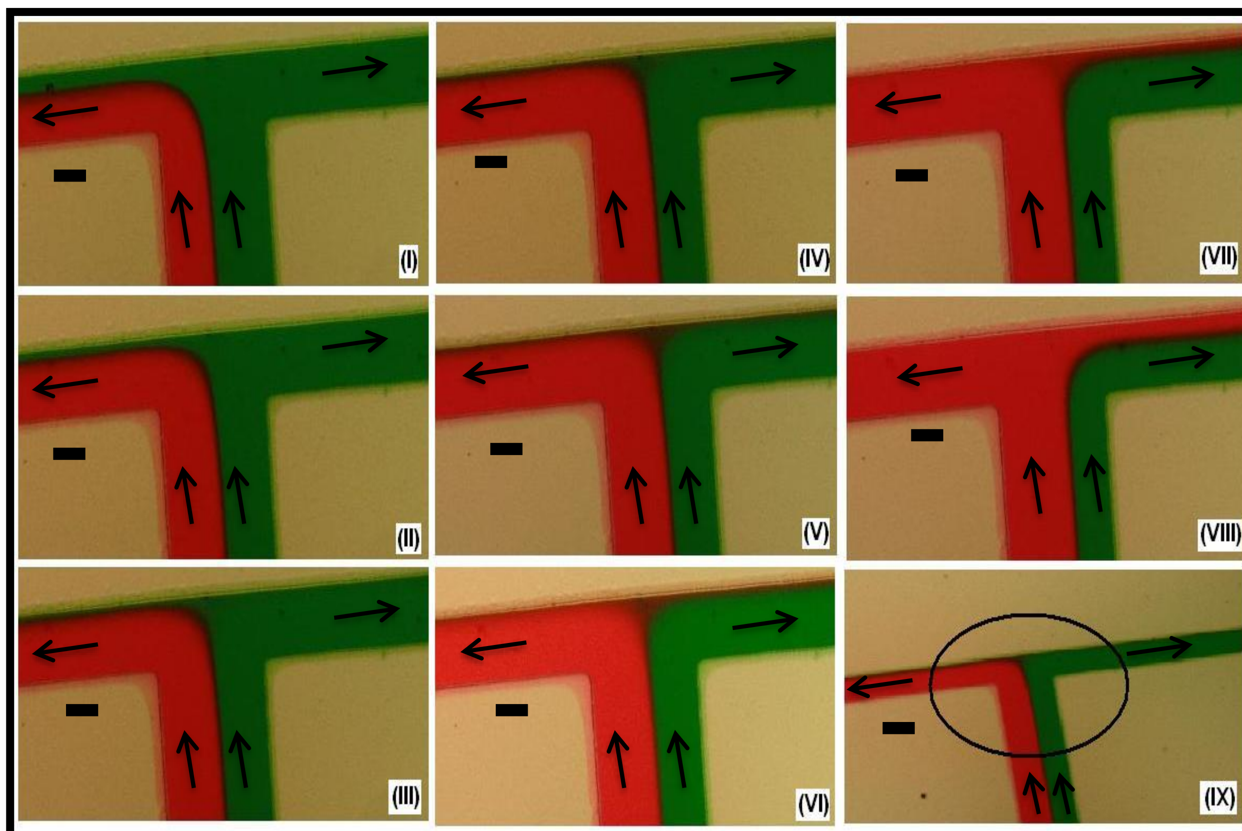

Figure 4.9 – H-shaped curve with two liquids without mixing (▬ 50 μm): (I), (II), (III) and (IV) Modulation of the green liquid with a slightly larger flow rate than the red liquid; (V) equalized flow rates for liquids; (VI), (VII) and (VIII) Modulation of the green liquid slightly lower than that of the red liquid; (IX) Region chosen for image enlargement and evaluation of modulation.

The observations in the microfluidics are mostly based on laminar flow regimes, where there is predominance of viscous forces over the inertial ones, resulting from the combination of dimensions, microchannel geometries and liquid viscosity. These surface phenomena of liquid-liquid interfaces, liquid-gaseous and liquid-solid have been the object of study of several research groups around the world, there is still the possibility of applications with electro-osmotic flows, to have a kinetic electromagnetic utilization of the flows and particles involved. By injecting the liquids into the microchannels, sometimes air bubbles may form inside the microchannels as well dirt particles appear over the viewing region within the microchannel. We can remove air bubbles in syringe, for this purpose we increased the volumetric flow rate as well.

We have presented the simulations and the laboratory experiments of the Y curve, as shown in Fig. 4.10, and comparison between simulation and experimental results, as shown in Fig. 4.11. The simulated parameters from Comsol, were used as guide for first round of experiments to set, volumetric flow rate independently in each syringe pump. Followed by experimental response, we used the out coming from experimental volumetric flow rate and inserted once more into a Comsol software, for each device tested. We were looking for a correlation between microchannel shape and mixing enhancement, taking into account well known pair of volumetric flow rate, binary mixture and chip geometry. Based on the parameters analyses from Comsol, we have created a passive micromixer, capable to enhance liquid mixing by convection, caused by channel geometrical aspects, such as curved channels that can generate a secondary flow causing predominant effect into main flow, creating also Dean vortex, as previously presented by (COOK at al., 2013; SUDARSAN et al., 2006). In Fig. 4.12, we observed multiple possibilities to change fluid configuration inside the channel, followed by changing volumetric flow rate ratio.

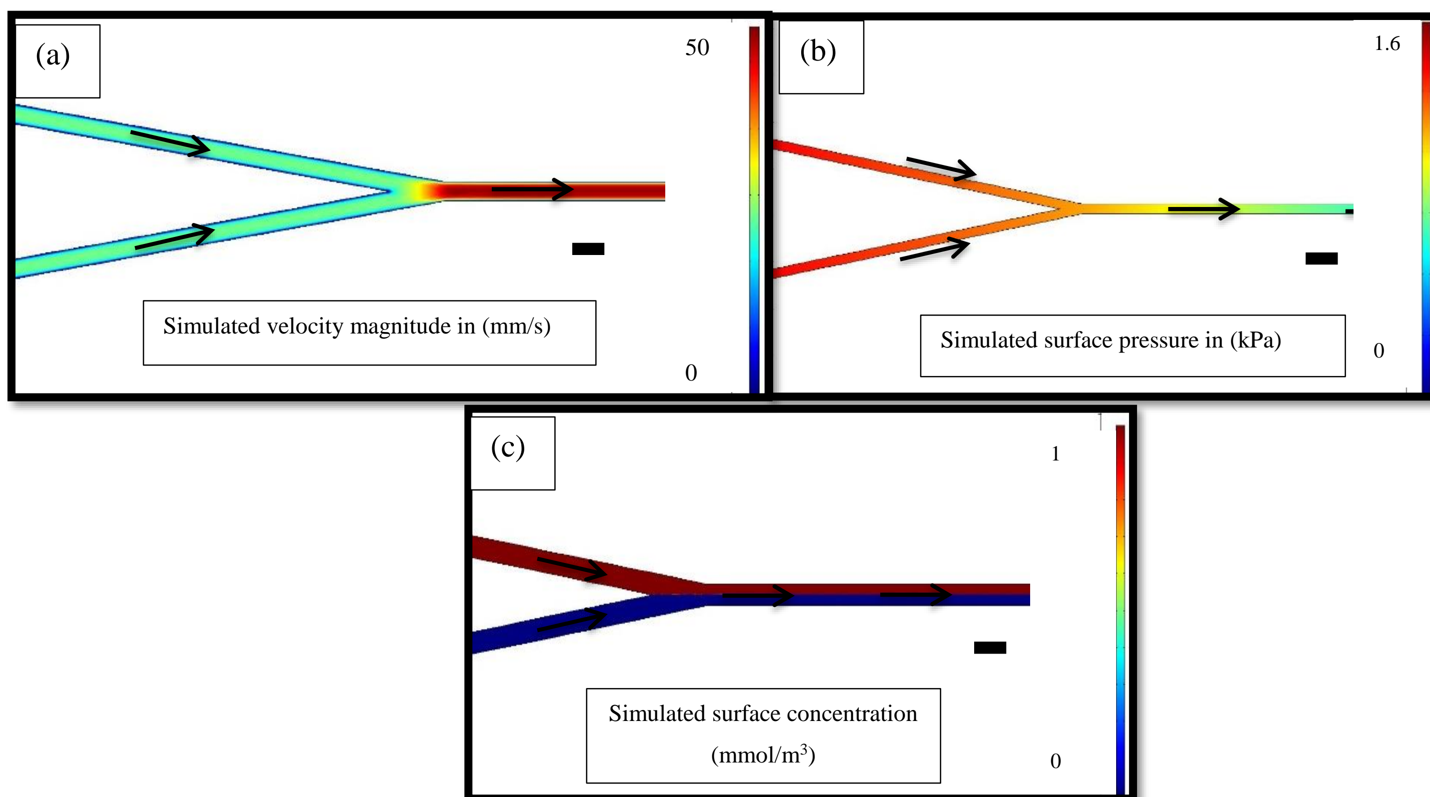

Figure 4.10 – (a) Fluid velocity along the microchannel in Y-Curve (▬ 50 µm). (b) Pressure along the microchannel at the Y-Curve. (c) Surface diffusion coefficient.

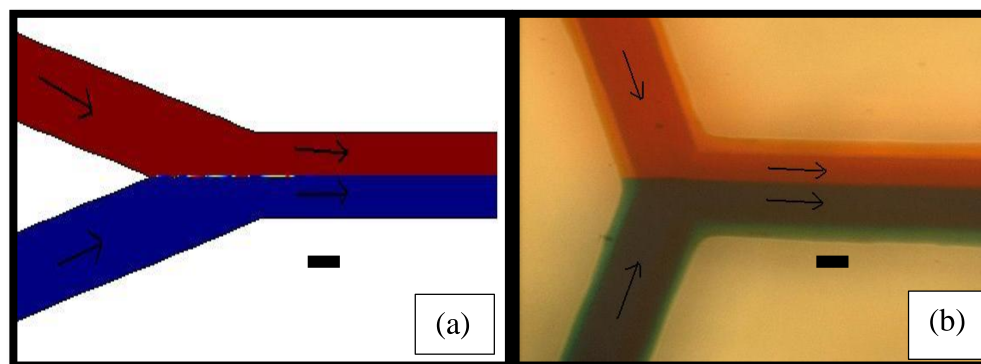

Figure 4.11 – Y-curve with two liquids without mixing (▬ 50µm): (a) Model simulated in Comsol; (b) Result obtained in laboratory.

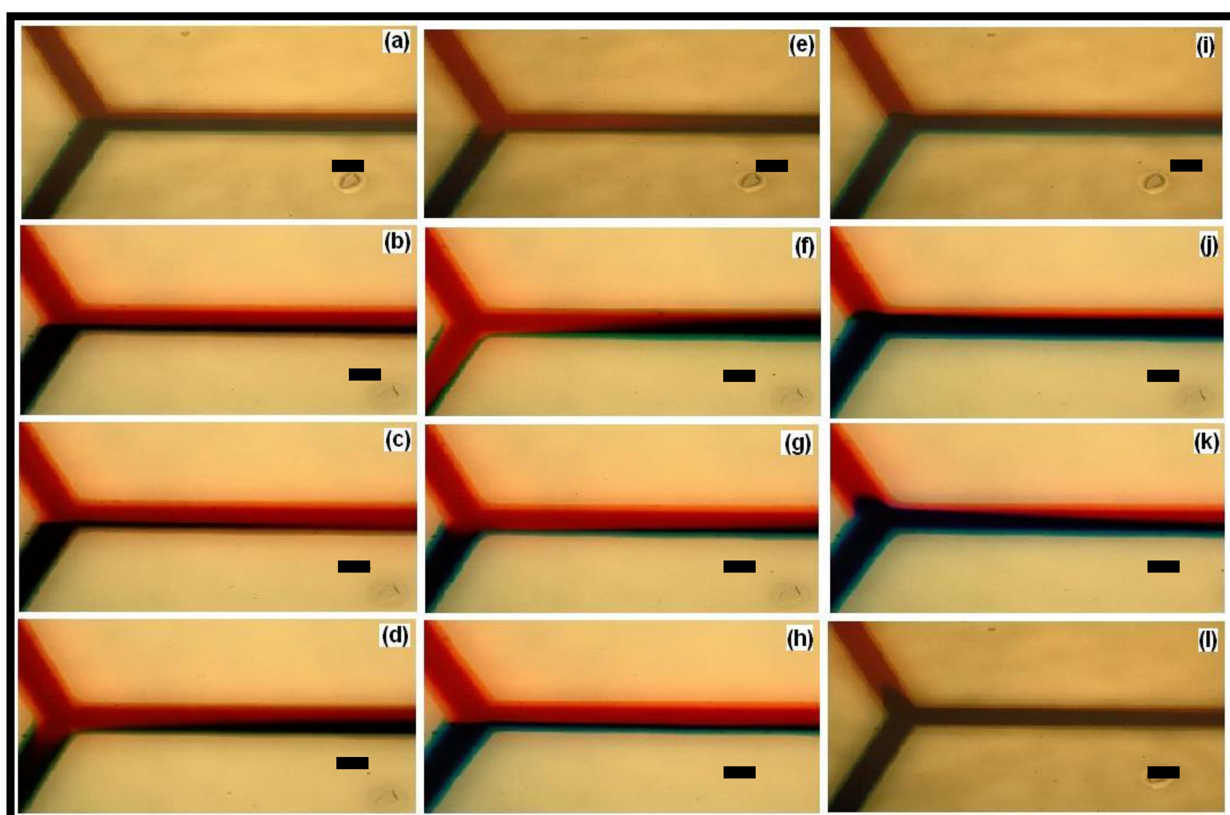

Figure 4.12 – Y- shaped curve with two unmixed liquids (▬ 50µm): (a) Equal volumetric flow rates for blue and red liquids; (b), (c), (d), (e), (f), (g) and (h) Modulation of the red liquid with a slightly larger volumetric flow rate than that of the blue liquid; (i), (j), (k) and (l) Modulation of the liquid in red slightly smaller than that of the blue liquid.

The area of constant Reynold number along the channel path, follows the same velocity gradient, because the calculations in Comsol were based in fluid velocity as floating parameter, converted from volumetric flow rate, as shown in Fig. 4.13

Figure 4.14 shows the laboratory tests of the cross curve aiming to have a control of modulation of the width of the flow lines from the flow, with the variation of the width of the central flow line shown in blue. This geometry is widely used in encapsulation processes, electro osmotic fluxes and for targeting cells, as presented by Tabeling et al. (2014) and Dittrich et al. (2006). Fig. 4.15 shows the simulation results in modulation of the width of the liquid in blue in the center of the device. This is the effect of non-mixing between the liquids, having the width control of the liquids from the applied flow. This opens possibility of applications in a cell targeting systems or cell aligners, as presented by Tabeling et al. (2014), Tan (2012) and Dittrich et al. (2006).

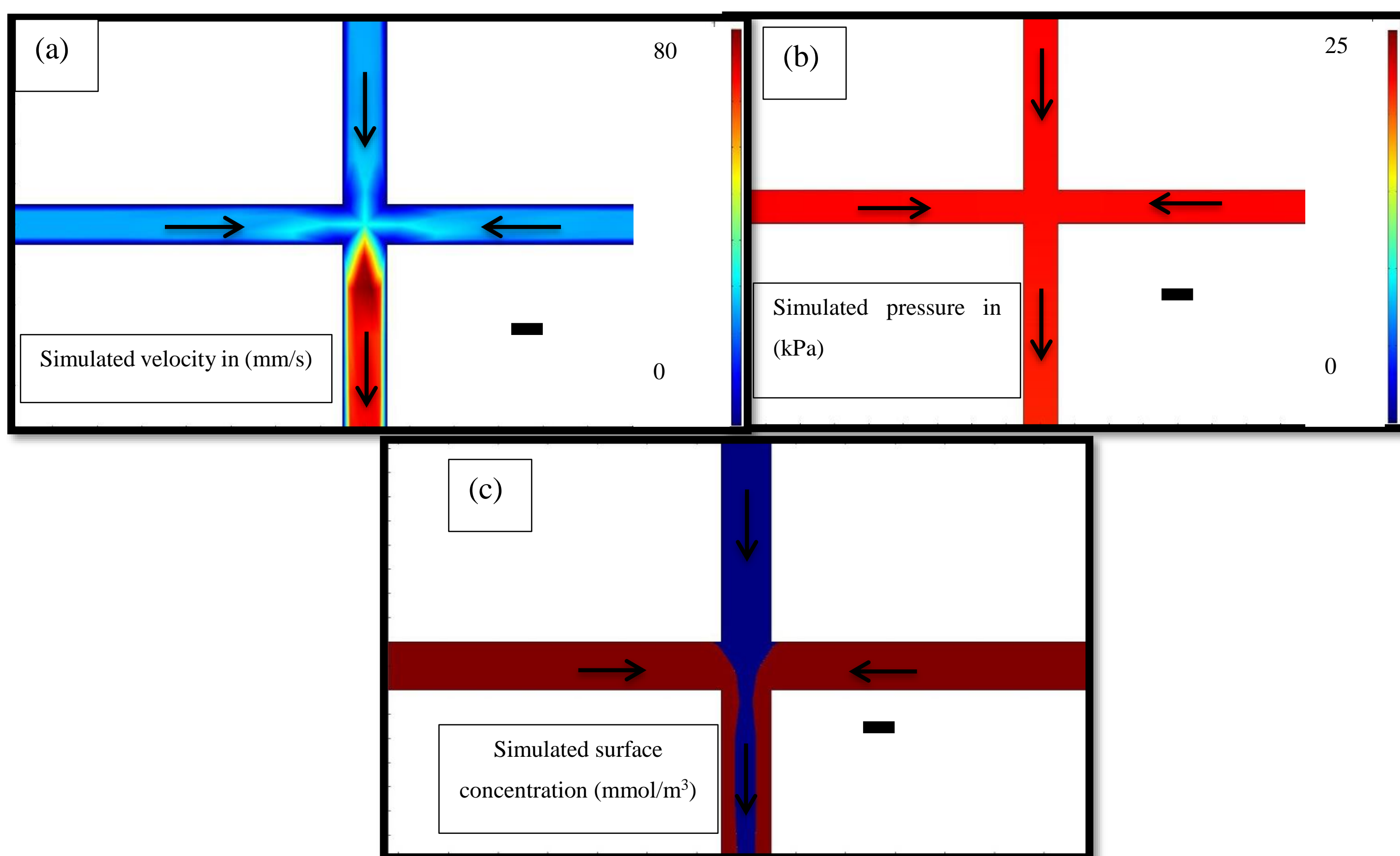

Figure 4.13 – (a) Velocity along the microchannel in the Cross Curve (▬ 50 μm). (b) Pressure along the microchannel in the Cross Curve. (c) Focused flow and graph of concentration, simulation in the Comsol in the Cross Curve.

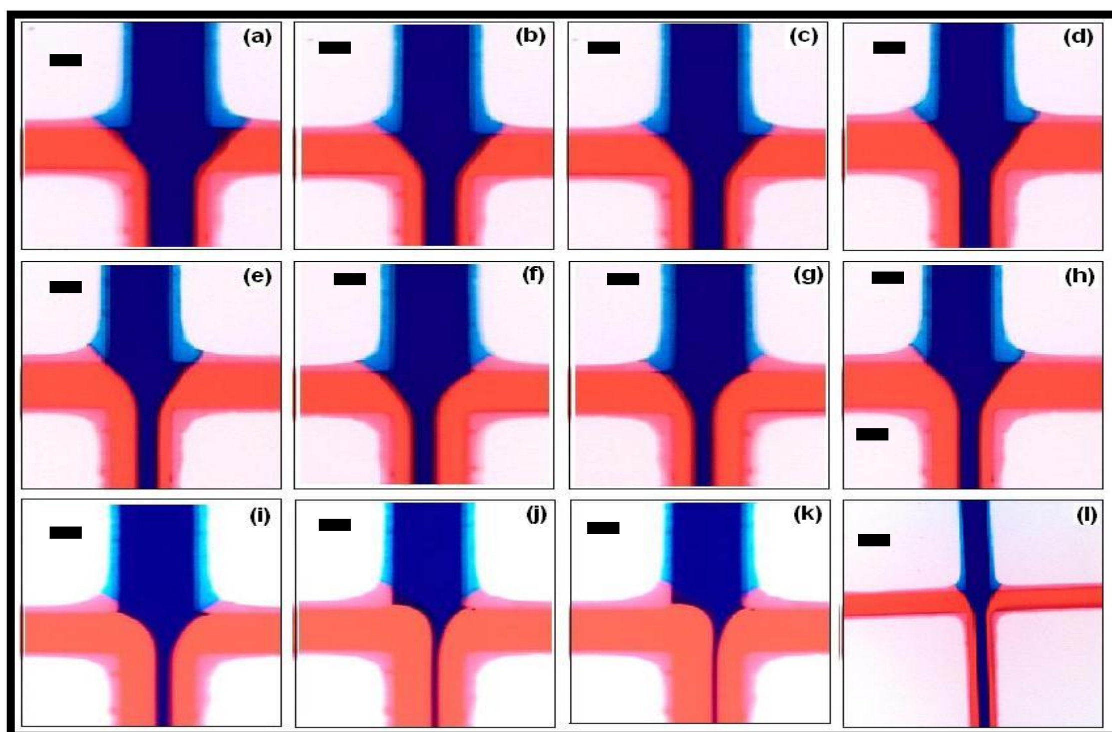

Figure 4.14 – (a), (b), (c) and (d) Modulation of the blue liquid with a slightly larger volumetric flow rate than the liquid in red; (e), (f), (g) and (h) Modulation of the blue liquid with flow approximately equal to that of the liquids in red; (i), (j) and (k) Modulation of the blue liquid with a slightly lower volumetric flow rate than the liquid in red (l) Same flow for the blue liquids and the two liquids in red (▬50μm).

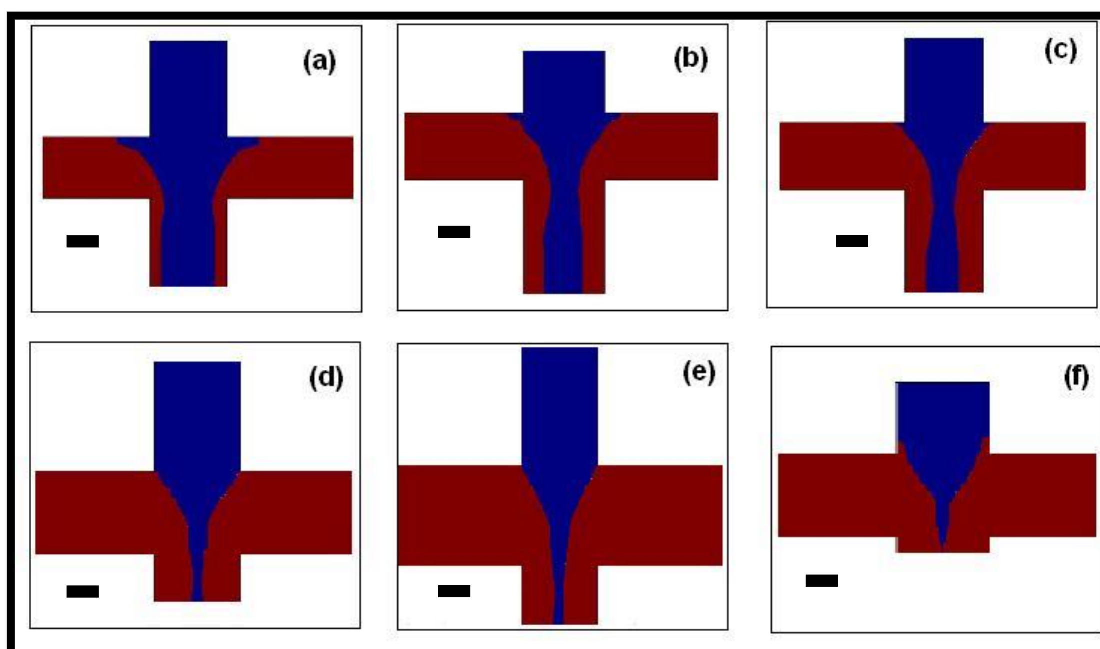

Figure 4.15 – (a) and (b) Modulation of the blue liquid with a slightly larger volumetric flow rate than the liquid ones in red; (c) Modulation of the blue liquid with flow approximately equal to the liquid in red; (d), (e) and (f) Modulation of the blue liquid with a slightly lower volumetric flow rate than the red liquids (▬50μm).

The T curve was simulated in the Comsol and some graphs were extracted, between them: velocity, pressure, Reynolds number and concentration, being often the concentration presented in the form of coefficient of diffusivity, as shown in Fig. 4.16. It is worth mentioning that the conditions adopted in the simulations were based on the dimensions of the device geometries, the viscosity of the liquids, in the case of water, and the injection rate, in order to make comparisons with laboratory tests, as shown in Fig. 4.17, for the experimental concentration surface area.

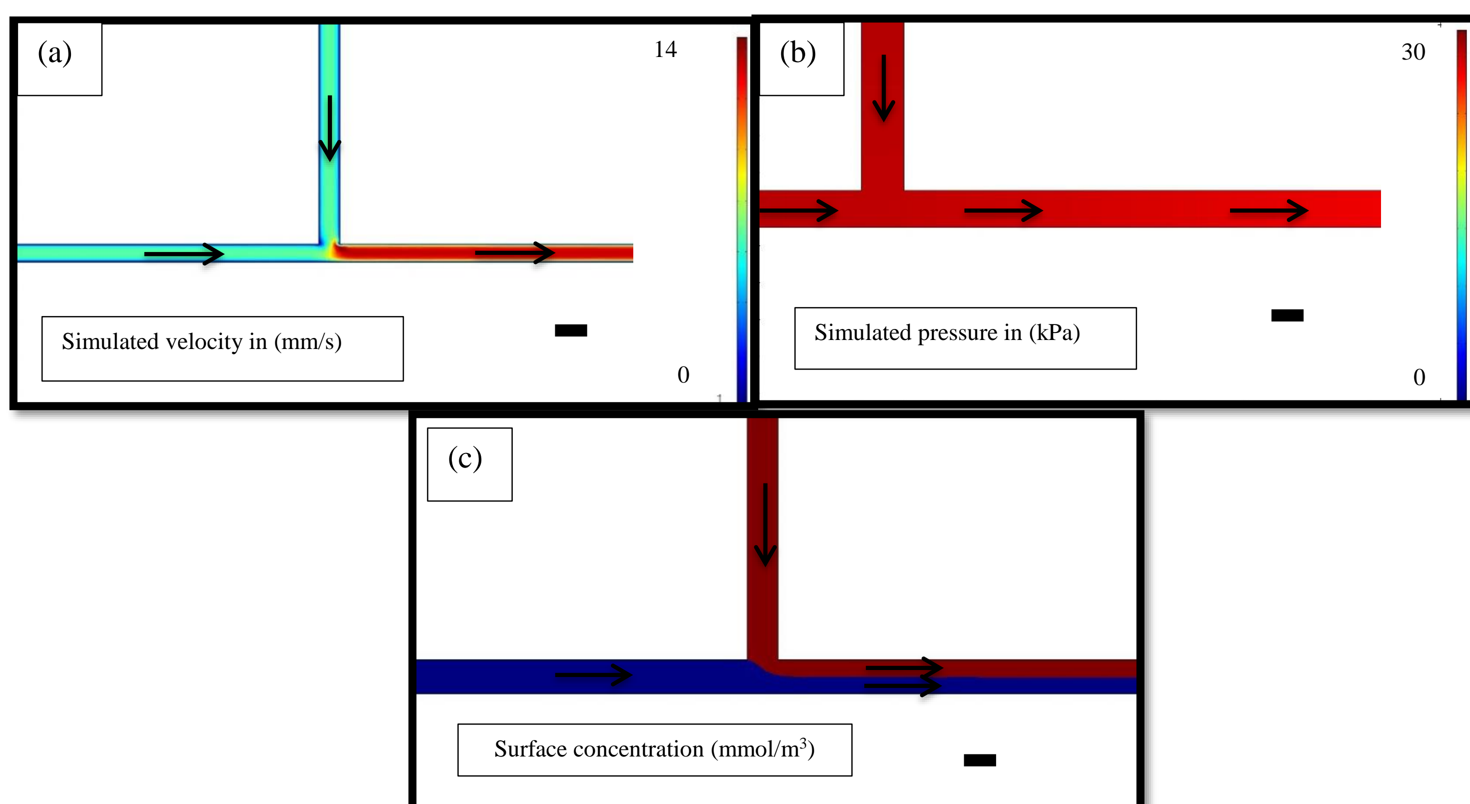

Figure 4.16 – (a)Velocity behavior along the microchannel in T-Curve. (b) Pressure behavior along the T-curve microchannel. (c) T-curve diffusivity of liquids (▬ 50µm).

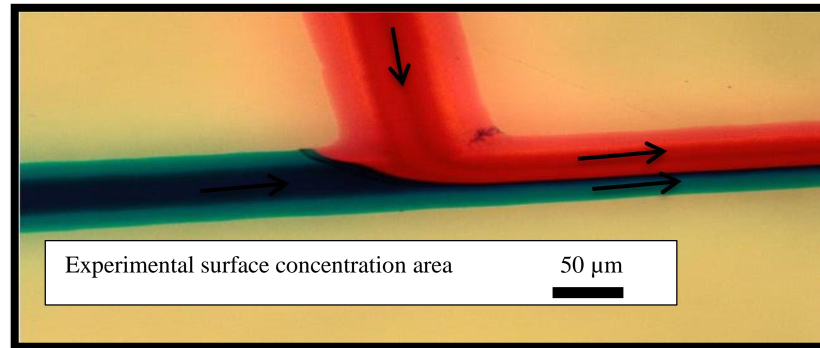

Figure 4.17 – T-curve shaped design, diffusion coefficient not increased along the channel path, with volumetric flow ratio Q_{blue}/Q_{red} (1:1).

Fig. 4.17 shows the deformation in the interface between the blue and red liquids, with the edge contour controlled by the flow applied to the entrance of each microchannel, the arrows indicate the flow direction along the microchannel. As in previous cases, the liquids have the same viscosity, and the system operates in the laminarity region, so there is no mixing between the liquids that follow in parallel modulated according to the applied flow. It can be observed that the edge contour of the "T" curve is even in the simulation in Comsol, as in the laboratory tests. An interesting possibility of application of the "T" curve is in the generation of microbubbles applied to encapsulations of drugs and or cells, micro emulsions and control of micrometric volumes (TABELING, 2014).

4.4.2. Microfluidic device application with performed experiments

In this section we present some laboratory tests with microfluidics devices, using the available laboratory facilities, such as syringe pumps, microscopes, power supply, function generator, LabVIEW software with data acquisition board, high precision multimeter, microfluidic devices, as shown in Fig. 4.18.

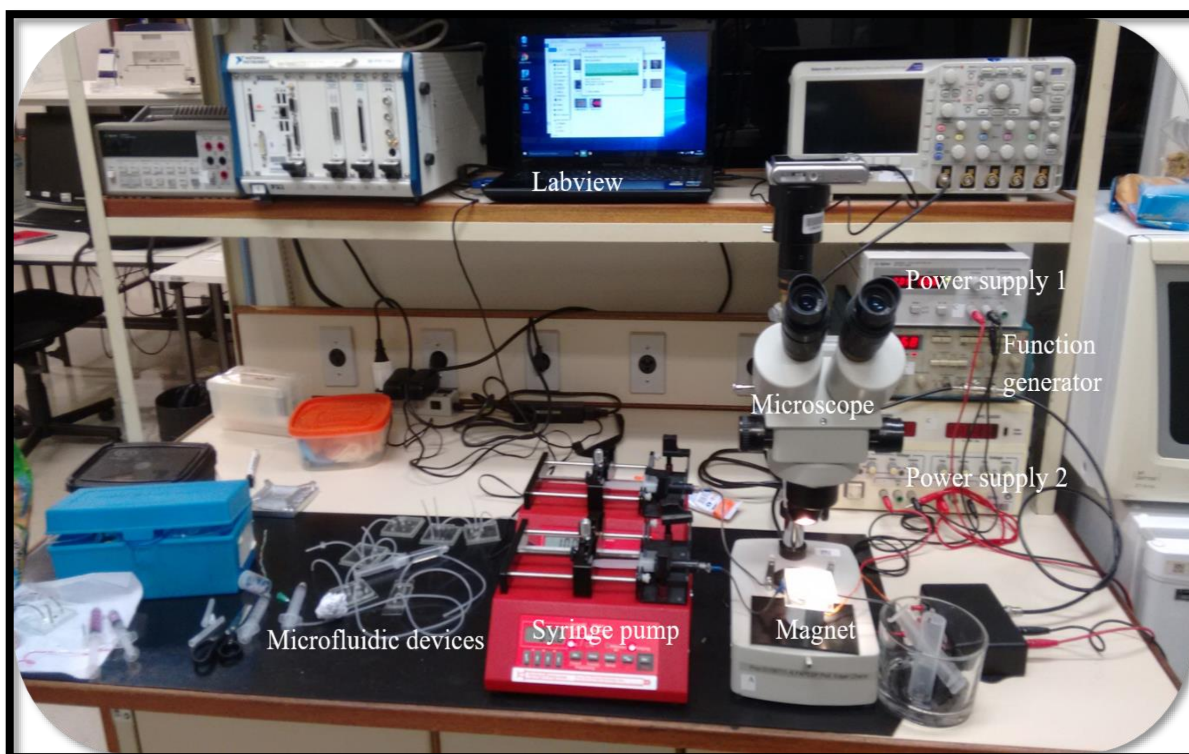

Figure 4.18 – Laboratory setup for performing microfluidics experiments.

We have highlighted some experiments in this section, some of them needed to be discussed in more detail. We tested the spiral shaped design for enhance liquid mixtures, this device is known as passive spiral mixer (looking like a concentric spiral), as shown in Fig. 4.19. The experimental procedure adopted for the test was to insert the red colour liquid into the microchannel using a syringe pump to a certain extent and subsequently withdrawing the pump and observing the displacement of the liquid by the capillarity forces along the microchannel.

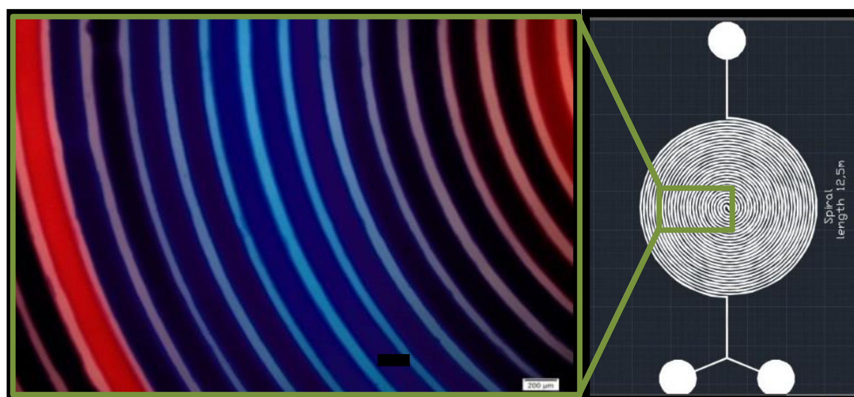

Figure 4.19 – Spiral concentric diffusivity scale along the microchannel (▬ 50 μm).

Fig. 4.20 shows laboratory experiments with details of the geometry of the device in the case of H curve. The coefficient of diffusivity between the blue and red liquids modifies along the curse of curved microchannel, showing as a micro-mixer with optimized performance, this principle can be applied in several areas, such as the chemical and petrochemical industry, pharmaceutical industry, medicine, among other areas (MADOU, 2011).

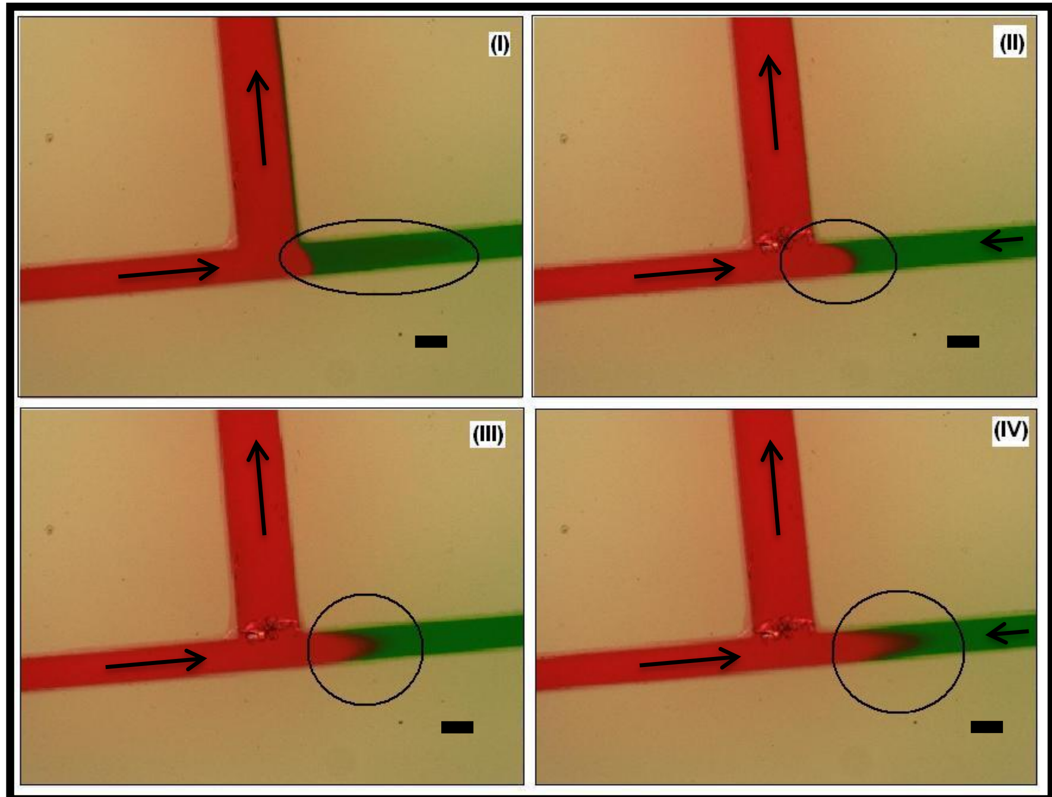

Figure 4.20 – Curve H laboratory test, red liquid capillary effect: (I) Strangulation of the green liquid with the decrease of the flow in relation to the red liquid; (II), (III) and (IV) Deformation between the liquids generated by the shear point (▬ 100µm).

Fig. 4.21 shows that the unbalance of the flows causes the viscous forces to create a shear point between the liquids, which is the deformation generated at the liquid-liquid interface, resulting in advance of the red liquid flow in relation to the green. It can be observed that the shear stress increases, and that at the center of the microchannel reaches the maximum value, we achieved the same result that reported in (MADOU, 2011).

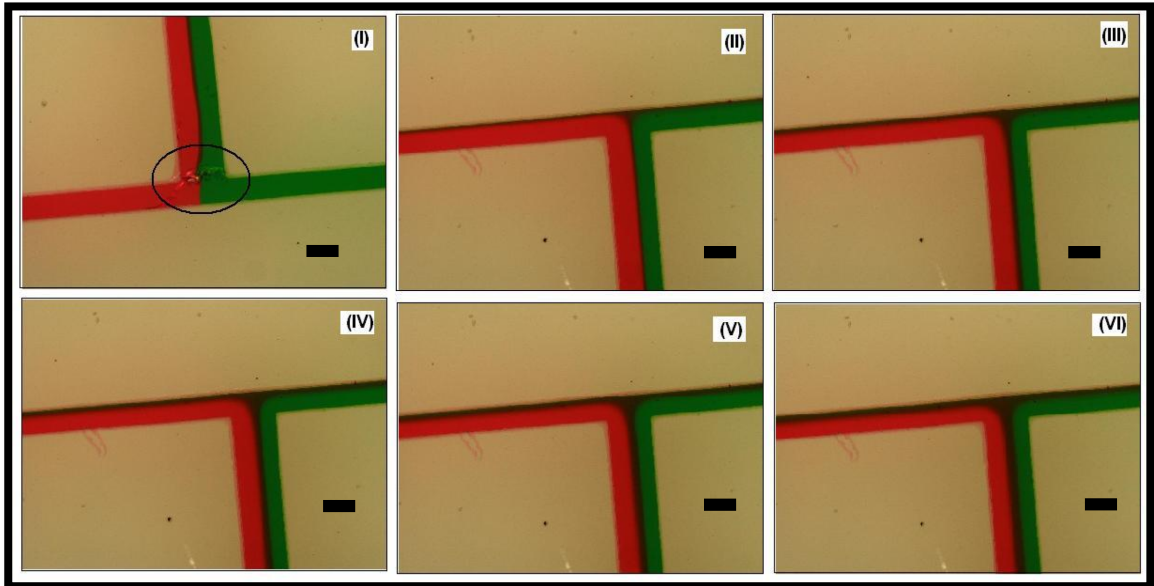

Figure 4.21 – Curve H, laboratory test diffusivity control from the flow: (I) Dirt particle generating instability at the liquid-liquid interface; (II), (III), (IV), (V) and (VI). Controlling the diffusivity with the increase of the flow applied in the system (▬ 100μm).

It is possible to highlight a certain condition that was at first considered as undesirable, however, later it ended up generating interesting ideas for diffusivity control. During the experiment the microchannel was contaminated with the entrance of a dirt particle that obstructed the microchannel, however, as the liquid injections were made, this particle was accommodated according to Fig. 4.21, it can be observed that the particle began to generate enhanced mixing of liquids, in this way, the diffusivity coefficient increases with the increase of the flow rate, making the diffusivity coefficient in these conditions directly proportional to the volumetric flow rate. It can be observed that for the liquid-liquid interface before the particle, the interdiffusivity line is infinitesimal, and after the particle this line of interdiffusion increases, becoming more accentuated, due to the instability generated, as can be observed in Fig. 4.22 and Fig. 4.23. These result converge with those reported by Gou et al. (2018) and Zhang et al. (2013) regarding inertial microfluidics applications.

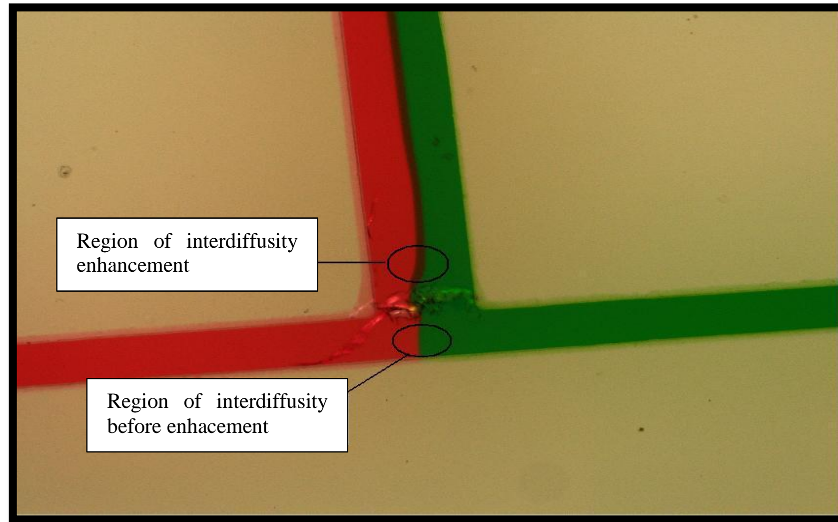

Figure 4.22 – Dirt particle and region at the liquid-liquid interface before and after instability, Qred = Qgreen = 100 µl/min.

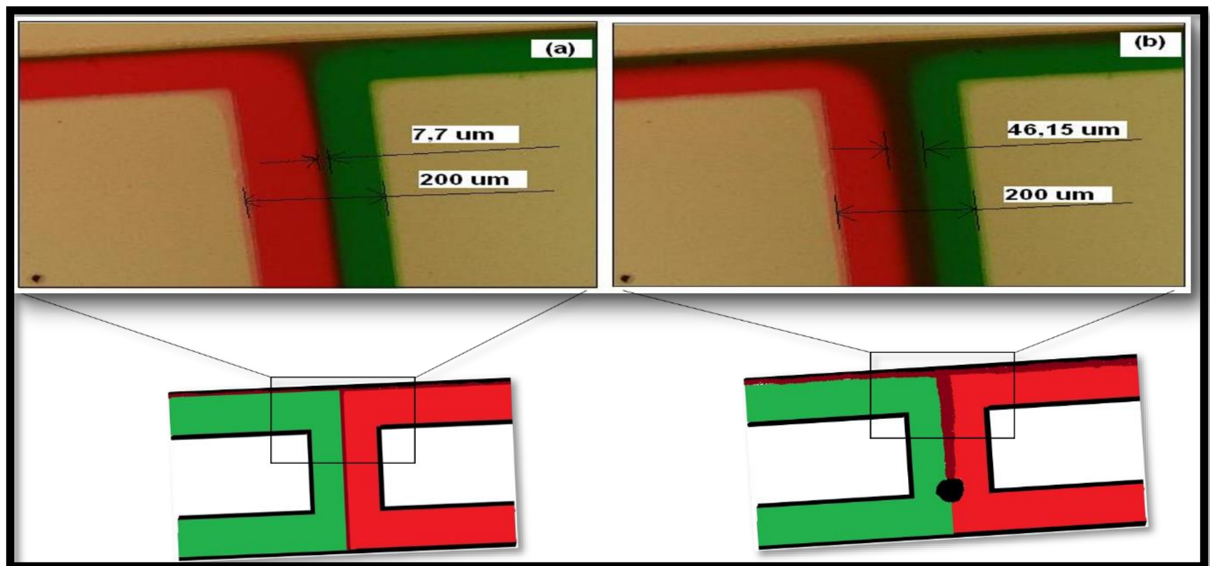

Figure 4.23 – Measurement of the diffusivity region Qred and Qgreen = 50 ul/min. (a) Line of diffusivity without mixing enhancement element (b) Line of diffusivity with mixing enhancement element.

In Fig. 4.23 the diffusivity region in part (a) of the figure is generated without instability at the liquid-liquid interface, while part (b) shows a considerable gain in the region of enhanced mixing, this increase was due to the instability generated by the particle at the liquid-liquid

interface. Based on these measurements, calculations of percentage diffusivity were made based on the area occupied by the liquids. Using cross multiplication / rule of three methods, dividing the thickness of the diffusivity line into brown, by the line occupied by the liquids in the microchannel of 200 µm, it leads to results similar to those in literature (GOU et al., 2018; ZHANG et al. 2013). The percentage diffusivity coefficient (D1), referring to part (a) of the Fig. 39(a), was equal to D1 = 3.90%, and the percentage diffusivity coefficient with instability (D2) referring to part (b) of the Fig. 39(b) remained the same at D2 = 23%. Based on the regions of diffusivity with and without the particle induced instability it can be seen that with the creation of instability and enhancement of diffusion coefficient in percentage, it had an increase of approximately 20%. This, indicates that the more regions of instabilities that are created along the liquid-liquid interface, the larger the mixture between the liquids. This creates new possibilities of optimization of the structures presented in this work. In future work, regions of instability can be optimized for the optimization of mixtures.

4.5. Active microfluidic device applied to enhancement of liquid mixtures

We have developed a novel fabrication technique, for an active mixing microfluidic device coupled to a magnetic actuator, using low-cost materials and fast prototyping. The active mixer was fabricated with glass, PMDS used as structural support and as thin-film membrane with neodymium iron-boron (*NdFeB)* magnet, and its characterization was done by gradient color analysis. The concept of the liquid mixing applications, with a PDMS membrane operating with frequency oscillation performed from 0 Hz to 11 Hz, with incremental step of 1 Hz. The actuation system allowed establishing the correlation between the mixing enhancement and frequency of oscillation, where two-stream lines form the mixture in laminar flows, with Reynolds number smaller than 10. We demonstrated that the highest enhancement mixture is reached at 7 Hz.

The active mixer devices are based on disturbances induced by external fields and used for fast and controlled mixing of fluids in microchannels (VLADISAVLJEVIĆ, 2013; MOISEEVA, 2011). If flows in microchannels hereby the Reynolds numbers of the liquids are far below the critical Reynolds number. The transversal disturbance is needed for making the interface between the two mixed phases to become unstable for mixing enhancement (AUGUSTIN, 2009; Li, 2010). Our actuator causes a pressure-driven disturbance through electromagnetic physical effect. The device consists of two functional layers both fabricated with PMDS. The upper PDMS layer provides a compliant membrane with an *NdFeB* permanent

magnet attached for actuation, while the lower PDMS layer incorporates the microchannels and the mix chamber, as shown in Fig. 4.24.

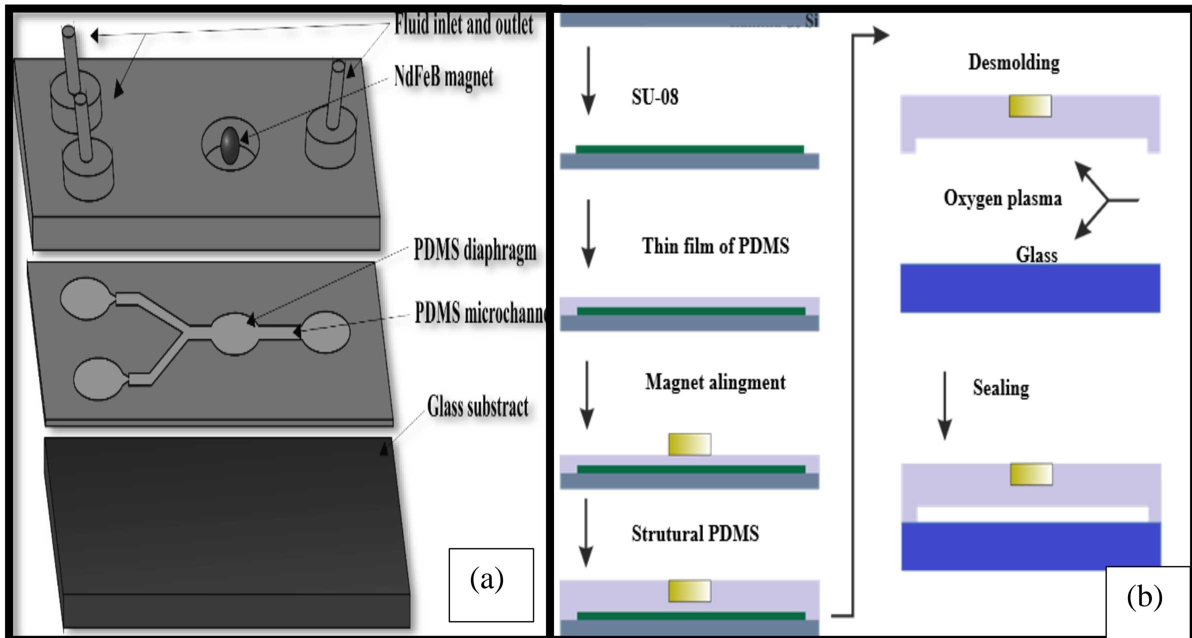

Figure 4.24 – Multilayer structure schematic of the mixer design and fabrication process step by step. (a)Active micromixer formation by three layers, from bottom to top, glass, membrane and structural PDMS. (b) Microfabrication step by step of micromixer.

We demonstrated such capabilities through various videos recorded with a CCD camera. This device is designed properly with flows in symmetry, then it allows controlling the distribution of the species by changing the input volumetric flow rate and membrane vibration frequency (ZHANG, 2013; NGUYEN, 2006). The measurements were performed to detect enhanced mixture in water with dye colors. As a proof of concept, we presented a system, that takes advantage of good sensitivity for small liquid disturbance (CHIA, 2011), height dimension of hundreds of micrometers, using small liquid volume of 1.40 µl inside the microchip. The device consists of two layers of PMDS as shown in Fig. 4.24, where the top layer receives the silicone tubes for inlet and outlet of the fluids, while the bottom layer incorporates the microchannels and the mixing chamber with the PDMS diaphragm attached. The dimensions of the microchannel are: width of 100 µm, depth of 80 µm and length of 5 cm. We attached a permanent spherical magnet (diameter 3mm) on top of the PDMS membrane and

the electromagnetic performance was given by a commercial 7.5w electromagnet coupled below the device.

Microchannels: An SU-8 layer, deposited by the spin coating technique, receives the desired design through high-resolution direct-writing photolithography (µPG 101 from Heidelberg Instruments, Germany). The Dow Corning Sylgard 184 PDMS is prepared: base and curing agent in the ratio of 10:1. After depositing the mixture on the mold, the assembly is subjected to vacuum pressure of 50 mTorr for removal of air bubbles. After 60 min at 100°C in a hot plate, the PDMS is polymerized incorporating the design of the microchannels printed on its surface.

Magnet alignment: The magnet is centered over the actuation chamber. A subsequent 2mm high PDMS layer (structural PDMS) is deposited around the assembly for the purpose of housing the coil and the fluid inlet and outlet tubes. In this step, the magnet is used to protect the diaphragm membrane being withdrawn after the polymerization of the structural PDMS while the coil and the tubes remain attached to the device. Again the polymerization process takes place after 60 min at 100°C in a hot plate. The detail of the coil and magnet over the reservoir is shown in Fig. 4.24. Finally, the PDMS layer molded with the microchannels and the structural PDMS are withdrawn from the SU-8 template.

Sealing: The sealing process of the PDMS with glass substrate improves adhesion between the parts. Irreversible sealing is achieved by oxidation of the surface of the glass and PDMS with O_2 plasma following the steps: 1) Immersion of the glass substrate and PDMS in a 10% KOH solution,80% isopropanol and 10% DI water for 30 seconds; 2) Nitrogen jet drying; 3) Exposure of plasma surfaces to 70 cm^3/min of O_2 at a power of 100 W for 20 seconds; 4) Alignment and manual mechanical pressure on surfaces for 3 minutes. The PDMS/Glass sealing process is shown in Fig. 4.24. This sealing was different from the presented in section 3.2.2.1, we have improved the PDMS-glass sealing, for avoid chamber collapse and blocking the channel, in this sense, we have added a KOH solution before start the sealing process.

Experiments were executed with a variable oscillation frequency between 0 and 11 Hz with a frequency step of 1 Hz. Evaluation of the mixer prototype, was carried out by studying the dependence of the mixing efficiency on the frequency of the magnetic drive. For this purpose, the measurement apparatus shown in Fig. 4.25 has been assembled. At constant flow rates of 20µl/minute, two syringe pumps were used to inject the blue dye, triphenylmethane, and the red amaranth dye diluted in deionized water. The mixer was placed on a commercial

7.5W power electromagnet powered by a driver circuit that supplied alternating current in response to the frequency chosen by the operator on the function generator. Finally, the device was monitored by a video camera attached to the microscope.

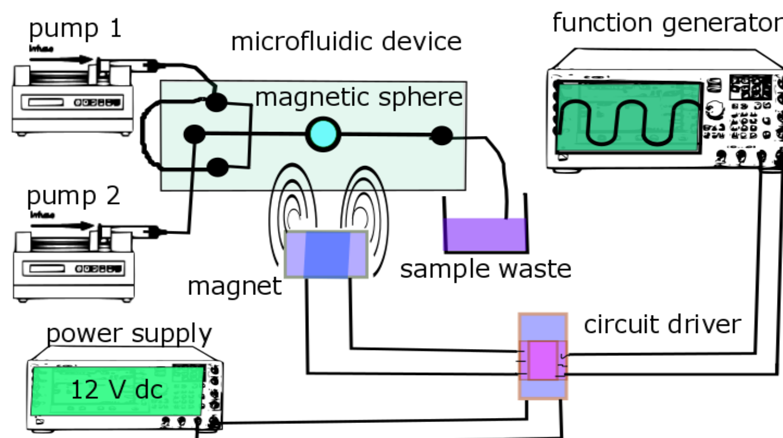

Figure 4.25 – Experimental setup with microfluidic plattform actuation.

Evaluation of the prototype, as shown in Fig. 4.26, has been performed by studying the dependence of its mixing efficiency on the driving frequency of magnetic actuation. The two upstream channels are for the introduction of standard sample solutions of freshly prepared blue and red dye in water. A microfluidic mixer and syringe pumps (SP101IZ, WPI) were used for controlling the flow rate. Microfluidic device with magnet actuation on the PDMS membrane in the mixing chamber. The membrane actuation can cause complete close of channel.

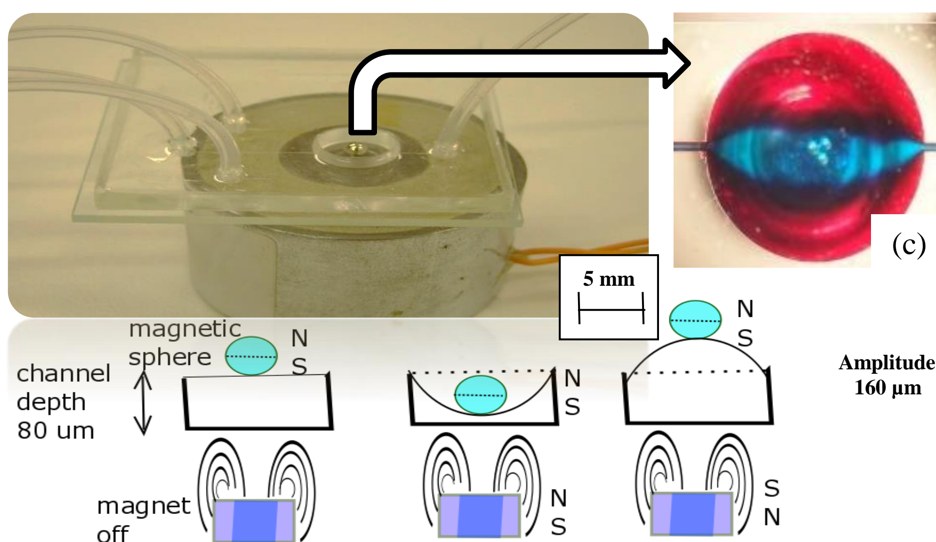

Figure 4.26 – Active micro mixer. (a) Device on top of electromagnet. (b) Chamber side view and actuation. (c) Chamber top view with liquid stream lines.

The experiments were performed at room temperature, around 25ºC, monitored via a reference temperature sensor. Experimental results show that this actuator is capable of enhancing the liquids mixing by changing the flow regime (from laminar to turbulent) and the mass diffusivity line by controlling the two key parameters for hydrodynamic instability in active micromixer: the magnitude and the frequency of the disturbance (LIU, 2010).

For each selected oscillation frequency, we recorded the actuation chamber. The measurements were performed by establishing the relationship between specific frequency of oscillation and enhanced mixing efficiency using qualitative measurements. Before every new measurement, we injected water to remove residual samples and we also removed air bubbles. When the two fluids come into contact within the microchannel in the form of a "ψ", the liquid-liquid interface is affect by membrane oscillation, the mixture happens slowly by diffusion until reaching the outlet reservoir. With the actuation, the insertion of inertial forces clearly accelerates the mixing process (LIU, 2010; NGUYEN, 2006).

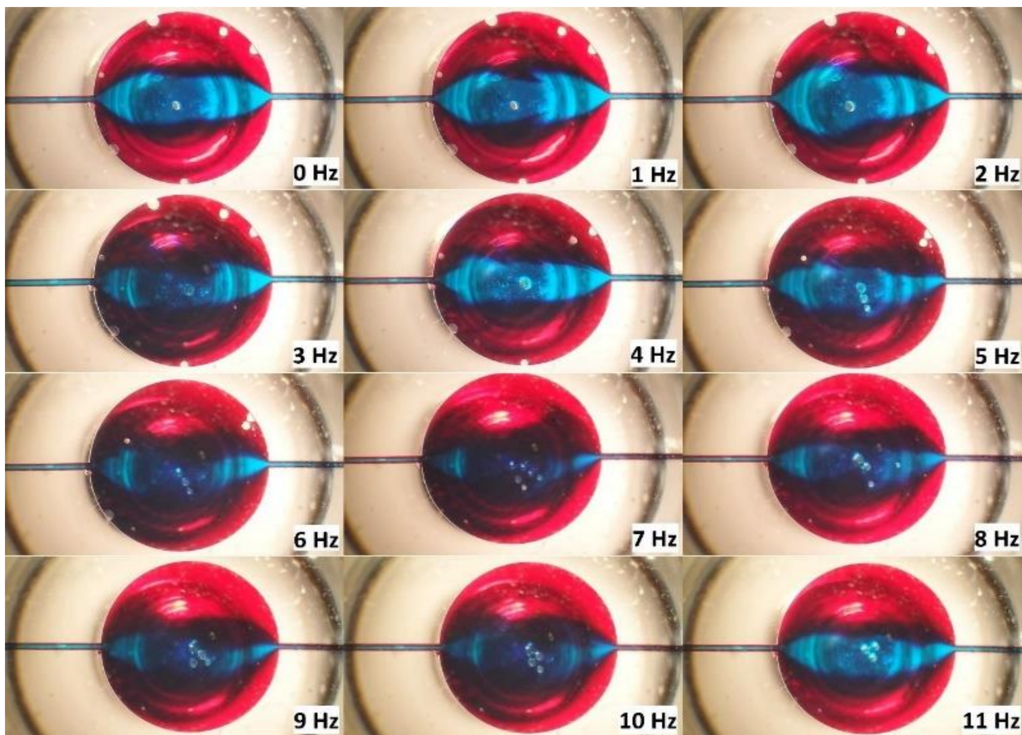

Figure 4.27 – Effect of frequency sweep on the inter diffusivity of liquids in the actuation chamber.

Images taken from the recorded high resolution video while the electromagnet's operating frequency was gradually increased from zero to 11Hz, are shown in Fig. 4.27. In the first image, still without performance (frequency zero), it is observed that the laminar flow

follows the reservoir even with the sudden change of the geometry of the microchannel. The pressure variation exerted by the magnet in the reservoir accelerates the mass diffusion process by increasing the thickness of the diffusivity line, which is darker in color.

Through visual analysis, it is noticed that the mixing intensifies gradually until the frequency reaches 11Hz, limiting oscillation for actuation frequencies up to 11 Hz. The process can also be evaluated by comparing the thickness of the diffusivity line before and after the mixing vessel. The detail of the diffusivity line in the input channel and the output channel is shown in Fig. 4.28. In a laminar flow regime, the diffusivity line has a thickness of about 20µm next to the mixing tank. After the mixer operation is on, the line thickness increased by 90%, reaching 38µm.

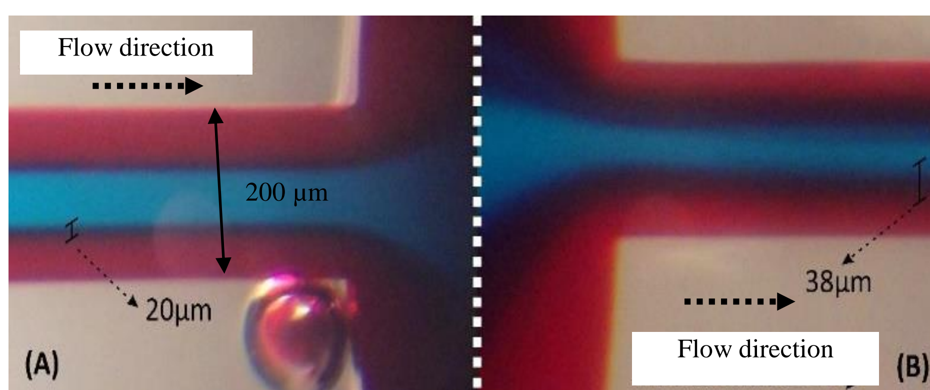

Figure 4.28 – Highest mixing effect for 7 Hz frequency oscillation.

4.6. Microfluidic droplet generation with detection system based on embedded ring shaped electrodes

Droplets size detection and control is critical in many applications, such as drug manipulation and delivery. In these type of applications, a closed loop control, that involves sensing feedback to actuators control, is necessary (LIU, 2010). Optical detection (NGUYEN, 2006), impedance detection (SCOTT, 2008) and capacitive detection (NIU, 2007; ELBUKEN, 2011) are the main techniques used to this end. Optical droplet detection normally needs a significantly complex setup: it comprises a device to insert the laser light and detect the scattered light using optical fibers positioned in the microfluidic channel. Although high sensitivity and reliability advantages, optical-based interrogation dependence on external equipment does not allow the fabrication of portable point-of-care lab-on-a-chip. Impedance detectors are easily fabricated and allow compact detection circuitry to portable devices.

However, even a small current passing through the fluid, can cause undesirable reactions and electrode degradation. On the other hand, capacitive detection allows the detection of different fluids without direct contact (RIBEIRO, 2015), because aqueous droplets have a different dielectric constant than the surrounding oil, for example, water has k=80 and silicon oil has k=20, these similar liquids properties were reported by LI et al., (2010). As the simpler thin-film electrodes are sensitive to droplet composition, interdigitated electrodes on-plane fabrication have been reported as reliable particle, cell and gas detectors. We used a particular case of interdigitated electrode, called ring-shaped electrode (RSE) to detect water/oil droplet size, volume and velocity. RSE takes advantage of a better capacitance per area ratio, improving the detector sensitivity and reliability.

Fabrication and experimental setup for droplet detection were developed, a sketch of the electrode structure is shown in Fig. 4.29. The designed sensor is formed by 14 electrode pairs and 500nm thickness metal film. Each electrode width and gap is 10μm, since it is the minimum achievable dimension in our fabrication process. Finally, the outer electrode radius is 600μm, resulting in a total occupied area less than 1.13mm², covered with a PDMS thin film of 5μm and PDMS channel sealed on top. More details of RSE fabrication in section 3.2.3.4.

In order to control the size of droplets, we used a Ψ -shaped microchannel system, as shown in Fig. 4.29. The spontaneous droplet formation in channels of 200μm width and 80μm height were controlled by two syringe-pumps at the rate range of 1 to 30μl/min. The RSE sensor, located after the T-junction, was protected by a 5μm thick PDMS layer to enter in direct contact with the fluids, as previously mentioned. Transparent mineral oil was used as continuous phase fluid or carrying liquid, while the aqueous red colorant droplet was used as the dispersed phase.

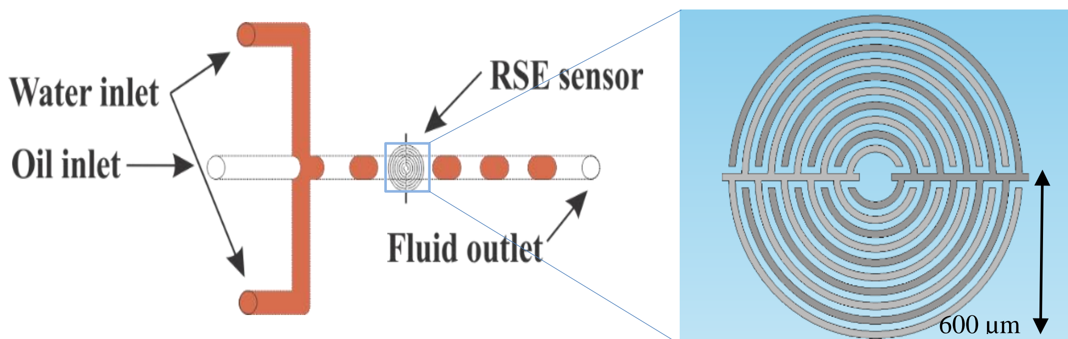

Figure 4.29 - Spontaneus droplet generation in a Ψ-Shaped microchannel and RSE sketch.

Droplet size and shape are determined by flow rates set on the syringe-pumps. The droplet formation spans two different regimes: the “dripping regime”, which produces spherical droplets, or the “squeezing regime”, which produces long plug-like droplets. This work was carried out in the plug-like “squeezing regime”.

4.6.1. Measurement procedure

Experimental setup was used to evaluate the RSE sensor response. A video recorder coupled to the microscope displays the droplet formation while the LCR meter monitor shows (HP 4284A), in real time, the capacitance of the RSE. In addition, an Agilent 34401A multimeter was used to acquire the sample temperature via PT100 reference temperature sensor. Finally, a computer with software developed in LabVIEW® presents the data and the camera images. Since the fluid permittivity varies with the temperature, the device temperature was monitored to ensure it was kept near to 25ºC, as shown in Fig. 4.30. The LCR bridge was configured to work at 100kHz and with a 1V amplitude to monitor the capacitance and parallel resistance of the electrodes. The Agilent multimeter measures four wire PT100 reference temperature sensor.

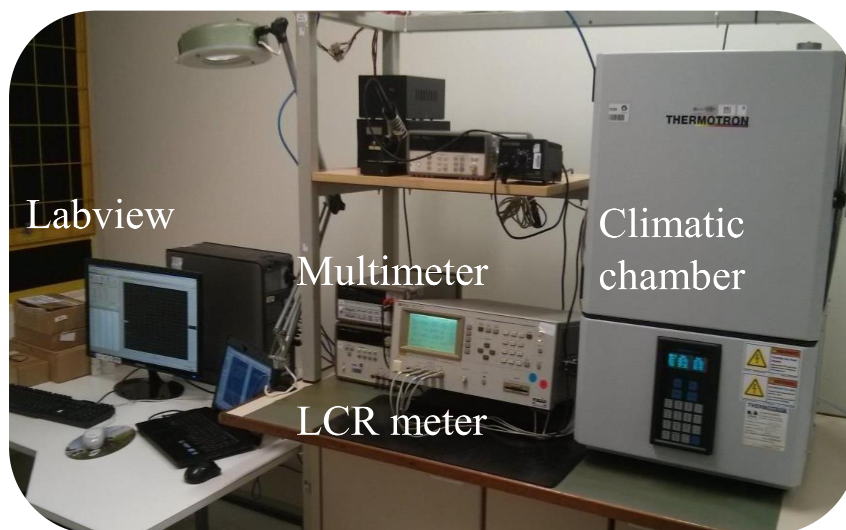

Figure 4.30 - Experimental setup used to acquire the capacitive and resistive response.

The four-wire measurement reduces the influence of the cables on the measured value, improving the accuracy of the results. During the measurements the system was placed in climatic chamber Termotron 3800 with constant temperature and humidity at 25 ° C and 60% Rh, respectively.

4.6.2. Fabrication and droplet detection experimental setup

In the graph of Fig. 4.31 the capacitance changing in accordance to the droplet passage over RSE sensor at 10µl/min flow rate is shown in Fig. 4.31. To relate the output signal to the flow rate parameters, images of droplet formation were captured with a camera coupled to a microscope. This enabled measurements of droplet size and shape. Each droplet of aqueous colorant represents a drop of about 40fF in the RSE capacitance.

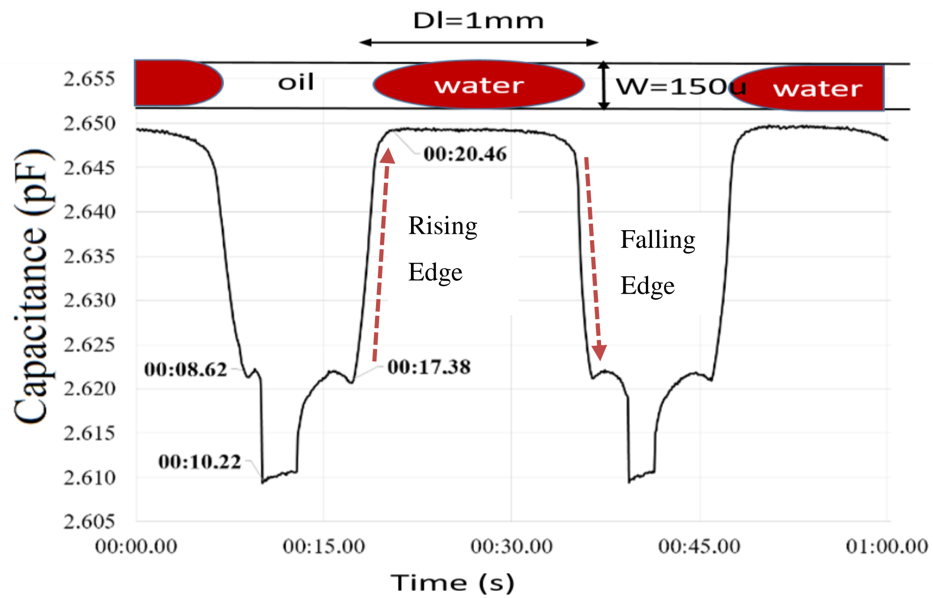

Figure 4.31 - Capacitance oscillation due to droplet water/oil passage during 60 seconds.

The pulse length when capacitance is down of 2.625pF determines the time that the droplet was over the capacitor while the peak value, when capacitance is over 2.645pF, determines the period in which the continuous phase fluid is flowing over the RSE. Taking in account the flow rate and the microchannel cross section, the droplet absolute speed, "|v|" can be calculated by Eqs. (4.3) and (4.4):

$$\boldsymbol{v} = \frac{\boldsymbol{Q}}{\boldsymbol{A_C}} \qquad \text{(Equation 4.3)}$$

$$\boldsymbol{d} = v.t = \frac{Q}{A_c}.t \qquad \text{(Equation 4.4)}$$

where, $\boldsymbol{Q}$ is the flow rate over the RSE sensor imposed by syringe pumps, and $\boldsymbol{A_C}$ is the microchannel cross-sectional area. In addition, one can calculate the droplet volume extracting the time $\boldsymbol{t}$ from the graph (time spent since the capacitance was below 2.645pF) and relate them to the flow rate, where, $\boldsymbol{d}$ is the droplet-traveled distance in the microchannel. Based on the Eq. 4.4, and data recorded from the capacitive sensor and image recorded from the CCD camera, we calculated the droplet size, speed and shape.

Increasing the flow rate of the aqueous colorant relative to the oil flow, it is possible to reduce the droplet size to less than the distance occupied by the sensor. The snapshot of this situation is shown in Fig. 4.32. In this case, the capacitance does not reach the peak value, in turn an average value is observed. For such situations, the droplet size cannot be determined, if two or more droplets cover the sensor field sensitivity, the measured value of capacitance is related to the average permittivity over the RSE. (This work was done in collaboration with prof. Fabiano Fruett and Dr. Luiz Eduardo bento Ribeiro from UNICAMP).

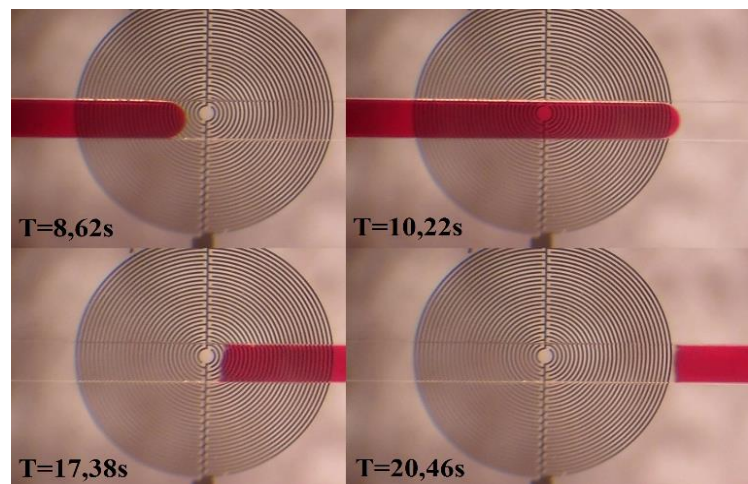

Figure 4.32 - Synchronized pictures of droplets over RSE sensor.

4.7. Sub terahertz sensor in microfluidic devices for determination and control of ethanol concentration on demand

In this part, we focused on the combination of microfluidic and millimeter-wave (mm-wave) technology, taking advantages of both areas, such as small sample volume, fast mixing, micro reactor characterization, fine adjust of concentration controlling, on-line detection in flux system of small sample volume. We worked on the development of a flexible platform for performing microfluidic experiments with an embedded spectroscopic sensor, which allows contactless non-invasive on-line measurements and characterization of liquids. We demonstrated such capabilities through various measurements in microfluidic environment operating in a laminar flow, with Reynolds number smaller than 16 and high Peclet number larger than 25700 in the micromixer and more than ten times smaller in joint section Pe = 2383. This high Peclet number, in mixing analysis, suggests that the convection prevails over diffusion mechanism (MADOU, 2002; PALACIOS 2010). Thus, if the device is properly designed, it allows controlling precisely the distribution of the species, causing fast mixing of them, changing the concentration simply by controlling their input mass flow rate. Choosing the appropriate fabrication process can be also a tricky part of the design and needs additional calibration allow concentration control. Another issue is the onboard instrumentation in these miniaturized devices, which can be a challenging and very expensive task. The design becomes even more complex including a sensing stage in the same chip. There is a long way between design conception and experimental performing, making it not very practical and not fast to performing experiments. Therefore, we proposed to use low-cost and fast prototyping microfluidic chips made on glass and polydimethylsiloxane (PDMS), to perform a binary mixing reaction, with contactless detection on-line and controlling on demand.

We used a capillary tube integrated into a low-loss waveguide cavity and attached in the outlet of microfluidic device. This type of coupling has the advantage of being a non-invasive and contactless technique (SIEGEL, 2004; CROWE, 2005; KUCHUK, 2012), using very low energy molecule excitation (MATVEJEV and STIENS et. al, 2010, 2011, 2012, 2013). In our system we had a low-power THz source with the emitted power below 1mW. In the first experimental setup, measurements with the sub-THz sensor were performed to detect water/ethanol mixtures concentration using standard samples, adding ethanol in a water volume. In the second setup, we introduced a serpentine shape with index mixing known in literature (KAKUTA et al., 2016; LEE, 2011). Syringe pumps were used for generating ethanol concentration and changing the species mass flow rate. After a step of concentration

characterization in micro mixer, we investigated the relationship between the flow rate and the global alcohol absorption, afterwards converted as the flow rate controlled alcohol concentration. We performed some specific ethanol concentrations on demand. The THz sensor has a dynamic range of 2.80 dB for small detection window of a few square millimeters coupled with a capillary tube, using a very small liquid volume of 1.40 µl inside of the microchip.

4.7.1. On-line sub-terahertz liquid sensor and experimental setup

A highly sensitive and extremely accurate integrated sensor configuration for THz absorption measurements in aqueous alcohol solutions was reported previously (MATVEJEV and STIENS, et al. 2011). The sensor configuration used an integrated, low-loss waveguide MATVEJEV and STIENS, et al. 2010) and a commercial capillary tube with an internal diameter of 320 µm. In this study, the sensor design has been adapted to perform measurements at 60 GHz, using a commercial millimeter wave vector Network analyzer (MVNA) machine, with the standard waveguide dimensions of 1.88mm × 3.76mm. In order to maximize the interaction between the THz wave and the injected liquid, the waveguide design is doubly conical, as shown in Fig. 4.33, in order to fit to the outer diameter of capillary tube (450 µm). The capillary tube is then inserted through the narrow wall of the waveguide, penetrating the waveguide perpendicularly to the wave propagation direction. As the THz incident wave penetrates through the capillary tube, part of the energy that it carries will be absorbed by the injected liquid.

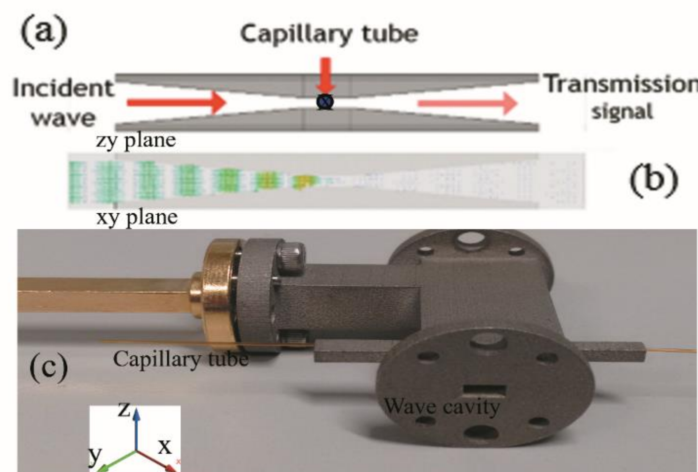

Figure 4.33 - THz sensing scheme. (a) Capillary tube inserted into wave path in ZY plane. (b) Electromagnetic field along the wave-guide in the XY plane. (c) Waveguide to be attached to the MVNA.

The absorption is calculated from the measured transmission signal, following the Beer-Lambert law (MATVEJEV and STIENS et al., 2010), as shown by Eqs. (4.5) - (4.6):

$$T = log_{10}\left(\frac{I}{I_0}\right) \qquad \text{Equation (4.5)}$$

$$I = I_0 e^{-\alpha z} \qquad \text{Equation (4.6)}$$

where $\boldsymbol{T}$ is the measured transmission signal, $\boldsymbol{I}$ is the intensity of the transmitted power, I_0 is the intensity of the incident power, $\boldsymbol{\alpha}$ is the absorption coefficient and z is the equivalent propagation distance inside the capillary tube. By normalizing the THz absorption coefficient of a solution to the THz absorption coefficient of pure water, equivalent propagation distance z can be cancelled from the Eq. 4.6. The permittivity changes lead to changes of the liquid absorption. Which leads to an increase/decrease in the measured transmission signal. The alcohol and water permittivities follow a second order Debye model at this frequency range MATVEJEV and STIENS, et al. 2010; LIU et al., 2010). The serpentine shaped devices were fabricated by wet etching profiles on the glass substrate and sealed with polydimethylsiloxane (PDMS) treated by oxygen plasma, described in chapter 3. Microchannel profiles obtained in glass with average surface roughness measured less than 80 nm, with channel width of 346 µm, depth of 50 µm and length of ~12cm, as shown in Fig. 4.34.

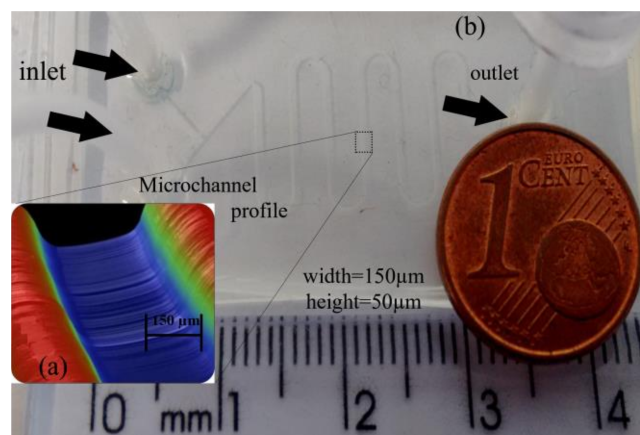

Figure 4.34 - Microchannel and micromixer. (a) 3D image of microchannel profile measured by profilometer. (b) Microfluidic device fabricated in a glass microscope slide and sealed by PDMS.

Chemical reactors in microscale dimensions require different solutions to be produced together and mixed fast, allowing the dynamics of the reactions to be explored, rather than the diffusion dynamics of the molecules (MADOU, 2002; TABELING, 2014). The dimensionless number that helps to understand mixing reactions mechanism is the Peclet and Dean number k, in curved channels, Eq. (4.7) and Eq. (4.8) (MADOU, 2002):

$$Pe = \frac{UL}{D} \qquad \text{Equation (4.7)}$$

$$k = Re\sqrt{\frac{D_h}{2R}} \qquad \text{Equation (4.8)}$$

where, ***U*** is the average velocity, ***L*** is characteristic length of main channel and ***D*** is the diffusion coefficient between species, ***Re*** is Reynolds number, ***Dh*** is hydraulic diameter and ***R*** is the center line radius curvature. The Peclet number is an easy way to discover, which interaction prevails in the mixing reaction, the diffusion or convection between species in a binary mixture: the higher *Pe* number, the more convection dominates over molecular diffusion. The convection results in faster mixing process than diffusion. However, in curved channels, the direction of curvature alternates to create Dean vortices in opposing directions, generating a secondary flow through the channel. This can allow for increasing mass transfer, in our serpentine shaped micromixer on the principles of enhancing secondary flow; the Dean effects can allow for increased species interfacial area, which promotes mixing, for this we decided to use the serpentine shaped geometry, also because it is reported in literature to exhibit high mixing performance with index number of 0.8 (HAMEDI et al., 2016; LEE et al., 2011). It was proved experimentally, by A. J. Sudarsan et al, that with k > 1.7 the enhancing of secondary flow experimentally (COOK at al., 2013; SUDARSAN et al., 2006), as shown in Fig. 4.35.

The Dean flow effect in curved microchannels is presented and described in Fig. 3.35. (A) Idealized Dean flow mediated rotation sequence (*"i"*and *"o"* denote the inner and outer channel walls). At low k (upper part), two parallel streams of different species (yellow and black) entering a curved microchannel segment experience minimal perturbation to the laminar flow. At k~10 (lower part), the transverse flow, generated by the counter rotating Dean vortices in the upper and lower halves of the channel, transports the inner (yellow) stream toward the outer wall while the outer (black) stream is pulled inward, causing the positions of each species

to be transposed. (B, upper) Schematic of the curved microchannel geometry investigated (100 µm wide; 29 µm tall; 630 µm radius of curvature) (COOK at al., 2013; SUDARSAN et al., 2006). The transverse flow field was examined at the entrance to the curved segment and at a location of 1.5 mm downstream. Analytically computed velocity and concentration profiles are shown (Left, lower) beside confocal cross-sectional images of the transverse flow in the microchannel (Right, lower) at flow rates ranging from 2.6< Re <45.1 (0.7 <k<12.1). The boxed area represents conditions under which the transverse flow induces 90° rotations in the upper and lower halves of the channel. (C) Top-view images of aqueous streams labeled with blue and yellow dye in a curved microchannel segment (200m wide; 29m tall; 630m radius of curvature). At k~1.0 (upper) the streams flow in parallel along the entire length, whereas at k~14.2 (lower) the blue stream is transported from the inner to the outer wall (SUDARSAN et al., 2006).

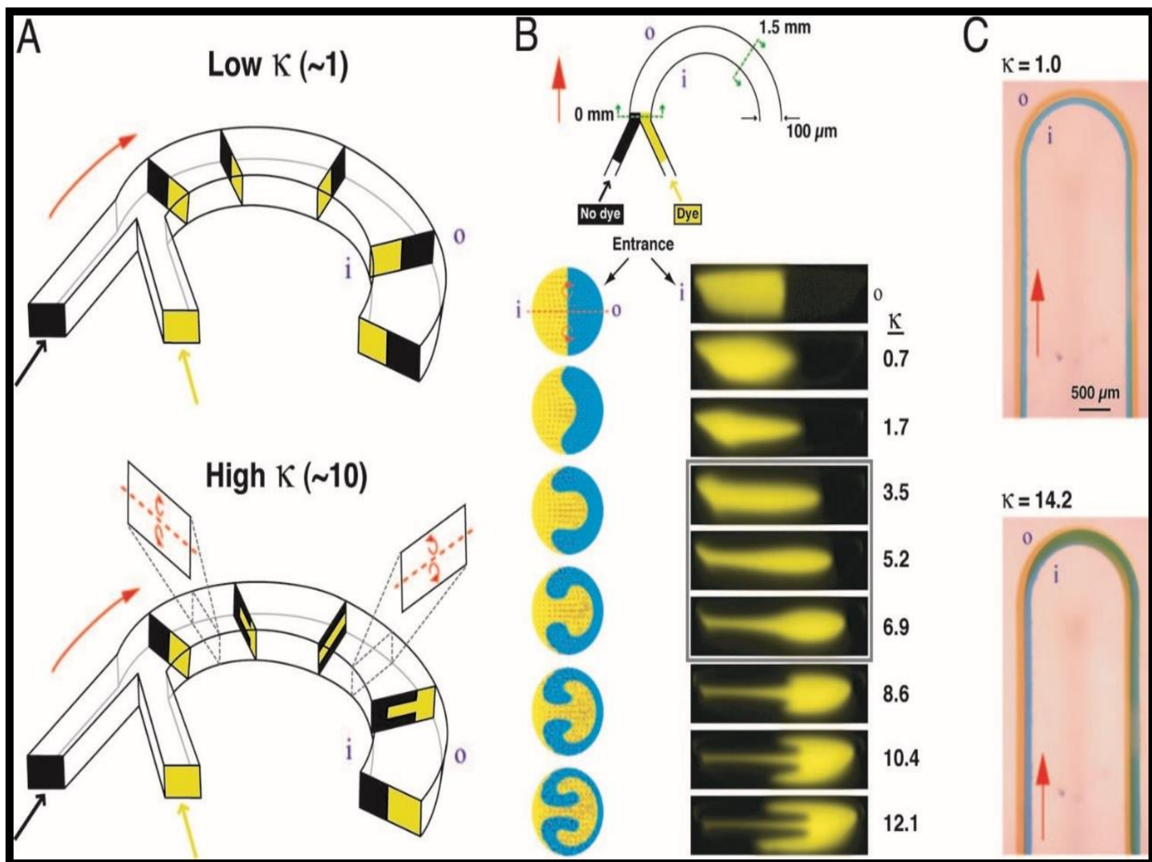

Figure 4.35 – Dean vortices effect and generation of secondary flow. (SUDARSAN et al., 2006).

We performed calculations based on liquid properties of water and ethanol found in literature (KUCHUK et al., 2012), as shown in Table 4.6.

TABLE 4.6. Typical liquid properties at room temperature (20ºC) (ZAKURENOV et al., 1975; STREET et al., 1996).

Liquid	Density ρ (g/cm^3)	Viscosity μ (mPa.s)
Water*	0.978	1.002
Ethanol	0.789	1.200

The values for pure samples (water or ethanol) were used to calculate some parameters for the water-ethanol mixture in flow, such as, Reynolds and Peclet number. Considering constant flow rate equal to 50µl/min of water/ethanol, the diffusion coefficient of water/ethanol at room temperature equal to 1.2 x10^{-5}cm^2/s.

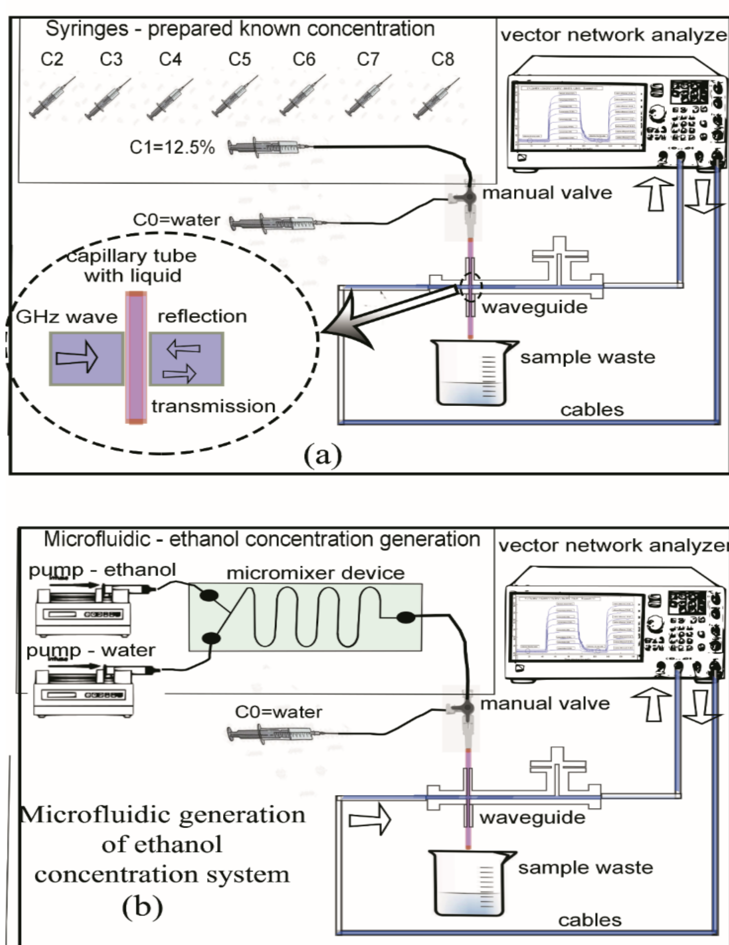

Figure 4.36 - Two configurations of the microfluidic chemical sensing platform: (a) Validation with standard samples solutions of alcohol. (b) Microfluidic configuration: passive micromixer characterization and flow control by syringes pumps.

The whole procedure involved two main configurations: the first one aiming at acquisition of the system response for alcohol concentration, with pre-prepared known concentrations ranging from 0%(v/v) to 100%(v/v). The second configuration was made by adding the micromixer device and syringe pumps as an alcohol concentration generator. In this second setup, the calibration and controlling was made by flow rate ranging. At first, we started with validation procedure using standard samples solutions and plastic syringes with calibrated volume of 3 ml, as shown in Fig. 4.36 (a), followed by the micromixer characterization procedure and controlling of alcohol concentration, as shown in Fig. 4.36 (b). The THz detection part was connected to the Millimeter-wave Vector Network Analyzer or MVNA (*AB Millimeter*, France).

Small volume of standard samples of aqueous ethanol solutions freshly prepared by dilution of the pure ethanol (absolute ethanol, VWR Chemicals) with water were injected by the syringe through the capillary tube. The results of this procedure were used further as a background for characterization of mixtures in the microfluidic chip. For the second configuration, we added a serpentine passive micromixer into the system, and samples of pure water or alcohol were controlled individually, using syringe pumps (SP101IZ, WPI). The experiments were performed at room temperature (approximately 25ºC), monitored via reference temperature sensor, as shown in Fig. 3.37.

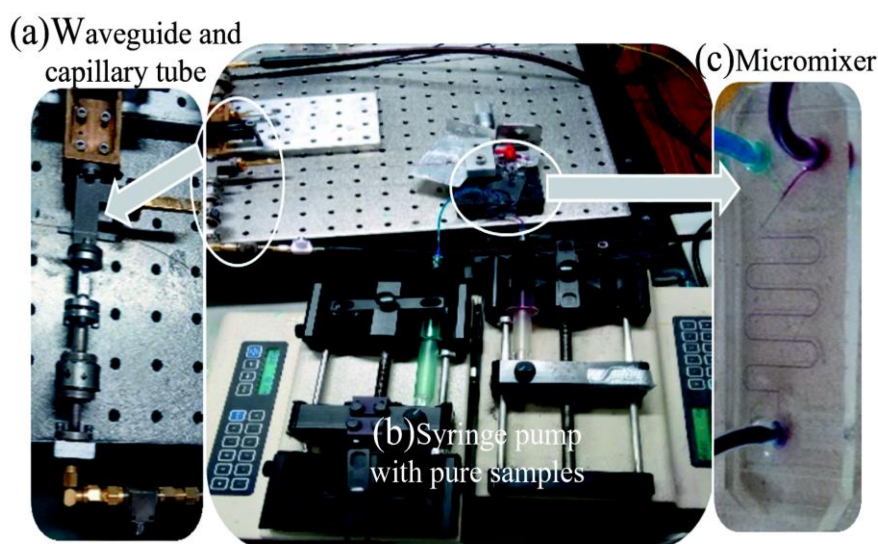

Figure 4.37 - Experimental setup. (a) Capillary tube integrated into a wave-guide. (b) Syringe pumps and mass flow rate controlling. (c) Micromixer with blue dye color (ethanol), red dye color (water) and purple as real liquid mixture along the microchannel.

The signal variation was monitored on-line on the MVNA display and the row data were recorded for subsequent calculations, post-processing and analyzes. The data processing was performed in MATLAB (Mathworks, MA, USA). The setup consists of a serpentine shaped working channel outlet coupled to a waveguide, as shown in Fig. 4.37 (a). The two upstream channels were used for introduction of standard sample solutions of water-ethanol mixtures and water in Falcon tube 50 ml, using vortex mixer and manual shaking. They were freshly prepared by dilution of pure ethanol with water. The mixing enhancement is determined by chaotic convection (PALACIOS et al., 2010; OCOLA et al., 2013). For comparison, we measured both dye colored and pure (not colored) samples. We obtained quite small relative signal changes difference within 0.01 dB, this is the limit of detection of this setup sensor, for the cases of pure water and red dye colored water, pure ethanol and blue dye ethanol. The reproducibility of each measurement point with error bar smaller than 0.07 dB.

4.7.2. Sub-terahertz sensor response, calibration and controlling of ethanol concentration

During the calibration process, the amplitude signal changes have been recorded for 0%, 12.50%, 25%, 37.50%, 50%, 62.50%, 75%, 87.50% and 100% ethanol solutions in volume/volume proportion (v/v). For each concentration point 16 measurements were made in different days and the average values for the system validation were calculated. These measurements were performed to avoid drift caused by MVNA source variation, as shown in Fig. 4.38.

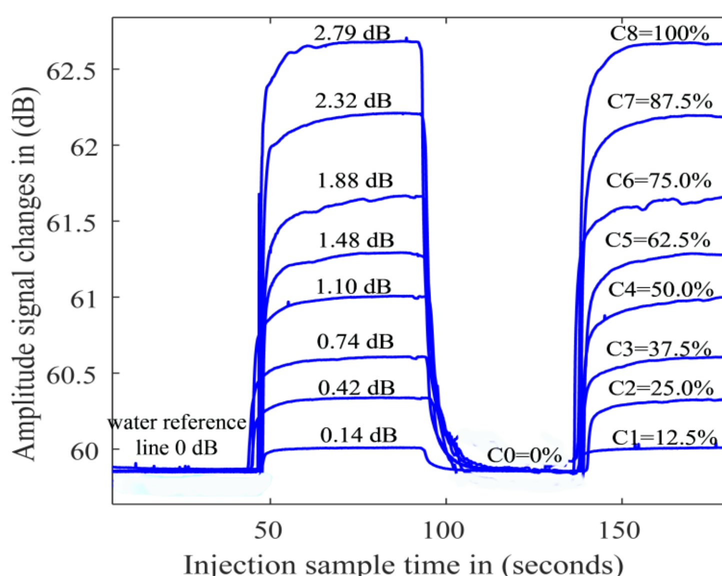

Figure 4.38 - Sub-THz sensor response versus ethanol concentration for known ethanol concentration freshly pre-prepared.

Before every new measurement, we injected water for purging the liquid via, including microchannel and capillary tube. We always took the relative signal changes referred to the water signal. In this case, the cleaning procedure was used to reduce small variations caused by residual liquid samples in the microchannels and capillary tube. In this procedure, all samples were manually injected alternately using the same injection time, as shown in Fig. 4.39.

Monitoring the amplitude signal changes in decibels (dB), we established the relationship between the signal changes and the ethanol concentration, as shown in Fig. 4.38. Applying the fit data equation for raw data, using the least square regression and residual, we obtained Eq. (4.8):

$$Y = 2.2\, e^{-8} X^4 - 5.3 e^{-6} X^3 + 5.2 e^{-4} X^2 + 6.6\, e^{-3} X - 2.8 e^{-3} \qquad \text{Equation (4.8)}$$

where, Y is the signal change in (dB) and X is the concentration of the ethanol in % (v/v).

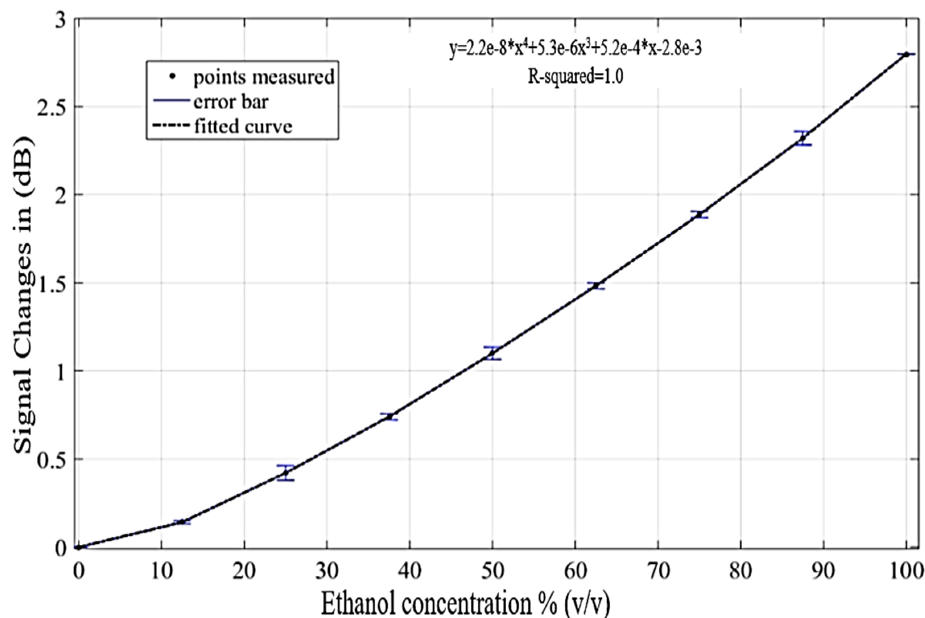

Figure 4.39 - Fitted curve of raw data, THz sensor response for known ethanol concentration.

The typical regression coefficient is close to 1.0 and the highest residual was found to be smaller than 0.01dB. With Eq. (4.8), we can determine the ethanol concentration of unknown sample with good accuracy and precision with sensitivity between 0 to 2.79 dB, taking into

account the non-linearity aspect in water-ethanol mixtures, as previously reported by V. Matvejev et al. (2010-2013).

In this second approach, the serpentine shaped passive mixer was added in the system. The detection was made by capillary tube coupled in the micromixer outlet. Pure samples of water and ethanol were injected and controlled individually by two syringe pumps. First in this procedure, we fixed the mass flow rate of water in 50 µl/min to simplify the possible flow rate ranging combinations, and sweeping the ethanol mass flow rate, from 7.5 to 125 µl/min to characterize the mixture concentration. In parallel, we established the relation between ethanol concentration and mass flow rate, as shown in Table (4.7). For the recorded points at the alcohol mass flow rate with 7.5 µl/min, 25 µl/min, 50 µl/min, 75 µl/min, 100 µl/min and 125 µl/min, in every new measurement we waited for stabilization during 10 minutes. We observed that for the ethanol flow rate less than 7.5 µl/min, the concentration was 0%(v/v) of ethanol concentration, and for the flow rate larger than 125 µl/min, the concentration detected was 100%(v/v) of ethanol is presented in Fig. 4.40.

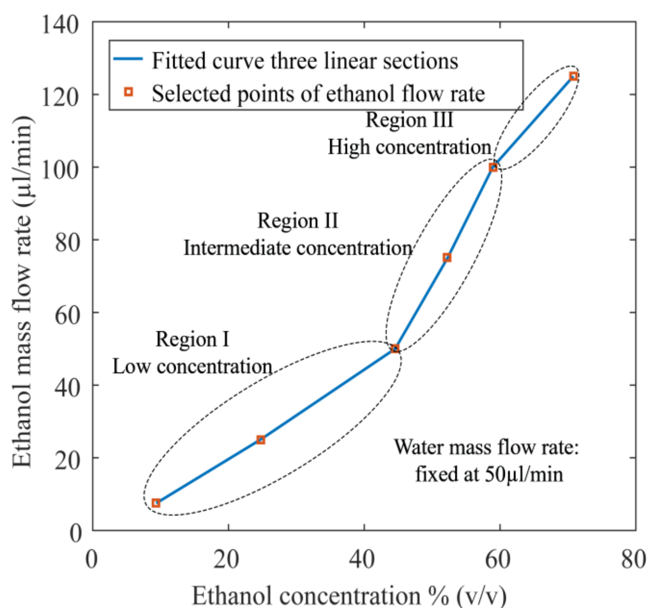

Figure 4.40 - Experimental correlation between ethanol mass flow rate in ethanol concentration.

We observed that the ratio flow rate for ethanol control is limited ranging from 0.15 to 2.5. In others words, when the ethanol flow rate is 2.5 times bigger than the water flow rate, the ethanol prevails in the flow inside the microchannel. The opposite happens when the ethanol flow rate is 0.15 times smaller than water flow rate; it leads to the water signal prevailing, and

the sensor just detected water in the outlet of micromixer. This microfluidic system generates binary liquid mixture, mixing two miscible liquid phases, the first being pure ethanol solution and the second pure water. In binary mixtures characterization, the factors determining the mixing time of both liquids are fundamental. We achieved laminar flow in our device, with small Reynolds numbers, in the range $5.34 < Re < 16.26$. The behavior of alcohol concentration was strongly affected by the mass flow rate variation and three well-defined regions can be distinguished: for low concentration, intermediate and high concentration, as shown by Fig. 4.40. We compared the ideal concentration expected from second theoretical model based on liquids volume ratio without taking into account some geometric asymmetries and non-linearities involved in water-ethanol mixture, such exothermic process reported and volume loss (KUCHUK et al., 2012; LEE, 2011; KAKUTA et al., 2011, 2016; MATVEJEV, STIENS et al., 2011).

TABLE 4.7 The Characterization of water-alcohol mixtures into a microfluidic device and joint section, based on mass flow rate sweeping. Expected alcohol concentration versus real concentration measured, the alcohol absorption measured was translated in sample concentration.

Ethanol volumetric flow rate (µl/min)	**Volumetric flow rate ratio (Q_{etha}/Q_{H2O})**	**Analytical ethanol concentration based on volumetric flow rate ratio % (v/v)**	**Real ethanol concentration measured % (v/v)**	**Reynolds number***	**Peclet number in joint section***	**Dean number***
<7.5	None	<13.04	0.000	Water	None	None
7.5	0.15	13.04	9.35	5.34	3177	4.56
25	0.50	33.33	24.71	6.97	4144	5.94
50	1.00	50.00	44.55	9.29	5526	7.93
75	1.50	60.00	52.27	11.62	6908	9.91
100	2.00	66.67	58.94	13.94	8289	11.89
125	2.50	71.43	70.80	16.26	9671	13.88
>125	None	>71.43	100.0	Ethanol	None	None

*Calculations were made based on water physical properties.

The process mixing reaction mechanism was predominantly governed by convection following the dimensionless numbers with high Peclet number, $25700 < Pe < 78220$. These elevated values suggest that the diffusion forces are acting much slower than the hydrodynamic transport phenomena. The Dean number calculated range is $4.56 < k < 13.88$ in the curved micromixer. In some particular flows, the secondary flow is enhanced and took into account in mixing. The Dean number indicates that mixing is also affected by enhancement secondary flow in range of $k > 1.7$ as reported by Cook *et al.* (2013) and Sudarsan *et al.* (2006). In our experimental setup, there is another issue to consider in global mixing effect: the joint section that connects micromixer to mm-wave sensor via capillary tube attached in outlet, with length of 50 cm, this also affects the total fluid sample path, before the effective measurement happens. Because of this and for comparison reasons we took into account the *Pe* in a capillary tube (Pe_2), $3177 < Pe < 9671$, Pe_2 is 8 times smaller than *Pe* in the microchip. It means that geometric aspects of the micromixer and joint section are more important for the mixing. As well, repeating C-shaped units, six times, it can turn the fluid through 180° to induce chaotic advection and passively enhance the mixing of the streams (HAMEDI et al. 2016, LEE, 2011).

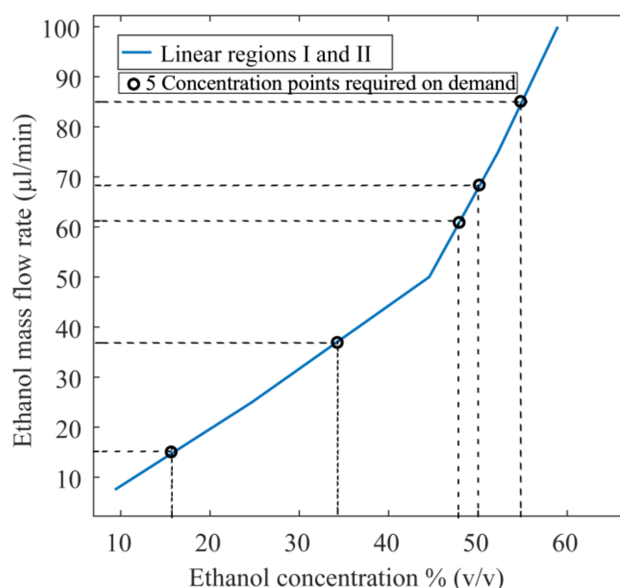

Figure 4.41 - Experimental calibration of linear control, in micromixer device ethanol concentration, with five required concentration points on demand, for each selected concentration point there is a specific experimental mass flow rate, in this particular, to reach desired concentration.

For calibration, we started with equal water and ethanol flow rate (Qa = Qb). In this case, both liquids are flowing in equalized way, which ideally leads to the same occupied

volume inside the channel. For example, assuming a flow rate of 50 µl/min for liquids, the expected ethanol concentration is 50 % (v/v), however in our system, we achieved an ethanol concentration of 44.55 % (v/v). The response variation is 4.55%, where part of this variation comes from the line width variance caused by chosen microfabrication process. In fact, for controlling the alcohol concentration on-line one needs an additional calibration step, afterwards to be able to control precisely the ethanol concentration on demand.

The calibration system is based on experimental results as shown in Fig. 4.41. We observed three well-defined regions and selected two of them, regions I and II, and applied the linear fit for each region separately, as shown in Fig. 4.41.

Based on these regions in Fig. 4.41, we took into account two fit equations for regions I and II, which are the fit data, presented by Eqs. (4.7) and (4.8), respectively. Finally, we have applied the described calibration for determination of the ethanol concentration in five required points on demand. The results reported in Table 4.8 were obtained by using pure samples of alcohol and water, controlling the liquid mixture concentration, fixing water mass flow rate in 50 µl/min and setting five different mass flow rate for alcohol, calculated by Eqs. (4.9) - (4.10):

$$Q_{low} = 1.21C_{low} - 4.206 \qquad \text{Equation (4.9)}$$

where Q_{low} is the flow rate concentration for the low concentrations region (region I, shown in Fig. 4.57 and C_{low} is the low concentrations range between 9.35% to 44.55%. The R-square 0.9992 for fit data equation, as shown in Eq. (4.9), for reducing approximation error into the calculation.

$$Q_{int} = 3.468C_{int} - 105.1 \qquad \text{Equation (4.10)}$$

where Q_{int} is the flow rate concentration for the intermediate concentrations between regions I and II, shown in Fig. 4.57, C_{int} is the intermediate concentrations range between 44.55% to 58.94%. The R-square is 0.9982 for the data fit, shown in Eq. (4.10).

Once calculated and discovered the flow rate effect in the ethanol concentration, we choose five random concentrations spots as a proof of concept, with two points at low concentration and three points at intermediate concentration, as shown in Table 4.8.

TABLE 4.8. Calculated flow rate for required concentration on demand. Comparison between ethanol concentrations controlled on demand and measured.

Required concentration on demand % (v/v)	**Calibrated volumetric flow rate (µl/min)**	**Real measured concentration %(v/v)**	**Required and measured concentration difference %(v/v)**	**Percentage Difference (%)**
C1 = 17.00	16.36	16.72	-0.28	-1.65
C2 = 34.00	36.93	34.23	0.23	0.67
C3 = 48.00	61.36	47.68	-0.32	-0.67
C4 = 50.00	68.30	50.19	0.19	0.38
C5 = 55.00	85.64	54.68	-0.32	-0.58

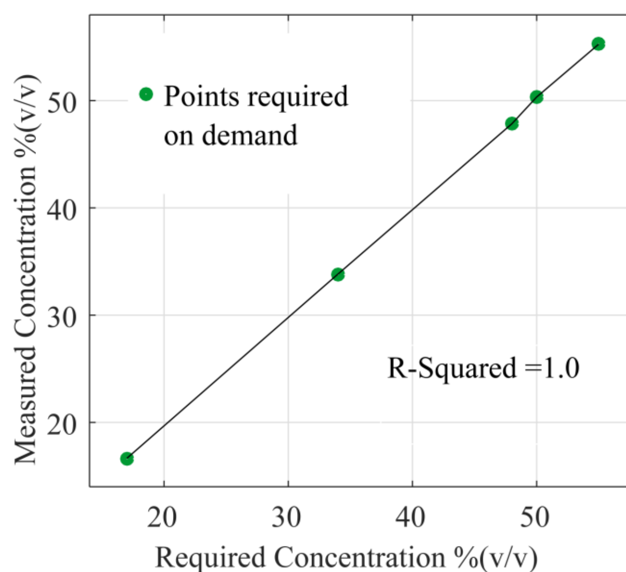

Figure 4.42 - Comparison between points of required ethanol concentration on demand versus real concentration measured.

All measurements were recorded for comparison between demanded and measured concentrations. To calculate the precision of the system for generating and controlling ethanol concentration, we plotted the expected concentration versus measured, as shown in Fig. 4.42. As a result, we fitted this curve with R-squared 1.0, showing how precise and accurate is the proposed method. We presented a full platform, with capability of mixing two liquids and control their final concentration precisely on demand.

5 CONCLUSIONS AND FUTURE WORK

5.1. Conclusions

In conclusion, we fabricated several new Lab-On-a-Chip devices using microfabrication techniques and developing new microfabrication protocols in substrates: silicon, glass and PDMS. The microfabrication stages were divided into three main steps: the application of the optimized etching processes to obtain the microchannels, the microchannel sealing and insertion of micro tubes. The process of etching of the silicon in *KOH* allows the fabrication of channels with widths of 50µm to 100µm obtaining depths of up to 25µm to 50µm, respectively, without formation of 'V-Groove' in the microchannels, maintaining an anisotropic profile surface with good uniformity (low random roughness) and residue-free. The best results were obtained for the *KOH* solution at a temperature of 80ºC, with the concentration of 42% KOH, with the use of magnetic and motor agitation, with the silicon foil inserted in a motor-driven substrate holder, maintaining a rate of almost constant etching of 1µm/minute with good agreement with (CYRO, 2004 and PAL, 2017), with the average roughness up to 40 nanometers, thus do not generate undesirable secondary flow induced by the roughness effect.

The process of wet etching with HF solutions allowed to obtain microchannels with depths up to 100 µm, but in this work, it was limited to channels depths of 30 µm to 60 µm, with good agreement results with (SCHIANTI, 2008; COLTRO, 2008). As indicated by the simulated models, the microchannels forms were obtained with an isotropic profile surface, with good uniformity and free of residues, generated in etching. The most prominent results were obtained with sequential etching in the BOE solution, HF + H_2O solution (1:1) and 38% HCl solution. Each step was performed at room temperature using magnetic stirring and rinsing in DI water at the end of the processes. The average etching rate for the Perfecta substrates was approximately 9 µm/minute not remaining constant throughout the process, with a mean roughness of 132 nm to 471 nm. The microchannel systems obtained on PDMS substrate, with SU-8 molds in quartz and silicon substrates, make it possible to obtain microchannels with fixed depths, in the case of this work 63 µm. This is limited to the manufacturer's specification, referring to the photoresist family SU-8, having superior reproducibility compared to the processes applied in silicon and glass. SU-8 enabled replication of devices quickly and effectively, while the interconnection step can be inserted into the curing of the PDMS.

We made several comparisons between the theoretical, simulated and experimental models. The full protocol of microfabrication processes is promising for applications of

microfluidic systems in a variety of areas in particular for pressure sensor membranes in silicon, due to the high reproducibility of processes, low cost, production time and compatibility of processes and materials with other stages of microfabrication.

The microchannels sealing was done by direct and irreversible sealing of the PDMS, applied at room temperature on silicon, glass and PDMS substrates. After treatment of the substrate and PDMS contact surfaces, the best results were obtained with values greater than 95% of the welded surface area, reaching in most cases 100%, after applying manual pressures uniformly. Same result as achieved in (SCHIANTI, 2008). Thus allows for the fabrication of encapsulated structures without leakage. Critical points that are considered for good sealing: cleaning of contact surfaces, flatness of substrates, quality and time of oxygen plasma in the surfaces treatment, and the use of pressure at suitable points. These are fundamental for good process reproducibility without leaks.

The method applied for interconnection was the direct bonding of the silicone tubes to the PDMS, during curing process of the PDMS itself, thus reducing a microfabrication step. A system of manual alignment of the tubes with the inlet and outlet reservoirs of the devices was developed. Acrylic replicas of the devices containing only holes at the points of the reservoirs were developed, since this was a manual alignment. Diameters of 3 mm were adopted for a greater margin in the processes of alignment and fixation of silicone tubes. The positioning system made the alignment of the tubes with the reservoirs possible, with a good quality, making interconnection processes reproducible. Points to consider from this step are: the diameter of the reservoirs, the cleaning of the tubes, the cleaning of the positioners, the correct alignment and fixing of the tubes and extraction of the metal guides.

The modeling of the constructed microfluidic systems presented a flow with typically laminar behavior, with low Reynolds number values, from 0.8 to 3, calculated from the fabricated dimensions and the conditions applied in the laboratory experiments, as well as the results of numbers of Reynolds obtained in the software, were in the range of 0.01 to 0.10. Both in the theoretical and in the simulation, the input variables were the microchannel dimensions, viscosity and liquid flow. The calculated liquid velocities were between 8.4 mm/s to 110 mm/s, and in the simulation from 3 mm/s to 80 mm/s, the mean pressures inside the microchannels were calculated and were in the range of 82 Pa up to 1.0 kPa, in the simulated model the values were between 120 Pa to 2 kPa. Different dyes food colors diluted in water, with high contrast were used as path tracers and for diffusivity lines enhancement observation. Using optical

microscope to inspect, it was possible to observe some regions of mixing, regions generated in the liquid-liquid interfaces and enhancement of liquid diffusivity along the microchannels. These changes are directly related to volumetric flow rate, viscosity, geometry and pressure. Considering the geometries of the devices, in the geometry of the curve H and Spiral obtained a greater mixture than in the Y, T and Cross curves, all of them being submitted to the same type of regime, that is, the laminar regime. In the case of Spiral, it is possible to observe a greater mixture of liquids due to its geometry that imposes changes of the axial velocity along the path, since the liquid is being modeled as a particle in the laminar regime, thus promoting a greater degree of mixing between the liquids. The cross-curve showed to be very promising in the application of cell targeting, involving its cytometry, since the control of the width of the liquid in the central part depends, in this specific case, only on the applied flows.

Further, we presented novel design of an active magnetic mixer and experimental results that show that the magnetic action is able to accelerate the mixing of liquids by inserting inertial forces, consequently raising the number of Reynolds, in the initially laminar regime of the fluids to be mixed. The mass diffusivity line had its thickness significantly increased to a frequency of 7Hz, as a consequence of the acceleration of the mixing process. Another phenomenon observed was the release of bubbles from the reservoir with the increase of the frequency of actuation. Bubbles may adversely affect the performance of microfluidic devices and various efforts have been devoted to the removal of bubbles from microfluidic systems (LOCHOVSKY et al., 2012). Also, controlling two key parameters to generate the hydrodynamic instability: the intensity of the force generated and the frequency of actuation, the mixing speed can be adjusted to the values desired by the user. A proposal for a fully integrated electromagnetic actuator has been developed, which can be used as a valve, an active mixer or pump fluids in microchannels. The actuator has high compatibility with microfluidic systems based on PDMS and can be alternative to the actuators presented today in the literature such as solenoids, thermal actuator, manual actuator and pneumatic actuators (ZOLFAGHARIAN et al., 2016; KABLE et al., 2016). The manufacture of prototypes allowed the characterization of the actuators in applications enhanced liquid mixtures in microchannels up to 90%.

We used the Ψ-shaped microchannel in a multiphase microfluidic system to produce controlled droplets of aqueous colorant in mineral oil carrying liquid that were detected by a capacitive sensor formed by RSE. Through video synchronization, the real time data obtained from the sensor were validated. Results showed a consistent capacitance variation in accordance with the fluid passing over the sensor. Real time capacitive measurements can be used in

microfluidics devices to control valves and pumps to achieve desired droplet size in biphasic mixtures. This method should find several practical applications including drug delivery and food encapsulation. Furthermore, in dripping regime, the droplet velocity and volume can be estimated using the proposed RSE sensor. RSE micro sensor takes advantage of a better capacitance per area ratio, improving the detector sensitivity and reliability. Where, the capacitance due to the permittivity of the fluid varies in the range of 30 femtoFarad, the ring-shaped electrodes are more suitable for applications requiring substances selective to the target analyte.

We also have presented a method for convenient determination of on-line ethanol concentration. Using THz sensor coupled into a microfluidic platform, for linear generation and controlling of binary mixtures concentration in two specific ranges regions at low concentrations from 10 to 44 % (v/v) and intermediate concentration from 45 to 71 % (v/v) which a precision of 0.32 %(v/v). Using mixing reaction mechanism predominantly controlled by convection, with the Pe number bigger than 25700 in the micromixer, following the Pe number in joint section, that is bigger than 2383 and Reynolds number between 5 and 16. As demonstrated for water - alcohol mixtures, with mass flow rate of alcohol ranging between 7.5 µl/min and 125 µl/min, changing the Dean number between 1.2 and 8.6 that causes secondary flow enhancement in $k>1.736$ as known improving the mixing. On-line THz measurements can be used in microfluidics devices for on-line monitoring mixtures concentration with high reproducibility and reliability. Results showed a good agreement between the concentration generated and obtained, with small variation of 0.32% between alcohol concentrations required on demand and measured, for 1.40 µl total volume sample in the micromixer and residence time between 0.48 and 1.46 seconds. As an advantage over other sensing methods, this THz sensor can be easily attached to the microfluidic platform, through simple mechanical coupling of a glass capillary tube to the outlet microchannel. Due to its flexibility, this system can be used in a beverage and chemistry industry, to perform measurements and on line control, with very small samples down to 150nL. Future perspectives are related to creation of a full platform for liquid THz spectroscopy in real time, sensing and following the chemicals reaction in loco along the microchannel. With mm-wave sensor with wide dynamic range and attached in substrate of the main channel work, it should allow us to evaluate the mixing performance on line.

5.2. Final considerations and Future works

The results described in this research are quite motivating for the continuation of future work, since they allow the visualization of a series of possibilities of future works, which will be based on the simulated models and the microfluidic systems that were manufactured in this research. It is known that it is of great technological interest to make operations and control of fluids, allowing the passage of liquids or not, controlling in this way the entry and exit of different liquids by different microchannels for different inputs or outputs. Each new feature added in the systems needs fabrication procedure modification, it is necessary to insert new microfabrication techniques, to build these more complex Microfluidic platforms, approaching each time the so-called Lab-On-a-Chip, laboratories in Chip literally. The computational modeling using COMSOL allows a good starting point in the preparation of new systems, and the insertion of new areas, such as Biological, Chemistry, Optofluidics, Magneto fluidics, Electro kinetics, Condutometric Detection Capacitively coupled (C_4D). The starting parameters obtained in the simulated and theoretical models that directly involve the microfabrication are: geometric format, aspect ratio, materials for microfabrication and applied area.

Based on the obtained results, we list below several areas where novel microfluidic devices can be developed for applications in LOC.

The possibility of insertion of a measurement system, such as well-known ion-sensitive sensors (ISFET) in silicon microchannels on the same substrate, can be considered to analyze interaction reactions in microchannels. The possibility to integrate in the same chip a terahertz wave-guide and microfluidic channel which was realized successfully in the present work, could benefit to achieve high precision and real time measurements for Lab-On-a-Chip applications. The insertion of resistors for temperature control in some chemical reactions, microelectronic pressure sensor of microfluidic systems, can be beneficial for studies and control of pressures along microchannels. Other possibilities include capacitively coupled conduction detection - C_4D, insertion of interdigitated electrodes for capacitive detection, electrodes to control electroosmotic fluxes, insertion of micro pillars and micro orifices for the generation of turbulent micro vortices in migration processes; optical detection with the insertion of optical fibers in specific sections along the microchannels, deposition of thin films for water treatment and elimination of microorganisms. Application of new geometries using the results obtained in this work, combining the different geometries, aiming at the optimization of processes in micro mixtures with subsequent chemical analysis. Magnetic coupling with the

external magnets or coils projected on the same substrate of the microchannels, for the detachment of magnetic particles inside the microchannel, as well as other possibilities of new experiments can be also foreseen.

6 LIST OF PUBLICATIONS

6.1. Peer-reviewed journal

S. M. da Silva Junior, J. Stiens, J. W. Swart, S. Moshkalev, Y. Zhang, V. Matvejev, C. De Tandt. Sub-Terahertz sensor in microfluidic devices for on-line determination and control of ethanol concentration. Journal of Vacuum Science & Technology B, Nanotechnology and Microelectronics: Materials, Processing, Measurement, and Phenomena (JVST-B 2017). Published on JVSTB web site: http://avs.scitation.org/doi/10.1116/1.4991891. JVST-B Vol 35 Issue 6 (2017) DOI /10.1116/1.4991891. (Journal publication).

S. M. da Silva Junior, J. Stiens, J. W. Swart, S. Moshkalev, Y. Zhang, V. Matvejev, C. De Tandt. Microfluidic devices on glass for liquid mixtures concentration with coupled Thz sensor. Journal of Integrated Circuits and Systems (JICS 2018). Published on JICS web site: http://ojs.fei.edu.br/ojs/index.php/JICS/article/view/10. JICS Vol 13 No 2 (2018) DOI: https://doi.org/10.29292/jics.v13i2.10. (Journal publication).

6.2. Peer-reviewed conferences

S. M. da Silva Junior, M. H. O. Piazzeta, S. Moshkalev, J. W. Swart. Microfluidic devices applied to liquid mixtures. Proceedings book pages 74 and 75. LNLS, Campinas, Brazil. July 24th - July 25th. IV Workshop em Microfluídica 2014. (Poster presentation).

S. M., da Silva Junior, M. H. O. Piazzeta, S. Moshkalev, J. W. Swart. Microfluidic devices with Hydrodynamics and Mixture applications. Proceedings book pages 36 and 37. LNLS, Campinas, Brazil. July 23th - July 24th, 2015. V Workshop em Microfluídica 2015. (Poster presentation).

S. M. da Silva Junior, J. Stiens, J. W. Swart, S. Moshkalev, Y. Zhang, V. Matvejev, C. De Tandt. THz sensor in microfluidic devices for on line determination and control of ethanol concentration. Presentation number 7C-4 on 61st International Conference on Electron, Ion, and Photon Beam Technology and Nanofabrication. Coronado Springs, Orlando, United States. May 30 - June 2, 2017. 61st EIPBN 2017. (Oral presentation).

S. M. da Silva Junior, L.E. Bento Ribeiro, J. W. Swart, S. Moshkalev, J. Stiens, F. Fruett, A. Flacker. Fabrication and Evaluation of an Active Electromagnetic Mixer for Lab-on-a-Chip Applications. Presentation number P12-02 on 61st International Conference on Electron, Ion, and Photon Beam Technology and Nanofabrication. Coronado Springs, Orlando, United States. May 30 - June 2, 2017. 61st EIPBN 2017. (Poster presentation).

S. M. da Silva Junior, J. Stiens, S. Moshkalev, J. W. Swart, A. Flacker, Y. Zhang, V. Matvejev, W. Vandermeiren, C. De Tandt. Microfluidic Devices and Gigahertz Sensor Applied to measurements of Liquid Mixtures Concentration. USP, São Paulo, Brazil. July 31 - August 2, 2017. VII Workshop Microfluídica 2017. (Oral presentation).

S. M. da Silva Junior, J. Stiens, J. W. Swart, S. Moshkalev, Y. Zhang, V. Matvejev, W. Vandermeiren, C. De Tandt. Microfluidic devices and Gigahertz sensor applied to measurements of liquid mixtures concentration. Proceedings published on Institute of Electrical and Electronics Engineers and Institution of Engineering and Technology (IEEE), available on IEEE Xplore digital library: http://ieeexplore.ieee.org/document/8112978/, 32nd Symposium on Microelectronics Technology and Devices. Fortaleza, Ceará, Brazil. August 28 - September 1, 2017. SBMicro Chip on the sands 2017. (Oral presentation).

S. M. da Silva Junior, J. Stiens, J. W. Swart. Microfluidic devices and Gigahertz sensor applied to measurements of liquid mixtures concentration. Abstract published on book proceedings ISBN: 9781728122175, page 65. Presented on 1st Latin American Electron Devices Conference. Armenia, Colombia. February 24 - February 27, 2019. LAEDC 2019. (Oral presentation).

6.3. Conferences

S. M., da Silva Junior, S. Moshkalev, J. W. Swart, D. de Lara. Microfluidics process fabrication. UNICAMP, Campinas, Brazil. December 11th, 2013. SISNANO WORKSHOP 2013. (Poster presentation).

S. M. da Silva Junior, S. Moshkalev, J. W. Swart, A. Flacker. Microfluidic devices on glass, silicon and polydimethylsiloxane with Micro pillars applying to Micromixers.

UNICAMP, Campinas, Brazil. April 14th - 15th, 2016. XI Workshop on Semiconductors and Micro & Nano Technology 2016. (Poster presentation).

S. M. da Silva Junior, J. Stiens, J. W. Swart, S. Moshkalev, Y. Zhang, V. Matvejev, C. De Tandt. “Coupling of a sub-THz liquid sensor for online microfluidic sensing”. Royal Military Academy, Brussels, Belgium. February 16th, 2017. URSI Benelux Forum 2017. (Poster presentation).

7 REFERENCES

ABGRALL, P. and GUE, A. M., 2007. Lab-on-chip technologies: making a microfluidic network and coupling it into a complete microsystem—a review. Journal of micromechanics and micro engineering, 17(5), p. R15.

AKBARI, M., SINTON, D., & BAHRAMI, M. (2009). Pressure drop in rectangular microchannels as compared with theory based on arbitrary cross section. Journal of Fluids Engineering, 131(4), 041202.

AUGUSTIN, M. A., & HEMAR, Y. (2009). Nano-and micro-structured assemblies for encapsulation of food ingredients. Chemical society reviews, 38(4), 902-912.

ATENCIA, J., and BEEBE, D.J., 2004. Controlled microfluidic interfaces. *Nature, 437*(7059), p.648.

BAHRAMI, M., M. MICHAEL YOVANOVICH, and J. RICHARD CULHAM. "A novel solution for pressure drop in singly connected microchannels of arbitrary cross-section." International Journal of Heat and Mass Transfer 50.13-14 (2007): 2492-2502.

BARBAROTO, P. R., FERREIRA, L. O., and DOI, I., "Micromachined scanner actuated by electromagnetic induction."*Optomechatronic Systems III*. Vol. 4902. International Society for Optics and Photonics, 2002.

BASSOUS, E., Fabrication of novel three-dimensional microstructures by the anisotropic etching of (100) and (110) silicon. IEEE Trans. Electron Devices, ED-25 (1978) 1178-1185.

BATCHELOR, G. K. An introduction to fluid dynamics. USA: Cambrige University Press, (Reprinted 2002).

BEAN, K. E., Anisotropic etching of silicon. IEEE Trans. Electron Devices, ED-25 (1978) 1185-1193.

BESSELER, E., "Construção e caracterização de um reator indutivo: ICP para corrosão de materiais." (2008).

BILENBERG, B. NIELSEN, T., CLAUSEN, B., KRISTENSEN, A. PMMA to SU-8 bonding for polymer based lab-on-a-chip systems with integrated optics. Journal of Micromechanics and Microengineering. Vol. 14, 814-818, 2004.

BOGOJEVIC, D., CHAMBERLAIN, M. D., BARBULOVIC-Nad, I. and WHEELER, A. R., 2012. A digital microfluidic method for multiplexed cell-based apoptosis assays. Lab on a Chip, 12(3), pp.627-634.

BRUUS, H. Theoretical Microfluidics, N.Y: Oxford University Press, (2008).

BSOUL, A., PAN, S., CRETU, E., STOEBER, B. and WALUS, K., 2016. Design, microfabrication, and characterization of a moulded PDMS/SU-8 inkjet dispenser for a Lab-on-a-Printer platform technology with disposable microfluidic chip. Lab on a Chip, 16(17), pp.3351-3361.

CAMPO, A. D. and C. GREINER, SU-8: a photoresist for high-aspect-ratio and 3D submicron lithography. Journal of Micromechanics and Microengineering, 2007. 17(6): p. R81.

CHEN, Y.; PÉPIN, A.; Electrophoresis 2002, 22, 187.

CHIA, B. T., HSIN-HUNG L., and YAO-JOE Y., "A novel thermo-pneumatic peristaltic micropump with low temperature elevation on working fluid. "*Sensors and Actuators A: Physical* 165.1 (2011): 86-93.

COLLINS, S.D., Etch stop techniques for micromachining, J. Electrochem. Soc., 144 (1997) 2242.

COLTRO, W. K. T., da SILVA, J.A.F. and CARRILHO, E., 2008. Fabrication and integration of planar electrodes for contactless conductivity detection on polyester-toner electrophoresis microchips. Electrophoresis, 29(11), pp.2260-2265.

COMSOL USERS MANUAL. "Comsol Multiphysics Users Guide." (2011).

COOK, K. J. et al. “Mixing Evaluation of a Passive Scaled-Up Serpentine Micromixer With Slanted Groover”, J. Flui. Eng.-T. Asme. 135, 081102-1 (2013).

CROWE, T. et al., “Opening the terahertz window with integrated diode circuits,” IEEE J. Solid-State Circuits **40**, 2104-2110 (2005).

CUSSLER, E. L., "Diffusion. Mass Transfer in Fluid Systems", 2nd edition, Cambridge University Press, 1997.

CUTKOSKY, M.R. PDMS Process Notes. 2008. [08-12-2018]; Available from: http://bdml.stanford.edu/twiki/bin/view/Rise/PDMSProceSS.html

DÉVELOPPMENT, Y., 2015. Microfluidic applications in the pharmaceutical, life sciences, in-vitro diagnostic, and medical device markets.

DITTRICH, P. S. and MANZ, A., 2006. Lab-on-a-Chip: microfluidics in drug discovery. *Nature Reviews Drug Discovery, 5*(3), p.210.

DONOVAN, K. J., 2014. Computational Fluid Dynamics Modeling of Two-Dimensional and Three-Dimensional Segmented Flow in Microfluidic Chips.

DUFFY, D. C., McDONALD, J.C., SCHUELLER, O.J. and WHITESIDES, G.M., 1998. Rapid prototyping of microfluidic systems in poly (dimethylsiloxane). Analytical chemistry, 70(23), pp.4974-4984.

ELBUKEN, C. et al., "Detection of microdroplet size and speed using capacitive sensors."*Sensors and Actuators A: Physical* 171.2 (2011): 55-62

ELWENSPOEK, M. and JANSEN, H., Silicon Micromachining, Cambridge University Press, Cambridge - UK (1998) 30.

FALKOVICH, G., “Fluid Mechanics.” Cambridge University Press (2011).

FOX, R. W., MACDONALD, A. T. PRITCHARD, P. J. Introdução à mecânica dos fluidos. SP: Editora LTC. ed.7, (2010).

GABRIEL, M., JOHNSON, B., SUSS, R., REICHE, M., EICHLER, M. Wafer direct bonding with ambient pressure plasma activation. Microsystem Technologies. Vol. 12, n.5, 397- 400, 2006.

GAD-EL-HAK, M. The Fluid Mechanics of Micro devices—The Freeman Scholar Lecture. ASME-AMER SOC MECHANICAL ENG: New York, v.121, p. 5-33, mar 1999.

GAD-EL-HAK, M. et al., ed. The MEMS handbook. Vol. 2. Florida: CRC/Taylor & Francis, 2006.

GAIDUK, A. P., and GALLI, G., "Local and global effects of dissolved sodium chloride on the structure of water." The Journal of Physical Chemistry Letters 8.7 (2017): 1496-1502.

GAJDA, M. A., AHMED, H., SHAWAND, J. E. A., PUTNIS, A., Anisotropic etching of silicon in hydrazine, Sensors and Actuators A, 40 (1994) 227.

GOU, Y., JIA, Y., WANG, P. and SUN, C., 2018. Progress of Inertial Microfluidics in Principle and Application. Sensors, 18(6), p.1762.

GRAVESEN, P. Microfluidics: a review. Journal of Micromechanics and Micro engineering, England, v.3, p. 168-182, 1993.

GREENWOOD, J. C. (1988). Silicon in mechanical sensors. Journal of Physics E: Scientific Instruments, 21(12), 1114.

HAMEDI, M. M. et al., "Coated and Uncoated Cellophane as Materials for Microplates and Open-Channel Microfluidics Devices", Lab. Chip 16(20), 3885-3897 (2016).

HAMMACHER, J., et al., Stress engineering and mechanical properties of SU-8-layers for mechanical applications. Microsystem Technologies, 2008. 14(9): p. 1515-1523.

HORN, H. W., SWOPE, W. C., PITERA, J. W., MADURA, J. D., DICK, T. J., HURA, G. L. AND T. HEAD-GORDON, J. Chem. Phys. 120, 9665 (2004).

ILIESCU, C., TAY, E.H.F., XU, G., YU, L. M., SAMPER, V. A dielectrophoretic chip packaged at wafer level. Microsystem Technologies. Vol. 12, n. 11-12, 987-992, 2006.

JANASEK, D., FRANZKE, J., MANZ, A., 2006, Scaling and the design of miniaturized chemical-analyses systems. *Nature, 442*(7101), p.374.

JIA, Z. J., FANG, Q., FANG, Z.L. Bonding of glass microfluidic chips at room temperatures. Analytical Chemistry. Vol. 76, 5597 -5602, 2004.

KAKUTA, N. *et al.* "Simultaneous imaging of temperature and concentration of ethanol-water mixtures in microchannel using near-infrared dual-wavelength absorption technique," Meas. Sci. Techno. **27**, 115401 (2016).

KAKUTA, N. *et al.* "Temperature imaging of water mixtures in a microchannel using thermal sensitivity of near-infrared absorption," Lab Chip **11**, 3479-86 (2011).

KAMBLE, HARSHAD, ET AL. "Cell stretching devices as research tools: engineering and biological considerations." Lab on a Chip 16.17 (2016): 3193-3203.

KESTIN, J., SOKOLOV, M., & WAKEHAM, W. A. (1978). Viscosity of liquid water in the range− 8 C to 150 C. Journal of Physical and Chemical Reference Data, 7(3), 941-948.

KHALID, N., KOBAYASHI, I. and NAKAJIMA, M., 2017. Recent lab-on-chip developments for novel drug discovery. Wiley Interdisciplinary Reviews: Systems Biology and Medicine, 9(4), p. e1381.

KUCHUK, V. I., SHIROKOVA, I. Y., GOLIKOVA, E. V., Glass Phys. Chem.+ 38: 460 (2012).

KULKARNI, A. S. (2004). Effects of surface roughness in microchannel flows (Doctoral dissertation, University of Florida).

KUNCOVA-KALLIO, J. and KALLIO, P. J., PDMS and its Suitability for Analytical Microfluidic Devices. in Engineering in Medicine and Biology Society, 2006. EMBS '06. 28th Annual International Conference of the IEEE. 2006.

LEE, C. Y., CHANG, C.L., WANG, Y.N. and FU, L.M., 2011. Microfluidic mixing: a review. International journal of molecular sciences, 12(5), pp.3263-3287.

LEE, D. B., 1969. Anisotropic etching of silicon. Journal of Applied physics, 40(11), pp.4569-4574.

LEE, S. J.; SUNDARARAJAN, N. Microfabrication for Microfluidics. Artech House: Norwood, MA, 2010; pp 2.

LI, L., & ISMAGILOV, R. F. (2010). Protein crystallization using microfluidic technologies based on valves, droplets, and SlipChip. Annual review of biophysics, 39, 139-158.

LIU, D., CITO, S., ZHANG, Y., WANG, C. F., SIKANEN, T. M., SANTOS, H. A., “A versatile and robust microfluidic platform toward high throughput synthesis of homogeneous nanoparticles with tunable properties.” Adv. Mater. 27, 2298– 2304 (2015).

LIU, G., SHEN, C., YANG, Z., CAI, X., & ZHANG, H. (2010). A disposable piezoelectric micropump with high performance for closed-loop insulin therapy system. Sensors and Actuators A: Physical, 163(1), 291-296.

LIU, L., XU, H., LICHTENBERGER, A. W., WEIKLE II, R. M., “Integrated 585-GHz hot-electron mixer focal-plane arrays based on annular slot antennas for imaging applications,” IEEE T. Microw. Theory 58, 1943-1951 (2010).

LO, R. C. Microfluidics technology: future prospects for molecular diagnostics. Advanced Health Care Technologies, 3, pp.3-17 (2017).

LOCHOVSKY, C., YASOTHARAN, S., & GÜNTHER, A. (2012). Bubbles no more: in-plane trapping and removal of bubbles in microfluidic devices. Lab on a Chip, 12(3), 595-601.

MADOU, M. J., 2011. Fundamentals of Microfabrication and Nanotechnology, Three-Volume Set.

MALA, G. M., & LI, D. (1999). Flow characteristics of water in microtubes. International journal of heat and fluid flow, 20(2), 142-148.

MARK, D., HAEBERLE, S., ROTH, G., VON STETTEN, F., & ZENGERLE, R. (2010). Microfluidic lab-on-a-chip platforms: requirements, characteristics and applications. In Microfluidics Based Microsystems (pp. 305-376). Springer, Dordrecht.

MATVEJEV, V., DE TANDT, C., RANSON, W., STIENS, J., R. VOUNCKX, D. MANGENLINGS, “Integrated waveguide structure for highly sensitive THz spectroscopy of Nano-liter liquids in capillary tubes” Prog. Electromagn. Res. **121**, 89-101 (2011).

MATVEJEV, V., DE TANDT, C., RANSON, W., STIENS, J., “Wet silicon bulk microchannel THz waveguides for low-loss integrated sensor applications.” 35th International Conference on Infrared, Millimeter and Terahertz, Italy, (2010).

MATVEJEV, V., ZHANG, Y., STIENS, J., “High performance integrated terahertz sensor for detection of biomolecular processes in solution.” IET Microwaves, Antennas and Propagation **8**(6), 1-7 (2013).

MATVEJEV, V., ZIZI, M., STIENS, J., “Hydration shell parameters of aqueous alcohols: THz excess absorption and packing density”, J. Phys. Chem. B. **116**(48), 14071–14077 (2012).

McDONALD, J. C.; WHITESIDES, G. M.; Acc. Chem. Res. 2002, 35, 491.

McDONALD, J. C., et al., Fabrication of microfluidic systems in poly(dimethylsiloxane). ELECTROPHORESIS, 2000. 21(1): p. 27-40.

MESSAOUD, A. Y., E. SCHEID, G. SARRABAYROUSE, AND A. CLAVENE. "W. KERN AND DA PUOTINEN." RCA Rev 31 (1970): 187.

MOISEEVA, E. V., FLETCHER, A. A., & HARNETT, C. K. (2011). Thin-film electrode based droplet detection for microfluidic systems. Sensors and Actuators B: Chemical, 155(1), 408-414.

NGUYEN, N. T., LASSEMONO, S., & CHOLLET, F. A. (2006). Optical detection for droplet size control in microfluidic droplet-based analysis systems. Sensors and actuators B: Chemical, 117(2), 431-436.

NGE, P. N. et al., “Advances in microfluidic materials, functions, integration, and applications”. Chem. Rev. 113, 2550–2583 (2013).

NIU, X., ZHANG, M., PENG, S., WEN, W., & SHENG, P. (2007). Real-time detection, control, and sorting of microfluidic droplets. Biomicrofluidics, 1(4), 044101.

OCOLA, L. E., PALACIOS, E., “Advances in ion beam micromachining for complex 3D microfluidics”, J. Vac. Sci. Technol. B 31, 06F401 (2013).

PAL, P., & SATO, K. *Silicon wet bulk micromachining for MEMS*. Pan Stanford. (2017).

PALACIOS, E., OCOLA, L. E., JOSHI-IMRE, A., BAUERDICK, S., BERSE, M., and PETO, L., “Three-dimensional microfluidic mixers using ion beam lithography and micromachining”, J. Vac. Sci. Technol. B 28, C6I1 (2010).

PARK, J.S., Song, S.H. and JUNG, H.I., 2009. Continuous focusing of microparticles using inertial lift force and vorticity via multi-orifice microfluidic channels. Lab on a Chip, 9(7), pp.939-948.

PAN, Y.J., YANG, R.J. A glass microfluidic chip adhesive bonding method at room temperature. Journal of Micromechanics and Microengineering Vol.16, 2666-2672, 2006.

PRENTNER, S., et al. "Effects of channel surface finish on blood flow in microfluidic devices." Microsystem technologies 16.7 (2010): 1091-1096.

QU, W., MALA, G. M., & LI, D. (2000). Heat transfer for water flow in trapezoidal silicon microchannels. International Journal of Heat and Mass Transfer, 43(21), 3925-3936.

REISMAN, A., BERKENBLIT, M., CHAN, S. A., KAUFMAN, F. B., and GREEN, D. C. The controlled etching of silicon in catalized ethylenediamine-pyrocatechol-water solutions, J.Electrochem.Soc., 126 (1979) 1406.

RIBEIRO, L. E. B., et al. "Analysis of the Planar Electrode Morphology Applied to Zeolite Based Chemical Sensors." Sensors & Transducers 193.10 (2015): 80.

RIBEIRO, L. E. B., PIAZZETTA, M. H., GOBBI, A. L., COSTA, J. S., DA SILVA, J. A. F., & FRUETT, F. (2010). Fabrication and characterization of an impedance micro-bridge for lab-on-a-chip. ECS Transactions, 31(1), 155-163.

SABRY, M-N. "Scale effects on fluid flow and heat transfer in microchannels." IEEE Transactions on components and packaging technologies 23.3 (2000): 562-567.

SAUL, CYRO KETZER, and IX–Microelectronica CYTED-Subprograma. "Corrosão Anisotrópica de Silício em Soluções Alcalinas Fundamentos e Aplicações Cyro Ketzer Saul." (2004).

SAYAH, A., & GIJS, M. A. (2016). Understanding the mixing process in 3D microfluidic nozzle/diffuser systems: Simulations and experiments. Journal of Micromechanics and Microengineering, 26(11), 115017.

SCHIANTI, J. D. N., 2008. Sistemas de microcanais em vidro para aplicações em microfluidica (Doctoral dissertation, Universidade de São Paulo).

SCHIANTI, J. D. N., & Rúbio, M. R. G. (2017, August). Parylene-C film as hydrophobic surface in glasses microfluidic devices for double emulsions. In Microelectronics Technology and Devices (SBMicro), 2017 32nd Symposium on (pp. 1-4). IEEE.

SEIDEL, H., CSEPREGI, L., HEUBERGER, A. and BAUMGARTEL, H., Anisotropic Etching of Crystalline silicon in Alkaline Solution, J. Electrochem. Soc., 137 (1990) 3612-3626.

SCOTT, R., SETHU, P., & HARNETT, C. K. (2008). Three-dimensional hydrodynamic focusing in a microfluidic Coulter counter. Review of Scientific Instruments, 79(4), 046104.

SIEGEL, P. H. “Terahertz Technology in Biology and Medicine,” IEEE T. Microw. Theory, **52**, 2438-2447 (2004).

SQUIRES, T. M., QUAKE, S.R., Microfluidics: Fluid physics at the Nano liter scale. Reviews of Modern Physics. Vol. 77. 977-1026. 2005.

STREET, R.L., WATTERS, G.Z. AND VENNARD, J.K., 1996. Elementary fluid mechanics (p. 757). New York: John Wiley & Sons.

SUDARSAN, A. P., UGAZ, V. M., “Multivortex Micromixing”, P. Natl. A. Sci. USA 103(19), 7228-7233 (2006).

SUN, Y. and Y.C. KWOK, Polymeric microfluidic system for DNA analysis. Analytica Chimica Acta, 2006. 556(1): p. 80-96.

SWART, J. W. (2008). Semicondutores: Fundamentos, técnicas e aplicações. Editora da UNICAMP.

TABATA, O., ASAHI, R., FUNABASHI, H., SHIMAOKA, K., and SUGIYAMA, S., Anisotropic etching of silicon in TMAH solutions, Sensors and Actuators A, 34 (1992) 51.

TABELING, P. "Recent progress in the physics of microfluidics and related biotechnological applications." Curr. Opin. Biotech. **25**, 129–134 (2014).

TAN, C., LO, S.J., LEDUC, P.R. and CHENG, C.M., 2012. Frontiers of optofluidics in synthetic biology. Lab on a Chip, 12(19), pp.3654-3665.

TANG, S.K. and WHITESIDES, G.M., 2010. Basic microfluidic and soft lithographic techniques. In Optofluidics: Fundamentals, Devices and Applications (pp. 7-32). McGraw-Hill.

TERRY, S. C.; JERMAN, J. H.; ANGELL, J. B.; **IEEE Trans. Electron Devices** 1979, ED-26, 1880.

TURATTI, L. G., & Brasil, C. S. WTProcess, (2003) (Master Dissertation).

UNGER, M. A., CHOU, H. P., THORSEN, T., SCHERER, A., & QUAKE, S. R. (2000). Monolithic microfabricated valves and pumps by multilayer soft lithography. Science, 288(5463), 113-116.

UTKE, I., MOSHKALEV, S., & RUSSELL, P. (Eds.). (2012). Nanofabrication using focused ion and electron beams: principles and applications. Oxford University Press.

VLADISAVLJEVIĆ, G. T., KHALID, N., NEVES, M. A., KUROIWA, T., NAKAJIMA, M., UEMURA, K., & KOBAYASHI, I. (2013). Industrial lab-on-a-chip: Design, applications and scale-up for drug discovery and delivery. *Advanced drug delivery reviews*, *65*(11-12), 1626-1663.

XIA, Y. and G.M. WHITESIDES, SOFT LITHOGRAPHY. Annual Review of Materials Science, 1998. 28(1): p. 153-184.

WHITESIDES, G. M., 2006. The origins and future of microfluidic. *Nature, 442*(7101), p.368.

WU, Z., et al., Polymer microchips bonded by O2-plasma activation. ELECTROPHORESIS, 2002. 23(5): p. 782-790.

YAGER, P., EDWARDS, T., FU, E., HELTON, K., NELSON, K., TAM, M.R. and WEIGL, B.H., 2006. Microfluidic diagnostic technologies for global public health. Nature, 442(7101), p.412.

YANG, J., QI, L., CHEN, Y. and MA, H., 2013. Design and fabrication of a three dimensional spiral micromixer. Chinese Journal of Chemistry, 31(2), pp.209-214.

YANG, R.J., FU, L.M. and HOU, H.H., 2018. Review and perspectives on microfluidic flow cytometers. Sensors and Actuators B: Chemical.

ZAKURENOV V.M.; KONYAKHIN V.P.; NOZDREV V.F.: The Viscosities of Ethanol-Cyclohexane Mixtures. Zh.Fiz.Khim. 49 (1975) 548-549.

ZHANG, J., YAN, S., YUAN, D., ALICI, G., NGUYEN, N.T., WARKIANI, M.E. and LI, W., 2016. Fundamentals and applications of inertial microfluidics: a review. Lab on a Chip, 16(1), pp.10-34.

ZHANG, Z., KAN, J., CHENG, G., WANG, H., & JIANG, Y. (2013). A piezoelectric micropump with an integrated sensor based on space-division multiplexing. Sensors and Actuators A: Physical, 203, 29-36.

ZHU, T., CHENG, R., LEE, S.A., RAJARAMAN, E., EITEMAN, M.A., QUEREC, T.D., UNGER, E.R. and MAO, L., 2012. Continuous-flow Ferro hydrodynamic sorting of particles and cells in microfluidic devices. Microfluidics and nanofluidics, 13(4), pp.645-654.

ZOLFAGHARIAN, A., KOUZANI, A. Z., KHOO, S. Y., MOGHADAM, A. A. A., GIBSON, I., & KAYNAK, A. (2016). Evolution of 3D printed soft actuators. Sensors and Actuators A: Physical, 250, 258-272.

ZUBEL, I., and BARYCKA, I., Silicon anisotropic etching in alkaline solutions I: The geometric description of figures developed under etching Si (100) in various solutions, Sensors and Actuators A, 70 (1998) 250.

8 APPENDIX

1) Cell Reynolds number has no good agreement with analytical solution.

The Reynolds Number is fundamental to the analysis of fluid flow. The Navier-Stokes interface automatically calculates the local cell Reynolds number, Eq. A.1:

$$Re^c = \frac{\rho v h}{2\mu} \qquad \text{Equation (A.1)}$$

where $\boldsymbol{Re^c}$ is the cell Reynolds number, $\boldsymbol{\rho}$ is the density, $\boldsymbol{\mu}$ is the fluid dynamic viscosity, $\boldsymbol{h}$ is the element length (from Comsol element cell size) and $\boldsymbol{v}$ is the magnitude of the velocity vector for the velocity scale (as described in Eq. 2.3). The cell Reynolds number is a predefined quantity available for visualization and evaluation (typically it is available as: spf.cellRe), as shown in Fig. A.1 (COMSOL USERS MANUAL).

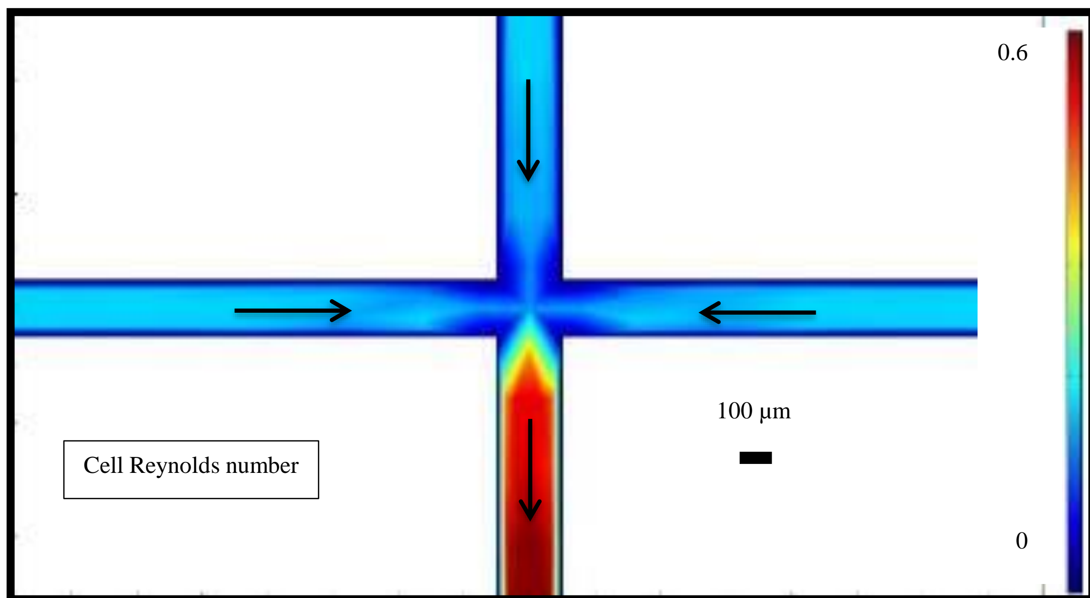

Figure A.1 – Cell Reynolds number plot with channel width of 100 µm and depth of 33 µm.

In this case, it is no possible to make comparison between analytical solution and native cell Reynolds number from Comsol. For example, Reynolds number calculation for rectangular

channel, dimension w=100 µm, h=33 µm, Q=50 µl/min, water properties at 20 ºC, the analytical solution is Re=12.53 and Comsol solution is Re_c=0.25, it means model is around of 50 times larger than Comsol solution, as shown in Table A.1. Thus occurs, because element length h used for calculated cell Reynolds number is 50 times smaller than microchannel width. Table A.1 shows results from experiments and simulation at Comsol, however due to cell Reynolds calculations in Comsol is different from analytical solution, they cannot be compared.

Table A.1 – Results obtained in the experiments and simulation at Comsol.

Substrate Material	Reynolds number (Re)	Cell Reynolds in Comsol* (Re^c)
Silicon	3.27	0.08
	1.73	0.04
	3.15	0.06
	1.70	0.03
PDMS	2.47	0.02
	2.68	0.02
Glass	1.41	0.03
	1.27	0.03
	0.79	0.01
	0.89	0.01
	1.71	0.03
	1.05	0.02
	0.99	0.02
	3.18	0.10
	2.74	0.08

2) Mesh criteria: there are nine predefined mesh in Comsol: extremely coarse, extra coarse, coarser, coarse, normal, fine, finer, extra fine and extremely fine. They can guide to different number of freedom elements, time for converge solution, size of mesh element min and max, quality of mesh element min and max.

We tested different mesh sizes: a) Number of degrees of freedom solved for: 8165. Solution time (Study 1): 9 s. (Fine). Working set: 618MB Virtual memory: 871MB.

b) Number of degrees of freedom solved for: 15037.Solution time (Study 1): 80 s. (Extra fine) Working set: 1.2GB Virtual memory: 1.2GB.

c) Number of degrees of freedom solved for: 262829. Solution time (Study 1): no convergence. (Custom mesh) Working set: 1.2GB Virtual memory: 1.2GB.

For the case b), we found a good agreement, between time to converge solution, error, size of mesh element min=5μm and max=30μm, quality of mesh element min=0.19 and max=0.99. Based on these parameters we decide to use in all simulated models extra fine mesh, as shown in Fig. A.2.

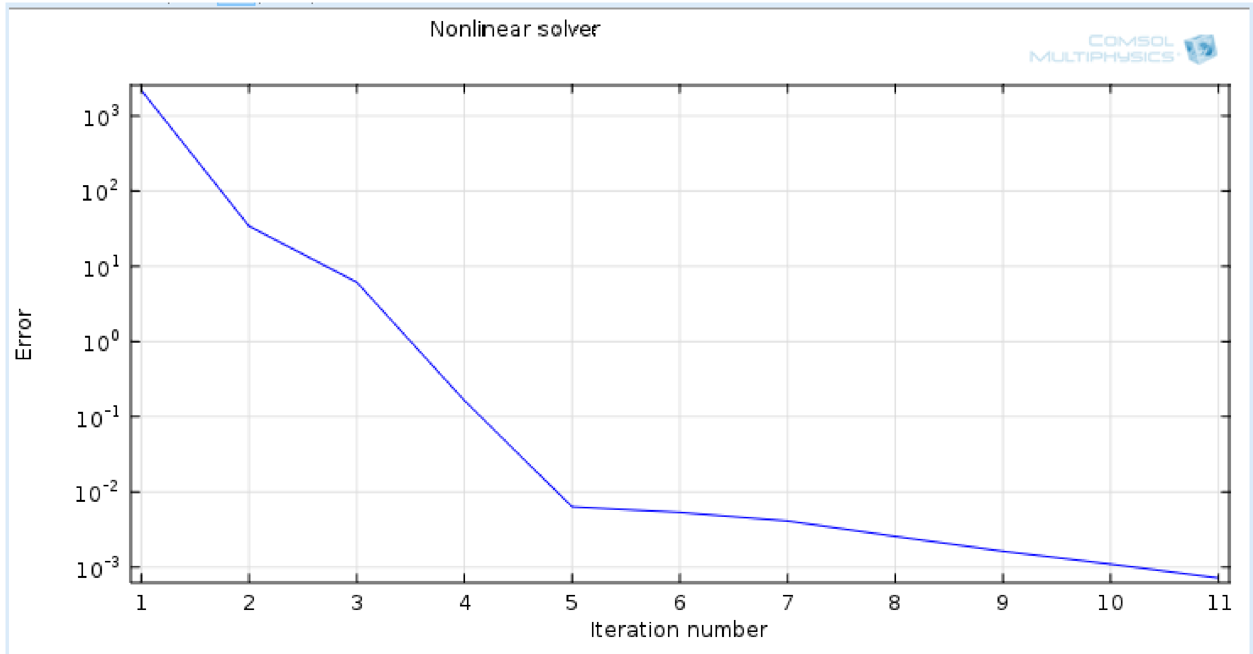

Figure A.2 – Plot of error and iteration number to converge solution.

3) 2D models are limited in relation to 3D models. Comsol has improved 2D simulation features: e.g drag force is taking into account in Shallow Channel Approximation, this method is applied for 2D models simulation. The form of this term is Eq. A.2:

$$F_u = \frac{-12\mu \boldsymbol{v}}{dz^2} \qquad \text{Equation (A.2)}$$

where $\boldsymbol{\mu}$ is the fluid's dynamic viscosity (SI unit: kg/(m·s)), $\boldsymbol{v}$ is the velocity field (SI unit: m/s), and $\boldsymbol{dz}$ is the channel thickness (SI unit: m). The shallow channel approximation takes the effect of top and bottom boundaries into account by adding a drag term as a volume force to the fluid flow equation. This term represents the resistance that the parallel boundaries place on the flow; however, it does not account for any changes in velocity due to variations in the cross-sectional area when the channel thickness differs, only in 3D models (COMSOL USERS MANUAL).

4) Mesh in Finite Element Modeling. The finite element analysis is a numerical method to solve partial differential equations. The finite element method relies on meshing the spatial domain into multiple elements. A finer mesh with more elements provides a more accurate solution, but a finer mesh requires longer solving times than a cruder mesh (LEE, 2010).

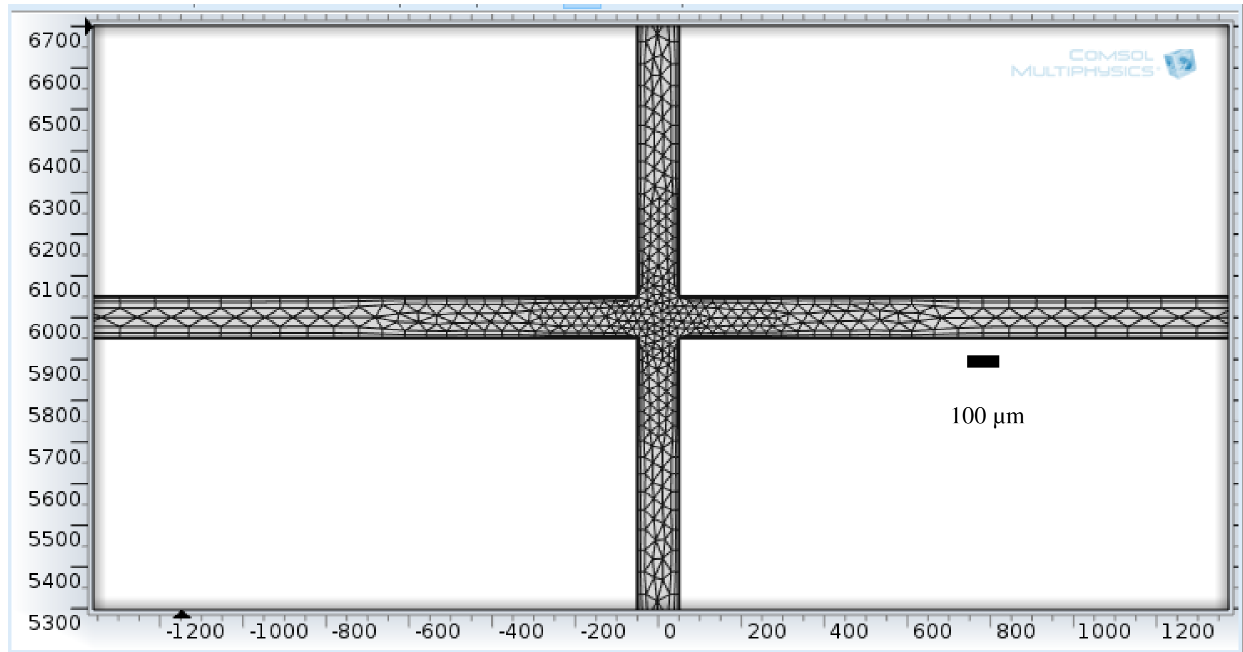

Figure A.3 – Plot of free tetrahedral mesh with a COMSOL Multiphysics ® predetermined element size of "extra fine" was utilized.

The finite element method utilizes an iterative process to calculate a solution to all couple field variables, as shown in Fig. A.3, free tetrahedral elements. When performing finite element modeling, the user must first build the geometry. Models, material properties, and boundary conditions are applied to the geometry and then meshed. Upon meshing, the computations begin. The major challenge is the successful convergence of the algorithms, which then produces a solution. If the algorithms diverge, the user has no results. The user must then confirm all values are correctly entered and well defined problem boundary conditions (DONAVAN, 2014).

5) Discretization: the element types used in the finite element formulation. From the Discretization of fluids list select the element order for the velocity components and the pressure: P1+P1, P2+P1, or P3+P2.

P1+P1 means linear elements for both the velocity components and the pressure field. This is the default element order for the Laminar Flow interface. Linear elements are computationally cheaper than higher-order elements and are also less prone to introducing spurious oscillations, thereby improving the numerical robustness, as shown in Fig. A.4.

P2+P1 means second-order elements for the velocity components and linear elements for the pressure field.

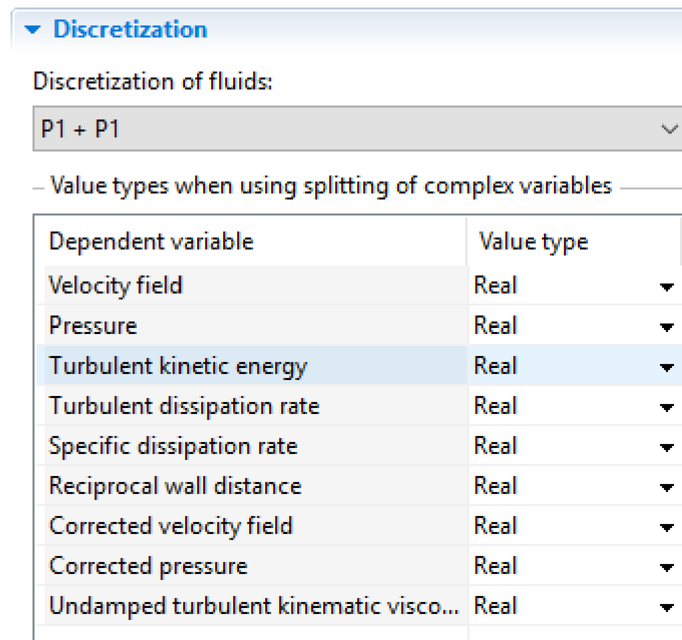

Figure A.4 – Parameters of fluid discretization P1+P1 utilized in COMSOL.

This is the default for the Creeping Flow interface because second-order elements work well for low flow velocities. P3+P2 means third-order elements for the velocity components and second-order elements for the pressure field. This can add additional accuracy but it also adds additional degrees of freedom compared to P2+P1 elements. We selected the discretization P1+P1 base on computer limitation.

COMSOL USERS MANUAL. "Comsol Multiphysics Users Guide." (2011).

DONOVAN, K.J., 2014. Computational Fluid Dynamics Modeling of Two-Dimensional and Three-Dimensional Segmented Flow in Microfluidic Chips.

LEE, S. J.; SUNDARARAJAN, N. Microfabrication for Microfluidics. Artech House: Norwood, MA, 2010; pp 2.

ABSTRACT

The miniaturization process allows reactions of liquid mixtures and faster analyzes, in smaller volumes, with portable and more reliable devices. The main challenges are in the manufacturing with high precision and integration of microchannels with sensors. We have developed complete protocols for obtaining microchannels with integrated actuators and sensors, involving conventional microfabrication and characterization techniques compatible with clean room facilities. Resulting in devices fabricated in silicon, glass and polydimethylsiloxane (PDMS), with microchannels widths between 100 and 458 μm, depth between 20 and 64 μm. We present new methodologies for Lab-On-a-Chip (LOC) applications: 1) System with microchannels integrated to a capacitive sensor. 2) Active mixer with electromagnetic actuators in microchannels. 3) Passive mixer with coupled terahertz sensor for control of concentration of ethanol on demand. We present the complete microfluidic system for the micro droplets generation of water/oil and micro capacitive sensor, for detection and control of volume and droplet velocity up to 1mm in length. We present an active mixer, with integrated PDMS membrane with electromagnetic actuators, establishing the correlation between the liquid mixture improvement and the oscillation frequency. We present sub-THz sensor coupled to microfluidic platform with non-invasive, contactless and label-free measurements for determination of ethanol concentration and control on demand. We demonstrated on-line sensing, operating at 60 GHz, with a dynamic range of 2.79 dB, ethanol concentration control with a variation of 0.32% (v / v) and passive micro-mixer with curved channels operating in laminar flow with number of Reynolds <16.26 and Peclet> 25700. In addition, we present a preliminary study with simulation of finite element method (FEM) in comparison with theoretical models. We presented the fluid characterization regime and application of microfluidic devices.